IMPERIAL COLLEGE LONDON

Laser cooling of CaF molecules

Valentina Zhelyazkova

A thesis submitted in partial fulfillment for the
degree of Doctor of Philosophy

Department of Physics

July 2014

Declaration of Originality

I declare that, unless otherwise stated, the work presented in this thesis is my own. Where I have used the work of others the sources are appropriately referenced. All presented data was taken and analyzed by me. The rate equation model as well as parts of sections (7.6.3) and (7.6.4) were contributed by M. Tarbutt.

Parts of the work described in this thesis have been published in the following article:

V. Zhelyazkova, A. Cournol, T. E. Wall, A. Matsushima, J. J. Hudson, E. A. Hinds, M. R. Tarbutt and B. E. Sauer. Laser cooling and slowing of CaF molecules, *Phys. Rev. A*, **89**, 053416, May 2014

Abstract

Cold and ultracold molecules are highly desirable for a diverse range of applications such as precision measurements, tests of fundamental physics, quantum simulation and information processing, controlled chemistry, and the physics of strongly correlated quantum matter. Although laser cooling has been enormously successful in cooling atomic species to extremely low temperatures, this technique has long been thought to be infeasible in molecules because their complex structure makes it difficult to find a closed cycling transition. Recently, however, several diatomic molecules, one of which is CaF, have been shown to possess a convenient electronic structure and highly diagonal Franck-Condon matrix and thus be amenable to laser cooling.

This thesis describes experiments on laser cooling of CaF radicals produced in a supersonic source. We first investigate the increased fluorescence when multi-frequency resonant light excites the molecules from the four hyperfine levels of the ground $X^2\Sigma^+(N = 1, v = 0)$ state to the first excited $A^2\Pi_{1/2}(J' = 1/2, v' = 0)$ state. The number of photons scattered per molecule increases significantly from one or two in the single frequency case to more than 50 before the molecules get pumped into the $X^2\Sigma^+(N = 1, v = 1)$ state.

We demonstrate laser cooling and slowing of CaF using counter-propagating laser light which causes the molecules to scatter more than a thousand photons on the $X(N = 1, v = 0, 1) \leftrightarrow A(J' = 1/2, v' = 0)$ transition. The effect of the laser cooling is to slow a group of molecules from 600 $\mathrm{m\,s^{-1}}$ to about 580 $\mathrm{m\,s^{-1}}$ and to narrow their velocity distribution from an initial temperature of 3 K down to 300 mK. In addition, chirping the frequency of the cooling light to keep it on resonance with the decelerating molecules doubles the deceleration and further compresses the velocity distribution. The effect of the laser cooling is limited by the optical pumping of molecules in the $X(N = 1, v = 2)$ state.

Acknowledgements

The work described in this thesis would not have been possible without the help, guidance and support of many people. First of all, I would like to thank Ed Hinds for giving me the opportunity to work in the group and for setting such high standards for research.
I have been incredibly fortunate to have Mike Tarbutt as a teacher and supervisor and would like to thank him for his patience and for never being too busy to explain things to me. I am very grateful for his constructive criticism and thorough reading of this thesis.
I am also very happy to have had Ben Sauer and Jony Hudson as supervisors. I want to thank Ben for his help in the lab, guidance and dry sense of humor. Many thanks to Jony for his support and for always making me find things out by myself. I have learnt a lot from Ben and Jony both in and outside of the lab and thank them for their friendship. I don't think I would have made it without the pub sessions.
I am extremely lucky to have worked with two excellent postdocs. I would like to thank Thom for making the first years of my PhD exceptionally enjoyable. We have shared many fruitful discussions and cups of tea. I am indebted to Anne for all her hard work and dedication during the later stages of the project that naturally led to the good results we had.
I also had a great time in Bay 3 and would like to thank Aki, Joe and Jack for their help and for making the lab such a nice place to work. You made the dye laser disasters much easier to bear! Special thanks to the Huxley people for the support (moral and otherwise), the stimulating discussions and all the fun we had.
Many thanks to Jon and Steve for getting things done so quickly and to Val for always being able to help. Special thanks to Sanja for her support and friendship. Finally, a big thank you to all the members of CCM for making my PhD such a fulfilling experience and for making me feel at home.

I owe a lot to my parents and family and thank them for their understanding, endless love and support. I want to thank Brendan for his infinite patience, for putting up with me while writing this thesis and for giving up his monitor and desk so I have a place to work.

Contents

List of Figures

List of Tables

Chapter 1

Introduction

There has been a growing interest in the study of dilute cold molecular gases for a variety of applications including precision measurements, tests of fundamental physics, quantum information (QI), astrophysics, many-body physics and cold chemistry [1]. Laser cooling is an efficient and well established technique for atoms in the gaseous phase, but is not traditionally used to cool molecules because their complex structure makes it difficult to find a closed cycling transition. However, recently several diatomic molecules have been shown to possess the highly diagonal Franck-Condon (FC) matrix and convenient electronic structure needed for laser cooling [2, 3].

Calcium fluoride is one of the viable candidates for laser cooling. This thesis describes work on laser slowing and cooling of CaF radicals produced in a supersonic source. In the experiment, the laser light resonant with a closed rotational and almost closed vibrational transition is counter-propagating to the molecular beam. The molecules that have interacted with the laser light are decelerated and have their velocity spread bunched. In addition to that, we chirp the frequency of the cooling beams so that they stay on resonance with the slowing molecules. The laser cooled molecules have been decelerated from a starting speed of 600 $\mathrm{m\,s^{-1}}$ to a final one of approximately 560 $\mathrm{m\,s^{-1}}$, while the final temperature is approximately 300 mK.

The results presented in this thesis in a way parallel the first laser cooling experiments on neutral sodium atoms from a thermal beam from the 1980s. Thus, a good place to begin this chapter is by a brief summary of the history of laser cooling. The reader is referred to the review article [4] and to [5] for more details.

1.1 Laser cooling atoms

Laser cooling of atoms has played a central role in the development of physics in the second half of the 20^{th} century. The ability to slow atoms down with near-resonant light and confine them in space presents an intriguing possibility for exploring quantum phenomena

and offering a test ground for theory. Laser cooling thus holds a paramount place in metrology and has dramatically improved the precision of atomic clocks. Laser cooling has also been essential in the realization of trapped ions as the first scalable quantum computation architecture fulfilling many of the DiVinzenco criteria [6] and has made it possible to reach the regime of quantum degeneracy [7].

1.1.1 The principle of laser cooling

Using resonant laser light is a very effective way of controlling an atom's motion. The underlying principle is very simple. When an atom of mass m absorbs a photon from a light field resonant with an atomic transition, it receives a momentum kick in the direction of propagation of the laser beam (or the $\vec{k}$-vector of the light). Upon absorption, the atom's velocity is reduced by the recoil velocity $v_r = \hbar k/m$. The atom must decay from its excited state before it can absorb a photon again. Spontaneous emission, however, is a spatially isotropic process and has no net effect on the atom's motion. After many absorption-spontaneous emission cycles the atom is slowed down preferentially in the direction of laser propagation. The force exerted by the laser field on the atomic motion is what we will refer to as the *spontaneous* or *scattering* force. Usually, the laser frequency is tuned slightly below the atomic transition frequency. Then, in order to absorb a photon, the atom must be moving towards the laser beam at some velocity v which will Doppler-shift it into resonance with the laser light. This results in a net force opposing the atomic motion proportional to its velocity and is what is referred to as 'Doppler cooling'. This viscous force can be applied in all six spatial dimensions to capture the atoms in a so-called 'optical molasses'.

1.1.2 A brief history of laser cooling

The interaction between atoms and light has long been studied both theoretically and experimentally. The history of slowing down atoms by radiation pressure dates back to 1933 when Frisch demonstrated that a sharply collimated beam of atomic sodium can be deflected by resonant radiation from a lamp [8]. The theoretical interest in using the mechanical properties of light to control the atomic motion preceded some of the experiments. In 1962 Askar'yan proposed the idea that intensity gradients can exert substantial forces on atoms due to the induced dipole moment [9]. A few years later, in 1968, Letokhov suggested that the dipole force can be used to trap atoms at the nodes or antinodes of a standing wave light field red-detuned from an atomic resonance [10]. The first suggestion to use laser light tuned close to an atomic resonance to velocity-analyze or slow down and subsequently trap a beam of sodium atoms came in the 1970 paper by Ashkin who was the first to realize that the interaction between the laser light and atoms falls into two categories - the spontaneous force due to the absorption and emission of photons and the

dipole force proposed by Askar'yan [11].

In the 1970s, the advance of the tunable lasers stimulated new experiments to test the suggested theories. The first observation of deflection of a beam of neutral sodium atoms by resonant laser light, similar to the earlier experiment by Frisch, was demonstrated in 1972 [12]. The idea of laser cooling of atomic vapor was later proposed in 1975 by Hänsh and Schawlow [13]. In the same year Wineland and Dehmelt had a similar idea but in the context of trapped ions [14]. Both proposals were based on the Doppler effect - this is where the term *Doppler cooling* originates. In 1978 Wineland *et al.* demonstrated the first radiation pressure cooling of Mg^{2+} ions in a Penning trap [15].

It is unsurprising that laser cooling was first demonstrated on trapped ions as they are localized in space. Extending laser cooling to neutral particles proved significantly more difficult as the thermal atomic beam sources (usually from an oven) used at the time produced atoms of velocities as high as 1000 $\mathrm{m\,s^{-1}}$ [16]. The first experiments demonstrating the effect of laser cooling in neutral atoms were aimed at slowing the atomic beam with the laser light counter-propagating to the atomic motion. The popular choice of atom at the time was sodium - it has a convenient structure with one unpaired electron in $3^2S_{1/2}$ ground state and transitions to the excited $3^2P_{3/2}$ state (the so-called D_2 line) at 588.9 nm which are accessible by dye lasers. The ground state has two hyperfine components ($F = 1$ and $F = 2$), both of which need to be connected to the excited state to avoid off-resonant optical pumping [17]. In the first experiments the velocity distribution of the atomic beam following the action of the laser light was determined by fluorescence from weak probe laser intersecting the atomic beam at an angle $\neq 90°$ (the resulting Doppler shift is a direct measure of the velocity). Here it is important to note that the counter-propagating laser beams not only slow the atoms but also reduce the spread of the atomic velocity distribution and thus the translational temperature. The reason for this is the following. The atoms traveling at a velocity v_0, with respect to which the cooling beams are tuned, are scattering first at a fast rate and then more slowly as they decelerate and are shifted out of resonance with the cooling beams. Those atoms initially traveling faster than v_0 will start scattering slowly, then more rapidly as they come into resonance and finally slowly again, while atoms with too low initial velocities will decelerate little. Thus, atoms from a range of velocities around v_0 are pushed into a narrower bunch around a lower velocity. This laser cooling process was theoretically studied by Minogin in 1980 [18].

The first convincing demonstration of laser cooling of a thermal beam of sodium atoms by counter-propagating laser light was demonstrated by Andreev and co-workers in 1980 at the Academy of Sciences of the USSR in Moscow [19]. The group at Moscow published several papers on theory and experiments in laser cooling [18, 20]. However, these first laser cooling experiments on sodium atoms were limited by the following effect: as an atom slows down, it becomes shifted out of resonance with the frequency of the cooling/slowing laser light and eventually ceases to scatter photons. This limits the range of velocities on

which the cooling acts and also the amount by which the atoms can be decelerated.
There are two ways to address this problem - either to introduce a spatially-varying magnetic field along the beam line which Zeeman-shifts the slowed atoms back into resonance or to chirp the laser light so that it follows the decelerating atoms. The fist experiment demonstrating a considerable velocity reduction of a Na beam (40% of the starting velocity) was reported by Phillips and Metcalf in 1982 at the National Bureau of Standards or NBS (today NIST) in Washington, USA [16]. In this pioneering experiment, the authors used a spatially varying magnetic field to adiabatically follow the changing Doppler shift of the slowing atoms. In addition, the circular polarization of the of the cooling light ensured that the scattering took place on the 'stretched' $3^2S_{1/2}(F = 2, m_F = 2) \rightarrow 3^2P_{3/2}(F = 3, m_F = 3)$ transition in order to avoid optical pumping. The work of Phillips and Metcalf is also of particular importance because the authors investigated in detail the issue of optical pumping which was not previously considered by the group in Moscow [20]. By extending the spatially varying magnetic field and doubling the field change the group at NBS was able to achieve even further deceleration to 4% of the initial velocity and significant velocity bunching corresponding to an effective temperature of 70 mK [21].
The method of frequency chirping the laser light to stay on resonance with the decelerating atoms was first suggested by Lethokhov in 1976 [22]. Phillips was entirely aware of this technique and proposed a method to apply the frequency chirp directly to the laser [23] but decided to first try the Zeeman cooler 'because it would be most fun' [17]. Nevertheless, Prodan *et al.* demonstrated the effect of chirping the laser light in 1984 [24].
Both the Zeeman slower and the frequency chirp techniques proved to be equally good[1] at slowing and cooling the atomic beams. In fact, the two papers demonstrating the stopping of atoms and even the reversal of their velocity using either the Zeeman slower [25] or the frequency chirp technique [26] appeared in the same issue of *Physical Review Letters* in 1985, one printed after the other.
The field of laser cooling continued to make big strides in the 1980s. However efficient laser cooling had proven to be in slowing the atoms from their initial thermal velocities, it would have been of little use if one could not capture and ideally trap the slowed atoms. The next step in the development of laser cooling was to apply laser beams red-detuned from the atomic transition in all three dimensions and to thus introduce a velocity-dependent restoring force for the atomic cloud in a so-called 'optical molasses'. In 1985 Chu *et al.* at Bell Laboratories demonstrated the first optical molasses in which atoms were confined in space by the viscous laser cooling force reaching a temperature of 240 μK, densities of $\sim 10^6$ cm^{-3} in a volume of 0.2 cm^3 with a decay constant of 0.1 s [27]. The optical molasses proved to be an invaluable tool for understanding sub-Doppler cooling effects which can reduce the temperature well below the Doppler limit [28].

[1] In [24] the authors suggest that the laser-chirping method might have a slight advantage over the Zeeman slower.

Further, an inhomogeneous magnetic field together with the appropriately chosen circular polarization of the laser light can be used to create a position-dependent trapping force in addition to the velocity-dependent cooling force. This is the principle behind the magneto-optic trap (MOT). In 1987 the first MOT was realized at the Bell Laboratories [29] in which more than 10^7 Na atoms at densities greater than 10^{11} cm^{-3} were held in the trap for 2 min. In 1997 Steven Chu, Claude Cohen-Tannoudji and William Phillips received the Nobel prize in Physics 'for development of methods to cool and trap atoms with laser light'.

Since the late 1980s the MOT has played a major role in the development of physics and paved the way to the first realization of a Bose-Einstein condensate (BEC) in an atomic gas by Eric Cornell and Carl Wieman in 1995 [7]. This was possible as once trapped magnetically the atoms can be subjected to evaporative cooling to reach temperature as low as 170 nK and density of 2.5×10^{12} cm^{-3} [30]. Today the majority of laser cooling experiments rely on the MOT as a starting point.

1.2 Why are cold molecules important

Because of their complex structure in terms of energy states, molecules offer exciting possibilities for exploring novel physics. The field of cold and ultracold molecules is so rich that it brings together research from a variety of traditionally disjoint fields including particle physics, astrophysics, quantum chemistry, quantum information and simulations, condensed matter physics and nuclear physics to name a few [31]. The field has rapidly grown from a few research groups in the 1990s to include hundreds of researchers nowadays.

The main applications of cold and ultracold molecules can be grouped in the following categories.

1.2.1 Many-body interactions

Even the simplest heteronuclear diatomic molecules have an important advantage over any atom because they interact very strongly with external electric fields and are easy to polarize. For some measurements, where the polarization of the system is important, molecules can offer much higher sensitivity than atoms.

Polar molecules interact strongly with one another via the long range dipole-dipole interactions which are fundamentally different from the short-range Van Der Waals interaction ($\propto r^{-6}$) between atoms. Ultracold (with temperatures in the the sub-mK range) molecular gases thus have unique properties that might pave the way to fundamental quantum physics discoveries.

A Bose-Einstein condensate (BEC) of polar molecules, for example, would exhibit the

properties of a quantum fluid of strongly and anisotropically interacting particles. Such a molecular BEC would also have fundamentally different properties than its atomic counterpart and could be used to study the link between BECs in dilute gases and in dense liquids.

The study of ultracold fermionic molecules is also of great interest. In such a system it is possible to create a Bose-Einsten condensate from a system of fermions rather than bosons. A molecular BEC of fermionic dimers has been experimentally demonstrated by sweeping the magnetic field across a Feshbach resonance in a ultracold gas of ^{40}K atoms [32] and by three-body recombination near a Feshbach resonance in a spin mixture of ^{6}Li atoms [33]. These experiments highlight the difference between weakly bound dimers composed of fermionic and bosonic atoms. While bosonic dimers decay quickly through inelastic atom-atom or atom-molecule collisions, dimers of fermions are remarkably stable with long lifetimes of the order of hundreds of ms [32] - much longer than the timescales for elastic collisions and thermalization. In such a system it is possible to examine the cross over between Bardeen-Cooper-Schrieffer (BCS) state of weakly correlated pairs of fermions to the BEC of diatomic molecules [34–36]. At low temperatures such a Fermi gas with attractive interactions is predicted to undergo a phase-transition into a superfluid BCS state in which two fermions form a Cooper pair. It is also possible to tune the molecular superfluid continuously between two limits - a BCS type of superfluidity characterized by correlated atom pairs in momentum space and a Bose-Einstein condensate in which spatially localized pairs of atoms are bound together. There has been a longstanding theoretical interest in the BEC-BCS crossover [37, 38] as this feature of attractively interacting Fermi gases can occur in a range of systems varying from high-temperature superconductors to neutron stars and QCD.

It has been predicted that a dipolar gas coupled to an optical lattice would exhibit a variety of exotic many-body states like supersolid, checkerboard and collapse phases [39, 40], in addition to the superfluid and Mott insulator phases already present in atoms. In order to explore these phenomena, cold polar molecules in the sub-μK temperature range are required.

1.2.2 Precision measurements and tests of fundamental physics

One of the most exciting applications of cold molecules is in tests of fundamental physics as this area extends beyond the traditional scope of reach of experimental atomic and molecular physics.

1.2.2.1 Time variation of fundamental constants

A fundamental physical constant of a theory can be defined as any constant that the theory cannot explain and is thus entirely determined by measurement [41]. The Standard Model,

for example, is characterized by 22 free parameters that cannot be determined from the theory and are therefore constants. However, in some extensions to the Standard Model some of the constants may change. Some of the high-dimensional modern theories aiming at the unification of gravity with the other three forces for example suggest that some of the fundamental constants may vary with time or space [42].

In the late 1990s astronomical observation from type Ia supernovae added to mounting evidence of the accelerated expansion of the universe. It is hypothesized that this expansion is driven by an unknown 'dark' energy which constitutes more than 68% of the mass of the universe. This unsettling discovery spurred the birth of many theories trying to explain the mechanism of action behind this phenomenon. In addition to the cosmological constant, which is a homogeneous constant energy density term, scalar fields which potentially vary in space and time were needed to explain the accelerating expansion of the universe. Some of the theories [43] suggest that the accelerated expansion of the universe can be explained by a so-called 'chameleon' scalar field which acquires effective mass depending on the local density of matter. These models also suggest a non-zero coupling strength to the fundamental forces that could lead to a variation of the fundamental constants with time, position or the local density of matter. The transitions in atoms and molecules provide a sensitive probe for the proposed variations of two of these constants: the electron-to-proton mass ratio ($\mu = m_e/m_p$) and the fine structure constant α. The different electronic energy scales (e.g. gross, fine and hyperfine structure) in an atom or molecule depend in different ways on α and μ [1]. In addition to that, molecules have rotational and vibrational transitions which depend in yet another way on these two constants making them a sensitive probe for these variations. So far the only way to look for variations in α and μ has been to study absorption and emission spectra of the same transition from different interstellar gas clouds in the line of sight of distant quasars. Astronomical data offers surprisingly good accuracy permitting measurements of $\Delta\alpha/\alpha$ and $\Delta\mu/\mu$ with precision of one part in 10^5 over time intervals of the order of 10 Gyr. However, different analysis of the astronomical data have led to contradictory results with some finding variations [44, 45] while others do not [46, 47].

Comparing laboratory-based and astronomical measurements of specific spectroscopic transitions can also place limits on $\Delta\alpha/\alpha$ and $\Delta\mu/\mu$. For example, measurements of two transition frequencies in the CH molecule to a precision of a few Hz has been used to place stringent limits to the variation of the two constants with the local density of matter in the Milky way: $\Delta\alpha/\alpha = (0.3 \pm 1.1) \times 10^{-7}$ and $\Delta\mu/\mu = (-0.7 \pm 2.2) \times 10^{-7}$ [48]. The inversion splitting in ammonia is also very sensitive to μ and a molecular fountain is being built to measure it [49].

1.2.3 Tests of fundamental symmetries

The Standard Model of physics has embedded in it three types of discrete symmetries: charge conjugation (or the replacement of particles with their anti-particles) (C), parity reversal (P) and time symmetry (T). The laws of physics are expected to be invariant under these symmetries. The first experimental evidence that one of these symmetries is violated came in 1956 when Wu *et al.* demonstrated that the direction of emitted electrons in the decay of ^{60}Co was asymmetric in space [50]. This suggested that weak interactions violate parity. A few years later, it was also found that kaon decays exhibit a slight asymmetry under the combined CP operation. The accepted symmetry of nature under which the laws of physics are Lorentz invariant has thus come to be the combined CPT symmetry.

1.2.3.1 Search for the electron EDM

The existence of a permanent electric dipole moment (EDM) in atoms, molecules or elementary particles (e.g. the electron, neutron or proton) would imply a violation of the parity (P) and time-reversal (T) symmetries. Since CP can be violated, assuming that nature is CPT invariant, is it is expected that the T symmetry can also be violated. Because the Standard Model incorporates a mechanism for breaking the CP symmetry, it also predicts a mechanism for the breaking of T-symmetry, but due to a fortuitous cancellation, it predicts exceedingly small values of the EDMs [1]. The Standard Model predicts a value of the electron EDM (eEDM), for example, of less than 10^{-36} e·cm which is too small to be detectable in any present experiment. However, some of the supersymmetric theories predict higher values of the eEDM that could in principle be measured. Finding a precise value for the electron EDM is a way to probe physics beyond the Standard Model [51].
The permanent EDM of an elementary particle $d_{e,n,p}$ (where the subscript refers to electron, neutron and proton) is aligned along the direction of the spin of the particle $\vec{\sigma}$. The electric dipole moment of an electron, for example, is thus $\vec{d}$=$d_e\vec{\sigma}$. The existence of d_e would imply that the electron energy in an applied external electric field -$\vec{E}\cdot\vec{d}$ depends on whether the electron spin is aligned parallel or anti-parallel to the electric field $\vec{E}$. However, because it is a charged particle, the electron cannot be simply placed inside an electric field. Instead, one can use an atom or molecule with a valence electron and look for the energy difference between two states differing in their spin orientation. Measuring $\vec{d}$ essentially involves polarizing the atom or molecule with an external electric field $\vec{E}$ and looking for the interaction energy $\eta\vec{d}\cdot\vec{E}$ where η is the polarizability of the system. According to Schiff's theorem [52] for a system of point particles in which only electrostatic forces are acting, the parameter η is zero. Intuitively, this means that the bound electron will not 'see' the applied electric field because it will be shielded by the other charged particles surrounding it. However, there are two limitations to this theorem: first, the charged particles inside the atom/molecule are not point-like and second, the theorem does not include relativistic

effects. It turns out that for a suitably chosen atom/molecule $\eta \neq 0$. The parameter η can be particularly large for heavy atoms and molecules because of relativistic effects. For example, the Tl atom is very sensitive to the eEDM with $\eta \sim -585$. Molecules offer even higher sensitivity. The polarization is usually small in atoms in laboratory-based fields because it involves mixing of electronic levels which are of the order of 10^{15} Hz apart. However, heavy polar molecules can amplify the applied laboratory field to a very high degree because it mixes different rotational levels typically of the order of tens of GHz apart.
So far the measurement of the value of d_e to the highest precision has been achieved in experiments with beams of polar molecules - in a supersonic beam of YbF molecules [53] (with result $|d_e| < 1.06 \times 10^{-27}$ e·cm) and in a cryogenic buffer gas source of ThO [54] ($|d_e| < 8.7 \times 10^{-29}$ e·cm). These experiments have sensitivity which depends on the interaction time with the molecules. There has been a proposal and an experiment is currently underway at Imperial College to apply laser cooling to YbF and make a molecular fountain to increase considerably the interaction time for the experiment [55].

1.2.3.2 Parity violations

In the Standard Model parity violation is well understood in the context of the weak interactions. In β-decay it is mediated by the weak charged currents $W^{+/-}$. Parity violation has also been observed in atoms [56] where it is mediated by the weak neutral currents. Parity violation has never been observed in molecules.
Chilarity[2] plays a central role in nature. One might expect that isomers which are mirror images of one another (or enantiomers) are equally common, but this is not the case. For example, all naturally occurring amino acids and therefore peptides, enzymes, proteins, etc. are left-handed. Often enantiomers have crucially different chemical properties[3]. It is thought that the weak force affects left-handed and right-handed molecules in a different way resulting in a small difference in the energy spectrum of enantiomers of chiral molecules. It is still debatable exactly what role parity violation of weak interactions has played in establishing the chilarity in biomolecules [57]. It is of interest to investigate this question experimentally. So far the most studied species are CH-XYZ where X, Y and Z are three different halogens. However, in these species the largest predicted energy shift is 50 mHz [58] while the current experiments have a precision of about 50 Hz [59]. Recently, much bigger energy shifts have been predicted in larger molecules that can be created in supersonic beams [60].
Parity violation also has a role in nuclear effects. One possibility is that spin-dependent parity-violating weak interactions in the nucleus can induce an anapole moment [61]. An

[2] A chiral molecule (or a molecule which has a handedness) is a molecule whose mirror image cannot be superimposed on itself.

[3] For example, S-limonene smells of citrus fruit, while R-limonene smells of turpentine. There is also the infamous case of the drug Thalidomide marketed in the 1960s. The drug was used to treat morning sickness but was later associated with a high rate of incidence of birth defects.

experiment to measure the anapole moment in the ^{137}Ba nucleus in a supersonic beam of BaF molecules is currently underway at Yale University [60]. Promising candidates to study molecular parity violation effects are laser-cooled RaF [62] and SrF. There has been some work on combining traveling-wave Stark deceleration and laser cooling in SrF in order to increase the interaction time for the measurement [63].

1.2.4 Quantum information processing

Molecules are a promising candidate for a quantum computation architecture as they bring together the advantages of both atoms (scalability to a large number of bits) and trapped ions (strong interactions). Polar molecules also offer the advantage that they interact via the long range dipole-dipole interactions.
Several proposals have been made for quantum information processing schemes with cold molecules. In one proposal [64], the qubits are the electric dipole moments of polar molecules aligned parallel or anti-parallel to an external electric field. The molecules are held in a 1D trap array with the electric field gradient providing the possibility of addressing each particular molecule individually. The bits are coupled via dipole-dipole interactions which provide entanglement. In this configuration one can have of the order of 10^4 qubits that can perform 10^5 CNOT gates in about 5 s.
Another proposal suggests using the strong dipole-dipole force between cold molecules to couple them to superconducting microwave strip line resonators [65].

1.2.5 Controlled quantum chemistry

Finally, an area that has attracted considerable interest is the study of collisions and chemical reactions in cold molecules. In the 1-100 mK temperature regime molecules are in their ground rotational state and can be easily trapped. This creates the possibility to measure collision and reaction cross-sections [66].
When molecules interact the centrifugal barrier due to the rotational motion of the complex may suppress the collisions. The total scattering wave function can be decomposed into contributions from the different angular momenta of the rotation complex called partial waves. Contributions from several partial waves are undesirable because they might give rise to multiple scattering resonances and partial wave interference phenomena. In the ultracold temperatures regime (<1mK), however, the collisions are entirely dominated by single partial wave scattering: $s-$wave scattering for bosons or distinct particles and $p-$wave scattering for fermions.
In addition to this, the long deBroglie wavelength of ultracold molecules fundamentally changes the nature of the reaction dynamics and collisions of even large molecules exhibit significant quantum effects. In this regime many-body interactions become dominant and the outcome of the reaction may depend entirely on the spatial confinement of the molecules

making it possible to manipulate the collisions and study controlled chemistry. Chemical reactions in the cold and ultracold regimes are generally very efficient [67, 68] and tunneling becomes the dominant pathway.

1.2.6 Temperature requirements

Molecules offer exciting possibilities to explore novel physics. In order to explore these possibilities it is essential that the samples are cold and preferably trapped to prolong the interaction time as much as possible. Different applications of cold molecules have different temperature requirements that we have summarized in table (1.1).

Application	Temperature	Phase-space density ($\hbar^3$)	Number density (cm^{-3})
Tests of fundamental physics	∼1K	10^{-17}-10^{-14}	10^6-10^9
Electric dipole interactions	∼1K	10^{-14}	$>10^9$
Cold controlled chemistry	<1K	10^{-13}-10^{-10}	$>10^{10}$
Quantum computation	∼1K	-	-
Ultracold chemistry	$< \mu$K	10^{-5}	$>10^9$
Quantum degeneracy with molecules	100 nK	1	$>10^{13}$
Optical lattices of molecules	100 nK	1	$>10^{13}$
Novel quantum phase-transitions	<100 nK	10	10^{14}

TABLE 1.1: The temperature requirements for different applications of cold molecules. The table is adapted from [1].

1.3 Methods for making cold and slow molecules

Several methods have been developed to achieve dense samples of cold polar molecules. Because of their complex structure, molecules are much harder to manipulate than atoms. The methods for producing cold and/or slow molecules can be divided into two categories: i) direct methods in which stable molecules are directly manipulated, and ii) indirect methods that rely on the assembly of the molecules from ultracold atomic species.
Here we will briefly describe a few of the routinely applied techniques. The list is not exhaustive and the reader is referred to [69], [31] and [1] for a more detailed discussion.

1.3.1 Direct methods

1.3.1.1 Buffer gas cooling

In buffer gas cooling a cryogenically cooled noble gas (usually ^{3}He, ^{4}He or Ne) acts as a refrigerant for an atomic or molecular sample. The hot atoms/molecules of interest are allowed to thermalize with the buffer gas through elastic collisions. The thermalization takes place inside a cryogenic cell kept at the same temperature as the buffer gas. Usually the buffer gas and cryogenic cell are kept at a few K but it is possible to reach temperatures as low as 300 mK with a dilution fridge and with the appropriate amount of ^{3}He. In the case of molecules the buffer gas also cools the rotational temperature. This technique is very efficient because of the high elastic scattering cross-section of helium with any atom or molecule (of the order of 10^{-14} cm^2) and the considerable vapor pressure of helium at temperatures down to 200 mK.
The buffer gas cooling technique was first demonstrated by Doyle *et al.* [70] and can be applied to a wide range of atoms and molecules regardless of their internal state. There are many techniques for loading the species of interest inside the buffer gas cell e.g. laser ablation [71], beam injection, by an oven, gas discharge etc.
The molecules cooled by the buffer gas can be further trapped in a magnetic trap [72] or a microwave trap [73]. In the former case it is possible to reach temperatures down to 300 mK [74]. One can also form a molecular/atomic beam by a hole in the side of the buffer gas cell. The forward velocity of the beam can be tuned within a narrow range by changing the flux of helium (e.g. 150-250 m s^{-1} for YbF [75]). The molecules can also be guided out of the buffer gas region by a magnetic guide as demonstrated by Patterson *et al.* [76].
An improved deign for the buffer gas cell was suggested by Liu *et al.* in 2011 [77] in which a second stage is added to the buffer gas cell and the slow molecules are hydrodynamically extracted. In this method it is possible to achieve very low velocities of the molecular beam in the effusive regime ($\sim$ 40 m s^{-1} for CaH) and high fluxes of molecules ($\sim 10^9$ molecules per pulse).
Buffer gas cooling is an efficient technique for producing a high flux ($> 10^8$ molecules/sr) of

cold (of the order of a few K) molecules with low speeds ($\sim 100\ \mathrm{m\,s^{-1}}$). Buffer gas cooling has been applied to a number of diatomic molecules e.g. CaH [78], ThO [79], YbF [80], PbO [70] and CaF [81] and some rare-earth atoms [82, 83].

1.3.1.2 Sympathetic cooling

Sympathetic cooling is a technique in which molecules thermalize with laser-cooled atoms. The molecules are trapped in a microwave, electrostatic or ac trap and elastic collisions with the ultracold atoms reduce the thermal energy of the molecular species making it possible to achieve temperatures in the μK regime. There have been proposals for sympathetic cooling of LiH [84] and NH [85], and recently sympathetic vibrational cooling of trapped $BaCl^+$ molecular ions has been demonstrated [86].

1.3.1.3 Manipulation of the molecular motion with external fields

The motion of atoms and molecules can be manipulated with a sequence of inhomogeneous optical, electric or magnetic fields with the interaction being quantum-state dependent. Historically, Stern and Gerlach were the first to demonstrate in 1922 that one can use an inhomogeneous magnetic field to sort the atomic quantum states through space quantization. Since then the idea to control the motion of atoms and molecules state-selectively has been developed and used extensively.

A polar molecule possesses a permanent dipole moment μ^e which for a diatomic molecule is oriented along the internuclear axis. This dipole moment can be acted upon with external electric fields to affect the molecular motion in a similar fashion to the way charged particles can be accelerated or decelerated, albeit with a smaller interaction energy.

The energy levels of an atom or molecule can be found by diagonalizing the Hamiltonian describing it. In an interaction with an external electric or magnetic field the field-free energy levels are shifted and split into new states which can be found by considering the new Hamiltonian with the perturbation terms H_{Stark} or H_{Zeeman}. The evolution of the field-free energy states depends on the specific characteristics of the atom or molecule in question. Here we will consider how electric fields can be used to manipulate certain polar molecules. A similar principle holds for magnetic fields and paramagnetic molecules (see [87] for a detailed discussion).

In the presence of an external electric or magnetic field the total angular momentum $\vec{J}$ of a molecule can only have discrete orientations in space and magnitude $\hbar\sqrt{J(J+1)}$ while the projection of $\vec{J}$ along the axis defined by the external field is given by $\hbar M$ with $M = -J, -J+1 \ldots J$. The vector $\vec{J}$ precesses around the direction of the external field, while the states with different M have different energies.

The presence of an electric field $\vec{E}$ shifts the energy of a certain quantum state by an amount $-\mu^E \cdot \vec{E}$ the projection of the molecule's dipole moment μ^e onto $\vec{E}$. In some states μ^E is

aligned parallel with the external field. These states are lowered in energy in the presence of $\vec{E}$ and are thus called 'high-field seeking' states. Other states, in which μ^E is anti-aligned with $\vec{E}$, have their energy raised and are thus called 'weak-field-seeking'. One can use the induced energy shift to cause the molecule in the relevant state to climb a potential hill and lose kinetic energy. The motivation for such a manipulation is to slow down fast traveling molecules (e.g. from supersonic velocities $\sim 600\ \mathrm{m\,s^{-1}}$) to low velocities so that they can be trapped.

In a Stark decelerator a high electric field is applied to a long array of electrodes creating an inhomogeneous pattern. The switching of the electrodes from positive to negative voltage is timed so that molecules in a low-field-seeking state are constantly climbing a potential hill which reduces their kinetic energy. The typical energy shifts induced in the external electric fields are rather modest - for example, the energy shift in a 200 kV/cm field for a CO molecule in the right state is 1.71 $\mathrm{cm^{-1}}$ [87]. As a consequence, many stages are needed to decelerate the molecular beam appreciably. In addition to that, the Stark decelerator acts on molecules with a narrow range of velocities and does not change the phase-space density of the sample.

Stark deceleration is a very efficient technique of removing kinetic energy from the molecular beam in which it is even possible to bring the molecules to rest. The only disadvantage is that it is relatively technically demanding. Stark deceleration was first demonstrated in 1999 on a beam of CO molecules whose velocity was reduced from 225 $\mathrm{m\,s^{-1}}$ to 98 $\mathrm{m\,s^{-1}}$ [88]. A wide range of molecules has now been decelerated, for example, ND_3 and NH_3 [89], OH [90], SrF [63], YbF [91, 92] and CaF [93]. In the current experiments it is possible to decelerate polar molecules to a mean speed adjustable in the 10-100 $\mathrm{m\,s^{-1}}$ range while the longitudinal velocity spread corresponds to a translational temperature in the 10-100 mK range. Recently, a traveling wave decelerator [94] has been demonstrated in which a traveling 3D trap is used to both focus and decelerate the molecules.

The Zeeman [95, 96] and optical [97] decelerators act in a way analogous to the Stark decelerator but rely on the force exerted by magnetic and optical fields respectively. These decelerators are useful for atoms and molecules which are not amenable to Stark deceleration.

In addition to reducing the forward velocity of the molecular beam, one can use external fields to confine the transverse motion of the molecules and thus focus or guide them. To create a 'lens' for the molecular beam, the exerted force should be harmonic. For polar molecules in a low-field seeking state which experience a quadratic (linear) Stark shift, one has to create an electric field which has a value of zero on the beam axis and increases linearly (quadratically) with increasing distance from the center. One can use quadrupole or hexapole fields created by applying voltage to four or six cylindrical electrodes with their axis of symmetry parallel to the forward motion of the molecules. This type of electric field can focus diatomic and symmetric top molecules in a low-field-seeking state [98–100].

Longer hexapole and quadrupole configurations in which the molecules undergo several oscillations are usually referred to as 2D traps or guides. A curved guide, for example, can be used to transport only molecules below a certain threshold velocity as faster molecules are not able to follow the curved trajectory. This type of guide has been used to create a slow beam of ND_3, H_2CO [101], CH_3I and C_6H_5CN [102]. It has even been demonstrated that a storage ring can be used to keep ND_3 molecules together while they travel a distance of over one mile [103].

So far we have only considered the manipulation of low-field seeking states. High-field-seeking states present a problem. In order to confine these states one has to create an electric field maximum. Unfortunately, this is forbidden by Maxwell's equations. There is, however, a strong demand to develop methods to manipulate molecules in high-field seeking states as all ground state molecules and heavy polar molecules in low lying states are high-field seeking. Ground state molecules are of particular interest as inelastic collisions are suppressed in samples of ground state molecules.

It is possible to create a field configuration which has a saddle point on the molecular beam axis so that the high-field-seeking molecules are focused along one direction and defocused along the orthogonal one. By alternating the field configurations it is possible to achieve a stable trajectory and guide the high-field seeking states. This scheme is called an alternating-gradient (AG) focussing and is extensively used to stabilize the motion of charged particles in an accelerator. It is thus possible to focus and guide polar molecules in high-field seeking states. AG guiding and/or deceleration has been demonstrated in CO molecules by Bethlem *et al.* [104], ND_3 molecules in both a high- and low- seeking state by Junglen and coworkers [105] and in CaF in a high-field seeking state by Wall *et al.* [93, 106].

1.3.1.4 Molecular traps

A sample of a large number of molecules at low temperatures and moving at sufficiently low velocities must be stored in a trap to allow for a longer interaction time and open the possibility for further cooling in order to explore the regime of quantum degeneracy.

Several methods have been developed to trap the molecules from a buffer gas source or after they have been decelerated from a supersonic beam. It is more straightforward to trap states which are attracted to low-field regions in either a magnetic of electric field because it is easy to create a magnetic or electric field minimum in space. Electrostatic and magnetic traps act on molecules in weak-field seeking states. These types of traps are relatively easy to implement, have a trap depth of 0.5 - 1 K and can be loaded from a buffer gas source or a decelerator. For example, in 2005 van de Meerakker *et al.* demonstrated deceleration of a beam of OH radicals and subsequent trapping of the molecules in an electrostatic quadrupole trap [107]. In this experiment approximately 10^5 molecules in the

($X^2\Pi_{3/2}, J = 3/2$) state were trapped at densities of around 10^7 cm^{-3} and temperatures in the 50-100 mK range. Deuterated ammonia has also been trapped in an electrostatic trap at similar densities and temperature of 25 mK [89]. Magnetic trapping of CaH molecules at temperatures of 300 mK has been been demonstrated by Weinstein *et al.* [78].

Electrostatic and magnetic traps only work for weak-field seeking states. As mentioned above, the ground state of any molecule is high-field seeking. Trapping molecules in their ground state is desirable as in that state there are no inelastic collisions which can lead to trap losses and it is thus possible to use evaporative cooling or sympathetic cooling to further cool the sample. We note that evaporative cooling has recently been demonstrated in excited state OH molecules in a magnetic trap [108] but this has only been possible because OH is a special molecule in that it has a very favorable ratio of elastic to inelastic scattering cross-section.

It is possible to come up with a configuration of switching electric field potentials to trap molecules in a high-field seeking state as mentioned before. This is the principle behind the ac trap which is very similar to the Paul trap for ions. Different ac trap geometries have been investigated and realized [87]. For example, ND_3 molecules have been trapped in a cylindrical ac trap [109]. The problem with ac traps, however, is that they are very shallow compared to static traps (of the order of a few mK) and have a very small trapping volume ($\sim$mm^3 [109]).

It is also possible to trap molecules in optical dipole traps which are routinely used in atomic physics experiments [110] and rely on the interaction between the induced dipole moment and the intensity gradient of an off-resonant laser field. For example, cold Cs_2 molecules have been trapped in an optical trap [111]. However, optical traps are very shallow (trap depth $\sim$ 1 mK) and are characterized by a small trapping volume ($\sim 10^{-5}$ cm^3) which makes them non-ideal for molecules.

A very promising trap, especially for polar diatomic molecules including CaF, is the microwave trap suggested by DeMille *et al.* in 2004 [73]. This trap is the microwave analogue of the optical dipole trap and can be used to confine polar molecules in their absolute ground state. This is of particular interest as polarization of molecules in strong-field seeking states is expected to lead to exceptionally large elastic collisions cross section due to the long range dipole-dipole interactions. The microwave trap exploits the ac Stark shift associated with low-lying rotational transitions, inversion doublets or Λ/Ω doublets in polar molecules. The long wavelength of the microwaves makes it possible to achieve large trapping volumes of the order of 1 cm^3 while the trap depth can be $\sim$ 1 K. In order to achieve the ac Stark shift needed for this trap depth, a very intense electric field is needed ($\sim$ 3 MV/m [112]). DeMille and colleagues proposed that this field strength can be achieved in a standing wave configuration in a Fabry-Pérot type of resonator formed by two spherical copper mirrors. The only disadvantage is that still very high input power is needed ($\sim$ 2 kW [112]). The open geometry suggested by DeMille *et al.* makes loading of the trap

very easy and opens up possibilities for overlapping the trapped molecular sample with ultracold atoms and collisional cooling. Possible designs for the microwave trap have been investigated by D. Glenn [113] at Yale University and S. Truppe in our lab at Imperial College [112]. The microwave trap has not been tested with molecules yet but the progress made is very promising (see [112]).

1.3.1.5 Other direct methods

Other direct methods for producing slow and cold molecules include the counter-rotating nozzle technique [114, 115], crossed collisions [116] and cavity-assisted laser cooling [117]. A promising technique to cool polyatomic molecules to temperatures in the mK range is the optoelectric cooling demonstrated by Zeppenfeld *et al.* [118] in which suitably engineered electric trapping fields are used to remove the energy of polar molecules in a Sisyphus-type cooling cycle.

1.3.2 Indirect methods

The most efficient way to produce cold molecules in the sub mK regime is through direct assembly from atoms which are already ultracold. This approach benefits from the already existing methods for laser cooling and evaporative cooling to reach very low temperatures [30]. The two most commonly used techniques are through photoassiciation and Feshbach resonance.

1.3.2.1 Photoassociation

Photoassociation (PA) is historically the first technique used to create ultracold molecules from laser cooled atoms. It can be described as a three-body scattering process in which two colliding ultracold atoms interact with a photon from a resonant laser field to reach an excited and short-lived bound molecular state [119]. The efficiency of the conversion rate for the process free atoms→bound molecule depends on the Franck-Condon factor $F_{fv'}$ between the wavefunctions of the free atoms and the final bound state, the temperature and the phase-space density of the sample. The value of $F_{fv'}$ is suppressed by several mechanisms mostly due to the low density of the atoms and is particularly unfavorable for heteronuclear species. Because of this, the first experiments in PA were concerned with homonuclear molecules e.g. Na_2 [120], Rb_2 [121], Cs_2[122] and K_2 [123]. The technique was later extended to heteronuclear species e.g. KRb [124], NaCs [125] and RbCs [126].
Although it is possible to induce the binding of atoms into molecules without introducing translational heating of the sample, the newly formed molecules in PA are usually in a highly excited vibrational state. This is undesirable because collisions between vibrationally excited molecules can lead to heating. Some techniques have been developed to transfer the molecular population to a deeply bound ground state. For example, it is possible to

excite the molecule to an intermediate state which has a favorable overlap with the ground vibrational state [127, 128].

1.3.2.2 Feshbach resonance

Using a Feshbach resonance, a tunable external magnetic field is used to modify the potential energy of two colliding cold atoms in such a way that they reach a bound molecular state. The first demonstration of Feshbach molecules was observed in a BEC cloud of ^{85}Rb [129] and soon after in BECs of ^{133}Cs [130], ^{87}Rb [131] and ^{23}Na [132] and in degenerate or near-degenerate Fermi gases of ^{40}K [133] and ^{6}Li [134]. The first emergence of a molecular BEC from an atomic Fermi gas was demonstrated in 2003 [32, 33, 135]. A few years later Feshbach molecules were observed in Bose-Bose mixtures of ^{85}Rb-^{87}Rb [136] and Bose-Fermi mixtures of ^{87}Rb-^{40}K [137].
Similarly to PA, in the Feshbach resonance method the molecules are created in a highly excited vibrational state but can be transferred to the ground vibrational state by the STIRAP (stimulated Raman adiabatic passage) technique [138]. Recently, KRb Fescbach molecules in a 3D optical lattice have been used to study dipolar spin-exchange interactions [139].

The two indirect cooling methods have been very successful at creating ultracold molecules at densities of 10^{13} cm^{-3} and translational temperatures as low as 350 nK [138]. However, both techniques present several limitations. The first obvious disadvantage of these techniques is that they can only be used to produce molecules whose atomic constituents can be laser cooled and trapped. Most of the experiments in the field nowadays are concerned with bialkali molecules although some have attempted to extend the techniques to the alkaline earth metals [140].
The magnitude of the permanent electric dipole moment of the assembled molecules (D) depends on the difference in atomic number of the constituents. If the molecule is homonuclear $D = 0$. Nevertheless, it is possible to produce considerably polar molecules with these two indirect cooling methods with the highest polarity for LiCs of $D \sim 5.5$ Debye [141]. Perhaps the most significant disadvantage of the indirect cooling methods is their experimental complexity, poor conversion efficiency and the relatively low number of molecules ($\sim 10^4$) [138].
Recently, KRb Feshbach molecules in a 3D optical lattice have been used to study dipolar spin-exchange interactions [139].
Table (1.2) summarizes the temperatures and densities achievable with the existing methods for making cold molecules.

Method	Example molecule (dipole moment/Debye)	Temperature	Number of molecules or trap density	Reference
Direct methods				
• Buffer gas cooling	SrF (3.46)	∼1 K	10^{11} molecules/sr/pulse	[142]
• Buffer gas cooling	CaH (2.94)	800 mK	$5{\times}10^{12}$ cm^{-3}	[74]
and magnetic trapping	NH (1.39)	550 mK	10^{8} cm^{-3}	[143]
• Deceleration	OH (1.67)	50-500 mK	10^{7} cm^{-3}	[107]
and trapping		(electrostatic trap)		
	ND_3 (1.5)	5 mK	270 mm^3(m s^{-1})^3	[104]
		(ac trap)	(phase-space density)	
• Evaporative cooling	OH (1.67)	5 mK	$5{\times}10^{10}$ cm^{-3}	[108]
Indirect methods				
• Photo-association	RbCs (1.3)	100 μK	10^{4} molecules	[144]
• Feshbach resonance	KRb (0.566)	350 nK	10^{12} cm^{-3}	[138]

TABLE 1.2: Temperatures, number of molecules and density demonstrated so far in the state of the art cold molecules experiments.

1.4 Laser cooling molecules

Laser cooling of atomic species has proven to be an elegant and efficient technique to reduce the temperature of atoms from hundreds of K to the μK regime in a matter of milliseconds. Because there has been an increasing demand for ultracold polar molecules, over the past 10 years researchers in the field have re-examined the idea of laser cooling molecules.

The momentum of a photon in the visible part of the spectrum is of the order of $p_{\mathrm{ph}} \approx 10^{-28}$ kg m s^{-1}, while the momentum of an atom of mass 85 u (such as rubidium) moving at a velocity of 200 m s^{-1} is $p_{\mathrm{atom}} \approx 10^{-23}$ kg m s^{-1}. In order to reduce its velocity appreciably an atom needs to scatter of the order of 10^5 photons. It is thus essential that the atom always decays to a state addressed by laser light. In atoms it is usually easy to come up with such a closed cycling transition by making use of the angular momentum selection rules and choosing the correct laser polarization.

The electronic transitions in molecules are very similar to the ones in atoms and in principle one can use laser cooling on a molecular sample. There is, however, a problem: molecules have rotational and vibrational transitions in addition to the electronic ones already present in atoms. When a molecule changes electronic state, it is likely that it will also change its rotational and vibrational state. Traditionally, laser cooling has been believed to be implausible in molecules precisely because of the multitude of their energy levels. Usually, after scattering only a few photons the molecule ends up in a different state than the original one. The number of laser frequencies needed to address all possible molecular decay channels is thus impractical.

The vibrational transitions in a molecule are particularly problematic. While selection rules can be used to predict the change of rotational state in an electronic transition, there is no selection rule on the change of vibrational state. Rather, the probability of change of vibrational state in an electronic transition is determined by the square of the overlap integral of the respective vibrational wavefunctions in the relevant electronic manifolds. This

overlap integral squared is what is called the Franck-Condon factor. Usually, even in the absence of rotational branching, the molecule ends up in an vibrational state different than the initial one after scattering only a few photons and can thus no longer see the resonant light. The number of vibrational repump lasers needed to ensure a closed transition even for a simple diatomic molecule soon becomes daunting.

However, in certain diatomic molecules the internuclear potential and the equilibrium separation in the different electronic manifolds is very similar. This means that the vibrational state is not very likely to change in an electronic transition. The fact that such molecules exist and may be amenable to laser cooling has been realized only in the recent years.

In 1994 Bahns and colleagues suggested using laser light to cool molecules simultaneously rotationally, vibrationally and translationally [145]. The technique suggested by Bahns *et al.*, while applicable to a wide range of molecular species, was rather experimentally demanding. In 2004 DiRosa published a paper in which he suggested to trade the generality of the technique proposed by Bahns *et al.* for a much simpler one at the expense of the diversity of the molecules to which it is applicable. DiRosa pointed out that laser cooling as conventionally applied in atomic experiments can be extended to a narrow range of diatomic molecules which possess convenient electronic structure [2]. The author identified three spectroscopic criteria that a diatomic molecule must fulfill in order to be amenable to Doppler cooling: i) a strong one-photon dipole transition that ensures high photon scattering rate, ii) a highly diagonal Franck-Condon matrix to suppress vibrational branching and iii) no intervening electronic states to which the excited state can decay.

DiRosa pointed out that the molecules which possess a highly diagonal Franck-Condon (FC) matrix have spontaneous emission rates heavily weighted towards the ground vibrational state. To illustrate this point, consider a molecule excited from the ground vibrational state ($v'' = 0$) of the ground electronic manifold (X) to the ground vibrational state ($v' = 0$) in first excited electronic state (A). The probability of decay from the $A(v' = 0)$ state to the different vibrational states in the X electronic manifold (i.e. to $X(v = 0, 1, 2 \ldots)$) is determined by the spontaneous emission rates which we can designate as $A_{v'v}$. In diatomic molecules which have a diagonal FC matrix the band spontaneous emission rates have the property that $A_{00} \gg A_{01} \gg A_{02} \gg A_{03} \ldots$. This means that when excited on the $X(v'' = 0) \rightarrow A(v' = 0)$ transition, a molecule can scatter many photons before it populates excited vibrational states in the ground electronic manifold. By choosing a molecule with a favorable FC matrix and addressing some of the possible decays to excited vibrational states in the ground electronic state, one can ensure that a given molecule will scatter a high number of photons. The molecule will undergo a series of absorption-spontaneous emission cycles described by the Bernoulli sequence. If the molecule has a probability of decaying to a state not addressed by laser light p, then it has a probability P of going through N absorption-spontaneous emission cycles given by $P = (1 - p)^N$. When considering an ensemble of molecules, P is the fraction of molecules remaining after scattering

N photons, while $(1 - P)$ is the fraction of molecules lost from the cycle. The particular choice of molecule and application determine what values of P and N are acceptable and how many repump lasers are needed to realize those values.

Laser cooling in molecules can never be as efficient as it is in the traditionally used atoms (such as Na or Rb) because decays to dark states are inevitable. Nevertheless, a perfectly closed cooling cycle is not essential to get all the benefits of laser cooling such as its potential to increase the phase-space density of the sample by a factor of 10^6 [146].

In his paper DiRosa identifies about a dozen diatomic molecules as possible candidates for laser cooling, while also hinting that laser cooling would most likely not be possible in tri- and poly-atomic molecules. Those proposed by DiRosa are some monohydrides (BeH, MgH, CaH, SrH, BaH, NH and AlH) and some halides (AlF, AlCl, PbCl, CaCl).

The idea of laser cooling diatomic molecules was taken one step further in the 2008 milestone paper by Stuhl *et al.* [3]. In this paper the authors point out that in addition to the criteria listed by DiRosa, laser cooling can only be successful if the transition is closed rotationally. Consider a molecule which gets excited from a state with total angular momentum J'' to an excited state with total angular momentum J', ignoring for the moment hyperfine structure. The angular momentum selection rules dictate that the change of angular momentum in an electronic transition is $\Delta J = 0, \pm 1$. Thus, upon spontaneous emission from the excited state, even with a perfect Franck-Condon factor of unity, three rotational branches can be populated. Stuhl and colleagues suggested that two of the three decay channels in this rotational branching can be avoided by driving a $J'' \rightarrow J' = J'' - 1$ transition. When this is the case, the molecule has to return to the original J'' state upon spontaneous emission and the transition is rotationally closed. Stuhl *et al.* identify a chemically diverse set of diatomic molecules which satisfy all of the above criteria and are very attractive candidates for laser cooling. The authors suggest the molecules TiO and TiS in their ground state, FeC, ZrO, HfO, ThO and SeO in a metastable state and anticipate that other metal oxides, sulfides and carbides and metal hydrides and halides at the expense of hyperfine structure could also be suitable. Other species which have been identified as suitable for laser cooling are TlF [147], YbF [148], RaF [62, 149], BeF [150], some carbides [151], AlH and AlF [152], and BH [153].

In addition to the criteria listed above, when choosing a molecule for laser cooling one must also take into account the following practical considerations: i) is the molecule straightforward to produce in the gaseous phase, ii) does it have electronic transitions accessible by commercially available laser systems and iii) is there enough spectroscopic data available in the literature.

1.4.1 Current experiments

Since the 2004 paper by DiRosa the new field of laser cooling molecules has made enormous strides. In the past five years laser cooling has been demonstrated with very encouraging results on three species of diatomic molecules - SrF [154], YO [155] and CaF [156]. All three molecules satisfy the above criteria for laser cooling but none of them was amongst the originally proposed candidates in the papers by Stuhl *et al.* [3][4] and DiRosa [2].

In the current experiments the choice of molecule has been dictated partially by the available sources - cryogenic buffer gas sources in the case of SrF and YO and supersonic source in the case of CaF. These three molecules share some properties - they all have one unpaired electron localized on the heavier atom and $^2\Sigma^+$ character in the ground state. As this electron participates little in the chemical bond, the internuclear potential does not change much in the different electronic manifolds. The choice of such molecules for laser cooling has also been determined by the special interest in polar molecules with an unpaired electron for a variety of applications [65, 158–160].

The effect of laser radiation pressure in a diatomic molecule was first demonstrated in 2009 when Shuman *et al.* showed deflection of a SrF beam from a buffer gas source from optical cycling on the $X^2\Sigma^+ \leftrightarrow A^2\Pi_{1/2}$ transition [161]. Although the observed deflection was approximately 1 mm corresponding to a modest number of scattered photon ($N_{ph} \approx 140$), this was an important proof-of-principle experiment which paved the way for many exciting results in the years to come. The same group demonstrated in 2010 1D transverse cooling of the SrF beam from a starting temperature of 50 mK to a temperature of 15 mK [154] and in 2012 longitudinal slowing [162].

The prospect of creating a molecular magneto-optical trap (MOT) is particularly intriguing. The idea behind the magneto-optical trap is to use a magnetic field gradient and the appropriate laser beam polarization to introduce a position-dependent frequency-shift. This makes the atom or molecule more likely to absorb a photon from the counter-propagating beam and thus be subjected to a restoring force. The requirement to create a MOT is that the ground and excited states have differential Zeeman shifts.

A traditional MOT (the so-called type-I MOT), which is used in the majority of atomic systems, works on a $J'' \rightarrow J' = J'' + 1$ cycling transition. In a type-I MOT, the local magnetic field lifts the degeneracy from the ground state levels and for any laser polarization all ground state magnetic sublevels can get excited. This type of MOT is not applicable to molecules because a $J'' \rightarrow J' = J'' + 1$ transition is not rotationally closed.

The less common type-II MOT works on a $J'' \rightarrow J' = J''$ or $J'' \rightarrow J' = J'' - 1$ cycling transition. This type of MOT is the only choice for molecules. The type-II MOT is intrinsically less efficient than the type-I MOT but has been demonstrated in some atomic species

[4] Stuhl and colleagues shifted their attention from TiO to YO as the latter molecule has a shorter excited state lifetime and can thus scatter at a faster rate, more favorable Franck-Condon factors [157] and larger dipole moment of 4.5 D.

[163–166]. The damping and restoring force in such a MOT are smaller as it is possible for an atom or molecule to absorb a photon from the co-propagating laser beam instead of the counter-propagating one. In addition to that, in a $J'' \rightarrow J' = J''$ or a $J'' \rightarrow J' = J'' - 1$ transition 2/3 and 1/3 of the ground states levels respectively remain dark for any given laser polarization. One thus needs a mechanism to continuously remix those dark states into bright ones so that all atoms/molecules spend a fraction of their time in a bright state and the scattering rate does not go down to zero. In the simplest case - laser cooling in 1D and no trapping, one can apply a constant magnetic field at an angle to the laser polarization so that the dark states precess into bright ones [161, 167]. In the context of a MOT, however, a more complicated scheme is needed - the bright-dark states mixing can be done by applying a sudden electric field orthogonal to the local direction of the magnetic field [3] or by rapidly switching the laser polarization [155, 167].

In 2013 Hummon *et al.* demonstrated the first 2D MOT of YO molecules from a cryogenic buffer gas [155]. In that experiment the trapping was realized by rapidly switching the laser polarization between left and right circularly polarized together with changing the sign of the magnetic field. Hummon and colleagues were able to change the transverse temperature of the molecular beam by altering the relative phase ϕ between the switching of the laser polarization and the switching of the magnetic field sign. The lowest temperature they observed was 2 mK for $\phi = 0$ from a starting temperature of 25 mK - still well above the Doppler temperature of YO of 116 μK.

Very recently the first 3D molecular type-II MOT of SrF molecules has been realized by Barry *et al.* [168]. The authors were able to trap about 400 molecules at temperatures close to 2.5 mK with a trap lifetime of around 40 ms. This first demonstration of a 3D MOT was an important milestone in the field of cold molecules, but also raised a lot of questions for future experiments - such as the weaker than expected confining force and short trap lifetime.

Table (1.3) summarizes the three current experiments on laser cooling molecules, including the experiment described in this thesis. Laser cooling has proven to be very successful when applied to a limited range of diatomic molecules. This is a promising method to slow down molecular beams and can be particularly effective in buffer gas sources which provide a high flux of cold and already slow molecules. The laser cooled and slowed molecules can then be captured for example in a magneto-optic trap, a magnetic trap (if the molecule is paramagnetic) or a microwave trap. It might be even possible to reach temperatures in the sub-mK regime and perhaps quantum degeneracy if some more advanced techniques such as evaporative cooling are used on the laser cooled and trapped sample.

Molecule	Source	Calculated FC factors $q_{v',v''}$	Ref.	Number of vibrational repump lasers	Starting temperature	Final temperature
SrF	cryogenic buffer gas [142]	$q_{0,0} \approx 0.9814$ $q_{0,1} \approx 0.0181$ $q_{0,2} \approx 4.3\times10^{-4}$	[169]	2	a few K	2.5 mK (3D MOT [168])
YO	cryogenic buffer gas [70]	$q_{0,0} \approx 0.9944$ $q_{0,1} \approx 0.0038$	[157]	2	25 mK	2 mK (2D MOT [155])
CaF	supersonic source [170]	$q_{0,0} \approx 0.978$ $q_{0,1} \approx 0.021$ $q_{0,2} \approx 7\times10^{-4}$	[171]	1	3 K	300 mK [156]

TABLE 1.3: Current published results from laser cooling of molecules experiments. In all three molecules listed the laser cooling takes place on the $A^2\Sigma^+ \rightarrow X^2\Pi_{1/2}$ transition.

Chapter 2

Introduction to molecular physics

In a molecule, the presence of at least two nuclei introduces rotational and vibrational degrees of freedom in addition to the electronic ones already present in atoms. The extra degrees of freedom give rise to a much more complex energy level structure, but also present exciting opportunities for exploring new physics. The complexity of the molecular structure can be daunting but it is important to understand some basic principles in order to appreciate the excitement surrounding the rapidly growing field of cold and ultracold molecules.
Solving the time-independent Schrödinger equation for a multi-electron and a multi-nucleus molecule is a very complicated task. However, the problem can be simplified by noting that the mass of the electron is much smaller than the mass of the nucleus ($m_{\text{electron}}/M_{\text{nucleus}} \simeq 10^{-3} - 10^{-5}$), while the Coulomb forces acting on the electrons and nuclei are of comparable magnitude. Thus, the motion of the nuclei is much slower than the motion of the electrons - from the point of view of the electron, the motion of the nuclei is 'frozen'. The Born-Oppenheimer approximation essentially consists of separating the molecular wavefunction as a product of an electronic and nuclear part. The treatment can be further simplified as one can only concentrate on the outer shell electrons, similarly to the atomic case - X-ray diffraction studies suggest that the inner shell electrons in a molecule tend to be localized on their respective nuclei while the outer electrons are distributed throughout the whole molecule [172].

In this chapter, I will introduce the basics of molecular quantum theory the reader needs in order to follow the notations and understand the quantum states involved in the laser cooling transitions. The treatment is based on Herzberg [173], Atkins and Friedman [174], and Bransden and Joachain [172]. The reader is refereed to [31] for a short overview of the subject.

2.1 The Born-Oppenheimer approximation

The Born-Oppenheimer approximation allows one to solve approximately the time-independent Schrödinger equation (TISE) for a molecule. The derivations presented here are based on [172].

We will restrict our treatment to a system with only two nuclei, A and B, and N electrons. In the center-of-mass coordinates and relative coordinates, where $\mathbf{R}_{\mathrm{CM}} = \frac{\mathrm{M_A}\mathbf{R}_\mathrm{A}+\mathrm{M_B}\mathbf{R}_\mathrm{B}}{\mathrm{M_A}+\mathrm{M_B}}$, $\mathbf{R} = \mathbf{R}_\mathrm{A} - \mathbf{R}_\mathrm{B}$ and the electronic coordinates are $\mathbf{r}_i$, the Hamiltonian of the system can be written as:

$$H = \underbrace{-\sum_{i=1}^{n} \frac{\hbar^2}{2m_e}\nabla_i^2}_{T_e} \underbrace{-\frac{\hbar^2}{2\mu}\nabla_R^2}_{T_N} + V \tag{2.1}$$

Here T_e is the electronic kinetic energy, T_N is the nuclear kinetic energy (excluding the center of mass motion), μ is the reduced mass of the two nuclei and V is the Coulomb potential energy between the electrons and the nuclei. The TISE describing the system is:

$$(T_N + T_e + V)\Psi(\mathbf{R}, \mathbf{r_i}) = E\Psi(\mathbf{R}, \mathbf{r_i}) \tag{2.2}$$

The Born-Oppenheimer approximation consists of neglecting the nuclear kinetic energy term T_N in (2.2) as $m_e \ll \mu$. The next step is to fix the internuclear separation $\mathbf{R}$ so that it is a parameter rather than a variable. One can then solve the TISE for N electrons moving in the effective Coulomb potential created by the two nuclei for each discrete value of R. The electronic part of the TISE then becomes:

$$H_e\psi_q(\mathbf{R}; \mathbf{r}_i) = (T_e + V)\psi_q(\mathbf{R}; \mathbf{r}_i) = E_q(R)\psi_q(\mathbf{R}; \mathbf{r}_i) \tag{2.3}$$

Equation (2.3) can be solved using numerical methods to obtain the electronic eigenfunctions $\psi_q(\mathbf{R}; \mathbf{r}_i)$ and eigenvalues $E_q(R)$ for each fixed value of R and for a certain electronic state q. The eigenenergies depend only on the magnitude R of the internuclear separation $\mathbf{R}$. The wave functions ψ_q, on the other hand, depend both on R and the orientation of $\mathbf{R}$ in space - i.e. on the angles Θ and Φ in spherical polar coordinates.

For each fixed value of R, the electronic wave functions $\psi_q(\mathbf{R}; \mathbf{r_i})$ form a complete set: $\langle\psi_p|\psi_q\rangle = \delta_{pq}$. Thus, the complete molecular wavefunction can be expanded on the basis of the electronic eigenfunctions:

$$\Psi(\mathbf{R}, \mathbf{r}_i) = \sum_q \chi_q(\mathbf{R})\psi_q(\mathbf{R}; \mathbf{r}_i) \tag{2.4}$$

where the expansion coefficients $\chi_q(\mathbf{R})$ are the wavefunctions representing the nuclear motion (vibration and rotation). One can then substitute (2.4) in equation (2.2). Multiplying

both sides by ψ_n, integrating over the electronic coordinates and making use of the orthonormality condition $\langle\psi_n|\psi_m\rangle = \delta_{nm}$, allows us to arrive at an infinite set of coupled differential equations:

$$(E_n(R) - E)\chi_n + \sum_q \int d\mathbf{r_i}\{\psi_n^* T_N \psi_q \chi_q\} = 0 \tag{2.5}$$

Since both $\psi(\mathbf{R};\mathbf{r}_i)$ and $\chi(\mathbf{R})$ depend on $\mathbf{R}$, the Laplacian operator ∇_R^2 in T_N acts on the product $\psi_q\chi_q$. It is now time to make the *adiabatic* approximation - the nuclear motion is very slow compared to the electronic motion, and thus the electronic wavefunctions will adapt very quickly to a change in R. In effect, $\nabla_R\psi_q \ll \nabla_R\chi_q$ and the following approximation can be made:

$$T_N(\psi_q\chi_q) = -\frac{\hbar^2}{2\mu}\nabla_R^2(\psi_q\chi_q) \tag{2.6}$$

$$= -\frac{\hbar^2}{2\mu}\Big(\psi_q(\nabla_R^2\chi_q) + \chi_q(\nabla_R^2\psi_q) + \cancel{2(\nabla_R\psi_q)\cdot(\nabla_R\chi_q)}\Big) \tag{2.7}$$

Equation (2.5) can then be reduced to a much simpler equation involving only the nuclear wavefunctions:

$$(-\frac{\hbar^2}{2\mu}\nabla_R^2 + E_n(R) - E)\chi_n(\mathbf{R}) = 0 \tag{2.8}$$

This is the effective Schrödinger equation for a particle of mass μ moving in the electronic potential $E_n(R)$. It is useful to express the Laplacian in spherical polar coordinates:

$$-\frac{\hbar^2}{2\mu}\nabla_R^2 = -\frac{\hbar^2}{2\mu}\Big[\underbrace{\frac{1}{R^2}\frac{\partial}{\partial R}\Big(R^2\frac{\partial}{\partial R}\Big)}_{\text{vibration}} - \underbrace{\frac{\mathbf{N}^2}{\hbar^2R^2}}_{\text{rotation}}\Big] \tag{2.9}$$

where

$$\mathbf{N}^2 = -\hbar^2\left[\frac{1}{\sin\Theta}\frac{\partial}{\partial\Theta}\Big(\sin\Theta\frac{\partial}{\partial\Theta}\Big) + \frac{1}{\sin^2\Theta}\frac{\partial^2}{\partial\Phi^2}\right]$$

is the total angular momentum operator. Equation (2.8) can be solved by inserting a trial solution of the form $\chi(R,\Theta,\Phi) = R^{-1}f(R)g(\Theta,\Phi)$:

$$\Big[-\frac{\hbar^2}{2\mu}\frac{1}{R^2}\frac{\partial}{\partial R}\Big(R^2\frac{\partial}{\partial R}\Big) + \frac{\mathbf{N}^2}{2\mu R^2} + E_n(R) - E\Big]R^{-1}f(R)g(\Theta,\Phi) = 0 \tag{2.10}$$

Equation (2.10) can be divided by R^2 and re-written in a form in which it becomes apparent that a part only depends on Θ and Φ (angular part) and a part only depends on the internuclear separation R (the radial part):

$$-\frac{\hbar^2}{2\mu}\frac{R}{f(R)}\frac{d}{dR}\left[R^2\frac{d}{dR}(R^{-1}f(R))\right] + R^2E_n(R) - R^2E + \frac{1}{g(\Theta,\Phi)}\frac{\mathbf{N}^2}{2\mu}g(\Theta,\Phi) = 0 \tag{2.11}$$

The angular part has a standard solution - the spherical harmonics: $g(\Theta, \Phi) = Y_{NM}(\Theta, \Phi)$ where $N^2 Y_{NM}(\Theta, \Phi) = N(N+1) Y_{NM}(\Theta, \Phi)$.

2.1.1 The radial equation

The radial equation to be solved has the form:

$$\left[-\frac{\hbar^2}{2\mu} \frac{d^2}{dR^2} + \frac{N(N+1)}{2\mu R^2} + E_n(R) - E \right] f(R) = 0 \tag{2.12}$$

The first step to solving equation (2.12) is to recognize that the nuclear wavefunctions are well-localized around the equilibrium point R_e and the electronic energy $E_n(R)$ can be Taylor expanded around the equilibrium internuclear separation R_e:

$$\begin{aligned} E_n(R) &\simeq E_n(R_e) + \cancelto{0}{\left(\frac{dE_n}{dR} \right)_{R_e}} (R - R_e) + \frac{1}{2} \left(\frac{d^2 E_n}{dR^2} \right)_{R_e} (R - R_e)^2 + \dots \\ &\Rightarrow E_n(R) \simeq E_n(R_e) + \frac{1}{2} k (R - R_e)^2 + \dots \\ &\text{where} \quad k = \left(\frac{d^2 E_n}{dR^2} \right)_{R_e} \end{aligned} \tag{2.13}$$

The total energy E can be defined as:

$$E = E_n(R_e) + E_v + E_r \tag{2.14}$$

$$\text{where} \quad E_r = \frac{N(N+1)}{2\mu R_e^2} \tag{2.15}$$

It then becomes evident that to second order equation (2.12) is the quantum harmonic oscillator equation:

$$\left[-\frac{\hbar^2}{2\mu} \frac{d^2}{dR^2} + \frac{1}{2} k (R - R_e)^2 - E_v \right] \tilde{f}(R) = 0 \tag{2.16}$$

where the tilde signifies the fact that the solution is only valid for the strictly harmonic approximated potential (2.13). Equation (2.16) has the familiar analytical solutions involving the Hermite polynomials. The eigenstates of the exact harmonic oscillator can be written as $\tilde{f}_v(R)$ where v labels the vibrational state.
Finally, the total molecular wavefunction is the product of the electronic, rotational and vibrational parts:

$$\Psi_{n,v,N,M}(R, r_i) = \psi_n(R; r_i) R^{-1} \tilde{f}_v(R) Y_{NM}(\Theta, \Phi) \tag{2.17}$$

The most important result from the Born-Oppenheimer approximation is that the total molecular wavefunction can be factored out in an electronic, vibrational and rotational part. Note that in this treatment we have ignored some higher order corrections. One example is the centrifugal distortion term - when the two nuclei are rotating fast around

each other the internuclear separation increases. This stretching increases the moment of inertia which reduces the rotational frequency. Other effects we have ignored are the spin-orbit and spin-rotation interactions, Λ-doubling and hyperfine interactions.

2.1.2 The anharmonic quantum oscillator

Equation (2.16) has exact analytical solutions - the quantum harmonic oscillator eigenfunctions. However, as the internuclear separation R deviates from R_e, the effective electronic potential seen by the nuclei is no longer purely harmonic. This anharmonicity becomes important as higher vibrational states v are excited as this is when the effective particle of mass μ has a higher probability of being found far away from R_e. To approximate this anharmonicity, an extra term can be added to equation (2.13):

$$E_n(R) \simeq E_n(R_e) + \frac{1}{2}\Big(k(R-R_e)^2 - g(R-R_e)^3 + \dots\Big) \tag{2.18}$$

where $g(R-R_e) \ll k$. The energy levels of an anharmonic oscillator are given by:

$$E_v = hc\omega_e(v+\frac{1}{2}) - hc\omega_e x_e(v+\frac{1}{2})^2 + hc\omega_e y_e(v+\frac{1}{2})^3 + \dots \tag{2.19}$$

where $\omega_e y_e \ll \omega_e x_e \ll \omega_e$. Note that equation (2.19) suggests that the energy levels are not equally spaced. Rather, the separation between them decreases as v increases.
The exact form of the electronic potential as a function of the internuclear separation R can be obtained numerically by solving the TISE. It turns out that this potential can often be very well approximated by the Morse potential:

$$E_n(R) \approx D_e(1 - e^{-\beta(R-R_e)})^2 \tag{2.20}$$

where $D_e = \frac{\omega_e^2}{4\omega_e x_e}$ is the depth of the potential well, $\beta = \left(\frac{\pi\mu c\omega_e^2}{\hbar D_e}\right)^{1/2}$ is related to its width, and $R_e = \left(\frac{\hbar}{4\pi c\mu B_e}\right)^{1/2}$ (where B_e is the rotational constant) is the equilibrium separation. This type of potential accounts for that facts that in the limit as $R \to \infty$ the energy approaches that of the free atoms, while as $R \to 0$ $E_n(R)$ is dominated by the Coulomb repulsion between the two nuclei.

2.1.3 Energy scales in molecular transitions

The highest energy scale in a molecule is the energy associated with the transition between different electronic states E_{el} which is proportional to e^2/a_0 where a_0 is the Bohr radius [31]. Typical values of E_{el} are a few eV. The typical spacing between the vibrational energy levels deeply bound in the potential $E_q(R)$ is of the order $E_{vib} \sim \hbar\omega \sim 10^{-2}E_{el}$ where $\omega = \sqrt{k/\mu}$ for the effective spring constant k of the vibrational motion. The smallest energy scale in a molecule is that associated with a change of rotational state. In the rigid

rotor approximation, the rotational energy in a state N is $E_{rot} = \hbar^2 \frac{N(N+1)}{2I} \equiv BN(N+1)$ where I is the moment of inertia $I = \mu\langle R\rangle^2$ and $\langle R\rangle$ is the mean internuclear separation ($\langle R\rangle \sim R_e$). Typically, $E_{rot} \sim 10^{-4} E_{el}$ (e.g. in CaF B=10.1 GHz or 4.2×10^{-5} eV).

2.2 Spectroscopic notations

In a molecule, keeping track of the the ways the various electronic and nuclear angular momenta couple to each other can become a formidable task. Fortunately, the matter is not too complicated for a simple diatomic molecule.

2.2.1 Electronic angular momenta

In an atom, the motion of the electrons takes place in a spherically symmetric field of force but this is no longer the case in molecules. In a diatomic molecule the addition of a second atom breaks the symmetry and the new axis of symmetry is the internuclear axis z. The electronic orbital and spin angular momenta are still labeled by $\hat{\mathbf{L}}$ and $\hat{\mathbf{S}}$ respectively, but now they no longer commute with the electronic Hamiltonian H_e. Instead, the Hamiltonian commutes with the projections of $\hat{\mathbf{L}}$ and $\hat{\mathbf{S}}$ on the internuclear axis, designated as L_z and S_z respectively, and labeled by the quantum numbers Λ and Σ: $L_z|\Lambda\rangle = \hbar\Lambda|\Lambda\rangle$ and $S_z|S,\Sigma\rangle = \hbar\Sigma|S,\Sigma\rangle$.
In analogy with the atomic spectroscopic notation where the electronic state is labeled according to the magnitude of the electronic orbital angular momentum as $s, p, d\ldots$ for $L = 0, 1, 2, \ldots$, the molecular state is labeled by the value of Λ:

Λ value:	0	1	2...
label:	Σ	Π	$\Delta\ldots$

Here, Σ is the label of the quantum state and not to be confused with the projection of $\hat{\mathbf{S}}$ onto the internuclear axis.
The electronic Hamiltonian is invariant under reflections in any plane containing the internuclear axis. If A_y is an operator that performs a reflection in the molecule-fixed (x,z) plane then $[A_y, H_e] = 0$ and $A_y L_z = -L_z A_y$. The action of A_y on an eigenfunction of L_z with a corresponding eigenvalue $\Lambda\hbar$ is to convert it to the same eigenfunction with the eigenvalue $-\Lambda\hbar$. Since both functions have the same energy, the electronic energy terms that have $\Lambda \neq 0$ are *doubly degenerate* with each value of the energy corresponding to two states that differ by the direction of the projection of $\hat{\mathbf{L}}$ on the internuclear axis. This twofold degeneracy is only approximate and interactions between the rotational motion and the electronic states lead to a small splitting of the two states of opposite parity which is known as Λ-doubling. On the other hand, the Σ states corresponding to $\Lambda = 0$ are not degenerate as reflection through a plane containing the internuclear axis multiplies the

eigenfunction by a constant λ. As $A_y^2 = 1$, $\lambda = \pm 1$. One can distinguish two Σ states - Σ^+ which is left unchanged upon reflection in a plane containing the internuclear axis, and a Σ^- which changes sign under such a reflection.

The projection of the total electronic angular momentum on the internuclear axis is labeled by $\Omega = |\Lambda + \Sigma|$. The molecular state is labeled in analogy to the atomic case as: ${}^{2S+1}\Lambda_\Omega$. Finally, a unique letter designating the electronic state (e.g. $X, A, B, C \ldots$) precedes the ${}^{2S+1}\Lambda_\Omega$ term.

The nuclear spin angular momentum is labeled as $\hat{\mathbf{I}}$ as usual, while the angular momentum associated with the rotation of the nuclei is designated as $\hat{\mathbf{R}}$. The coupling of the different angular momenta in a diatomic molecule is labeled by the following convention:

$$\begin{aligned} \hat{\mathbf{N}} &= \hat{\mathbf{L}} + \hat{\mathbf{R}} \\ \hat{\mathbf{J}} &= \hat{\mathbf{L}} + \hat{\mathbf{R}} + \hat{\mathbf{S}} = \hat{\mathbf{N}} + \hat{\mathbf{S}} \\ \hat{\mathbf{F}} &= \hat{\mathbf{J}} + \hat{\mathbf{I}} \end{aligned}$$

The following spectroscopic notation is also worth mentioning. A transition associated a change of J (where J labels the total angular momentum state excluding the nuclear spin), $\Delta J = J_{\text{final state}} - J_{\text{initial state}}$, is labeled as R for $\Delta J = 1$, Q for $\Delta J = 0$ and P for $\Delta J = -1$. In addition to whether the transition is P, Q or R one can also specify in parenthesis the initial J state.

2.2.2 Hund's cases

The different modes of couplings of the angular momenta in diatomic molecules are known as Hund's cases a), b), c), d) and e). Here, we will only consider the Hund's case relevant for the laser cooling transition in CaF $X^2\Sigma^+ \rightarrow A^2\Pi_{1/2}$: the X and A states are best described in Hund's cases b) and a) respectively.

2.2.2.1 Hund's case a) coupling

In Hund's case a) the interaction between the nuclear rotation $\hat{\mathbf{R}}$ and the electronic motion is very weak. The electronic orbital and spin angular momenta are very strongly coupled to each other and to the internuclear axis. Both $\hat{\mathbf{L}}$ and $\hat{\mathbf{S}}$ precess around the internuclear axis and Λ, Σ and Ω are well-defined. The good quantum numbers are Λ, S, Σ, J and Ω

defined by:

$$\begin{aligned} L_z|\Lambda\rangle &= \hbar\Lambda|\Lambda\rangle \\ \hat{\mathbf{S}}^2|S,\Sigma\rangle &= \hbar^2 S(S+1)|S,\Sigma\rangle \\ S_z|S,\Sigma\rangle &= \hbar\Sigma|S,\Sigma\rangle \\ \hat{\mathbf{J}}^2|J,\Omega\rangle &= \hbar^2 J(J+1)|J,\Omega\rangle \\ J_z|J,\Omega\rangle &= \hbar\Omega|J,\Omega\rangle \end{aligned}$$

The Hund's case a) coupling scheme is shown schematically in figure (2.1).

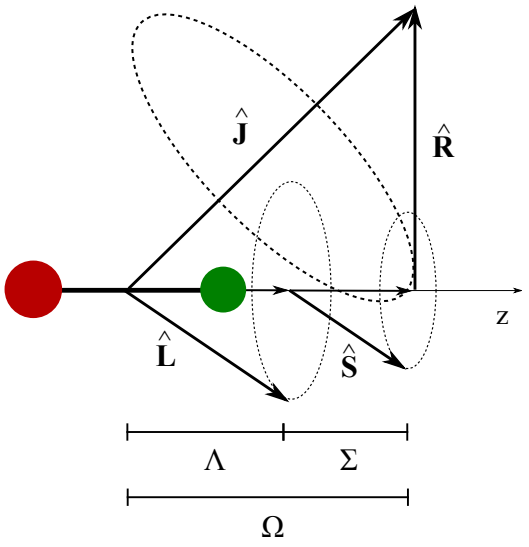

FIGURE 2.1: Hund's case a) coupling of molecular angular momenta.

2.2.2.2 Hund's case b) coupling

In Hund's case b) the rotational energy is much larger than the spin-orbit coupling and Ω is not well-defined. The electronic orbital angular momentum $\hat{\mathbf{L}}$ precesses around the internuclear axis. The rotational angular momentum $\hat{\mathbf{R}}$ first couples to $\hat{\mathbf{L}}$ to form a resultant $\hat{\mathbf{N}}$ which then couples to $\hat{\mathbf{S}}$ to form the total angular momentum $\hat{\mathbf{J}}$. The good quantum numbers are Λ, N, S and J defined by:

$$\begin{aligned} L_z|\Lambda\rangle &= \hbar\Lambda|\Lambda\rangle \\ \hat{\mathbf{N}}^2|(N,S)J\rangle &= \hbar^2 N(N+1)|(N,S)J\rangle \\ \hat{\mathbf{S}}^2|(N,S)J\rangle &= \hbar^2 S(S+1)|(N,S)J\rangle \\ \hat{\mathbf{J}}^2|(N,S)J\rangle &= \hbar^2 J(J+1)|(N,S)J\rangle \end{aligned}$$

The Hund's case b) coupling scheme is shown schematically in figure (2.2).

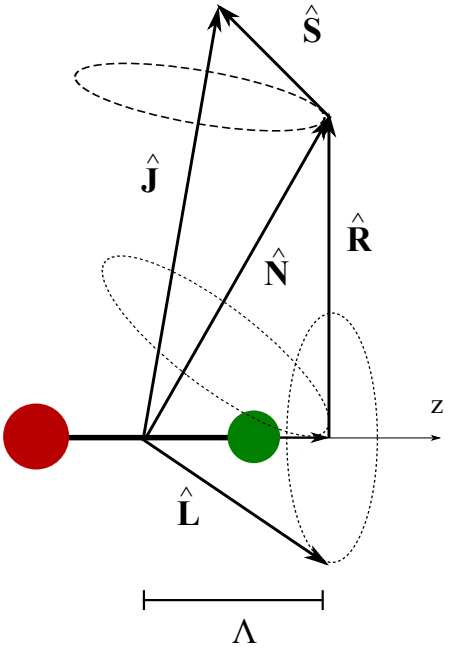

FIGURE 2.2: Hund's case b) coupling of molecular angular momenta.

Chapter 3

Laser cooling of CaF

In the experiments described in this thesis, the laser cooling of CaF takes place on the $X^2\Sigma^+(N = 1, v = 0, 1) \leftrightarrow A^2\Pi_{1/2}(J' = 1/2, v' = 0)$ transition, where v designates the vibrational state. Calcium fluoride has a favorable Frank-Condon (FC) matrix and the photon scattering takes place predominantly on the $A - X(0 - 0)$ transition. If $q_{v',v}$ is $A - X(v' - v)$ FC factor, we can estimate from the overlap of the vibrational wavefunctions in the approximate Morse potential in the two electronic manifolds that $q_{0,0} = 0.978$ and $q_{0,1} = 0.021$ (see section 3.2.3 for more details). To ensure enough scattering events, we close the vibrational leak to the $X(v = 1)$ state. In the current experiment, due to the experimental complexity arising from the hyperfine structure of CaF, we do not close the vibrational leaks to the $X(v \geq 2)$ states and once a molecule decays to the $X(v = 2)$ state it is lost from the cooling cycle. The laser scheme is depicted in figure (3.1).

Calcium fluoride is a viable candidate for laser cooling for several reasons. It has been

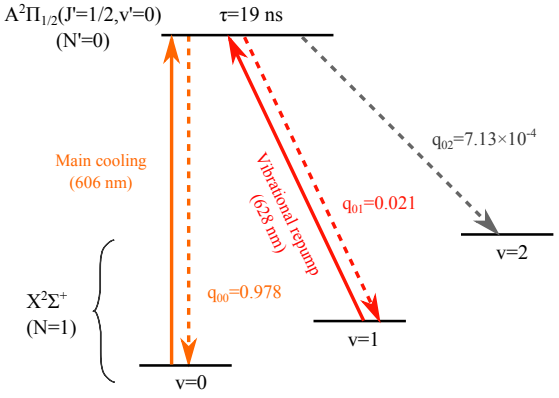

FIGURE 3.1: The laser cooling scheme. Solid lines represent laser light while dashed lines represent the possible decay channels. The rotational, fine and hyperfine structure is not shown.

extensively studied both theoretically and experimentally since the 1930s [175, 176]. Further spectroscopic studies [177–180] followed quickly after the invention of the dye laser

which made it possible to access various the electronic and rovibrational transitions. This comprehensive study means that the spectroscopy of this molecule is known to a very high accuracy, which is essential for laser cooling. Importantly, calcium fluoride has a short excited state lifetime of 19 ns [181] and no intervening electronic states to which the A state can decay, which ensures a fast scattering rate. The character of this molecule in the ground and first excited electronic state makes it possible to come up with a closed rotational transition: the choice of $N'' = 1 \rightarrow N' = 0$ type of transition ensures that the transition is rotationally closed - this is an essential requirement for laser cooling as pointed out in [3] and is discussed in more detail below.

In addition to this, the highly diagonal FC matrix of this molecule means that the vibrational state tends to not change in an electronic transition. In our scheme, we employ a vibrational repump laser acting on the $A - X(0 - 1)$ transition to ensure a vibrationally quasi-closed cooling transition. As the $A-X(0-0)$ and $A-X(0-1)$ Franck-Condon factors are expected to be approximately 0.978 and 0.021, it is reasonable to expect that each CaF molecule can scatter at least a thousand photons before it decays to the $X(v = 2)$ state. This is expected to be a sufficiently high number of scattered photons in order to demonstrate cooling and reduction of the velocity of the supersonic beam. In particular, CaF is a relatively light molecule (with a molecular mass of $m = 59.076$ u) and each absorption of a photon from the laser field will result in a change of velocity of $v_r = h/(\lambda m) = 0.011$ m s^{-1}. Even though the mean velocity of the supersonic beam is as high as 600 m s^{-1} (see chapter 4), the high recoil velocity, scattering rate and long interaction time mean that a significant slowing and cooling can be demonstrated.

Calcium fluoride is an interesting molecule as it has a reasonably large permanent electric dipole moment of 3.07 D [182] making it easy to manipulate with external electric fields and a good candidate for exploring the long range dipole-dipole interactions in molecules. There has been some work on Stark deceleration of CaF in our group [93, 106, 183, 184] and longitudinal laser cooling can be used to increase number of molecules accepted by the Stark decelerator [93].

3.1 Details of the X and A states of CaF

3.1.1 The $|X^2\Sigma^+\rangle$ state

In the ground electronic state of CaF the projection of the electronic orbital angular momentum on the internuclear axis is zero, i.e. $\Lambda = 0$. The state is best described in Hund's case b) basis. The electronic spin $\hat{\mathbf{S}}$ couples to the angular momentum of the rotating nuclei $\hat{\mathbf{N}}$ to form the total electronic angular momentum $\hat{\mathbf{J}} = \hat{\mathbf{S}} + \hat{\mathbf{N}}$. Each rotational level (except for $N = 0$) is split by the spin-rotation interaction into two components with $J = N \pm 1/2$. In the first excited rotational state $N = 1$, this gives rise to two J states: $J = 1/2$

and $J = 3/2$. Each of these two J states couples to the nuclear spin from the fluorine atom $I = 1/2$ to form four states labeled by F, the quantum number of the total angular momentum: $\hat{\mathbf{F}} = \hat{\mathbf{J}} + \hat{\mathbf{I}}$. The four hyperfine states in the $N = 1$ state are F=2,1$^-$,0 and 1$^+$[1].

3.1.2 The $|A^2\Pi_{1/2}\rangle$ state

The lowest-lying excited state in CaF $A^2\Pi_{1/2}$ is best described in Hund's case a) basis. The projection of the electron orbital angular momentum on the internuclear axis is 1 ($\Lambda = 1$ and the state has a Π-character). The electron spin $\hat{\mathbf{S}}$ couples to the orbital angular momentum $\hat{\mathbf{L}}$ to form two well-separated states where the projection of the total angular momentum on the internuclear axis is $\Omega = 1/2$ and $\Omega = 3/2$. The separation between these two states is determined by the spin-orbit coupling constant $\mathcal{A}$ which is 2200 GHz in CaF [185]. The two states are described approximately by pure Hund's case a) basis states: $|\Lambda\rangle|S\Sigma\rangle|\Omega, J, F\rangle$. However, since the spin-orbit interaction Hamiltonian is diagonal in this basis but the molecular rotation is not, the two states are best described by a linear superposition:

$$A_1 = c_1|A^2\Pi_{1/2}\rangle + c_2|A^2\Pi_{3/2}\rangle \tag{3.1}$$

$$A_2 = c_1'|A^2\Pi_{1/2}\rangle + c_2'|A^2\Pi_{3/2}\rangle \tag{3.2}$$

with the amplitudes depending on the relative strength of the spin-orbit interactions and the rotational energies. In this case, the coefficient matrix is mostly diagonal, i.e. the A_1 state is predominantly $|A^2\Pi_{1/2}\rangle$ and the A_2 state - predominantly $|A^2\Pi_{3/2}\rangle$. In addition, a third excited electronic state needs to be included to completely describe the state: the complete basis set is $\{|A^2\Pi_{1/2}\rangle, |A^2\Pi_{3/2}\rangle, |B^2\Sigma^+\rangle\}$ [171]. The degeneracy between the symmetric and antisymmetric superposition of the $\Lambda = 1$ state is lifted by interactions with the $|B^2\Sigma^+\rangle$ state. The frequency separation ΔE_Λ between the Λ-doublet states of opposite parity in the respective J state is given by $\Delta E_\Lambda = \Delta\nu_{fe}(J + 1/2)$ [185] and is approximately 1.35 GHz in the $J = 1/2$ state.

Finally, the nuclear spin $\hat{\mathbf{I}}$ couples to $\hat{\mathbf{J}}$ to give rise to two hyperfine states with $F = 1$ and $F = 0$ whose separation of 4.8 MHz [181] is too small to be resolved in the experiment. Note that the hyperfine splitting in the excited Π state is smaller than the one in the Σ ground state as an electronic wavefunction of Σ-character penetrates deeper into the nucleus and the coupling with the nuclear spin is stronger. It is also worth pointing out that even though the $A^2\Pi_{1/2}$ state is best described in Hund's case a) basis, a more detailed analysis reveals that N is still a good quantum number in that state and is effectively $N = 0$.

[1] There are two states with $F = 1$; we will use + and − signs to distinguish them.

3.1.3 The ground state Hamiltonian

Upon de-excitation from the A state, each of four hyperfine levels in the ground state can be populated. Therefore, the first step to laser cooling is to calculate the exact energy of each of the four ground state hyperfine levels. The complete molecular Hamiltonian in the ground electronic state can be written in a form in which the contributions from the vibrational, rotational and hyperfine parts are separated (as discussed in chapter 2):

$$H = H_{vib} + H_{rot} + H_{hfs} \tag{3.3}$$

The vibrational energy T_v is common to all the levels of interest and can be ignored for the moment. However, both H_{rot} and H_{hfs} depend on the internal (orbital, spin and nuclear) and the external (rotational) angular momentum of the molecule. In the $X^2\Sigma^+$ state there is no electronic orbital angular momentum and so the state is best described in Hund's case b) basis states: $|(N,S)J,F\rangle$. The hyperfine level splitting can be found by using the effective Hamiltonian as given by [186]:

$$\begin{aligned} H_{rot} &= B_{vN}\mathbf{N}^2 + \gamma_{vN}\mathbf{S}\cdot\mathbf{N} \\ H_{hfs} &= b_{vN}\mathbf{I}\cdot\mathbf{S} + c_{vN}\, I_z\, S_z + C_I\, \mathbf{I}\cdot\mathbf{N} \end{aligned} \tag{3.4}$$

where γ is the electron spin-rotation coupling constant, b and c are the isotropic and anisotropic spin-spin couplings, C_I is the nuclear spin-rotation coupling constant and z is taken to be along the molecular axis. Note that although the constants in equation (3.4) depend on the particular rotational and vibrational state, the dependence is very small [186] and we can ignore it for now[2].

The Hamiltonian (3.4) can be diagonalized analytically to obtain the energy levels $E_{N,J,F}$ [187]:

$$E_{N,N+1/2,N+1} = \frac{(\gamma + C_I)}{2}N + \frac{b}{4} + \frac{c}{4(2N+3)} \tag{3.5}$$

$$E_{N,N-1/2,N-1} = -\frac{(\gamma + C_I)}{2}(N+1) + \frac{b}{4} - \frac{c}{4(2N-1)} \tag{3.6}$$

$$\begin{aligned} E_{N,N\pm1/2,N} = &-\frac{1}{4}(\gamma + b + C_I) \\ &\pm \frac{1}{4}\sqrt{(\gamma - C_I)^2(2N+1)^2 + (2b + c - 2C_I)(2b + c - 2\gamma)} \end{aligned} \tag{3.7}$$

The values of the γ, b, c and C_I coefficient are taken from [186]: $\gamma = 39.6587$ MHz, $b = 109.1839$ MHz, $c = 40.119$ MHz and $C_I = 28.76$ kHz (note that spin-rotation coupling

[2]The corrections for the $v = 1, 2$ states is of the order of a few MHz and we can assume that the hyperfine energy splitting in the $v = 0, 1, 2$ manifolds are identical.

constant C_I is much smaller than the other constants). The energy levels with respect to the lowest hyperfine state $E_{1,1/2,1^+}$ are: $E_{1,1/2,0} = 76.25$ MHz, $E_{1,3/2,1^-} = 122.92$ MHz and $E_{1,3/2,2} = 147.82$ MHz. In the first stages of the experiment, we measured the frequency spacing of the hyperfine levels and fount it to be in very good agreement with the calculated values.

3.2 The laser cooling scheme

3.2.1 Closing the transition rotationally

We can ensure that the laser cooling transition is rotationally closed by making use of the selection rules governing an electronic dipole transition.

There are two selection rules relevant for the laser cooling transitions regardless of the Hund's case coupling scheme. The first rule is that the parity must change in an electronic transition. The second selection rule concerns the conservation of the total angular momentum and dictates that the final angular momentum quantum number F must change by $\Delta F = \pm 1, 0$ while transitions of the type $F = 0 \rightarrow F' = 0$ are forbidden.

The laser cooling of CaF is based on the $|X^2\Sigma^+, N = 1, J = 1/2, 3/2\rangle \leftrightarrow |A^2\Pi_{1/2}, J' = 1/2\rangle$ transition. The parity of the ground state is completely determined by the rotational

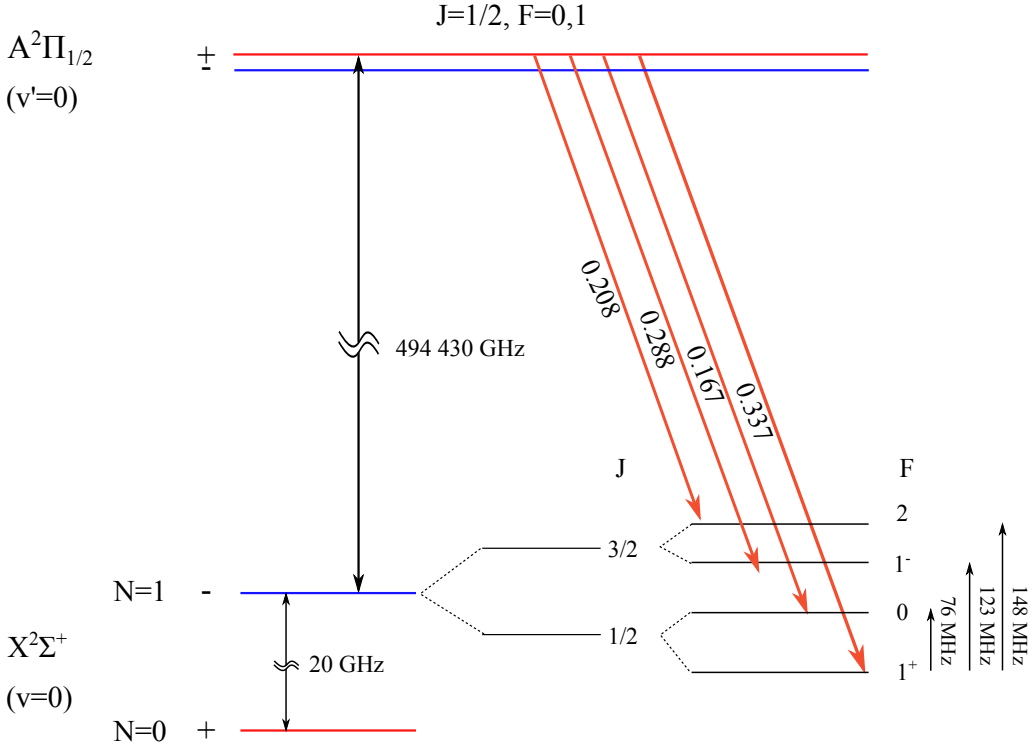

FIGURE 3.2: The main laser cooling transition in CaF on the $A - X(0 - 0)$ line. An excited molecule can decay to any of the four ground state hyperfine levels. The numbers indicate the branching ratios to the corresponding state.

angular momentum and is negative, while the excited state consists of the Λ-doublet states which are of opposite parity. By exciting the odd-parity $|X^2\Sigma^+, N = 1\rangle$ state to the even-parity component of the $|A^2\Pi_{1/2}, J = 1/2\rangle$ state, it is guaranteed that the molecules will return to the original rotational level. This is due to the fact that the $N = 2$ ground state is even-parity and decays to the $N = 3$ states are inhibited due to the angular momentum selection rule and the fact that when $N = 3$, $J = 5/2$ or $7/2$. We note that in principle hyperfine state mixing in the ground electronic state between the $|X^2\Sigma^+, N = 1, J = 3/2, F = 2\rangle$ and $|X^2\Sigma^+, N = 3, J = 5/2, F = 2\rangle$ states could lead to decays outside the laser cooling transition. However, the mixing is expected to be of the order $\left(\frac{|H_{\rm hfs}|}{10B}\right)^2 \approx 10^{-6}$ where $B = 10.1$ GHz is the ground state rotational constant.

3.2.2 Remixing of the dark states

After being excited to the $|A^2\Pi_{1/2}, J = 1/2\rangle$ state a molecule can decay back to any of the four hyperfine levels in the ground state. As the addressing laser light is linearly polarized, the $m_F = \pm 2$ magnetic sublevels in the ground state do not couple to the excited state. Because there is a decay channel to the $m_F = \pm 2$ states but no way out of them, the molecules will quickly become optically pumped into those dark states and the scattering process will slow down significantly. To remix the dark states, we apply a magnetic field of a few Gauss orthogonal to the molecular beam and at a 45° angle to the polarization of the laser light. This magnetic field continuously mixes the bright and dark states into each other at a rate comparable to the optical pumping rate [161, 167].

In more detail, the static magnetic field causes a remixing of the dark states in the following way. A magnetic field B along a direction (say y) causes a state vector $|\alpha\rangle$ to evolve during time t from $|\alpha\rangle$ to $\mathcal{D}_y(\omega_B t)|\alpha\rangle$ where $\mathcal{D}_y(\phi)$ is the rotation operator for rotation through an angle ϕ about the y-axis. The Larmor precession frequency ω_B is given by $\omega_B = \frac{g\mu_B B}{\hbar}$ where μ_B is the Bohr magneton and g is the Landé-g factor of the state. It is expected that a precession frequency ω_B of the order of the scattering rate would be most efficient for remixing of the dark states. The typical scattering rate in the experiment is of the order of $2\pi \times 1$ MHz (see chapter 6). The Landé-g factor of the $|N = 1, J = 3/2, F = 2\rangle$ state is $1/2$ and thus a magnetic field of a few Gauss should be optimal. Note that a magnetic field that is too small will cause a precession of the state that is too slow while a magnetic field whose value is too big will Zeeman shift the magnetic sublevels out of resonance.

3.2.3 Closing the transition vibrationally

The branching ratio for the decay from the upper state vibrational state v' to the lower vibrational state v is given by the square of the overlap integral between the vibrational wavefunctions in the two electronic states and is what is called the Franck-Condon factor

(FCF):

$$q_{v',v} = \Big(\int_0^\infty f^*_{v'} f_v \mathrm{d}R \Big)^2 \tag{3.8}$$

Calcium fluoride is a suitable candidate for laser cooling because of its highly diagonal Franck-Condon matrix. The FCFs can be calculated by using the two-step symplectic integrator method or a more sophisticated technique such as the one described by Pelegrini *et al.* in [188]. Here we show the FCFs in CaF calculated using a Mathematica notebook developed by Dan Farkas (Yale University) and Daniel Comparat [189]. The program constructs a Morse potential from the input molecular parameters and numerically integrates the Schrödinger equation to get the eigenfunctions. A two-step symplectic integrator is used for the numerical integration. The Franck-Condon matrix for CaF was calculated by using the molecular constants from [171] and the results are presented in table (3.1).

Figure (3.3) shows the electronic potential energy curves in the X and A states.

	$A(v'=0)$	$A(v'=1)$	$A(v'=2)$	$A(v'=3)$	$A(v'=4)$
$X(v=0)$	0.977644	0.0223381	1.71899×10^{-5}	4.26674×10^{-7}	8.52043×10^{-10}
$X(v=1)$	0.0216142	0.93480	0.0435343	4.51499×10^{-5}	1.72553×10^{-6}
$X(v=2)$	7.13437×10^{-4}	0.0407297	0.894827	0.0636474	7.82888×10^{-5}
$X(v=3)$	2.68897×10^{-5}	0.00201999	0.0575528	0.857548	0.0827322
$X(v=4)$	1.12588×10^{-6}	1.01753×10^{-4}	0.00381199	0.0722747	0.822814

TABLE 3.1: The Franck-Condon factors for the first five vibrational states of the $A - X(v' - v)$ transition in CaF.

Assuming that the transition is closed rotationally and there are no leaks to dark states, when excited to the $A(v'=0)$ state the majority of molecules (approximately 97.8%) will decay back to the ground vibrational state. However, a small fraction of the molecular population (∼2.16%) will end up in the $X(v=1)$ state and will be lost from the cooling cycle. If the leak to the $X(v=1)$ state is not closed, evetually all the molecules will be pumped in that state. The $A-X(0-0)$ and $A-X(0-1)$ transition frequencies correspond to wavelengths of 606 nm and 628 nm respectively. This means that we need a separate laser to act as a vibrational repump on the $A - X(0-1)$ transition.

Note that with one repump laser the laser cooling cycle is not completely closed vibrationally as the molecules will eventually get pumped into the $X(v=2)$ state. However, for reasons explained in the following section, we argue that providing the $A - X(0-1)$ transition frequency in addition to the main cooling light is enough to ensure that each molecule will scatter a sufficient number of photons for measurable slowing and cooling.

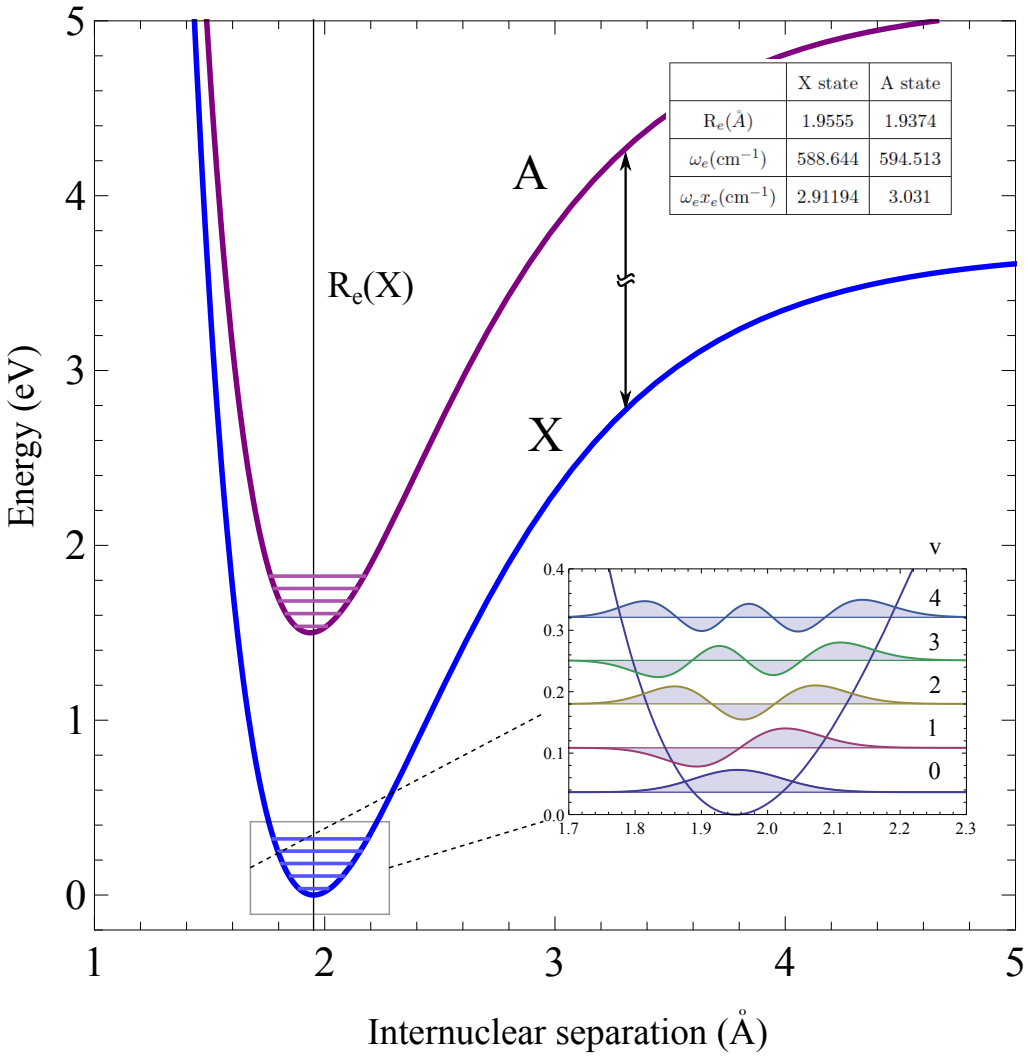

FIGURE 3.3: The Morse potential of CaF in the X and A states constructed using the constants in [171]. The separation between the A and X states is not to scale. The inset shows the first five vibrational wavefunctions (scaled by an arbitrary factor) in the ground electronic state.

3.3 Number of photons scattered

In the experiment we have a system with one excited state and many ground states to which a molecule can decay. Some of the levels to which an excited molecule can decay are coupled to the excited state by a resonant laser frequency and are 'bright', while some of them are not and are 'dark'. One can estimate how many photons on average a molecule will scatter before it decays to a dark state from probabilistic arguments.

The system can be effectively modeled like a three-level system. The molecule is continuously excited on transition $|1\rangle \rightarrow |2\rangle$ where the $|1\rangle$ state includes all 'bright' levels and the $|2\rangle$ is the excited state. Once in the excited state $|2\rangle$, the molecule can decay back to any 'bright' state $|1\rangle$ from where it can get excited again. Alternatively, the molecule can decay to some 'dark' state $|3\rangle$ at which point the scattering cycle stops. Let the probability that the molecule returns to its initial state $|1\rangle$ be p. The average number of photons N_{ph} that the molecule will scatter before it decays to a dark state is given by the geometric series:

$$\begin{aligned} N_{\text{ph}} &= \sum_{i=1}^{\infty} (i \text{ photons}) \\ &\times \text{ (probability of returning to state } |1\rangle \text{ } (i-1) \text{ times)} \\ &\times \text{ (probability of ending up in state } |3\rangle \text{ on the last decay)} \\ &= \sum_{i=1}^{\infty} i p^{(i-1)}(1-p) \\ &= \frac{1}{1-p} \end{aligned} \tag{3.9}$$

If only the $A-X(0-0)$ transition is addressed, $p \approx 0.978$ and $N_{\text{ph}} \approx 45$. If, however, both the $A-X(0-0)$ and $A-X(0-1)$ transitions are addressed and the FCFs are exactly as calculated in table (3.1), $p \approx 0.9776 + 0.02161$ and the number of scattered photons increases dramatically to $N_{\text{ph}} \approx 1250$. We need to note that while equation (3.9) is correct, the FCFs are not known well enough and small corrections to $q_{0,0}$ and $q_{0,1}$ lead to a big difference in N_{ph}.

The FCFs cannot be calculated to an arbitrary precision as the Schrödinger equation is always solved in an approximate potential of the internuclear separation. On the other hand, there are several experimental techniques to measure the FCFs - for example, by studying the saturation of laser-induced fluorescence [181] or by directly measuring the fluorescence on the corresponding band [148, 153], but inevitably there is always some uncertainty associated. In the case CaF only the $A-X(0-0)$ FC factor has been measured. Its value was found to be $0.987^{+0.013}_{-0.019}$ [181] and the calculated value in (3.1) is within the experimental uncertainty of this measurement. Nevertheless, in out laser cooling scheme, it should be possible for each molecule to scatter thousands of photons even for a conservative estimate of the FCFs.

3.4 The scattering force

3.4.1 The scattering force in a two-level atom

When an atom at rest is illuminated with near-resonant light, it will experience a momentum kick upon absorbing a photon from the light field in the direction of the $\vec{k}$ vector of the light. The scattering rate is given by $\Gamma\rho_{ee}$ where Γ is the spontaneous decay rate of the excited state and ρ_{ee} is the probability of the atom being in the excited state. Therefore, the average force the atom will experience as a result from the absorption followed by spontaneous emission is given by:

$$F_{\text{sp}} = \hbar k \Gamma \rho_{ee} \tag{3.10}$$

A value for ρ_{ee} can be obtained by solving the optical Bloch equations and the form of the scattering force can be expressed as:

$$F_{\text{sp}} = \hbar k \frac{\Gamma}{2} \frac{s_0}{1 + s_0 + (2\delta/\Gamma)^2} \tag{3.11}$$

where s_0 is the saturation parameter, $s_0 = 2|\Omega|^2/\Gamma^2 = I/I_{\text{sat}}$ where $I_{\text{sat}} = \pi hc\Gamma/(3\lambda^3)$ is the saturation intensity for a two-level system and Ω is the Rabi frequency, and δ is the detuning from the atomic resonance. The force saturates in the limit of $s_0 \to \infty$ to a maximum value of $\hbar k\Gamma/2$ as the maximum value of ρ_{ee} is $1/2$. Note that increasing the intensity actually only increases the force up to a limit as for intensities that are too high, the stimulated emission rate increases and stimulated emission causes momentum kicks in the the same direction as absorption. The force in equation (3.11) is known as the light (or radiation) pressure force, scattering force or dissipative force. It is a dissipative force and can be used to cool as spontaneous emission is an irreversible process. The scattering force is limited by the spontaneous emission rate Γ.

3.4.2 Laser cooling in a two-level system

In order to achieve any cooling on an atomic sample, a velocity-dependent force is needed. We can include the atomic Doppler shift in equation (3.11) by replacing δ with $\delta + \vec{k} \cdot \vec{v}$. We can then do a Taylor expansion around $v = 0$ and arrive at an expression for the force exerted on the atomic sample by the laser field consisting of a velocity-independent term and a velocity-dependent term:

$$F = F_{\text{sp}} - \beta v$$

where

$$\beta = -\hbar k^2 \frac{4 s_0 (\delta/\Gamma)}{\left(1 + s_0 + (2\delta/\Gamma)^2\right)^2} \tag{3.12}$$

Note that such a force compresses the velocity distribution of the atomic sample for $\delta < 0$, i.e. for red-detuned light. Since the temperature of a dilute gas is defined by the Maxwell-Boltzmann distribution, the laser radiation pressure force, which has a linear dependence on velocity, can be used to bunch the velocity distribution and cool the sample.

3.4.3 Scattering rate in a multi-level system

In the discussion so far, we have only considered the two-level case. In reality, the excited atom or molecule often can decay to a different ground state than the original one. In order to come up with a closed cycling transition, one needs to connect all accessible ground state levels to the excited state.

When a two-level system is driven at an intensity much higher than the saturation intensity of the transition, the steady state distribution of the atomic/molecular population is such that 1/2 is in the excited state and 1/2 is in the ground state. In a system with one ground and one excited state the scattering rate is given by:

$$R_{\mathrm{sc}} = \frac{\Gamma}{2} \frac{I/I_{\mathrm{sat}}}{(1 + I/I_{\mathrm{sat}} + 4(\delta/\Gamma)^2)} \tag{3.13}$$

The situation changes, however, if there are more than one ground or excited states in the system. In this case, the atom/molecule will spend less time on average in any given level. For example, when there are N_{ground} ground states coupled to N_{excited} excited states, the highest scattering rate occurs when the occupancy of each level is $N_{\mathrm{excited}}/(N_{\mathrm{excited}} + N_{\mathrm{ground}})$ (see appendix A for more details).

In the CaF laser cooling experiment, there are 4 excited state and 24 ground state levels (including the magnetic sublevels). Solving the rate equations for the 28-level system reveals that the scattering rate can be well-approximated for a wide range of detuning and intensities by:

$$R_{\mathrm{sc}} = \frac{\Gamma}{7.5} \frac{I/(5I_{\mathrm{sat}})}{(1 + I/(5I_{\mathrm{sat}}) + 4(\delta/\Gamma)^2)} \tag{3.14}$$

The scattering rate is reduced compared to the two-level case due to the many levels involved. For high intensities, one expects that the molecular population will be equally distributed among the 28 levels and approximately 1/7 of the molecules will occupy the excited state rather than the 1/2 characteristic of the 2−level case. The numerical simulation suggests a slightly lower than expected effective scattering rate of $\frac{\Gamma_{\mathrm{eff}}}{2} = \frac{\Gamma}{7.5}$ probably due to the fact the scattering is slowed down because of the precession of the dark ground state magnetic sublevels into bright ones. The rate model also suggests that the new effective saturation intensity for the multi-level transition is $I_{\mathrm{sat,eff}} = 5I_{\mathrm{sat}}$ where I_{sat} is the saturation intensity for the 2−level system ($I_{\mathrm{sat}} \approx 4.9$ mW/cm^2 on the transitions of interest) and the new saturation intensity parameter is $s_{\mathrm{eff}} = I/I_{\mathrm{sat,eff}}$.

In the experiment typically $s_{\text{eff}} \approx 3$ for each transition corresponding to the scattering rate for zero-laser detuning of $R_{\text{sc}} \approx 5.2 \times 10^6$ photons/s.

3.5 Saturation intensity in a multi-level system

3.5.1 Saturation mechanisms

Consider an atom or molecule interacting with laser light near an electronic resonance. The spontaneously emitted photons following excitation are gathered by a detector. The number of photons scattered increases with the increasing intensity of the light driving the transition but will eventually saturate. If the excitation rate R greatly exceeds the excited state spontaneous decay rate Γ, then increasing the intensity of the resonant light does not result in a higher yield of photons. We will call this saturation mechanism 'saturation of the first kind' as it is often the dominant saturation mechanism in atomic systems.
A different type of saturation of the laser-induced fluorescence, which we will call 'saturation of the second kind', occurs when the excited state can decay to a non-resonant ground state. This is usually the dominant saturation mechanism in molecular experiments that use cw lasers as molecules usually have more than one ground states to which the excited state can decay. If the transit time of the molecule through the laser beam is T and the probability of decay to the resonant ground state is p, saturation of the second type occurs when $RT \gg \frac{1}{1-p}$.

3.5.2 Saturation intensity

The scattering rate and thus the laser cooling is critically dependent on the saturation intensity of the transition. It is important to consider several details regarding the saturation intensity of a multi-level system. This discussion is based on [181].
Consider a multi-level system in which the index i denotes any of the ground state levels and the index j denotes the excited state levels. For the case of the main laser cooling transition in CaF, i runs over the four hyperfine states $F = 2, 1^+, 0, 1^-$ in the $|X, N = 1\rangle$ manifold, and j runs over the two hyperfine states, $F' = 0, 1$, in the excited $|A, J' = 1/2\rangle$ state. Let the resonant angular frequency and the laser angular frequencies be labeled as ω_{ij} and ω_L respectively. The laser polarization is taken as the quantization axis (say z). The saturation intensity (characteristic of the saturation of the first kind) is defined by the equation $\frac{I}{I_{\text{sat}}} = \frac{2\Omega^2}{\Gamma^2}$ where Ω is the Rabi frequency of the transition. If $z_{ij} = \langle i|\hat{\mathbf{d}} \cdot \hat{z}|j\rangle$ is the matrix element coupling the states i and j by the electric dipole operator $\hat{\mathbf{d}}$ ($\hat{z}$ is a unit vector along the z-axis), the Rabi frequency for a given transition is $\Omega = E_0 z_{ij}/\hbar$ where the electric field driving the transition is $\mathbf{E} = E_0 \hat{z} \cos(\omega_L t)$. The spontaneous decay rate

for a state $|j\rangle$ to all possible ground states $|k\rangle$ is given by:

$$\Gamma = \frac{1}{\pi\epsilon\hbar c^3}\sum_k \omega_{jk}^3 z_{jk}^2 \tag{3.15}$$

Note that equation (3.15) is valid as the spontaneously emitted radiation is isotropic. That this is true in the case of interest can be verified from the branching ratios matrix (B.1) in appendix B - the molecule in any magnetic sublevel of an excited state j has non-vanishing branching ratios to ground state magnetic sublevels such that $\Delta m_F = 0, \pm 1$.
We can arrive at an expression for the saturation intensity by using the relation $I = \frac{1}{2}\epsilon_0 c E_0^2$ and equation (3.15):

$$I_{\text{sat}} = \frac{\pi h c \Gamma}{\lambda^3}\frac{\sum_k z_{jk}^2}{z_{ij}^2} \tag{3.16}$$

In the derivation of (3.16) all the angular frequencies ω_{jk} have been approximated by a constant angular frequency $\omega = 2\pi c/\lambda$ since, for our case, they vary only by one part in 10^4. It is useful to define the branching ratio r_{ji} for decays from an excited state j to ground states i by: $r_{ji} = z_{ji}^2/\sum_k z_{jk}^2$ where k runs over all possible ground states to which the excited state can decay. The expression for the saturation intensity then becomes:

$$I_{\text{sat}} = \frac{\pi h c \Gamma}{\lambda^3}\frac{1}{r_{ji}} \tag{3.17}$$

Inspection of (B.1) reveals that the branching ratios from the excited state to the $(J, F) = (3/2, 2), (3/2, 1), (1/2, 0)$ and $(1/2, 1)$ ground states are 0.208, 0.288, 0.167 and 0.337 corresponding to saturation intensities of 70.2, 50.7, 87.4 and 43.3 mW/cm^2.

Chapter 4

Making and detecting CaF molecules

The CaF molecules are created in a supersonic source by ablation of a solid Ca target in a mixture of a noble carrier gas and SF_6. Far away from the source the molecules are detected by laser-induced fluorescence (LIF). A schematic of the vacuum chamber which hosts the experiment is shown in figure (4.1).

In this chapter I outline the details of the molecular source and the detection. The theory

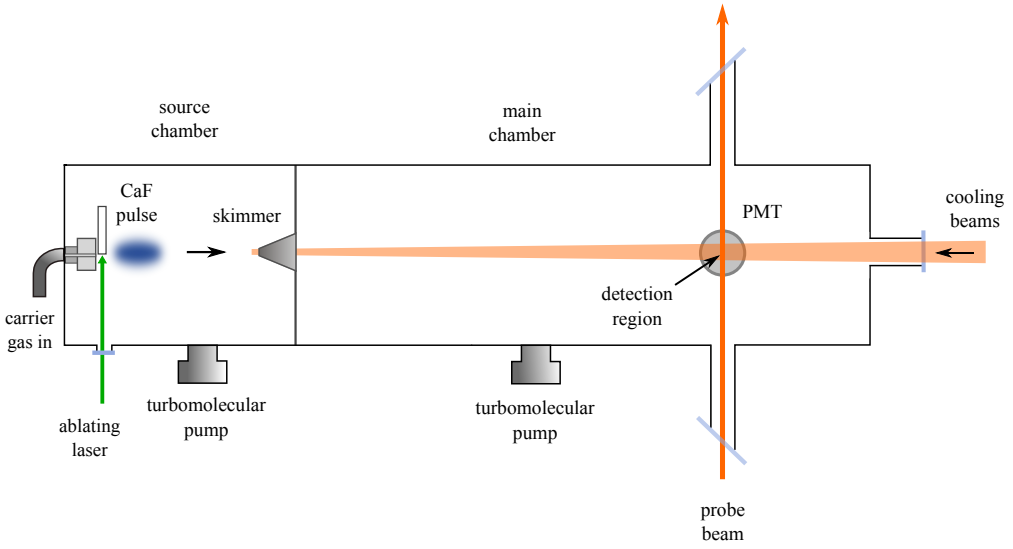

FIGURE 4.1: Lay-out of the experimental vacuum chamber.

of supersonic is given in reference [190] and is briefly described here.

4.1 The molecular source

4.1.1 Supersonic expansion

Many experiments in molecular physics rely on a source providing a large number of molecules in a desired quantum state. Pulsed sources of cold molecules with a narrow distribution in both initial position and initial velocity offer many advantages. Supersonic sources fulfill these criteria and provide a high flux of translationally, rotationally and vibrationally cold molecules in an interaction-free environment without imposing a big load on the vacuum system.

Supersonic expansion is historically a well-established method as the same type of expansion is used in converging-diverging supersonic rocket nozzles [190]. The basic principle of supersonic expansion is as follows. A high pressure gas with no net flow is held inside a container at a pressure p_0 and temperature T_0. The mean velocity of the gas particles is negligibly small and this stage is called the 'stagnation stage'. The gas is then allowed to expand into an environment where the pressure, p, is far smaller than p_0 (e.g. a vacuum chamber). The expansion takes place through a short converging nozzle for which an accelerated flow can be approximated as isentropic [190]. It is important to note that the dimensions of the nozzle must be larger than the mean free path of the gas particles (otherwise the produced beam will be effusive). This allows for collisions to occur among the gas particles as they exit the high-pressure gas region and creates a force toward the low pressure region. In particular, the particles nearest to the low pressure region are greatly accelerated resulting in a mean velocity of the gas exceeding the local speed of sound (hence the term 'supersonic'), provided that the pressure difference is great enough. The high forward velocity is acquired as a consequence of the inter-particle collisions at the nozzle. The spread of the molecular velocities after the transit through the nozzle is narrowed - i.e. the translational temperature is greatly reduced. An ideal gas thermodynamic analysis can be applied to the supersonic expansion process to arrive at an expression for the final velocity of the gas. In this treatment we ignore heat conduction and viscous effects - these approximations are valid as the flow time through the nozzle is short enough compared to the diffusion times.

The first law of thermodynamics states that the change of internal energy of a system (ΔU) is equal to the heat added minus the work done by the system, i.e. $\Delta U = \Delta Q - \Delta W$. In the case of adiabatic expansion, $\Delta Q = 0$ and $\Delta W = pV - p_0V_0$. Equating the total energy

of the gas before and after the expansion we arrive at the equation:

$$\begin{aligned} U_0 + \cancelto{0}{\frac{1}{2}m\bar{v}_0^2} + p_0V_0 &= U + \frac{1}{2}m\bar{v}^2 + pV \\ H_0 &= H + \frac{1}{2}m\bar{v}^2 \\ \Rightarrow h + \frac{1}{2}\bar{v}^2 &= h_0 \end{aligned} \tag{4.1}$$

where m is the total mass of the gas, $\bar{v}$ is center of mass velocity, H is the enthalpy of the system (defined as $H = U + pV$), and h is the enthalpy per unit mass. Note that the important quantity in the expansion is enthalpy rather than the internal energy as the flow is driven by the pressure gradient [190]. As the gas expands its enthalpy and temperature decrease at the expense of its forward center of mass velocity $\bar{v}$.
Recall that the heat capacity at constant pressure is defined as:

$$C_p = \left(\frac{\partial Q}{\partial T}\right)_p = \left(\frac{\partial H}{\partial T}\right)_p \tag{4.2}$$

Combining equations (4.1) and (4.2), we arrive at the expression:

$$\bar{v}^2 = 2(h_0 - h) = 2\int_T^{T_0} c_p dT = 2c_p(T_0 - T) \tag{4.3}$$

where c_p is the specific heat capacity (assumed to be constant over the expansion region). Finally, to relate the velocity to the mass of a gas particle, rather than the total mass of the gas, recall the ideal gas law : $pV = Nk_BT$, where N is the number of particles. Thus one can arrive at a new expression for C_p:

$$\begin{aligned} C_p = \left(\frac{\partial H}{\partial T}\right)_p &= \frac{\partial}{\partial T}(U + pV)_p \\ &= \left(\frac{\partial U}{\partial T}\right)_p + Nk_B \\ &= \left(\frac{\partial U}{\partial T}\right)_V + Nk_B \\ &= C_V + Nk_B = \frac{C_p}{\gamma} + Nk_B \\ \Rightarrow C_p &= \frac{Nk_B\gamma}{1-\gamma} \end{aligned} \tag{4.4}$$

where $\gamma = C_p/C_V = 5/3$ for an ideal monoatomic gas [1]. We have also used the fact that for an ideal gas the internal energy is a function of temperature only[1] and thus $\left(\frac{\partial U}{\partial T}\right)_p = \left(\frac{\partial U}{\partial T}\right)_V$. If each particle in the gas has a mass m_p, dividing both sides of equation (4.4) by the total mass of the gas Nm_p will give an expression for the specific heat $c_p = \frac{k_B\gamma}{m_p(\gamma-1)}$ that can

[1] This is true because there is no interaction between the gas particles.

be substituted in equation (4.3). Thus, the mean velocity of the gas after the supersonic expansion is:

$$\bar{v} = \sqrt{\frac{2k_B\gamma(T_0 - T)}{m_p(\gamma - 1)}} \tag{4.5}$$

where T_0 is the initial temperature of the gas. The gas cools to a low temperature as it expands. Once $T \ll T_0$ the gas reaches its terminal speed: $v_t = \sqrt{\frac{2k_B\gamma T_0}{m_p(\gamma-1)}}$.

4.1.2 The CaF source

So far we have considered the supersonic expansion of a monoatomic ideal gas. In many experiments, the expanding gas is seeded with a small amount of the molecular/atomic species of interest. In our source the seeding is done by ablating a solid target into the expanding supersonic beam. The supersonically expanding gas is referred to as the 'carrier gas' and is a noble gas such as helium, argon, krypton, xenon etc.

Figure (4.2) shows our CaF source. The CaF beam is created by ablating a solid calcium target in a carrier gas consisting of 98% argon (Ar) and 2% sulphur hexafluoride (SF_6). The carrier gas is contained in a line held at a pressure of 4 bar. The gas line is attached to the vacuum chamber through a solenoid valve. A spring-loaded teflon poppet seals the opening of the valve. A high voltage (about 250 V) applied to the valve causes it to open. The calium target is positioned inside the vacuum chamber a few millimetres away from the valve opening. The target consists of a 2 mm-thick strip of calcium glued to the rim of a steel disk. When the density of the gas pulse inside the vacuum chamber is optimal, a pulse of light from a Q-switched Nd:YAG laser, with a duration of 10 ns and a wavelength of 1064 nm, ablates the calcium target. The hot Ca atoms intersect the expanding gas. A chemical reaction takes place between the SF_6 and the Ca atoms forming CaF radicals among other products. The CaF radicals are entrained in the supersonically expanding jet. A skimmer with a 2 mm diameter hole, placed 70 mm downstream from the valve opening, selects the center portion of the molecular beam and limits transverse velocities to $\pm$ 5 ms^{-1}. The experiment is run at a repetition rate of 10 Hz.

4.1.3 Vacuum chamber assembly

A photograph of the vacuum chamber used in the laser cooling experiment is shown in figure (4.3). This vacuum chamber was inherited from T. Wall and used to host an experiment on Stark deceleration of CaF [183]. It consists of cylindrical segments with a cross section of diameter 20 cm and length along the axis of symmetry of 35 cm. The vacuum chamber assembly consists of two sections referred to as the 'source' and 'main' chambers. The separation between these two sections is defined by the steel wall in the middle of which is the skimmer. The source chamber is $\approx$ 40 cm long, while the length of the main chamber has varied from 1.63 m to 2.04 m throughout the course of the experiment (it is easy to

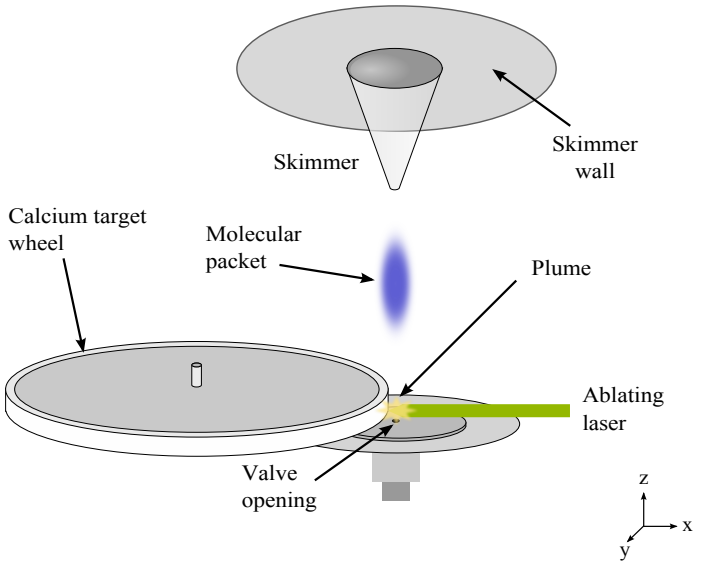

FIGURE 4.2: The CaF source.

remove and add segments). The extension of the vacuum chamber was necessary to ensure long enough interaction time between the molecules and counter-propagating laser beam. The detection region can be positioned either 1.2 m or 1.63 m away from the source (there are two sets of detection optics inside the vacuum chamber), depending on the experiment. Each of the main and source vacuum chamber assemblies is pumped by a 300 ls^{-1} turbomolecular pump. The base pressure in both sections of the vacuum chamber is about 2×10^{-7} mbar. When the valve is pulsed at 10 Hz and the backing pressure in the gas line is 4 bar, the typical time-averaged pressures in the source and main chambers rise to 10^{-4} mbar and 6×10^{-7} mbar respectively. This pressure can be varied by changing the amount by which the poppet is pulled back - either by changing the voltage sent to the solenoid valve or by adjusting the tension of the poppet spring.

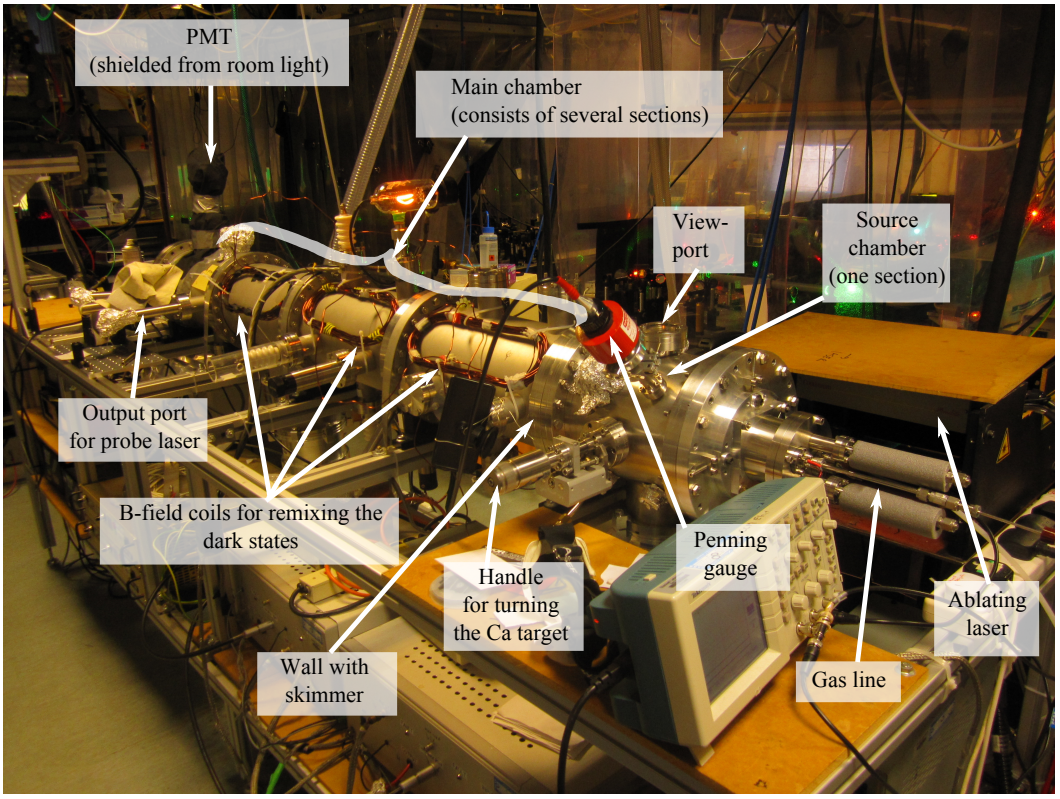

FIGURE 4.3: Picture of the vacuum chamber assembly for the laser cooling experiments presented in this thesis. The main vacuum chamber is extended to allow for a long interaction time with the molecules counter-propagating the laser beams.

4.1.4 Optimizing the CaF signal

There are several experimental parameters that can be varied to optimize the temperature, flux and center speed of the molecular beam. For our purposes, it is essential to have a source that delivers a high flux of rotationally, vibrationally and translationally cold molecules. In addition to this, it is important to have day-to-day stability over the longitudinal temperature and the center velocity of the beam as some of the experiments presented in this thesis are averaged over the course of a day or two.

The details of the supersonic sources are outlined in [170] - the CaF source is very similar to the YbF source described in that paper. Three main variables affect the longitudinal temperature of the beam : i) the separation between the valve opening and the target, ii) the power of the ablating laser and iii) the delay between the firing of the ablation laser and the opening of the solenoid valve. These variables can be controlled in the following way to guarantee a stable and optimal CaF beam. The separation in the x-direction between the valve opening and the calcium target can be carefully adjusted without the need to break the vacuum using a linear translation feedthrough. The Nd:YAG laser normally produces

a pulse of 10 ns duration and energy in the range of 35-50 mJ. The energy can be controlled by adjusting a variable filter at the output aperture or by varying the 'flash-to-Q' parameter (which defines the time over which the population inversion in the Nd ions builds up) from the computer. We varied the 'flash-to-Q' parameter in the 100-200 μs range and found the optimal value to be 160 μs. The delay between the opening of the valve and the firing of the ablating laser ('valve-to-Q' variable) is also computer-controlled. Note that it is necessary to have this delay because the valve responds with a delay to an external trigger. Changing the 'valve-to-Q' parameter affects the signal as it defines where the CaF molecules are seeded in the carrier gas pulse. We found that a 'valve-to-Q' delay of 450 μs[2] between the trigger for the valve and firing of the YAG laser maximized the CaF signal.

The plume that is created when the target is ablated is visible to the eye and its brightness and shape are a good indicator of the quality of the CaF signal. Prolonged ablation of a spot on the target leads to degradation of the surface and possibly deposits unwanted products on the surface, which reduces the signal. Because of this the target wheel needs to be rotated to a fresh spot after approximately 1000 shots. In addition, after all spots on the target have degraded, the target wheel is taken out of the chamber and cleaned by scraping the top layer off with a file. Usually, right after moving the target to a new spot, the LIF signal increases greatly, and after several shots it reaches a stable value possibly due to heating processes. The CaF signal can also be optimized by slightly changing the spot where the YAG laser hits the target and by varying the distance between the valve opening and the rim of the target wheel in the z-direction.
The flux of CaF molecules created is of the order of 10^9 molecules/sr/pulse [183].

4.2 Detection

The CaF molecules are detected by laser-induced fluorescence in the main vacuum chamber as shown in figure (4.4). A probe laser beam whose frequency is scanned around the $X^2\Sigma^+ - A^2\Pi_{1/2}\, P(1)$ transition intersects the molecular beam perpendicularly. The photons emitted at $\lambda = 606$ nm by the CaF molecules following laser excitation are gathered by collection optics inside the vacuum chamber and projected onto the face of a photomultiplier tube (Hamamatsu R374 PMT). The laser-induced fluorescence is reflected by a spherical mirror positioned one radius of curvature below the molecular beam and collected by two aspheric lenses located above the line of the molecular beam. The first aspheric lens is positioned one focal length above the molecular beam and collimates the collected fluorescence. The second lens projects the image onto the photocathode of the PMT with a magnification of 2. One of the two sets of PMT collection optics was installed in the vacuum chamber by R. Darnley, the reader is referred to [191] and [183] for more details. The overall efficiency of

[2] Including a valve response time of approximately 150 μs.

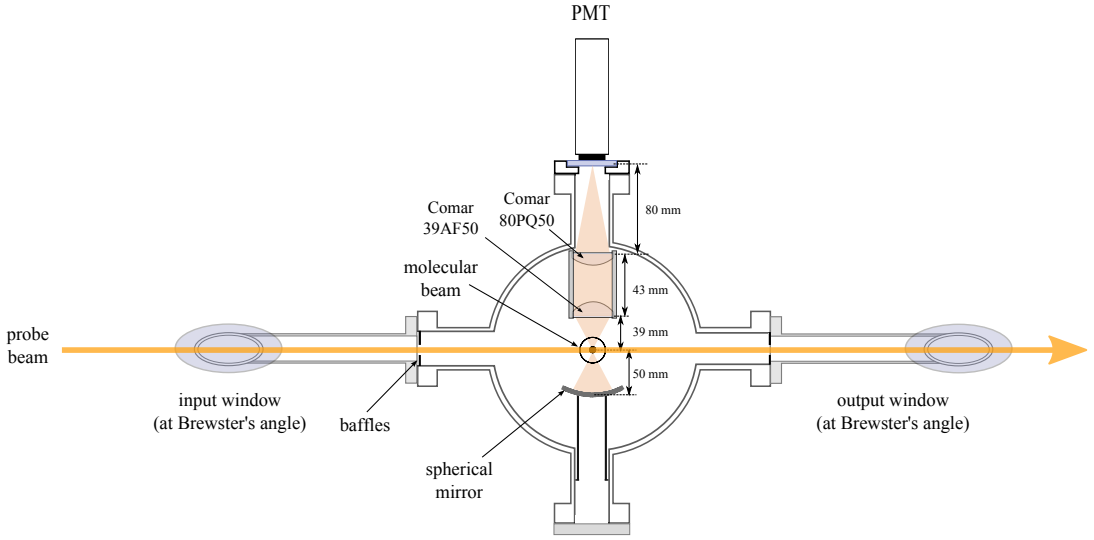

FIGURE 4.4: Schematic of the CaF beam machine and light-collection optics. The figure shows a cross-section of the vacuum chamber perpendicular to the forward motion of the molecules (coming out of the plane of the figure).

the detection (including the quantum efficiency of the PMT at 606 nm and the transmission losses from the optical surfaces) is estimated to be 1% [191]. The probe beam entrance and exit viewports are equipped with windows at the appropriate Brewster angle for a given probe beam polarization in order to minimize background scatter seen by the PMT. A mask under the PMT limits the imaged area from the interaction region. The dimensions of the mask are 10×20 mm and 20×20 mm[3] when the PMT is 1.2 m and 1.63 m away from the source respectively. The mask limits the Doppler contribution from the transverse velocities of the molecules to less than 6 MHz.

4.2.1 PMT electronics

When a photon hits the photocathode of the PMT, it can trigger an avalanche of electrons and a current pulse is given out by the PMT. This electron avalanche is caused by an applied bias voltage (typically in the of 1-1.5 kV range) between the PMT anode and cathode. Depending on the flux of photons, the PMT can be used in either 'photon counting mode' (with low flux of photons) or in 'current mode' (when the flux of photons is high enough). In all the experiments described in this thesis the PMT is in current mode. The current from the PMT is converted to a voltage and then amplified, as shown in figure (4.5). The first part of the amplifier acts as an integrator with a time-constant of 2 μs and a voltage-to-current conversion factor of 1.1×10^5 V/A. The voltage at the end of the integrator is passed on to an amplifier with a variable gain that is user-selected. The final voltage is then sent to the computer DAQ card.

[3]The long side is along the direction of the molecular beam.

Note that the photomultiplier tube is an extremely sensitive instrument. To avoid satura-

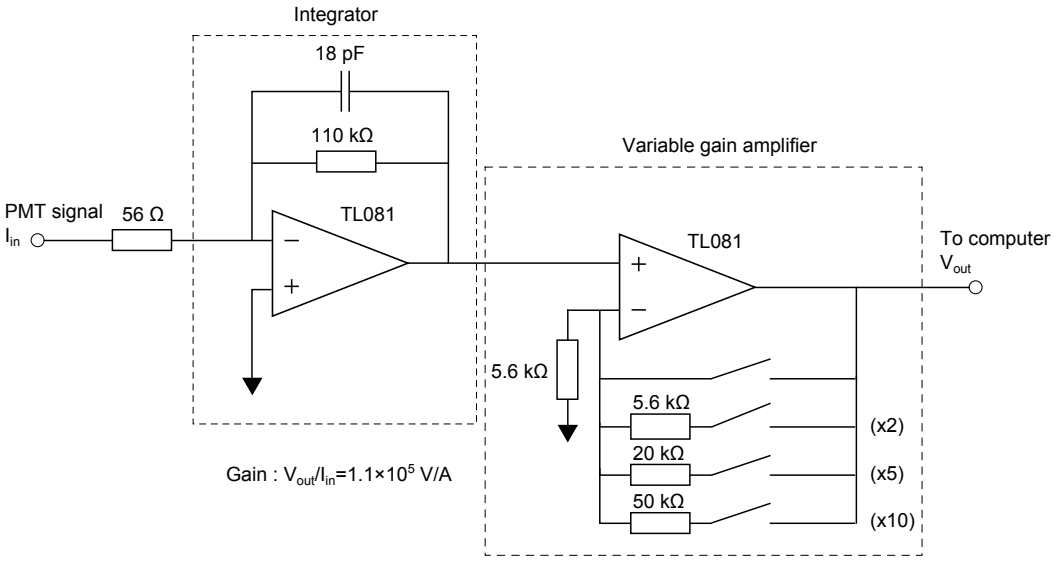

FIGURE 4.5: PMT pre-amplifier circuit diagram.

tion, care must be taken so the photocathode is well shielded from room lights. In addition to this, baffles inside the vacuum chamber are positioned so that no scattered rays from the probe or cooling laser beams make it to the PMT cathode.

4.2.2 The time-of-flight profile

The probe beam used to detect the molecules has a Gaussian intensity profile with a FWHM of 4 mm along the forward motion of the molecules. The transit time through the probe beam of a molecule traveling at at 600 ms^{-1} is approximately 6 μs. This transit time is long compared to the natural lifetime of the excited state of 19.2 ns [181]. For a molecule excited with a single frequency, there are many possible decay channels to different ground electronic state and hyperfine levels. Usually after scattering only a few photons the molecule decays to a dark state where it can no longer see the laser light. This limits the number of photons scattered by each molecule.

The idea of a time-of-flight measurement is simple - a molecule traveling at a velocity v will arrive at the detector positioned at a distance L in time t. Provided that the temporal resolution of the detector can be neglected, the obtained time-dependent signal can be used to deduce the velocity distribution of the molecular packet. A molecular packet with a Maxwellian distribution of velocities centered at v_0 produces a time-dependent signal h at a detector positioned at a distance L away from the source given by [1]:

$$h(t, t_s, s) = \frac{A(L-s)^4}{(t-t_s)^5} \exp\left[\frac{-mv_0^2}{2k_BT} \frac{(t_0 - s/v_0 - t + t_s)^2}{(t-t_s)^2}\right] \tag{4.6}$$

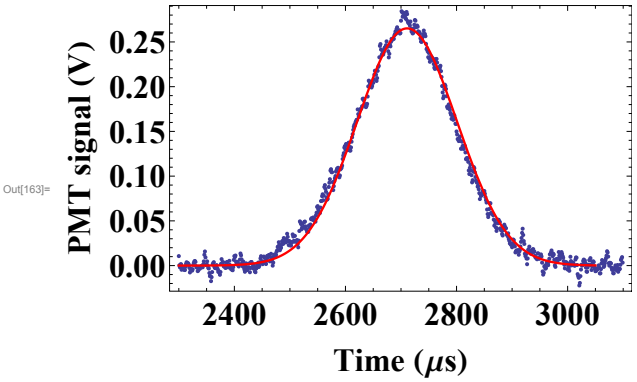

FIGURE 4.6: Time-of-flight (ToF) profile detected 1.63 m away from the source. The signal (blue dots) is fitted to equation (4.7) (red solid line). The fit gives a longitudinal temperature of 2.5 K.

where $t_0 = L/v_0$, s is the initial position of the molecule in the source, t_s is the time at which a molecule is born, and m is the atomic mass of the carrier gas. We can ignore s and t_s since usually the detector is far away from the source and $L \gg s$ and $t_0 \gg t_s$. Moreover, the range of arrival times is much smaller than the central arrival time and we can set $t \approx t_0$ in the denominator of the first factor in equation (4.6). Making these approximations we arrive at the expression for the molecular signal as a function of time:

$$h(t) = \frac{AL^4}{t_0^5} \exp\left[\frac{-mL^2}{2k_B T t_0^4}(t - t_0)^2\right]. \tag{4.7}$$

By fitting equation (4.7) to the time-of-flight measurement of the molecular beam shows one can extract the translational temperature and central velocity of the molecular beam. An example CaF time-of-flight profile detected with the PMT positioned 1.63 m away from the source is shown in figure (4.6). Note that the central arrival time of 2711 μs corresponds to a center velocity of 602 ms^{-1}, while the velocity predicted by equation (4.5) is 557 ms^{-1}. Previous work by T. Wall on the same beam machine has revealed that the measured center speed exceeds the theoretical value by 10%, regardless of the carrier gas [183] (Ar, Kr and Xe were used as the carrier gas). There are three possible reasons for the excess speed of the supersonic beam. Perhaps the dominant mechanism is heating of the soleniod valve which causes the initial temperature of the gas to be higher than room temperature as suggested by Tarbutt *et al.* in [170]. A small increase in the centre of mass velocity can be due to the fact that the expanding gas contains a small amount of SF_6. Sulfur hexafluoride has more degrees of freedom than a simple monoatomic gas and thus can transfer longitudinal kinetic energy to the expanding jet (in SF_6 $\gamma = 1.0984$ [192]). However, this effect only leads to an increase of the velocity of 0.2% as there is only 2% of SF_6 in the misxture. Finally, the increased velocity can be attributed to possible cluster formation in the noble gas in the process of expansion as the energy of formation is released as kinetic energy.

4.2.3 Building up the molecular spectra

In addition to the ToF profile for a single-frequency probe, we can obtain the molecular spectrum by scanning the frequency of probe laser and integrating the ToF profile obtained at each frequency. For example, the main laser cooling transition takes place on the $X^2\Sigma^+(N = 1, v = 0) \rightarrow A^2\Pi_{1/2}(J' = 1/2, v' = 0)$ transition at 494430 GHz. The hyperfine structure in the excited state is unresolved, so when the probe laser frequency is scanned over approximately 150 MHz around the transition frequency, the four ground state hyperfine levels can be resolved (figure (4.7)). Consider first the width of each hyper-

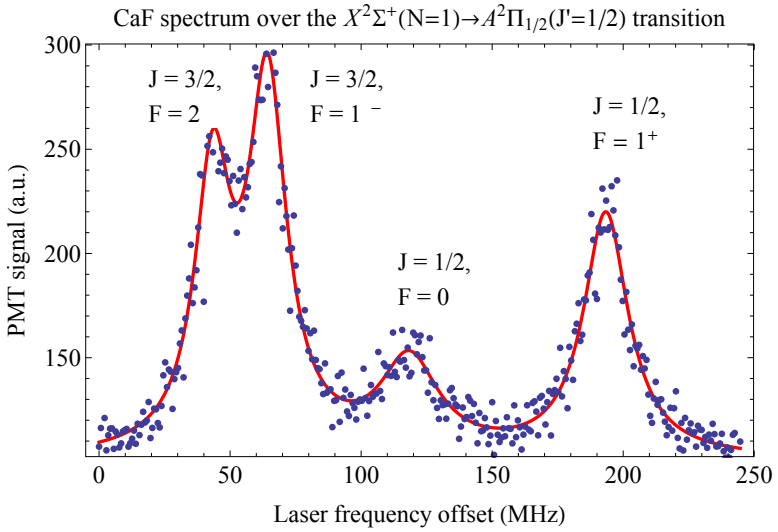

FIGURE 4.7: The CaF spectrum over the four hyperfine levels of the laser cooling transition (points) built up of 350 shots. The laser frequency is stepped by 0.7 MHz in between shots. The solid red line is a fit to the sum of four Lorentzian functions. The probe beam of power 0.3 mW has a Gaussian intensity profile with a FWHM of 3 mm.

fine transition. The mask under the PMT limits the transverse velocities of the molecules that get detected to $v_T \pm 2$ m s^{-1} which corresponds to a Doppler shift at full width of 6.6 MHz. The excited state spontaneous decay rate is $\Gamma/(2\pi) = 8.3$ MHz [181], and thus there is no Doppler contribution to the width of each line. The FWHM of the lines in figure (4.7) is approximately 20 MHz which is due to power-broadening. In the experiments presented in this thesis the probe beam has a Gaussian intensity profile with a FWHM of about 3 mm. The probe beam power is usually around 0.3 mW.

The height of each of the hyperfine components in figure (4.7) is determined by the statistical population of the state and also by the mean number of photons scattered by a molecule in that state. We need to note that source variations can lead to different relative heights of the hyperfine peaks. In order to accurately determine the amplitude of each peak, we measured the spectrum several dozen times with a stable source and fitted it to a sum of four Lorentzian functions. The peak heights normalized to the first peak height were found

to be $1, 1.21 \pm 0.13, 0.39 \pm 0.07$ and 0.98±0.10. Finally, we note that in figure (4.7) we have subtracted the background (of approximately 100 units on the scale shown) which is 'seen' by the PMT due to the off-resonant probe laser light in the vacuum chamber.

Chapter 5

The laser system

In this chapter, I describe the laser systems used for cooling and detecting the CaF molecules.

5.1 Overview of the laser system

A total of six lasers are necessary to carry out the experiments presented in this thesis. Two dye lasers are used for the laser cooling and one for the detection of CaF molecules; two other lasers act as pumps for the dye lasers. A temperature-stabilized He-Ne laser is used as a frequency reference as there are no convenient atomic lines in the vicinity of the transitions of interest.

All dye lasers used in this project are cw and with a ring type cavity. The main cooling laser (which we will refer to as v_{00}) and the vibrational repump laser (v_{10}) are both Coherent 699-21 operated with Rhodamine 6G and DCM dye respectively. The probe laser used to detect the molecules on the $A-X(0-0)$, $A-X(1-1)$ or $A-X(2-2)$ transition is a Spectra Physics 380D laser run with Rhodamine 6G dye. A Spectra Physics BeamLok 2080-15-SA argon ion laser with a maximum output of up to 30 W in the range 445-515 nm is used to pump the v_{00} and probe lasers with 6 and 4 W respectively. The v_{10} repump laser is pumped with 5 W of light at 532 nm provided by a Coherent Verdi V5 (frequency-doubled Nd:VnO_4 laser). The maximum powers available at the output of the three dye lasers with a fresh batch of dye and optimized intracavity elements are 300 mW (v_{00}), 150 mW (v_{10}) and 70 mW (probe laser). A lay-out of the optics table is shown in figure (5.1).

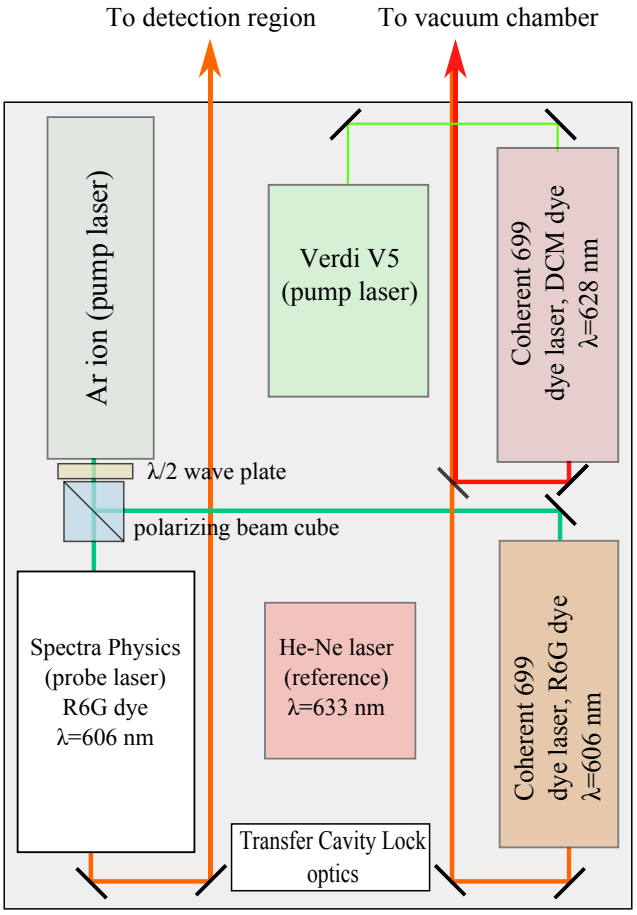

FIGURE 5.1: Lay out of the optics table - top view. The beam combining optics and the hyperfine states sidebands optics are omitted for clarity.

5.2 Laser cooling with dye lasers

Dye lasers offer a convenient way to access the transitions in CaF at 606 nm and 628 nm, even though the day-to-day maintenance of three dye lasers presents a technical challenge. Dye lasers offer certain advantages over other laser sources. They are tunable around a very broad range in the visible and near infrared spectrum for any given dye (e.g Rhodamine 6G can lase in the 570-650 nm range when pumped by Ar ion laser light). This wide range tunability of dye lasers is unparalleled by any other laser system and is particularly useful for molecular physics experiments as diatomic molecules have a multitude of rovibrational transitions spaced over tens of GHz. Dye lasers also provide very narrow linewidth of the laser light - of the order of 100 kHz and good TEM_{00} mode of the output beam.
There are, however, some disadvantages the dye laser user must get used to. In particular, mechanical and acoustical vibrations can cause frequency jitter of the laser light. In addition, the daily adjusting of the controls of the cavity-forming mirrors in order to optimize the power may cause movement of the output beam, while focusing of some mirrors (e.g. M5 and M2 in figure (5.2)) may change the size and mode of the output beam. In general, there are many movable parts inside the laser cavity and this causes many issues. Having a fluid lasing medium is by itself a source of numerous problems. The dyes are prepared according to standard recipes as given in the laser manuals and contain Rhodamine 6G dye dissolved in ethylene glycol (for the v_{00} and probe lasers) or DCM dye dissolved in benzyl alcohol (for the v_{10} laser). The dye solvents are moderately toxic and the DCM dye is known to be mutagenic and carcinogenic which raises health and safety concerns. The dye solutions are circulated at relatively high pressures - 20-30 psi for the Coherent 699 models and 90 psi for the Spectra Physics model. Faulty connectors or tubing with holes in it can have catastrophic consequences (as we have found on several occasions). The fact that the dye gets gradually used up means that the maximum output laser power decreases from day to day.

5.3 The ring cavity dye laser

The dye lasers used are traveling wave ring cavity dye lasers. Here we will briefly outline the theory of operation of bow-tie ring cavity dye lasers. The pump laser beam hits a carefully formed laminar flow of the dye solution causing a population inversion in the large organic molecules in the dye. The lasing mode is then defined by four mirrors. Figure (5.2) shows the schematic of the bow-type cavity. The figure is based on the Coherent 699-21 design, but the Spectra Physics dye laser used for the probe is very similar - the main difference is that the Coherent laser has the dye jet in the horizontal plane while in the Spectra Physics laser the plane is vertical.
Unidirectional laser operation is achieved by an optical diode. A three-plate birefringent

filter reduces the linewidth to 2 GHz. Single longitudinal mode operation is enforced by a thin etalon with a free spectral range of 200 GHz. The use of thick etalon permits the longitudinal mode to be scanned. The overall effective linewidth resulting from these three optical components is 20 MHz. Note that although the instantaneous linewidth of a single longitudinal mode is a fraction of a hertz, mechanical and acoustic disturbances cause jitter and broaden the mode. Thus, active stabilization is needed to achieve a narrower linewidth. To implement this, a portion of the output beam is sent to the laser's own temperature-stabilized Fabry-Pérot reference cavity. As the effective length of the laser cavity is scanned with the vertex-mounted Brewster plate, the output of the reference cavity is monitored by

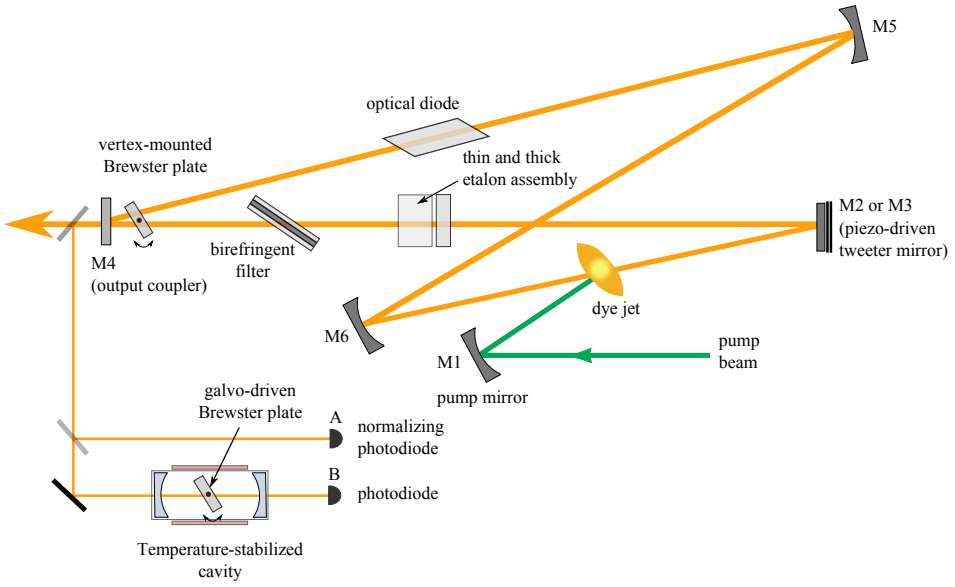

FIGURE 5.2: Schematic of the bow type cavity dye laser (Coherent 699-21 model).

a photodiode (photodiode B in figure (5.2)). A change of the laser frequency causes a change in the transmission through the reference cavity. In order to differentiate between intensity fluctuations and frequency change, a part of the output beam is sent to a normalizing photodiode A. The signals from photodiodes A and B are sent to the laser control box where they are subtracted to generate an error signal. The amplified error signal is used in a servo-loop to generate a lock point. The dye laser cavity is locked by adjusting the laser cavity by driving a high-frequency (∼100 kHz) piezoelectric mounted mirror ('tweeter' mirror M2 in figure (5.2)). Once the laser is in lock mode, its frequency can be scanned in the range 100 MHz-30 GHz by sending a voltage[1] to a galvo-driven Brewster plate inside the temperature-stabilized reference cavity.

[1]This voltage is in the −5 to +5 V range for the Coherent 699 lasers and in the $0 - 1$ V range for the Spectra laser.

5.3.1 Frequency stability

The frequency stability of the dye lasers is critical, in particular for the longitudinal laser cooling experiments. Nominally, the frequency jitter on the laser when in locked mode should be less than 1 MHz.

The spectral characteristics of the two Coherent 699 lasers were analyzed with a confocal scanning cavity (Thorlabs Fabry-Pérot interferometer SA200-5B). The Fabry-Pérot (FP) cavity acts as a very narrow band-pass filter whose length can be carefully tuned by using piezoelectric transducers. As the cavity length is scanned, the transmission of the laser light through the cavity is monitored on a photodiode as shown in figure (5.3).

In order to estimate the laser frequency jitter, we lock the dye laser to its reference cavity

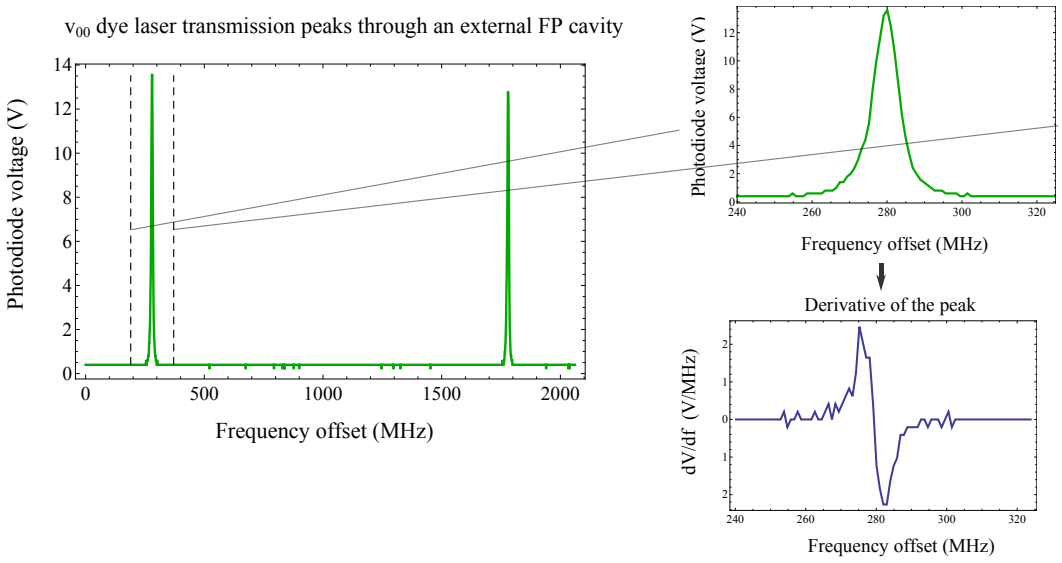

FIGURE 5.3: The v_{00} laser transmission peaks through an external Fabry-Pérot (FP) cavity with a free spectral range (FSR) of 1.5 GHz. The dye laser is locked to its reference cavity while the FP cavity length is scanned with a voltage ramp.

and fix the FP cavity length so that the transmission is about half the maximum value. The changes in transmission are recorded by a photodiode. Figure (5.4) shows the frequency variation over one second. The fluctuating voltage detected by the photodiode is mostly caused by changes of laser frequency as cavity length changes due to thermal fluctuations are unimportant on such a short timescale. The running difference of the voltage ΔV ($\Delta V = V_k - V_{k-1}$ where V_k is the detected voltage at the k^{th} sample point) is an indication of the short-term laser frequency jitter (the data points are taken every 0.5 ms). The mean of the short term frequency jitter is zero, while the standard deviation is 0.8 V which can be related to a frequency change of 0.33 MHz. The maximum change in frequency on this very short timescale is approximately 0.4 MHz - too small to be of any importance. However, it

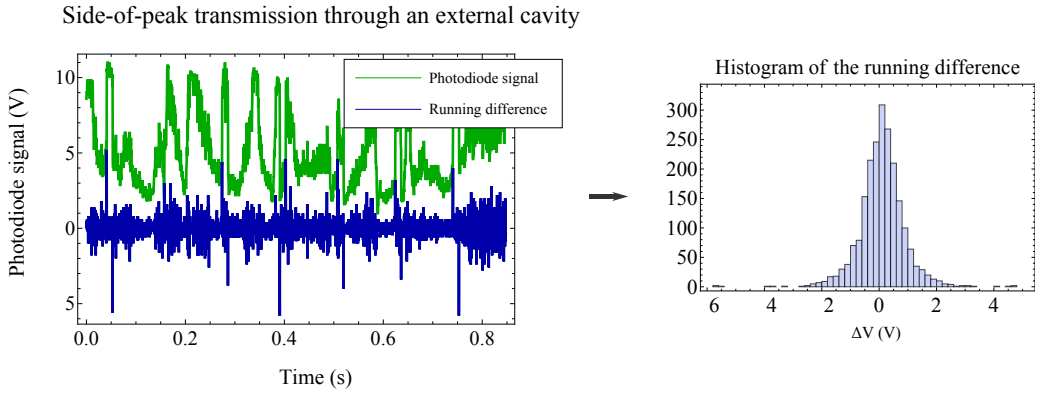

FIGURE 5.4: The frequency jitter of the laser beam is manifested as a change of detected voltage when the external cavity is not scanned (green trace). The cavity length is fixed so that the mean of the photodiode signal corresponds to the half maximum as compared to figure (5.3). The difference in photodiode voltage from point to point (blue trace) is indicative of the short-term frequency jitter.

is obvious from figure (5.4) that some much more striking changes happen on a time scale of approximately 50 ms corresponding to a frequency hops of approximately 4.5 MHz. These frequency hops are more significant as they are comparable to the spontaneous decay rate of the cooling transition: $\Gamma/(2\pi) = 8.3$ MHz. For the purposes of laser cooling a better frequency stability is desirable. To achieve that, we lock both the v_{00} and v_{10} lasers to a temperature-stabilized He-Ne laser with the Transfer Cavity Lock.

5.4 The transfer cavity lock

The long term frequency stability of the Coherent 699 lasers is quoted in the manual to be less than 200 MHz/hour. By referencing to a molecular transition we found that the frequency of each laser, when locked to its own reference cavity, drifts by several MHz/hour. Since it is desirable to achieve stability of the order of several MHz/10 hours, a better frequency reference is needed. We use a temperature-stabilized He-Ne laser as the both long (several hours) and short ($\sim$ 50 ms) timescale frequency reference.

5.4.1 The stabilized He-Ne laser

A He-Ne laser tube (JDS Uniphase model 1001) in a home-made thermal feedback lock is used as the frequency reference in this experiment. The He-Ne frequency is stabilized in the following way. The output He-Ne laser beam at 633 nm consists of several longitudinal laser cavity modes which are linearly polarized and orthogonal to each other in an alternating way. The modes are spaced by $c/2L$, where L is the length of the laser cavity and c is the speed of light. The gain curve of the He-Ne laser has a Gaussian shape with a full-width at half-maximum of $\Delta\omega$ =1500 MHz. For the cavity length of the He-Ne tube used in this experiment, the separation between the modes of orthogonal polarization is 620 MHz and only two modes are supported by the cavity. The relative intensity of each mode depends on their position on the gain curve. The polarization of each mode is linear and randomly oriented but orthogonal to the other mode. The two modes are separated by a polarizing beam cube and monitored by photodiodes. The photodiode signals are used in a home-made proportional and integral (PI) controller to stabilize the laser cavity length so that the relative intensity of the two modes is kept constant. In the current experiment, care was taken to orient the tube so that only one mode is present after the beam splitter once the He-Ne laser is in lock mode. The temperature-stabilized He-Ne laser drifts by $\approx$2 MHz on a $\approx$10 hour timescale.

5.4.2 The transfer cavity lock

The frequencies of the v_{00} and v_{10} cooling lasers are locked with respect to the He-Ne laser with the use of a transfer cavity lock (TCL) similar to the one described in [193]. The reference He-Ne beam and pick-off beams from the output of the two cooling lasers are coupled into a Fabry-Pérot interferometer (Thorlabs SA200-5B, with free spectral range of 1.5 GHz) as shown in figure (5.5). The cavity length is scanned by a TG 120 20 MHz function generator with a saw-tooth voltage ramp at a rate of 40 Hz. The signals of the three photodiodes monitoring the beams transmitted through the scanning cavity are sent to the data acquisition device together with the scan voltage. Each peak is fitted to a Lorentzian function and the position of the peak in terms of voltage sent to the cavity is

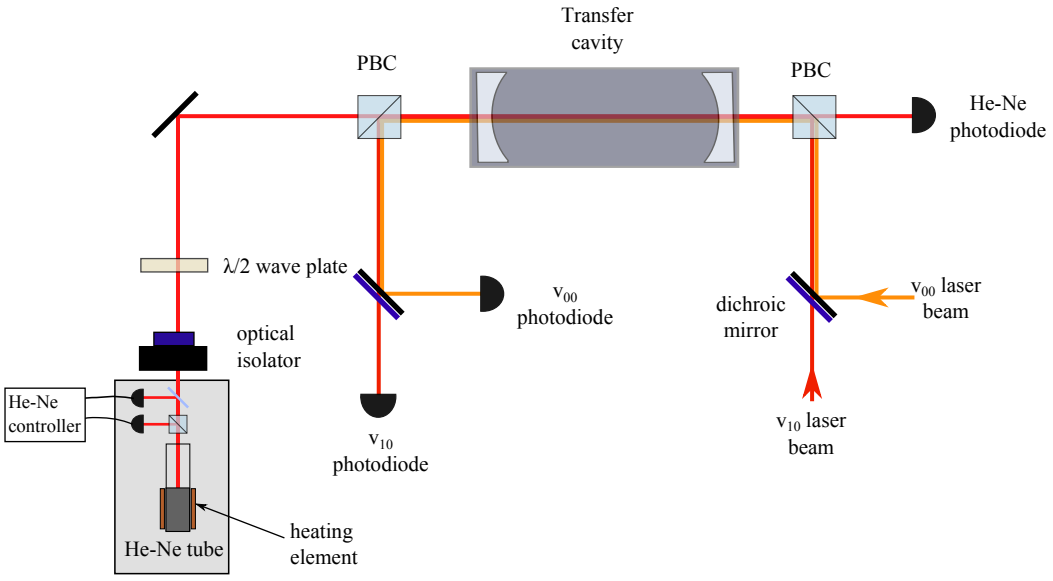

FIGURE 5.5: Transfer cavity lock optics set-up.

recorded by the software[2]. At the end of each iteration loop of the code, the positions of the He-Ne peak and the dye lasers peaks are compared and the voltage sent to the dye lasers is adjusted to keep the relative separation at a constant value as specified by the lock point. In order to account for the long term drifts of the transfer cavity length due to thermal fluctuations, the scanning voltage corresponding to the He-Ne peak is set to be the same for every iteration loop. This is done in the following way : if V_0^{Ref} is the voltage where the user wants to lock the He-Ne, then the difference at the k^{th} loop $\Delta V_k = V_k^{Ref} - V_{k+1}^{Ref}$ is added with a summing amplifier to the saw-tooth scanning voltage sent to the cavity. Thus, the stability of the Transfer Cavity Lock is limited by the stability of the temperature-stabilized He-Ne laser.

Figure (5.6) shows a schematic of the transfer cavity lock hardware. The difference between a dye laser peak set voltage and the actual voltage is displayed as an error signal. The voltage spread of the error signal corresponds to a frequency change of approximately 4.28 MHz/10 mV as determined by the voltage ramp and the FSR of the transfer cavity. The Transfer cavity lock was found to be stable to 0.1 GHz over several hours as verified by the molecular ToF signal and the wavemeter (Angstrom High-Finess wavemeter).

[2]The transfer cavity lock software was written in C# by Sean Tokunaga.

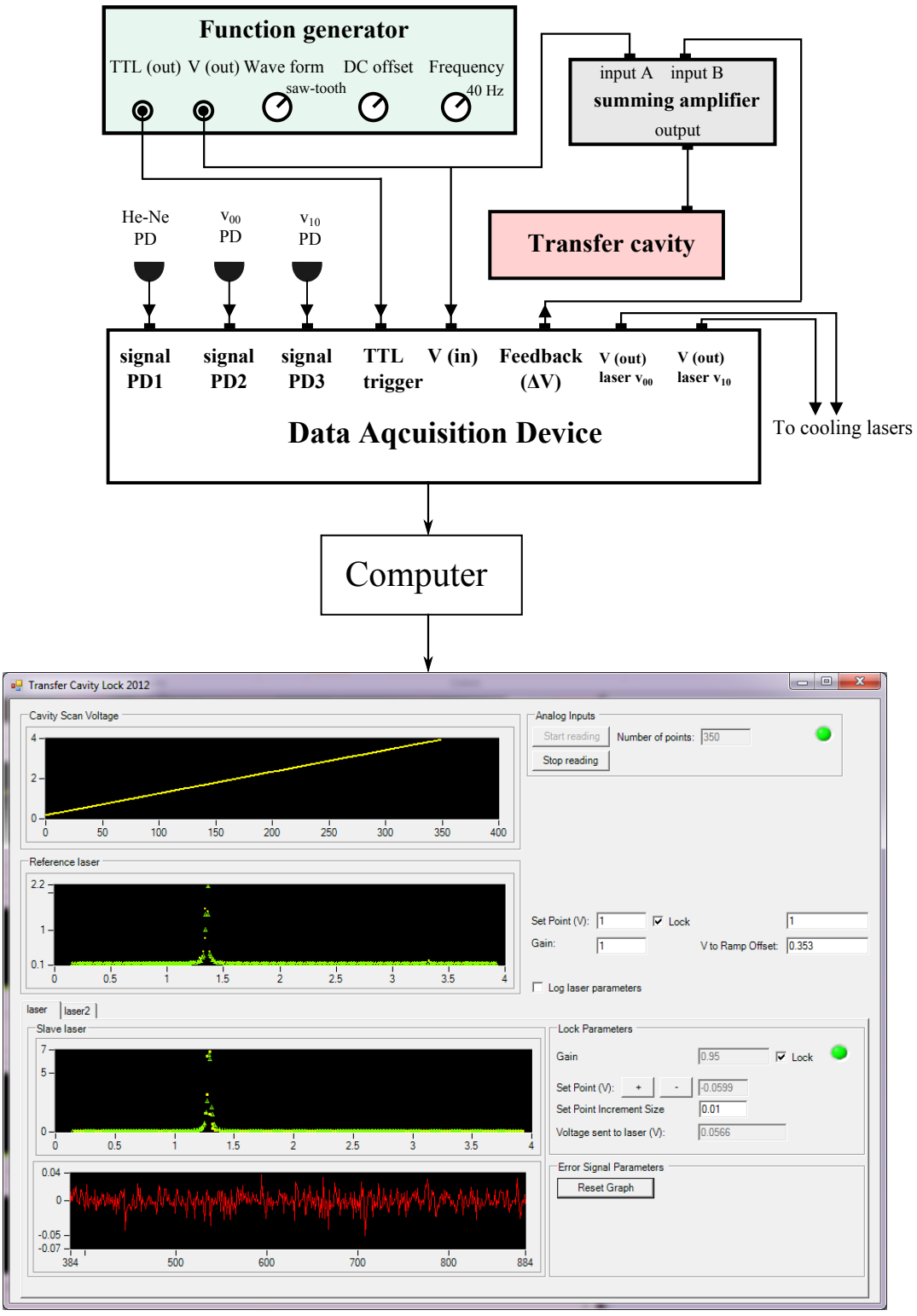

FIGURE 5.6: Top - the transfer cavity lock computer control. Bottom - the software interface.

Chapter 6

Optical cycling in a multi-level system

The efficiency of laser cooling is dependent on each CaF molecule scattering as many photons as possible in a quasi-closed cycling transition. In chapter 3, I discussed the laser cooling scheme on the $P(1)$ line with one vibrational repump in which the molecules cycle on the $X(N = 1, v = 0, 1) \leftrightarrow A(J' = 1/2, v' = 0)$ transition. The laser cooling light consists of a total of eight frequencies (four for the hyperfine levels in the $v = 0$ and $v = 1$ ground state vibrational manifolds respectively) connected to one excited state.
The first step to laser cooling is to address the four hyperfine levels in the $X(N = 1, v = 0)$ vibrational manifold. When this is done, the number of photons scattered by a single molecule increases dramatically even though the transition is only rotationally closed. Simply addressing the four hyperfine levels in the $X(v = 0)$ manifold of the laser cooling transition is not enough to demonstrate significant laser cooling as a molecule will scatter fewer than a hundred photons before getting pumped into the $X(N = 1, v = 1)$ state. Nevertheless, the enhanced fluorescence exhibited in this system is an important milestone in the road to laser cooling and can be used to verify the theoretical prediction for the scattering rate in a multi-level system.
In this chapter, I will explain in more detail how the number of photons scattered per molecule increases as the four hyperfine frequencies of the $v = 0$ laser cooling transition are added. Note that the data in this chapter is only preliminary to laser cooling - the reader can skip to chapter 7 without loss of coherence.

When a molecule is exposed to single-frequency resonant light, it will scatter photons until it decays to an off-resonant state. Consider a molecule in one of the four hyperfine levels of the $X(N = 1, v = 0)$ state. Following the probabilistic arguments from chapter 3, we can estimate that a molecule in a given hyperfine state will scatter on average $N_{\mathrm{ph}} = 1/(1 - r \times q_{0,0})$ photons, where r is the branching ratio to that state and $q_{0,0}$ is

the $A - X(0-0)$ Franck-Condon factor. Using the branching ratios from the $A^2\Pi_{1/2}$ to the ground $(J = 3/2, F = 2)$, $(J = 3/2, F = 1)$, $(J = 1/2, F = 0)$ and $(J = 1/2, F = 1)$ state from appendix A, we can estimate that molecules in each hyperfine state will scatter on average 1.25, 1.39, 1.18 and 1.49 photons before decaying to an off-resonant dark state (here we have taken $q_{0,0} = 0.978$). If, however, all four hyperfine transitions are addressed, the number of photons scattered per molecule in the $N = 1$ state will be much greater than the above values as N_{ph} increases as $1/(1-p)$ where p is the probability of decay to a bright state. This effect is what we will call 'optical cycling' or enhanced fluorescence.
It is useful to define a measure of the optical cycling which we refer to as the 'enhancement factor' E:

$$E = \frac{N_{\mathrm{ph}}(\sum_i^4 (f_i))}{\sum_i^4 N_{\mathrm{ph}}(f_i)} \tag{6.1}$$

where f_i is the frequency of the light addressing state i, $N_{\mathrm{ph}}(f_i)$ is the mean number of photons scattered when only transition i is driven and $N_{\mathrm{ph}}(\sum_i^4 (f_i)))$ is the mean number of photons scattered when all four transitions are driven.

6.1 The rate equation model

The problem of a multi-level molecule scattering photons when exposed to multiple resonant frequencies is more complicated than the simple probabilistic argument presented above. For example, the number of scattered photons per molecule in a $N = 1$ rotational state depends on the intensity with which each transition is driven and the interaction time between the laser and the molecule. We can model the evolution of the molecular population in a given state in terms of the coupled rate equations. The model was developed by M. Tarbutt and the main results will be presented here.
The molecules scattering on the $(X, N = 1, F) \leftrightarrow (A, J' = 1/2, F')$ transition can be modeled by the rate equations in which i ground states are connected to j upper states by resonant laser frequencies. The evolution of the molecular population in each state is governed by the following set of equations:

$$\begin{aligned} \frac{\mathrm{d}N_i}{\mathrm{dt}} &= \sum_j R_{ij}(-N_i + N_j) + \sum_j \Gamma r_{ij} N_j \\ \frac{\mathrm{d}N_j}{\mathrm{dt}} &= -\Gamma N_j + \sum_i R_{ij}(N_i - N_j) \end{aligned} \tag{6.2}$$

where N_i and N_j are the populations in the respective state, Γ is the excited state spontaneous decay rate and r_{ij} is the branching ratio from state i to state j. From the optical Bloch equations taken in the limit where the coherences have reached a steady state one

can find that the excitation rate for transition $i \rightarrow j$ is given by:

$$R_{ij} = \frac{\Gamma}{2} \frac{r_{ij} s}{1 + 4\delta^2/\Gamma^2} \tag{6.3}$$

where δ is the laser detuning from resonance, $s = I/I_{\text{sat}}$ is the saturation intensity parameter and I_{sat} is the two-level saturation intensity (see chapter 15 from [1]).
The model assumes that initially all 12 ground state levels (including the degenerate magnetic sublevels) in the $X(N = 1, v = 0)$ manifold are equally populated and then excited by linearly polarized light to the 4 excited excited state levels. In the model each transition is driven with the same intensity. The driving intensity can be varied and is usually chosen to reflect the typical experimental values. The model also assumes that each molecule interacts with a laser beam of a top-hat intensity profile and the interaction takes place for a variable time. For the results presented in this section, there is no detuning from resonance for each transition. The model also takes into account the branching ratios for the transitions from the excited to the ground states (appendix A).
The solution to the rate equations shows the evolution of the population of each state as a function of interaction time with the laser beam. The excited states population $N_j(t)$ for a given driving intensity can be obtained by solving the rate equations (6.2) and since Γ is known, one can calculate how many photons on average will be scattered per $N = 1$ molecule for a given interaction time. The time evolution of the ground state populations, on the other hand, can tell us if there is a particular state that empties out more slowly than the others and is thus more sensitive to the driving intensity.

6.1.1 Closing the four hyperfine leaks in the $v = 0$ manifold

Consider first the laser cooling transition in which the 12 states in the $X(N = 1, v = 0)$ manifold are connected to the four levels in the A state. The leak to the $X(N = 1, v = 1)$ manifold is included as a 13^{th} state that is not addressed by a laser frequency. For the moment, we will concentrate on the case in which there is no detuning δ, the addressing laser is linearly polarized, and there is no magnetic field to remix the dark states.
Consider first the case when only one hyperfine transition $X(J, F) \rightarrow A(J', F')$ is driven. In this case the molecules will quickly be pumped out in one of the other three hyperfine states after scattering only a few photons. The results of the model for the average number of photons scattered per molecule in the $N = 1$ state when a single transition is driven at $s = 1$ for an interaction time of 10 μs are shown in table (6.1). Increasing either the driving

ground state (J, F)	(3/2,2)	(3/2,1)	(1/2,0)	(1/2,1)
N_{ph}	0.299	0.278	0.107	0.4278

TABLE 6.1: The average number of photons scattered per $N = 1$ molecule when a single transition is driven at $s = 1$ and for an interaction time of 10 μs.

intensity I or the interaction time does not increase N_{ph} significantly as the molecules get pumped into an off-resonant state after scattering only a few photons. Nevertheless, something useful can be learned - the small $X(J = 3/2, F = 1, m_F = 0) \rightarrow A(F' = 0, m'_F = 0)$ coupling causes the $X(J = 3/2, F = 1, m_F = 0)$ state to empty out more slowly than the other ones and acts as a bottleneck. The $(J = 3/2, F = 1)$ state is thus more sensitive that the other three to the driving intensity. When the transition from that state is driven at $s = 5$ the number of photons scattered increases to 0.33.

Consider next what happens when two of the hyperfine transitions are addressed - say $(J = 3/2, F = 2)$ and $(J = 1/2, F = 1)$. We would expect that now a $N = 1$ molecule will scatter a slightly higher number of photons as compared to the single-frequency case above as there are two bright states instead of one. The solution to the rate equations suggests that when both transitions are driven, the mean number of photons scattered per $N = 1$ molecule increases to 0.839. This number of scattered photons corresponds to an enhancement factor of 1.15. Again, increasing the driving intensity or interaction time does not increase the enhancement factor significantly.

When all four transitions are driven, however, the enhancement factor depends strongly on the driving intensity. For linearly polarized light the $m_F = \pm 2$ ground state levels remain dark. The number of scattered photons will increase with increasing driving intensity or interaction time until the molecule gets pumped into these dark states. Figure (6.1) shows the predicted enhancement factor as a function of the driving saturation intensity parameter s per hyperfine transition when all four transitions are driven. The enhancement factor saturates with increasing driving intensity because the molecules soon get pumped the dark ground state magnetic sublevels in the $X(N = 1, v = 0)$ manifold. The model predicts that when the dark states are not destabilized the maximum number of photons scattered per $N = 1$ molecule is 8.13.

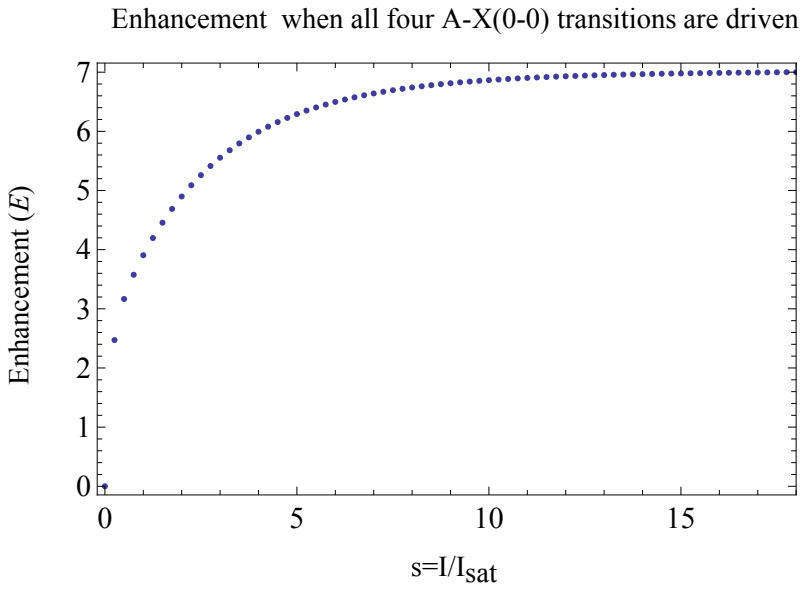

FIGURE 6.1: The enhancement factor predicted by the model when all four hyperfine transitions are driven. The interaction time is 10 μs. The enhancement factor saturates with increasing intensity because the molecules get pumped into the dark magnetic states.

6.1.2 The effect of the magnetic field

The results in subsection (6.1.1) do not take into account the effect of the magnetic field which remixes the dark ground states. The model can be modified to include the remixing of the dark states by assuming that the effect of the magnetic field is to damp out the population difference between the different magnetic sublevels. This means that if the population piles up in one state, the magnetic field will re-distribute it at a rate proportional to the Larmor precession of the spin in that state. The model investigates the effect of adding different components of the magnetic field and how that increases the number of scattered photons.

Figure (6.2 a) shows how the number of photons scattered per transition increases as a function of the driving intensity in the absence of an external magnetic field. When a magnetic field along the y-direction is added the number of photons scattered when each transition is driven separately increases slightly (figure (6.2 b)). The model suggests that the total number of photons scattered is maximized when $B_z = B_y = 2$ Gauss (figure 6.3). For this value of the magnetic field and when the driving intensity is high enough the number of photons scattered per $N = 1$ molecules increases to approximately 48.

Note that there is an optimal value for the magnetic field strength. If the magnetic field is too small, the precession rate of the dark state into bright ones is too low and is limiting the scattering rate while if the magnetic field is too high, the hyperfine levels will be Zeeman-shifted out of resonance with the addressing laser light.

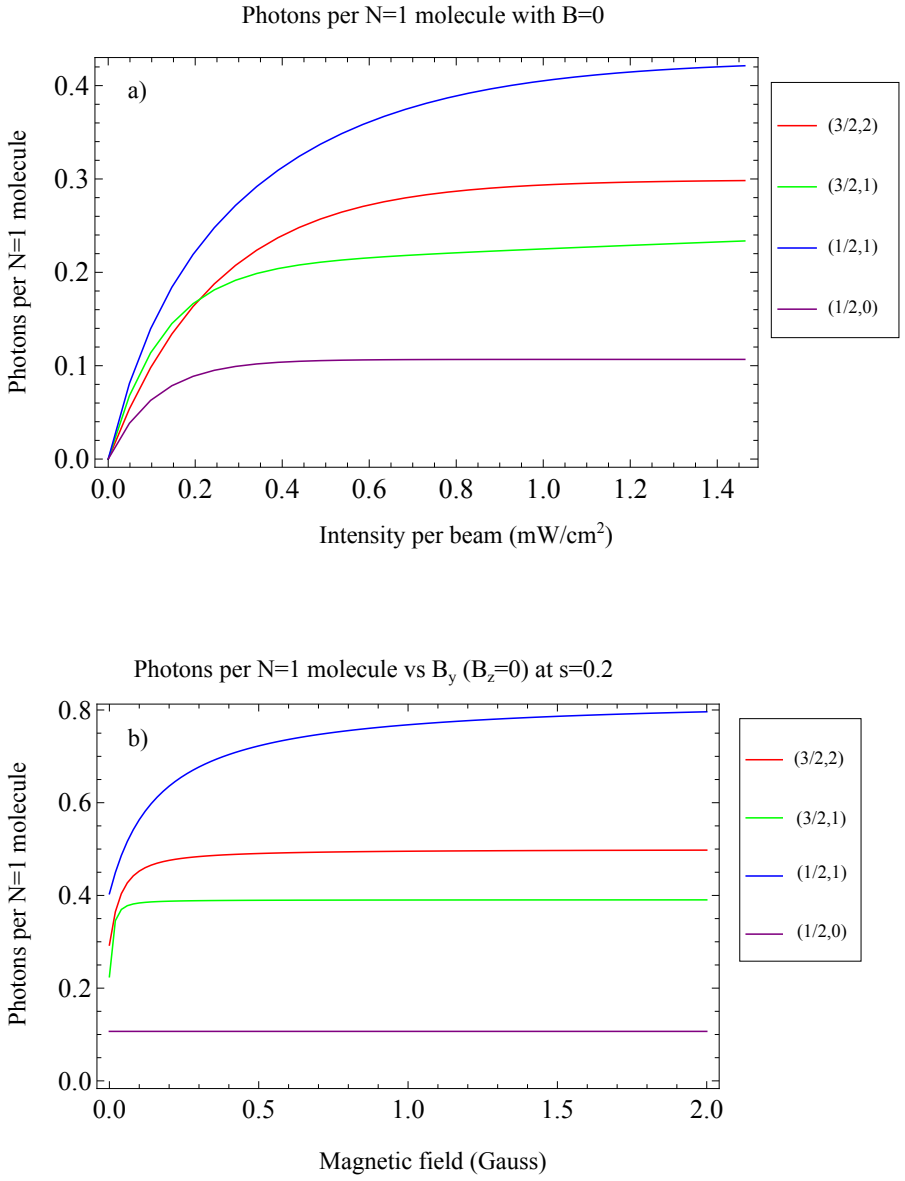

FIGURE 6.2: a) Number of photons scattered per $N = 1$ molecule when individual transitions are driven, as a function of the intensity per beam with no magnetic field and for an interaction time of 10 μs. b) The number of photons scattered per transition increases as a function of B_y. Note that the $(J = 1/2, F = 0)$ state is unaffected by the magnetic field as it should be because it does not have a dark magnetic sublevel.

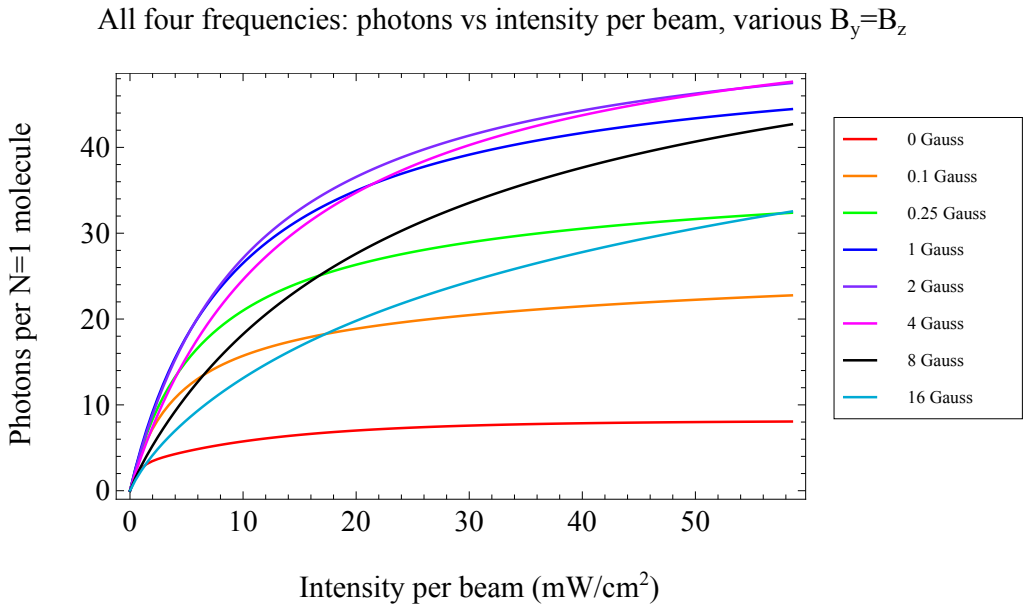

FIGURE 6.3: The number of photons scattered per $N = 1$ molecule when all four transitions are addressed. The interaction time is 10 μs.

6.2 Optical cycling in the low intensity regime

The first step to laser cooling is to build an experiment in which each of the four levels in the $(X, N = 1, v = 0)$ manifold is addressed with a separate frequency. The separations between the hyperfine states are in the radio frequency range (20-150 MHz) and one can use only one laser with inscribed frequency sidebands to address all of them. Ideally, the best approach is to use an electro-optic modulator (EOM), similarly to the laser cooling of SrF experiment [154]. Strontium fluoride has a very similar electronic structure to CaF, and has been transversely cooled on the $P(1)$ transition. However, the frequency spacing of the hyperfine levels in CaF is different than the ones in SrF - the choice of hyperfine frequency generating scheme is dictated by the exact frequency spacing and the commercial availability of EOMs/AOMs which are only made for a limited range of resonant frequencies.

There are two optical set-ups that were built in the laser cooling experiment. The first one consisted of three AOMs and the second one of one EOM and one AOM. The optical set-up with the three AOMs involved the use of many polarizing beam cubes, beam splitters, and half and quarter waveplates to recombine the laser beams and as a consequence approximately 70% of the laser power was lost due to the many optical reflections[1]. Eventually, the EOM-AOM frequency-generating scheme was adopted as it delivered more laser cooling power to the experiment. Nevertheless, the initial three-AOMs set-up had several advantages. For example, this set-up allowed us to optimize the molecular fluorescence by separately controlling the detuning and intensity of each hyperfine frequency.

In this chapter, I will outline how the laser cooling set-up was built chronologically. In the three-AOM set-up we investigated the resonant fluorescence in the low-intensity regime, while the higher laser power available in the AOM-EOM set-up allowed for investigating the saturation of the molecular fluorescence as a function of the intensity and pumping the molecules from the $X(N = 1, v = 0)$ to the $X(N = 1, v = 1)$ manifold.

6.2.1 The three-AOMs set-up

The scheme for addressing the hyperfine levels in the three-AOMs set-up is shown in figure (6.4) - it consists of one unmodulated laser beam and three frequency-shifted components each generated by an acousto-optic modulator.

[1] This loss was despite the fact that all optical elements were custom anti-reflection coated for light at 606 nm.

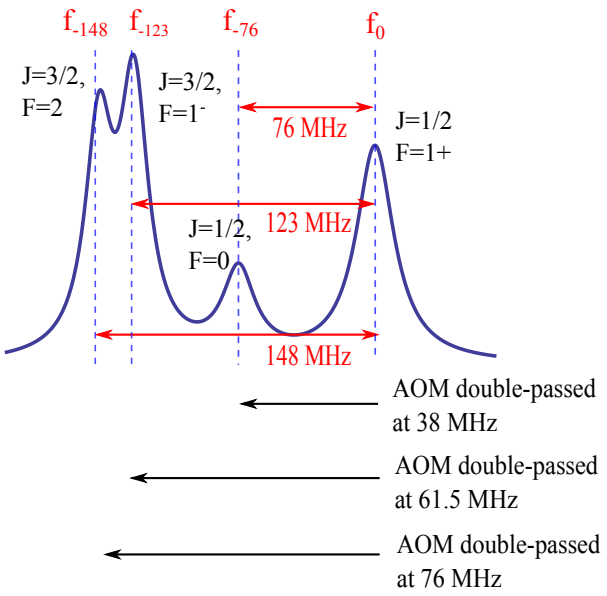

FIGURE 6.4: Addressing the four hyperfine levels of the $X(N = 1)$ state with three AOMs. When the unmodulated laser beam is resonant with the $(J = 1/2, F = 1)$ state, all hyperfine transitions are addressed. The four beams are labeled as f_0, f_{-76}, f_{-123} and f_{-148} to designate the frequency shift of each one of them with respect to the $(J = 1/2, F = 1)$ state.

6.2.1.1 The AOM in a double-pass configuration

The acousto-optic modulator works in the following way. A transducer is driven by a time-varying electric field and creates traveling sound waves inside a solid medium (e.g. glass or crystal). The sound waves cause a local change of the refractive index of the material and act as a diffraction grating for the laser light beam.
The principle of operation of an AOM can be envisioned as a Bragg scattering process [194]. The scattering is between a phonon from the acoustic wave and a photon from the light field. The photon has momentum $\vec{k}_{\text{photon}} = \frac{\Omega}{v_L}$, where Ω is the light frequency and v_L is the velocity of the light inside the crystal, and the phonon has momentum $\vec{\kappa}_{\text{phonon}} = \frac{\omega}{v_s}$, where ω is the modulation rf frequency and v_s is the speed of the acoustic wave inside the crystal ($\vec{k}_{\text{photon}} \perp \vec{\kappa}_{\text{phonon}}$). The first order energy and momentum scattering processes are:

$$\Omega_d = \Omega_i \pm \omega \tag{6.4}$$

$$k_d = k_i \pm \kappa \tag{6.5}$$

where the subscripts d and i refer to the diffracted and incident frequency and momentum of the photon and $+/-$ refers to absorbed/emitted phonon respectively. Note that higher diffracted orders than the $\pm 1^{\text{st}}$ are also possible.
Changing the modulation frequency ω leads to a change in angle of the diffracted orders. This limitation can be avoided in the double-pass configuration [194]. In this set-up, one of the diffracted orders is retroreflected back to the AOM where it is modulated a second time resulting in a total frequency shift of 2ω. From momentum conservation considerations, one can show that the wave vector of the incident beam and the wave vector of the double-diffracted beam are anti-parallel and perfectly overlapped spatially. Thus, even if the modulation frequency of the AOM is changed, the spatial orientation of the diffracted beam after the second AOM pass does not change. The use of a quarter wave-plate and a polarizing beam cube makes it easy to separate the incoming beam from the doubly-diffracted one (figure (6.5)).

A schematic of the optics table for combining the four laser-cooling frequencies is shown in figure (6.6). The output v_{00} laser beam is split into four parts three of which are frequency-shifted using a double-pass AOM arrangement. The four beams are then recombined on beam splitters. This arrangement is inherently lossy as each beam splitter discards about half the light. The final beam consisting of the four frequencies is shaped to have an Gaussian intensity profile with a $1/e^2$-radius of 1.5 mm. It enters the vacuum chamber perpendicularly to the molecular beam.

The rf frequencies for the AOMs are generated by VCOs and amplified by rf-amplifiers. The technical details of the AOMs are presented in table (6.2).

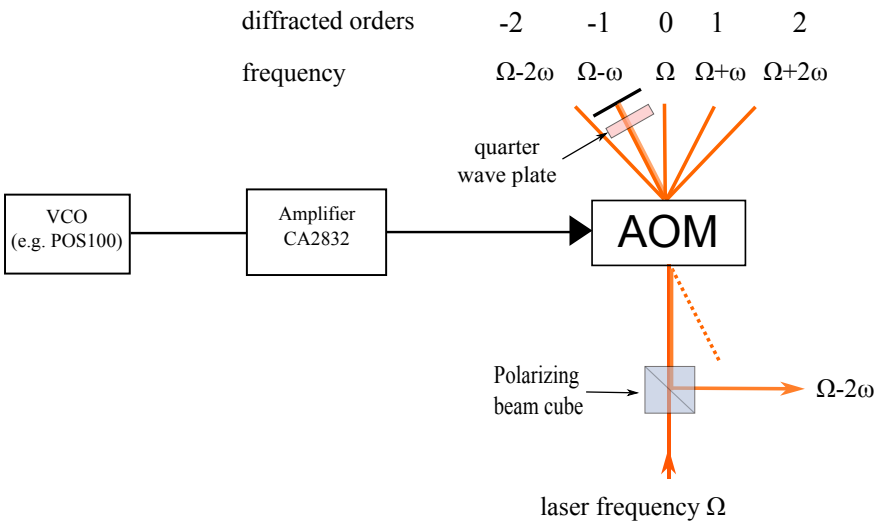

FIGURE 6.5: AOM double-pass configuration set-up.

AOM	RF source	RF frequency	Material	RF power (W)	Efficiency $\frac{\text{Power(diffracted beam)}}{\text{Power(incoming beam)}}$
IntraAction AOM-40 AF series	Mini-Circuits VCO POS50 (25-50 MHz)	38 MHz	glass	2.3 W	70%
Crystal Technology 3080-120	Mini-Circuits VCO POS100 (50-100 MHz)	61.2 MHz	TeO_2	0.5 W	80%
Crystal Technology 3080-120	Mini-Circuits VCO POS100 (50-100 MHz)	76 MHz	TeO_2	0.5 W	80%

TABLE 6.2: AOM parameters and technical details. The efficiency quoted is in single pass.

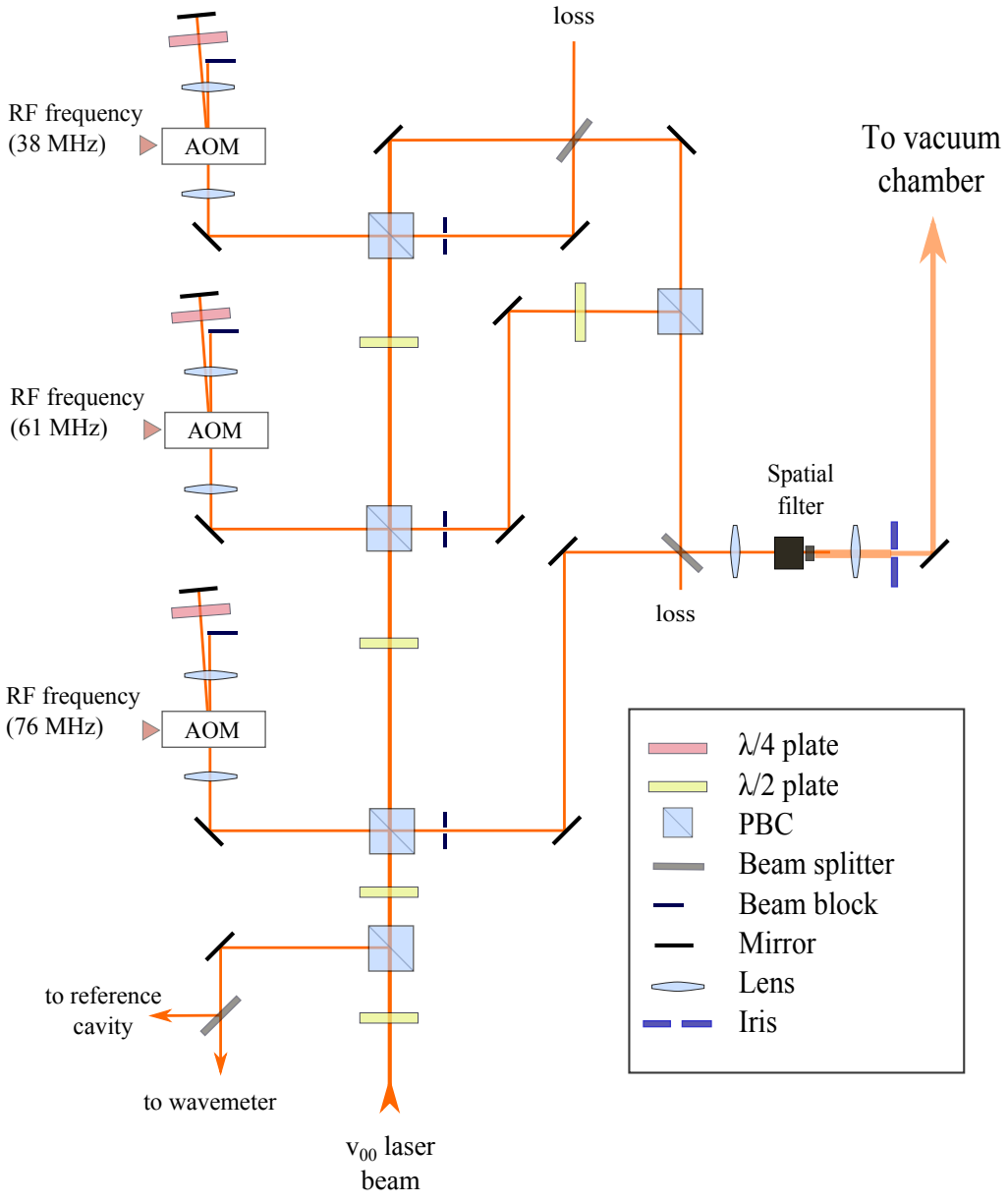

FIGURE 6.6: The three-AOMs set-up optics table diagram. The hyperfine frequency components consist of one unmodulated laser beam and three frequency-shifted ones.

6.2.2 Enhanced fluorescence in a multi-level system

The objective of the experiment is to make the CaF radicals scatter as many photons as possible. The first step to increase the fluorescence is to address each of the hyperfine levels in the $X(N = 1, v = 0)$ ground state. Thus, a molecule spends more time in a state where it can 'see' a laser frequency and cycles in the multi-level system before it is pumped into a dark state.

6.2.2.1 Example spectrum

The hyperfine structure of the $X^2\Sigma^+(N = 1, v = 0) \rightarrow A^2\Pi_{1/2}(J' = 1/2, v' = 0)$ transition can be resolved by scanning the laser around 494430 GHz. An example spectrum taken in the low intensity regime is shown in figure (6.7). The four hyperfine peaks in figure (6.7)

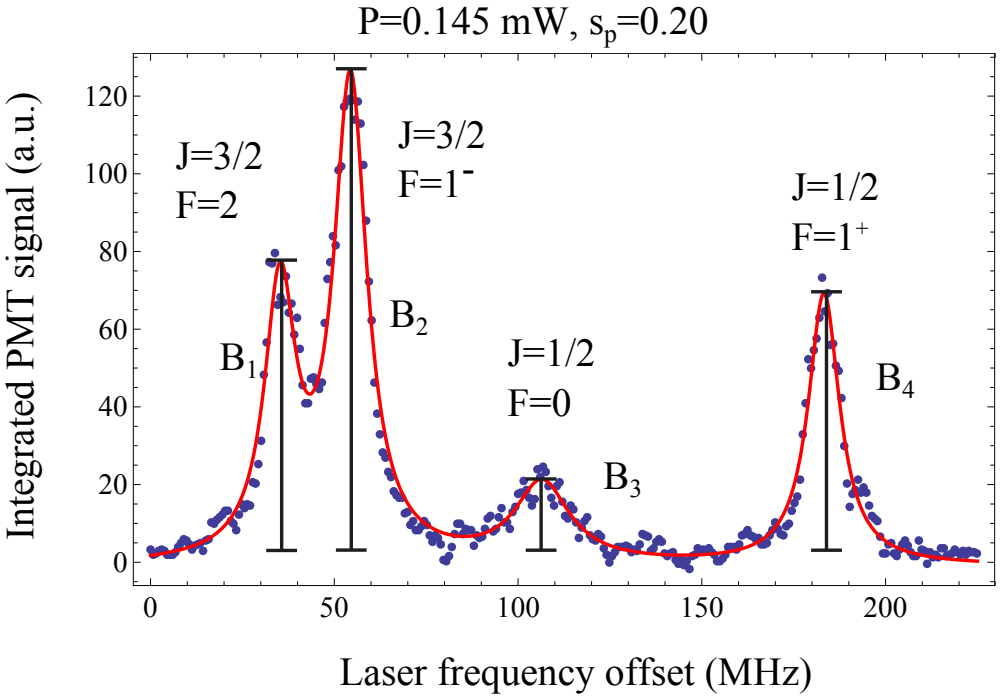

FIGURE 6.7: The four hyperfine levels of the $X(N = 1, v = 0) \rightarrow A(J' = 1/2, v' = 0)$ transition. The spectral features are fitted to the sum of four Lorentzian functions. The spectrum is taken with a probe beam of power 0.145 mW, the quoted saturation intensity parameter is the at the center of the beam.

are fitted to a sum of four Lorentzian functions:

$$L(x) = A + \sum_{i=1}^{4} \frac{B_i (D_i/2)^2}{\left(\frac{D_i}{2}\right)^2 + (x - C_i)^2} \tag{6.6}$$

where A is the background level, B_i is the height of each line, C_i the center frequency of the transition and D_i characterizes the width of the line. Note that the vertical scale in figure (6.7) is arbitrary because of the variable gain of the PMT pre-amp amplifier.
The spectrum shown in figure (6.7) is taken with an unmodulated probe beam from the v_{00} laser which intersects the molecular beam perpendicularly. The laser beam is collimated and shaped to have a Gaussian intensity distribution[2]. We define the Gaussian intensity profile as:

$$I(r,z) = \frac{P}{2\pi w(z)^2} \exp(-r^2/2w(z)^2) \tag{6.7}$$

where r is the radial distance from the center of the laser beam, z is the direction of propagation of the laser beam, P is the power and $w(z)$ is the $1/e^2$-radius at position z (for the data in this section $w = 1.5$ mm and does not change with z). Thus, we get the power when we integrate the intensity: $P = \iint I(r) r dr d\theta$. The intensity is highest in the center of the beam. Whenever appropriate, instead of the intensity we will state the intensity saturation parameter $s = I/I_{\text{sat}}$ where $I_{\text{sat}} = 4.88$ mW/cm^2 for the transition of interest. The peak value of s and I on the laser beam axis will be quoted as s_{p} and I_{p} respectively, while the average values will be simply designated as s and I ($s = s_{\text{p}}/2$ and $I = I_{\text{p}}/2$).

6.2.2.2 Evidence of cycling

In the three-AOM set-up each frequency-shifted beam is resonant with its target state when the unmodulated laser beam in resonant with the $(J = 1/2, F = 1)$ state. The height of that line is expected to increase as more and more resonant frequencies are added and this can be used to estimate the optical cycling. We can estimate the measured enhancement factor E (as defined in equation 6.8) by the height of the $(J = 1/2, F = 1)$ peak when all resonant frequencies are added to the laser light as:

$$E = \frac{\mathrm{B_{res}}(\sum_i^4 \mathrm{f}_i)}{\sum_i^4 \mathrm{B}_i(\mathrm{f}_i)} \tag{6.8}$$

where $\mathrm{B}_i(\mathrm{f}_i)$ is the amplitude of the relevant peak height when a single frequency f_i matches a hyperfine transition from the $X^2\Sigma^+(N = 1)$ to the $A^2\Pi_{1/2}(J' = 1/2)$ state and $\mathrm{B_{res}}(\sum_i^4 f_i)$ is the height of the resonant spectral feature when more than one transition - matching frequencies are present.[3]

[2] Unless otherwise stated, all data presented in this thesis is taken with laser beams of Gaussian intensity profile.

[3] For example, in the three AOM set-up, the frequency f_0 addresses the $(J = 1/2, F = 1) \rightarrow (A, J' = 1/2)$ transition, the frequency f_{-76} - the $(J = 1/2, F = 0) \rightarrow (A, J' = 1/2)$ transition etc. This means that in order to estimate the enhancement factor when all frequencies are present, one has to consider the height of peak B_1 of the spectrum taken with frequency f_{-148}, the height of peak B_2 of the spectrum taken with frequency f_{-123} and so on and compare the sum of those heights to the height of the resonant feature when all the frequencies are present. Note that in principle, if all transitions are driven with exactly the same intensity, there is no need to distinguish between the height of the different peaks taken with the different frequency components. Instead, one can sum up the heights of the four peaks B_i taken with one frequency

For illustrative purposes, consider first the case when only two of the hyperfine frequencies are present - say the f_0 and f_{-148} beams. It is instructive to consider this case as the spectrum gets more complicated when more frequency components are added. Figure (6.8) a) shows the CaF spectrum taken with the unmodulated laser beam f_0 in the low intensity regime with $s_\mathrm{p} = 0.21$. When the f_{-148} beam is scanned around the same transitions, one obtains an identical spectrum but shifted by -148 MHz with respect to the one taken with the f_0 beam (figure (6.8 b)). The two spectra in figure (6.8) a) and b) are not absolutely identical due to source fluctuations. Figure (6.8) c) shows the same transition but this time both frequencies are present. At the point in frequency at which both the f_0 and

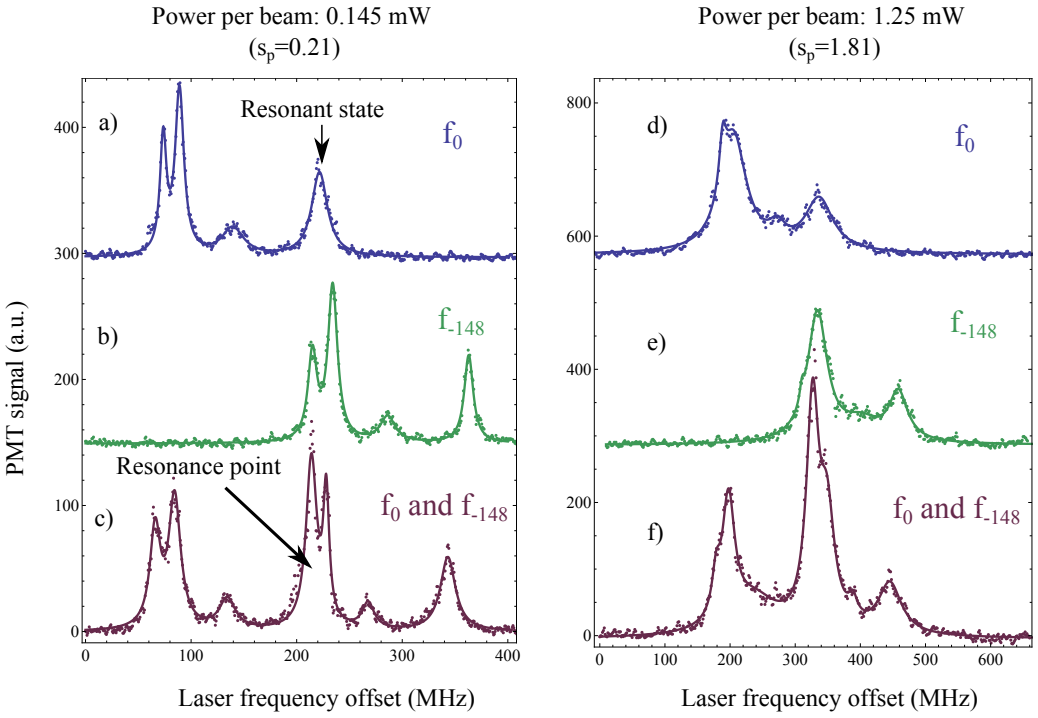

FIGURE 6.8: Scans over the four hyperfine states of the $(X, N = 1, v = 0) \rightarrow (A, J' = 1/2, v' = 0)$ transition taken in the low (left)and higher (right) intensity regime. The spectra are taken with f_0 beam only (a) and (d), the f_{-148} beam only (b) and (e) and both beams (c) and (f). The data is fitted to the sum of four (in the single frequency case) or seven (when the two frequencies are present) Lorentzian functions. The beams driving each transition are of similar intensity.

Note the different vertical scales between the low and high intensity cases.

f_{-148} beams are resonant with their respective transition the detected fluorescence is enhanced. Figure (6.8) d), e) and f) shows the same spectra but taken with higher intensity ($s_\mathrm{p} = 1.81$). The spectral features are power-broadened and it is difficult to resolve the

component. However, in the experiment, often the total laser power is not distributed equally in the four beams and this is why we need to distinguish between the heights of the peaks taken with different frequency component.

$(J = 3/2, F = 2)$ and $(J = 3/2, F = 1)$ states. When the two transitions are well saturated, we expect a molecule to scatter the maximum number of photons on each of the two transitions before falling out of the semi-closed cycling. However, the enhancement in the two-frequency case is too small to be detected in the experiment.

When all four frequencies are present in the laser cooling light we can observe optical cycling. Figure (6.9) shows the CaF spectrum taken with the four frequencies labeled f_0, f_{-76}, f_{-123} and f_{-148}. The optical cycling is signified by i) the increase of the height of the resonance peak and ii) the effect of the magnetic field on the observed fluorescence. The spectral features of the scan in figure (6.9) b) look much more complex compared to (6.8) c) and f) because the presence of the four frequencies means that at various points during the scan the CaF molecules are excited on different combinations of transitions. Because of the richness of the spectrum, it is not possible to fit the data to a sum of Lorentzian functions. Despite this complexity, we are only interested in the point at which all four frequencies are resonant.

The interaction length between the molecules and the laser light l_{int} can be taken to be defined by the full width of the Gaussian beam, i.e. $l_{\text{int}} = 6$ mm. This interaction length corresponds to an interaction time of 10 μs for the molecules traveling at 600 ms^{-1} with a correction of only ± 1 μs for the slowest/fastest molecules in the packet. The scattering rate is limited by the slowest transition (in this case $s_{\text{p}} = 0.79$). When we take the average value for s of 0.395, we find the model predicts that the number of photons scattered per molecule in $N = 1$ state when the four transitions are driven is 8.6 (see figure (6.3)).

From the height of the resonance peak in the presence of the magnetic field in figure (6.9) and the Lorentzian fits to the individual hyperfine levels we measure an enhancement factor as defined in equation (6.8) of 3.5 ± 0.3 (the error bar is from the average of several scans). The model predicts that when a single transition is driven the number of photons scattered per molecule in the (J, F) state is 0.5, 0.39, 0.11 and 0.8 for the $(3/2, 2)$, $(3/2, 1)$, $(1/2, 0)$ and $(1/2, 1)$ states (see figure (6.2) b)). Using these numbers and the measured enhancement factor we find that in the experiment approximately 6.3 ± 0.54 photons were scattered per molecule. This is slightly lower that the theoretical value given above. The lower experimentally observed value is expected as the four frequency components are not perfectly overlapped and have a non-perfect Gaussian intensity distribution.

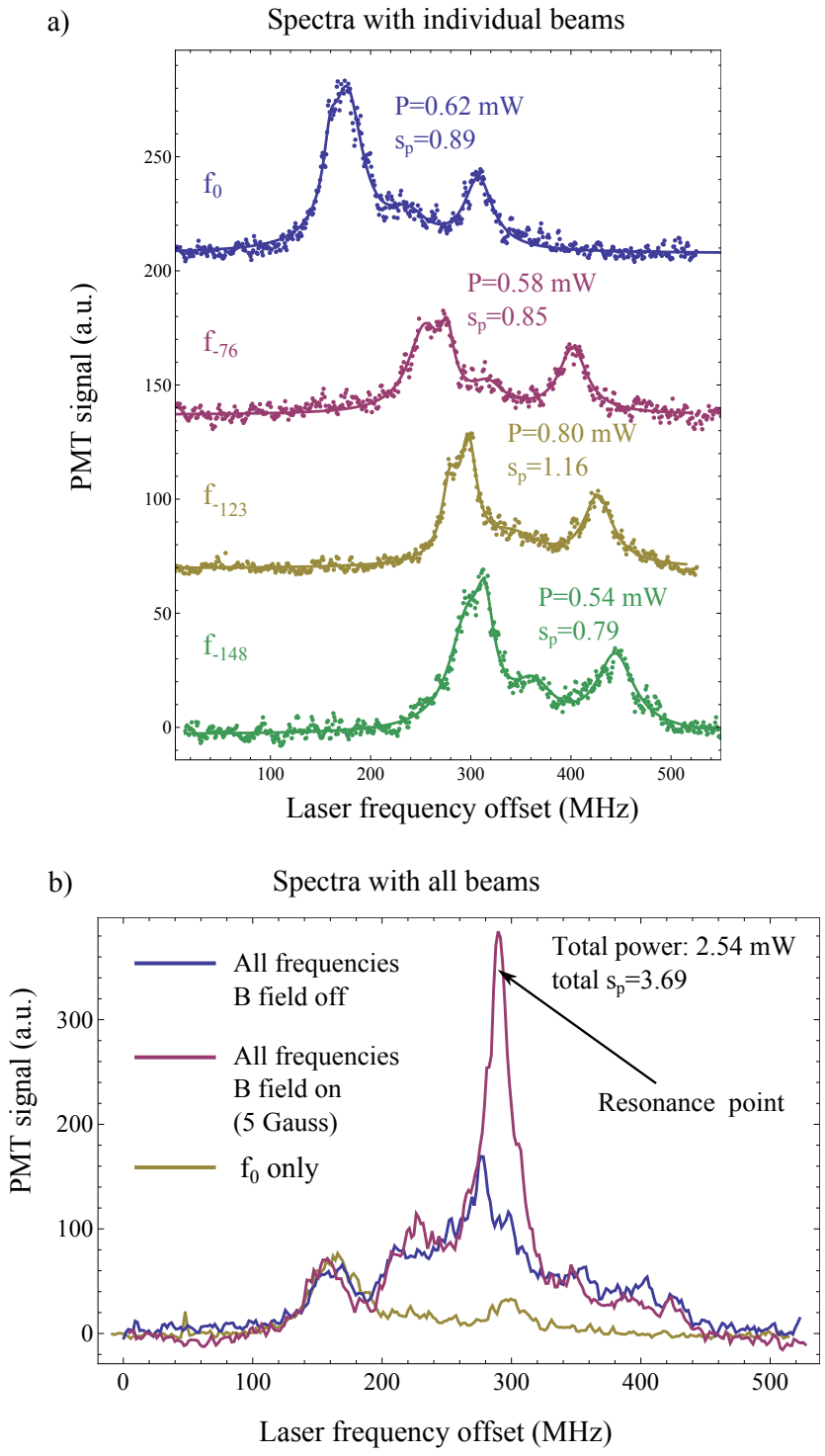

FIGURE 6.9: The spectrum over the $X^2\Sigma^+(N = 1, v = 0) \rightarrow A^2\Pi_{1/2}(J' = 1/2, v' = 0)$ transition taken with the four individual beams (a) and when all frequencies are present (b). The spectra are taken in the relatively low intensity regime ($s_p \sim 1$) and the spectral features are still resolvable. The vertical scale is the same in (a) and (b). The addition of the magnetic field increases the fluorescence by a factor of 2.3.

6.2.2.3 The effect of the magnetic field

The magnetic field in the interaction region is generated by two coils in the Helmholtz configuration. The fluorescence was maximized by finding the optimal current in the coils. The optimal value was found to be ≈ 5 Gauss at a 45° angle to the laser polarization. The precise angle was found to be unimportant as long as it was in the 40°-50° range.
The addition of the magnetic field of 5 Gauss increases the resonant peak height in figure (6.9) b) by a factor of 2.3±0.2. This implies that without the field the molecules have scattered enough photons to be pumped into the dark magnetic sublevels of the ground state. The model predicts an increase in the fluorescence by a factor of 2.52 (figure (6.3)) when each of the four transitions is driven at $s = 0.395$. However, this comparison is between zero field and $B_x = B_y = 2$ Gauss, whereas the Earth's magnetic field, which is in the 0.1-0.25 Gauss range, was not canceled in the experiment. The model predicts a fluorescence increase compared to zero field of a factor of 2.4 and 2.5 for $B_x = B_y = 0.1$ Gauss and $B_x = B_y = 0.25$ Gauss respectively. In fact, at such modest driving intensities, a very small magnetic field is enough to do the remixing of the dark states and increasing it further does not increase the fluorescence significantly.

6.2.2.4 Increasing fluorescence with increasing intensity and interaction length

The height of the resonant peak in figure (6.9) is expected to first increase linearly with increasing intensity and interaction time and eventually saturate. This saturation is governed by two different mechanisms in the two cases. The saturation with increasing intensity simply reflects the dependence of the scattering rate R_{sc} on the driving intensity I. The height of the resonance peak with increasing interaction time for a fixed laser intensity, on the other hand, will initially increase linearly until at some point the molecules have scattered a significant number of photons to be pumped into the $X(N = 1, v = 1)$ state - the saturation in this case will be due to this pumping.
Figure (6.10) shows the resonance peak height versus intensity for an interaction time of 10 μs. Two cylindrical lenses were used to shape the combined four frequencies as a rectangular beam of dimensions 10 mm × 2 mm, with the longer side parallel to the molecular beam. The red curve is the predicted by the simple scattering rate for a system with 12 ground states and 4 excited states: $R_{\text{sc}} = \frac{\Gamma}{4}\frac{I/I_{\text{sat}}}{1+I/I_{\text{sat}}}$, where I_{sat} is the 2-level saturation intensity. The blue curve is the number of photons scattered predicted by the rate equations model for the experimental value of the magnetic field. The experiment and two models are normalized to the results obtained at 5 mW/cm^2. There is a very good agreement between the data points and the simple scattering model. The peak height increases linearly with the driving intensity and barely begins to saturate. This suggests that in this optical set-up we are mostly in the linear regime of the scattering rate as a function of intensity as there is not much laser power available.

Consider now the increase of the resonant peak height with increasing interaction time.

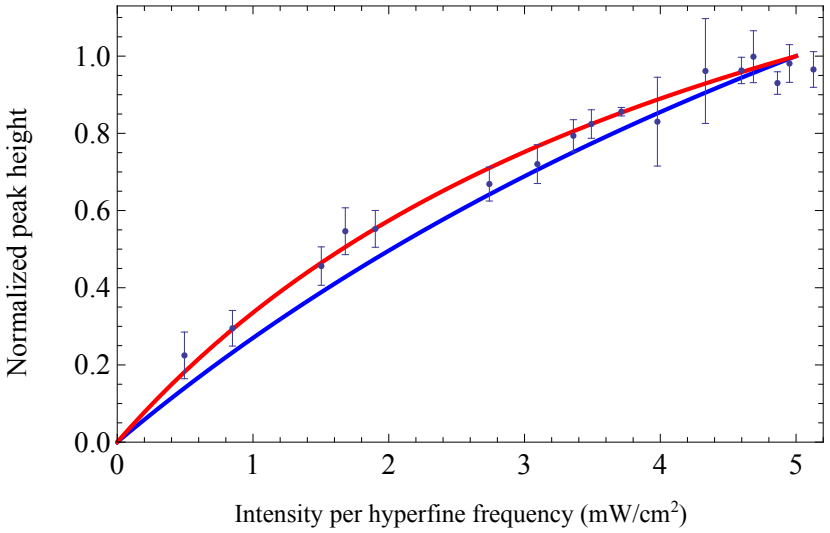

FIGURE 6.10: The normalized resonance peak height versus the driving intensity: blue points - data, red and blue curves - prediction of the simple scattering rate model and the rate equations model.

The interaction time between the laser light and the molecules is determined by the length of the long side of the rectangular beam and can be decreased by simply covering a part of the beam along its length. Example scans over the laser cooling transition with laser light containing all four frequency components for a variable interaction time are shown in figure (6.11). The height of the resonance peak increases with increasing interaction length while the spectral features away from the resonance peak are almost identical. This fact suggests that the increasing height of the resonance peak is indeed due to the optical cycling.

Figure (6.12) shows that the resonance peak height increases linearly with interaction time. This implies that the maximum available intensity and interaction length are not sufficient for enough scattering events to start pumping molecules into the $X(N = 1, v = 1)$ manifold. The figure also shows the prediction of the simple scattering model for the number of photons scattered as a function of the interaction time. Both the data points and the model are normalized to the values obtained at the maximum interaction length.

So far we have shown that the increase of the maximum fluorescence as a function of both the driving laser intensity and the interaction time agrees very well with the scattering rate model. The increase of the resonance peak height in the investigated cases is not in the saturation regime as not enough power is available in this optical set-up. In principle, long enough interaction time can compensate for modest intensities in terms of the net number of photons scattered. However, it is not very practical to rely on an interaction time that is too long. The goal of the experiment is to demonstrate longitudinal cooling in which the laser cooling beams are counter-propagating to the molecular beam. Since the mean

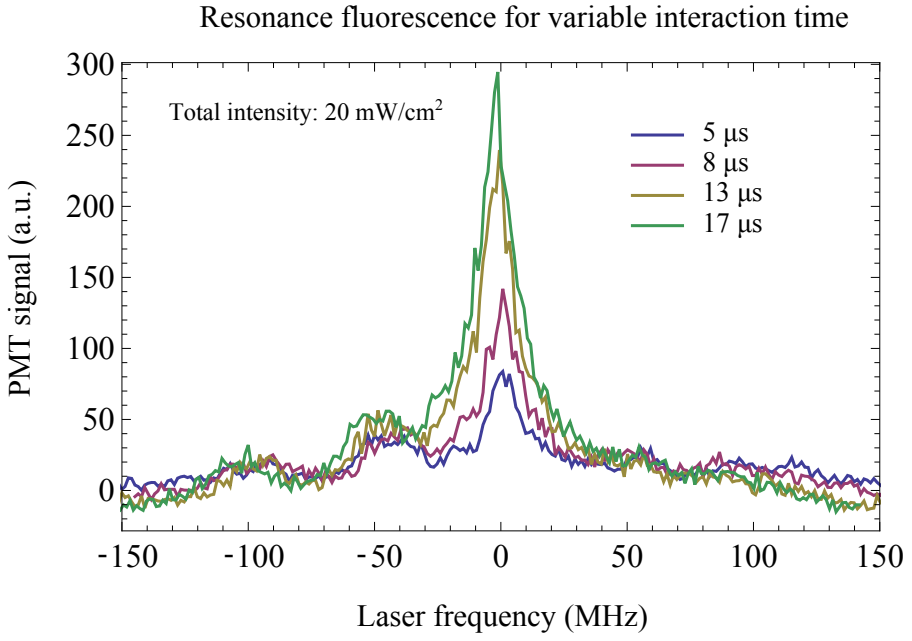

FIGURE 6.11: The effect of increasing the interaction time on the height of the resonance peak. Each transition is driven at $s_p \sim 1$. The vertical scale is different than the one in figure (6.9) b).

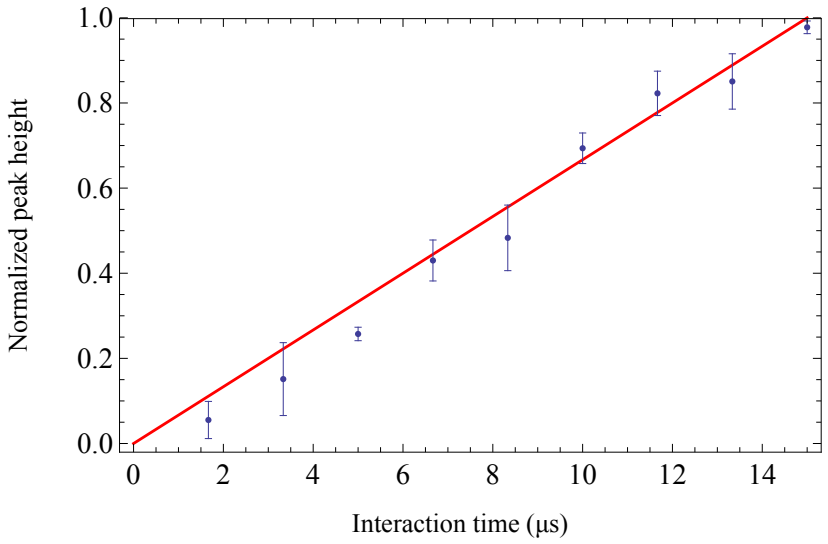

FIGURE 6.12: The height of the resonance peak for increasing interaction time. Points - data. Red line - prediction of the simple scattering rate model. Both experiment and model are normalized to the results at 15 μs.

velocity of the molecular beam is 600 $\mathrm{m\,s^{-1}}$, it is desirable that the scattering rate is high enough to ensure enough scattering events within a reasonable interaction length. One way

to achieve a higher scattering rate would be to reduce the size of the cooling beams and thus increase the intensity. However, the laser cooling effect is maximized and easiest to detect when there is a good overlap between the cooling beams and with the diverging molecular packet[4] and this constrains the size to which the laser beams can be focused.
The logical step was to come up with an alternative optical set-up for generating the hyperfine frequencies. This is why the three-AOM set-up was replaced with the EOM-AOM one in which much more laser power is available for laser cooling.

[4]For example, the transverse extent of the molecular packet 1.5 m from the source is $\approx$ 1 cm.

6.3 Enhanced fluorescence in the high intensity regime

As described in chapter 3, the scattering rate in a multi-level system is significantly reduced compared to the 2-level case and it is important to drive each transition at intensities significantly higher that the saturation intensity. The EOM-AOM set-up was used to maximize the laser power available for cooling.

6.3.1 The EOM-AOM set-up

The scheme for addressing the four hyperfine states of the laser cooling transitions is shown in figure (6.13). In this set-up, when the main laser beam is resonant with the $(J = 1/2, F = 0)$ state, the AOM and EOM frequency-shifted sidebands address their respective levels. A schematic of the optics table is shown in (6.14).

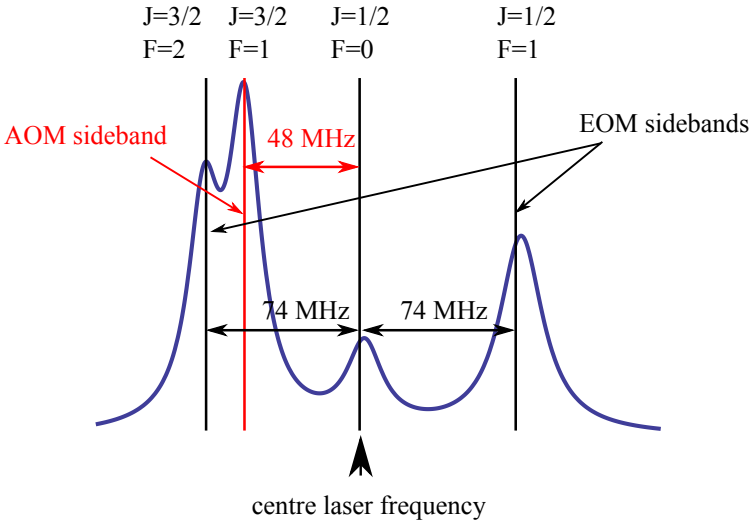

FIGURE 6.13: Scheme for generating the laser cooling hyperfine frequencies in the EOM-AOM set-up.

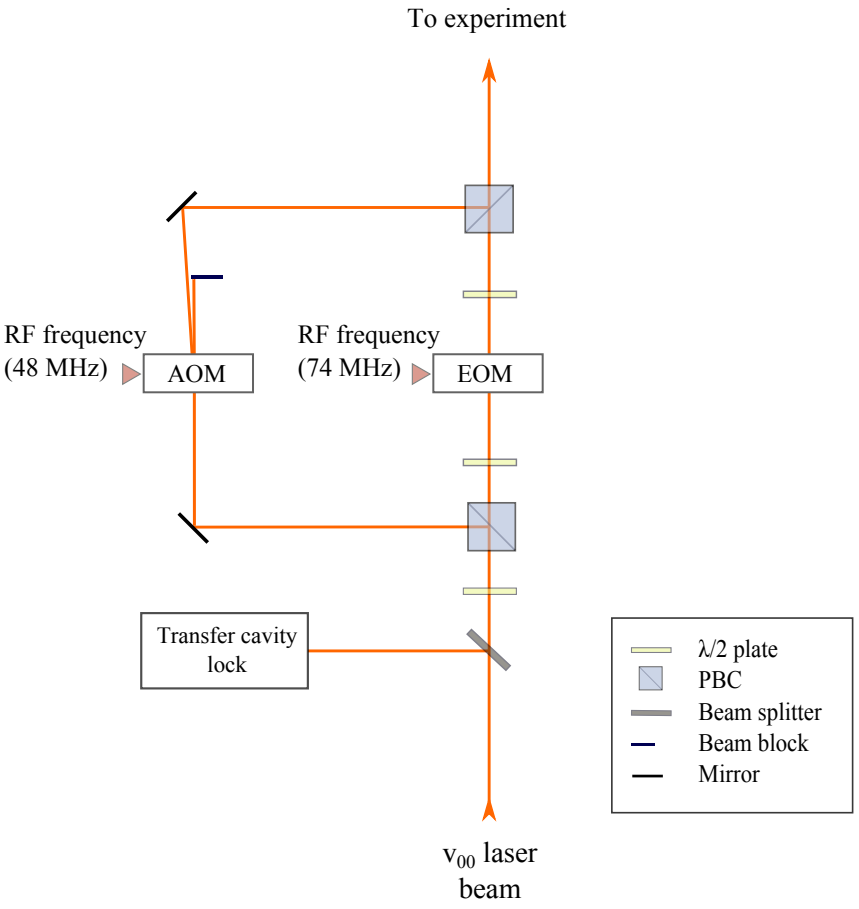

FIGURE 6.14: Optics set-up for combining the frequencies in the EOM-AOM set-up.

6.3.1.1 The electro-optic modulator

In an electro-optic modulator a sinusoidally time-varying electric field is applied across a non-linear crystal causing a change of its refractive index n. This electrically induced birefringence can be used to modulate the phase or amplitude of the laser light propagating through the crystal in a direction perpendicular to the applied electric field [195–197]. The relative polarization of the laser light with respect to the optical axis of the crystal determines whether the light is phase or amplitude modulated. In order to inscribe frequency sidebands, the EOM must be used as a phase-modulator and in this case the incoming laser beam polarization must be aligned with the optic axis of the crystal.
For a crystal driven at frequency ω, the phase shift produces sidebands on the laser of frequency Ω given by:

$$E(t) = E_0 \sum_{m=-\infty}^{\infty} J_m(M) \exp(it(\Omega + m\omega)) \tag{6.9}$$

where J_m are the Bessel functions. The reader is referred to [198] for derivation of equation (6.9). The index of modulation M is defined by:

$$M = \frac{\pi l n^3 r_x}{2d\lambda} V \tag{6.10}$$

where l and d are respectively the length and thickness of the crystal, λ is the wavelength of the laser, r_x is the electro-optic coefficient for the specific orientation of the crystal, n is the unperturbed refractive index of the material and V is the applied voltage across the crystal. Typically, a modulation index of $M < 1$ generates a carrier and two main frequency sidebands $\Omega \pm \omega$.
The voltage required to produce a phase shift of the output electric field of the laser light of π, V_π or the *half-wave voltage*, is an important parameter for a given crystal. For example, for a $LiTaO_3$ crystal of dimensions 3 mm × 3 mm × 40 mm and laser light with $\lambda = 600$ nm, $V_\pi \approx 150$ V. To supply directly such a high voltage at the frequency in the tens of MHz would be a technical challenge. Instead, a resonant RLC circuit can be built in which the resonant frequency $f_{\text{res}}=1/(2\pi\sqrt{LC})$ matches the required modulation. Here L, C and R are the effective inductance, intrinsic capacitance and resistance of the crystal at the given frequency (see appendix C for more details).

6.3.1.2 Generating the EOM sidebands

The EOM used in this experiment is Thorlabs EO-AM-NR-C1, anti-reflection coated for 600-900 nm. The EOM crystal (MgO-doped $LiNbO_3$) is in a resonant circuit with a resonant frequency $f_{\text{res}} = 74$ MHz and operating bandwidth of several MHz. The rf voltage

is generated by a voltage-controlled oscillator (Mini-Circuits VCO POS100) whose output is amplified by a 35 dB amplifier (Motorola CA 2832). The laser beam with inscribed frequency sidebands can be monitored on a scanning Fabry-Pérot interferometer (e.g. Thorlabs SA200 5B). As the amplitude of the VCO voltage is increased, higher orders appear at $\Omega \pm n\omega$ and the zeroth and lower orders are suppressed.

To address the hyperfine transitions in CaF we set the VCO voltage amplitude so that laser power is equally distributed between the carrier laser frequency and the ± 1 orders. Figure (6.15) shows a typical scope trace of the laser beam with inscribed sidebands.

In the EOM-AOM set-up significantly more power is available for laser cooling (a maxi-

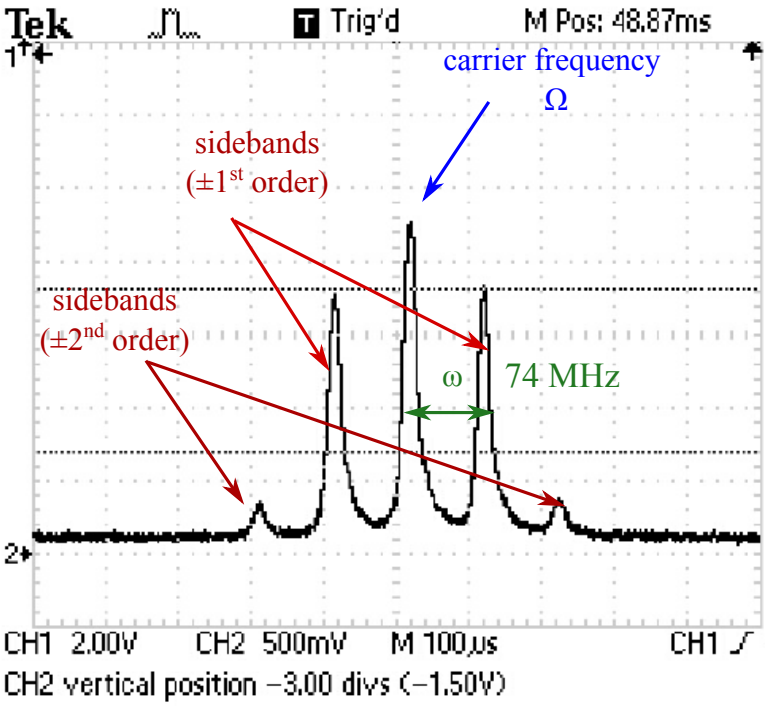

FIGURE 6.15: The laser beam with sidebands inscribed by the EOM - the beam power is distributed among the carrier frequency (Ω) and the first-order sidebands at $\Omega \pm \omega$. The sidebands at $\Omega \pm 2\omega$ are also visible.

mum of 75 mW compared to approximately 17 mW in the three AOM set-up).

6.3.2 Resonant fluorescence in the EOM-AOM set-up

Figure (6.16) shows an example scan over the four hyperfine levels of the laser cooling transition taken with a total power of 65 mW distributed roughly equally between the four

frequencies[5]. Similarly to the three AOMs set-up, the two laser beams have a Gaussian intensity profile with a FWHM of approximately 4 mm. When the spectrum is taken with only one frequency component (yellow trace in figure (6.16)) the spectral features are no longer resolvable because of the large power broadening at this high power. The natural linewidth of the transition is $\Gamma/(2\pi) = 8.3$ MHz. A saturation intensity parameter of $s = 24$ power-broadens the linewidth of the transition to $\Delta f_{\mathrm{PB}} = 8.3\sqrt{1+24} = 41.5$ MHz. The three frequency spacings between the four hyperfine states are 25, 47 and 76 MHz respectively and it is practically impossible to distinguish between the different hyperfine components. Because of this power-broadening, it is no longer possible to fit the single-frequency scan to a sum of four Lorentzian functions and thus estimate the enhancement factor in the usual way.

After a scan with all the frequencies one can see the resonance peak as before. The

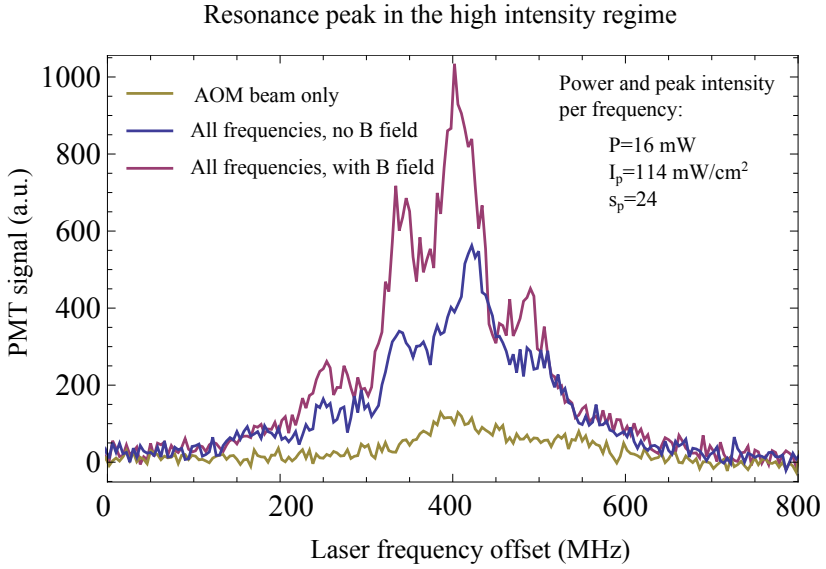

FIGURE 6.16: Scan over the laser cooling $A - X(0-0)$ transitions with all four hyperfine frequencies in the EOM-AOM set-up. The high power in the beam power-broadens the transition and it is not possible to distinguish individual hyperfine lines in the single-frequency scan (yellow). The vertical scale is different than the one in figure (6.9).

spectral features of the scan with all frequencies are more pronounced compared to the lower intensity regime (figure (6.9) b)). This is because the off-resonant excitations are more likely to happen with higher intensity.

The addition of the magnetic field increases the height of the resonance peak by a factor

[5]In the experiment we vary a $\lambda/2$ waveplate so that 1/4 of the total power is in the AOM beam and 3/4 is in the EOM beam. However, there are some unsuppressed ± 2 order sidebands inscribed by the EOM and some of the laser power in the EOM beam is lost and the four transitions are not exactly driven with the same intensities.

of 2.2±0.2. When each transition is driven at $s = 12$, the model predicts an increase of the number of photons scattered by a factor of 2.09 between $B_z = B_y = 0.1$ Gauss and $B_z = B_y$ =2 Gauss and an increase of 1.47 between $B_z = B_y = 0.25$ Gauss and $B_z = B_y = 2$ Gauss. At higher driving intensities the precise value of the Earth's magnetic field is more important. In is thus likely that the Earth's magnetic field at the interaction region is ~ 0.1 Gauss.

6.3.3 Saturation of the resonance peak height

Figure (6.17) shows the normalized peak height as a function of the laser intensity per, similar to figure (6.10) but now taken to higher power. We see that the peak height starts to saturate at intensities of about 50 mW/cm^2 as suggested by the rate equation model (figure (6.3)). The red curve in figure (6.17) is the scattering rate as predicted by the model

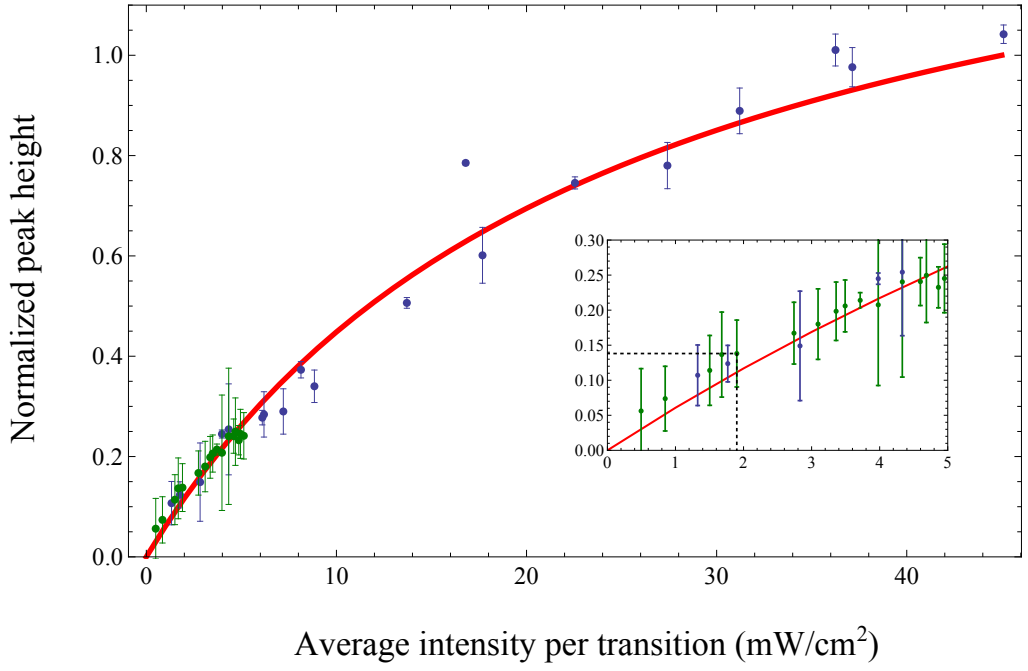

FIGURE 6.17: The height of the resonance peak normalized to the peak height at the full intensity available in the AOM-EOM set-up (blue points) and the three-AOMs set-up (green points). Red curve - number of scattered photons predicted by the rate equations model for an interaction time of 10 μs. Both experiment and model are normalized to the values at 50 mW/cm^2. The model suggests that 45 photons are scattered at the highest intensity in the figure. The inset shows the point for the example calculated enhancement factor of 3.5±0.3 calculated for the results in figure (6.9)).

for the given multi-level system. The data and the model are normalized to the results at 50 mW/cm^2.

Figure (6.17) also shows the data taken with the three-AOMs set-up from figure (6.10) (green points). The data points follow the model within good agreement, especially at lower intensities, and the two data sets are within good agreement. At higher intensities the experimental points lie slightly above the model curve. The reason for this is that at high intensities there is contribution to the fluorescence peak height from molecules which have not necessarily cycled over the four hyperfine levels but have been excited on single nearby transitions which are power-broadened into resonance. The experimental peak height seems to saturate at higher intensities than predicted by the model. A possible explanation for this is the Gaussian intensity profile of the laser beams which is not taken into account in the model. The Gaussian laser beams make a big difference to the point at which the resonance peak height saturates as the wings need very high intensities.
The rate equations model predicts that when each transition is driven at intensities ~ 50 mW/cm^2 each molecule scatters approximately 45 photons. Using the calculated number of photons scattered (through the estimated enhancement factor) in the low intensity regime (section (6.2.2.2)) of 6.3±0.54 we can estimate that in the high intensity regime approximately 45 photons have been scattered. This, however, is an upper limit to the actual number of photons scattered due to the contributed fluorescence of molecules which have not undergone optical cycling.

6.3.4 Pumping the molecules out of $(X, N = 1, v = 0)$ and into the $(X, N = 1, v = 1)$ state

With the higher laser power available in the EOM-AOM set-up it is easier to pump the molecules out of the $X(N = 1, v = 0)$ state and into the $X(N = 1, v = 1)$ one. To do this, we do the following pump-probe experiment. The pump, containing all four frequencies, is locked on resonance and intersects the molecular beam. To ensure that the molecules interact with the pump beam long enough to be pumped into the $X(N = 1, v = 1)$ state, the vacuum chamber was equipped with two long anti-reflection coated glass windows as shown in figure (6.18). The pump beam was then retroreflected many times with the use of two long mirrors (figure (6.19)). The molecules are probed 1.2 m away from the source by an independent laser.

Figure (6.20) shows data where the probe laser is scanned over the $A - X(0 - 0)$ transition at 494431 GHz and around the $A - X(1 - 1)$ transition at 494599 GHz. The pump beam has average intensity of 24 mW/cm^2 per hyperfine component (corresponding to a saturation intensity parameter $s = 4.9$). This intensity corresponds to a scattering rate of $R_{\rm sc} = \frac{\Gamma}{4}\frac{s}{s+1} = 1.1 \times 10^7$ photons per second. The beam is retroreflected once to allow for an interaction time of approximately 10 μs, long enough for the molecules to scatter more than 100 photons. When the pump beam is locked on resonance and the probe is scanned around the $A - X(0 - 0)$ transition, the population in the $X(N = 1, v = 0)$ is only

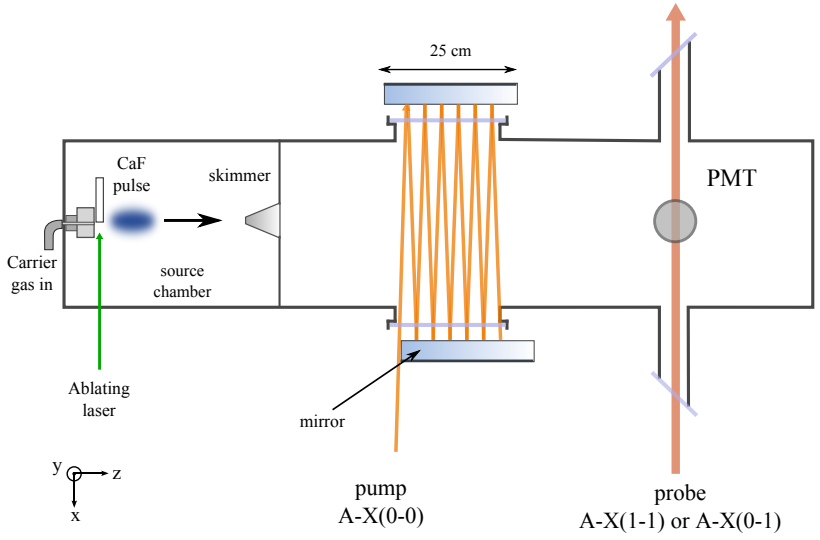

FIGURE 6.18: Pump-probe set up. The pump beam is retroreflected many times.

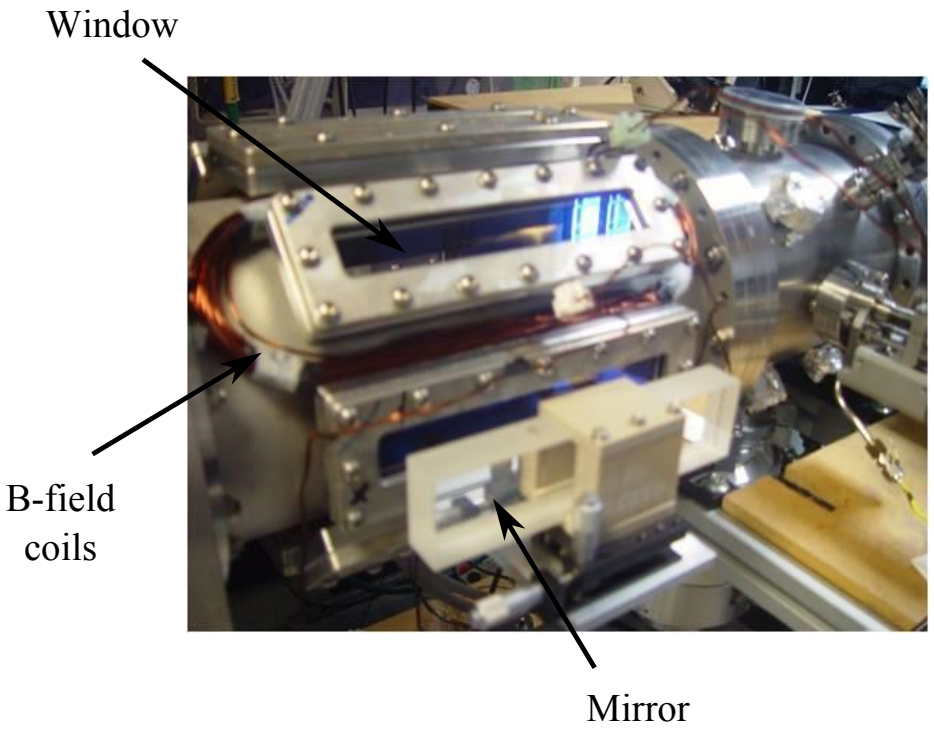

FIGURE 6.19: A photograph of the vacuum chamber section with long windows and mirrors. The pump beam is retroreflected many times to increase the interaction time. The number of depicted retroreflections is for illustrative purposes only and varies in the experiments.

(35±5)% of the original one (figure (6.20) a)). Recall that if p is the probability of decay to a dark state, the fraction P of molecules remaining after scattering N photons is given

by $P = (1-p)^N$. Asssuming that the scattering rate is as expected, the measured fraction of remaining molecules in the pump-probe experiments corresponds to a $A - X(0-0)$ Franck-Condon factor of 0.989.

Figure (6.20) b) shows a scan over the $A - X(1-1)$ transition. Note that this scan was taken on a different day than the one in figure (6.20) a) and for a slightly different experimental parameters. The pump beam has an average intensity of 25 mW/cm^2 per hyperfine component and the interaction time is 10 μs which should be enough for each molecule to scatter approximately ≈100 photons. There is some initial population in the $X(v=1)$ state (blue points), which is approximately only 10% of the population in the $X(v=0)$ state[6]. When the pump beam is on resonance, the population in the $X(v=1)$ state increases by a factor of 2.3. The expected increase following the agruments above is approximately 3.5-fold. The lower than expected detected population in the $X(v=1)$ state is most likely due to bad signal.

Once we know that the molecules get pumped into the $X(v=1)$ state, we can interrogate the $A - X(0-1)$ transition near 476958 GHz, accessible by the v_{10} repump laser. This is useful because the precise frequency of the transition is needed for the vibrational repump laser. Because of the off-diagonal $A - X(0-1)$ Franck-Condon factor, the strength of the transition is much weaker than either of the $A - X(0-0)$ or $A - X(1-1)$ transitions. To get a strong signal, the transition must be probed with higher intensity than usual. The average intensity of the probe is 212 mW/cm^2 (probe power of 60 mW in a Gaussian beam with $w = 1.5$ mm).

Figure (6.21) shows the four hyperfine ground state levels of the $X(v=1)$ manifold as the probe laser (the v_{10} laser in that case) is scanned over the $A - X(0-1)$ transition at 476957.9 GHz. The pump beam is has an average intensity of 50 mW/cm^2 per hyperfine component and is retroreflected many times to allow an interaction time of over 100 μs. A filter under the PMT blocks the probe light at 628 nm as the molecules excited on the $X(v=1) \rightarrow A(v'=0)$ transition mostly emit light at 606 nm (the wavelength of the $A - X(0-0)$ transition). The yellow points in figure (6.21) show the initial population in the $X(v=1)$ state. When the pump beam is on resonance the initial population in the $X(v=1)$ state increases by a factor of 3.7 (purple points in figure (6.21), fitted to a sum of four Lorentzian functions). This increase is present even in the absence of the magnetic field to remix the dark states. The rate equation model suggests that for the given driving intensities and in the presence of a small magnetic field with components $B_y = B_z = 0.1$ Gauss (similar to the Earth's magnetic field in the interaction region), the interaction time should be enough to allow for each molecule to scatter ~ 46 photons corresponding an increase of the population in the $X(v=1)$ by a factor or 4. The measured increase is smaller than this calculated value due to target variation.

[6]The signal from the $A - X(1-1)$ transition without a pump beam is too small to be fitted to a sum of four Lorentzian functions as usual.

The addition of the magnetic field of magnitude 5 Gauss further increases the signal (blue points in figure (6.21), fitted to the sum of four Lorentzian functions) as now the dark magnetic sublevels of the ground states are more effectively remixed. In this case the population in the $X(v = 1)$ state has increased by a factor of 4.6 compared to the original population in the state. The simple scattering model suggests that the number of scattered photons for the given driving intensity and interaction time is over 300 (assuming perfect remixing of the dark states). If this many photons have been scattered, there should be only 2% of the original population left in the $X(v = 0)$ state corresponding to an increase of the population in the $X(v = 1)$ state of a factor of 9.8. It is possible that some experimental imperfections are causing the lower population detected in that state - for example, target variation, pump and probe beams interacting with a different part of the molecular beam and lower scattering rate due to the laser power losses caused by the multiple retroreflections through the windows.

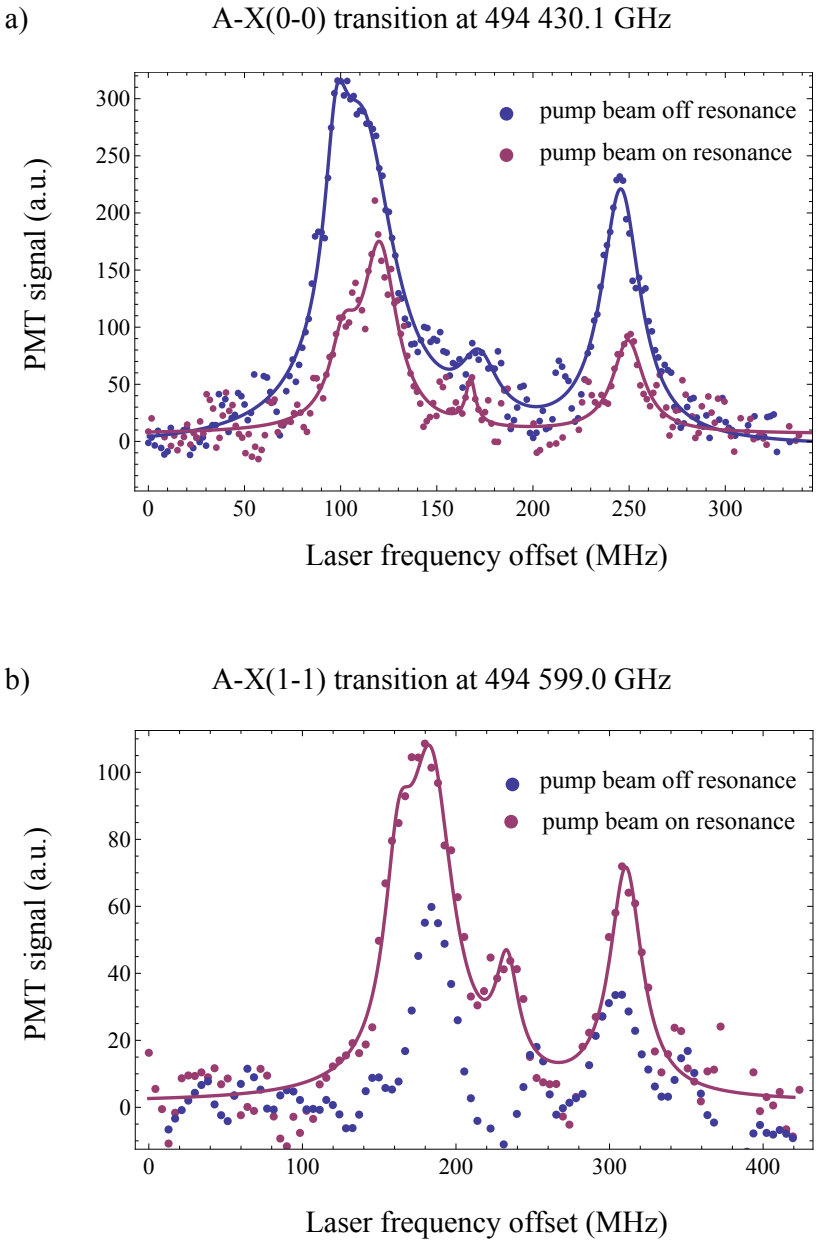

FIGURE 6.20: The pump laser (v_{00}) is locked on resonance. a) The probe laser (Spectra Physics) is scanned around $A - X(0 - 0)$ when the pump beam is off (blue) and on (purple) resonance. The four hyperfine peaks are fitted to a sum of four Lorentzian functions. When the pump beam is on resonance, only 35% of the original population is detecetd in the $X(v = 0)$ state. b) The probe laser is scanned around the $A - X(1 - 1)$ transition when the pump is off (blue) and on (purple) resonance. With the pump beam on resonance, the population in the $X(N = 1, v = 1)$ manifold increases by a factor of 2.3. The signal with the probe on resonance is fitted to a sum of four Lorentzian functions. The blue signal shows the original population in the $X(v = 1)$ state which is approximately 10% of the original population in the $X(v = 0)$ state. Note that the data sets in a) and b) were taken on different days.

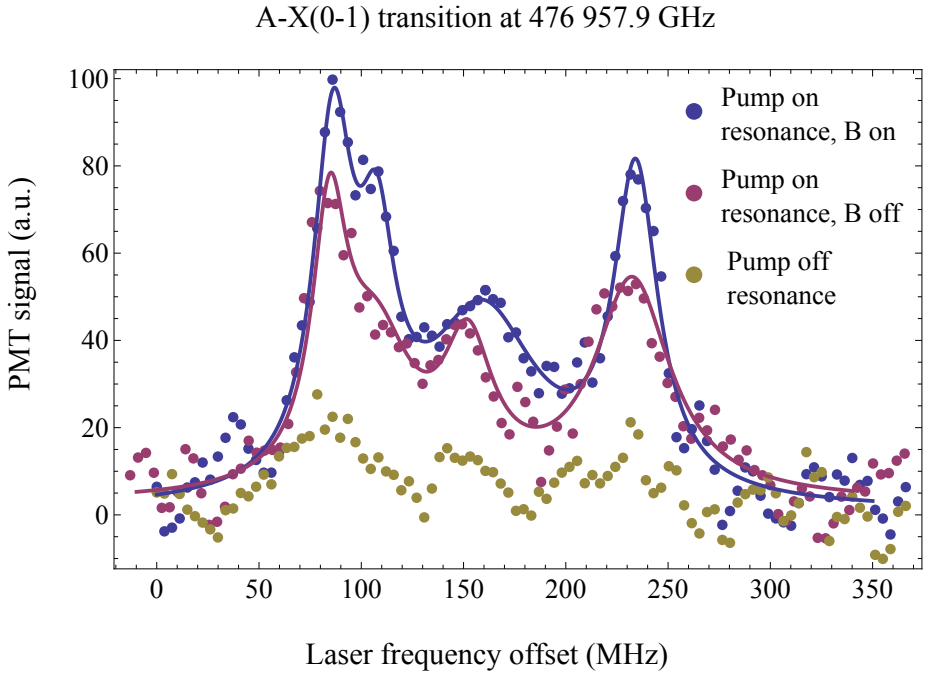

FIGURE 6.21: The pump laser is resonant with all hyperfine components of the $A - X(0 - 0)$ transition. The probe laser is scanned around the $A - X(0 - 1)$ transition. The magnetic field is approximately 5 Gauss. The signal with the pump on resonance is fitted to a sum of four Lorentzian functions.

6.4 Summary of the chapter

In this chapter, I presented results describing the increased fluorescence as the four hyperfine levels of the $X(N = 1, v = 0) \leftrightarrow A(J = 1/2, v' = 0)$ transition are addressed. When a molecule is illuminated by laser light resonant with more than one transition, it will scatter a higher number of photons than when it is excited on a single transition. This increase of fluorescence is what we refer to as 'optical cycling' and is an important stepping stone to laser cooling. We estimate that without a vibrational repump, in the experiment we can directly observe resonance fluorescence corresponding to each molecule scattering ~ 45 photons. The experimental results are within good agreement with the rate equation model describing the evolution of all states involved in the multilevel system for a range of intensities and interaction times.

We saw that when the four transitions are driven with enough intensity and for long enough interaction time, the molecules get pumped into the $X(N = 1, v = 1)$ state at which point the scattering cycle ceases. The number of photons a molecule will scatter before it gets pumped to the $X(N = 1, v = 1)$ state is determined by the $A - X(0 - 0)$ Franck-Condon factor ($q_{0,0}$). For $q_{0,0}$ in the range $0.978 - 0.987$ a molecule will scatter only 45-77 photons before decaying to a dark state which not sufficient to achieve significant cooling without a vibrational repump.

Chapter 7

Longitudinal laser cooling and slowing

7.1 Introduction

In this chapter I will present the laser cooling data which is central to this thesis. In the experiments described here the v_{00} and v_{10} cooling lasers are counter-propagating to the molecular beam. When the vibrational leak to the $X(v = 1)$ state is closed, a sufficiently high number of photons can be scattered (more than 1500) to produce a measurable laser cooling and slowing effect. The effect of the laser light is signified by the later arrival time of the on-resonant molecules. In addition to that, the slowed molecules are bunched which is suggestive of a laser cooling effect.

This chapter is organized as follows. I will first describe the set-up for the experiments presented. In subsection (7.5), I will present results in which the v_{00} light only is turned on for a short time and optically pumps the molecules into the $X(v'' = 1)$ manifold. This pumping-out experiment is important in order to determine which molecular velocity class interacts with the lasers and also to confirm the scattering rate predicted by the model. In section (7.6), I present the longitudinal laser cooling data in which the cooling pulse is applied for a variable duration τ. Finally, the effect of applying a frequency chirp to the laser light to enhance the cooling is presented in section (7.7).

7.2 Experimental set-up details

7.2.1 Generating and combining the laser cooling frequencies

The frequency sidebands required to address the hyperfine levels in the $X(N = 1, v = 0)$ and the $X(N = 1, v = 1)$ manifolds are generated by a combination of an AOM and EOM as described in chapter 6. The schematic of the optics table is shown in figure (7.1). Since the frequency spacing between the hyperfine states in the two vibrational manifolds

is essentially the same [186], we use the same AOM and EOM crystals to inscribe the frequency sidebands on the two lasers. Each of the v_{00} and v_{10} laser output beams is split in two paths by a polarizing beam cube and a half-wave plate. The v_{00} and v_{10} vertically polarized beams are first combined on a dichroic mirror (Thorlabs DMLP605) and then go through the EOM crystal. The horizontally polarized beams are separately modulated by the AOM and then combined on a dichroic mirror. The AOM and EOM beams are then combined on a polarizing beam cube. The power in each beam is distributed among the sidebands with a half-wave plate so that each hyperfine transition is driven with the same intensity. Pick-off beams from the output of the v_{00} and v_{10} lasers are sent to the Transfer Cavity lock.

An AOM (Crystal technology 3080-120, with a center frequency of 80 MHz), labeled as 'switching AOM' in figure (7.1), acts as a fast switch to turn the v_{00} beam on and off for a variable duration. The switching AOM is aligned so that when it is on, most of the outgoing light is in the first diffracted order while when it is off, the v_{00} light beam is blocked. The schematic of the switching AOM control is shown in figure (7.2). The v_{00} pulse is controlled by a TTL pulse sent by the computer to the AOM VCO through an RF switch. The RF switch ensures that no light is sent to the chamber when the TTL pulse is off. The switching AOM rise time was measured with a fast photodiode to be approximately 3 μs which is fast enough for the purposes of the experiment. A technical detail worth pointing out is that the AOM requires some warm-up time to reach its maximum efficiency and thus after it is pulsed on for the duration of interest, it is turned on again after the molecules are detected and turned off $\approx$ 10 μs before ablation.

While the v_{00} light is pulsed, the v_{10} light is applied continuously for the entire duration of the experiment. In that way the repump laser acts a clean-up beam for the molecules in the $X(N'' = 1, v'' = 1)$ state. A filter prevents the scattered red repump laser light from reaching the PMT. The final AOM in figure (7.1) is used for the frequency chirp of the cooling light (see section (7.7.1) for details).

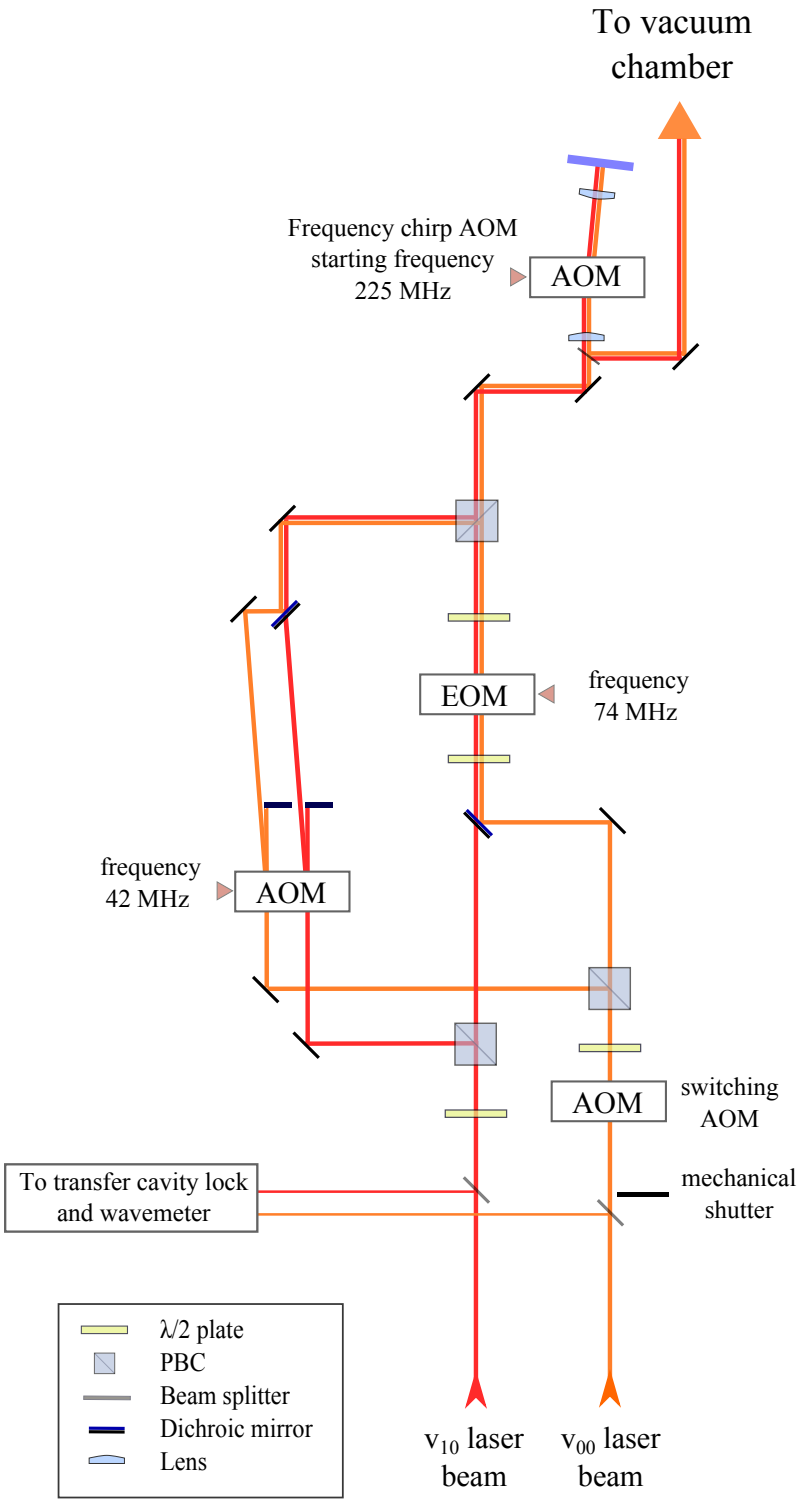

FIGURE 7.1: Schematic of the optics table for the longitudinal laser cooling experiments.

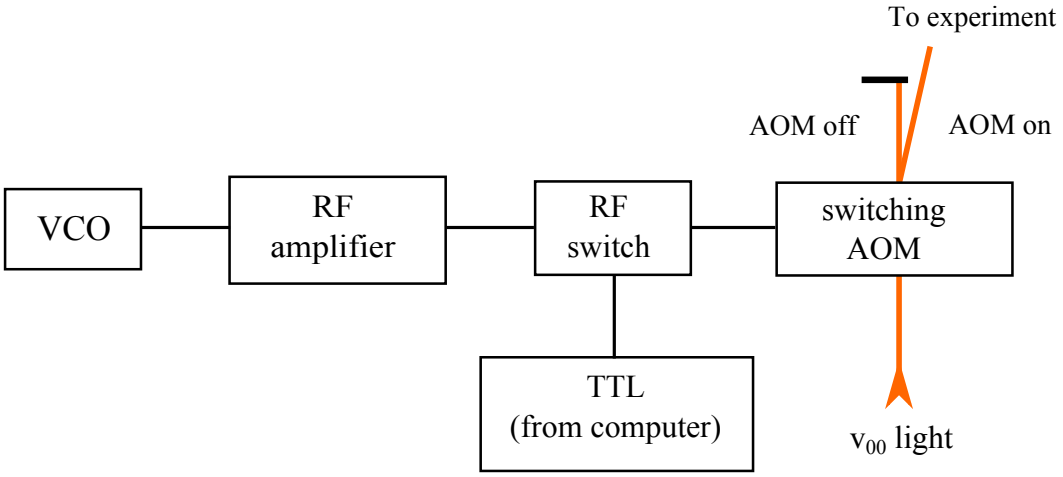

FIGURE 7.2: Control of the v_{00} light pulse. The switching AOM is turned on and off by a TTL pulse.

7.2.2 Detection

After interacting with the laser cooling light, the molecules are detected by a probe laser (Spectra Physics 380D) which intersects the molecular beam orthogonally. The probe laser is scanned over the four hyperfine components of the $P(1)$ branch of the $A^2\Pi_{1/2}(v) - X^2\Sigma^+(v)$ transition with $v = 0, 1, 2$. We will refer to this transition as $A - X(v - v)$. We note that in this chapter, we will use the double prime notation to refer to the state in which the molecules have ended up at the end of the cycling/laser cooling and we will use no primes to designate the original molecular state.

A mechanical shutter blocks the v_{00} light on alternate shots of the experiment in order to minimize the effect of the long term drifts of the Ca target. For every probe laser frequency two shots are taken - one with and one without the v_{00} light and two interleaved spectra are obtained.

7.3 Laser intensity

After all the laser cooling frequencies are combined, they are expanded in a 2:5 telescope and focused by a 2500 mm focal length lens so that they reach a focus near the skimmer as shown schematically in figure (7.3). The focusing of the laser cooling beams serves two purposes - i) it matches the divergence of the molecular beam and ii) it prevents laser light scattered off the skimmer from saturating the PMT.

We check that the four laser cooling beams are well overlapped along the molecular beam

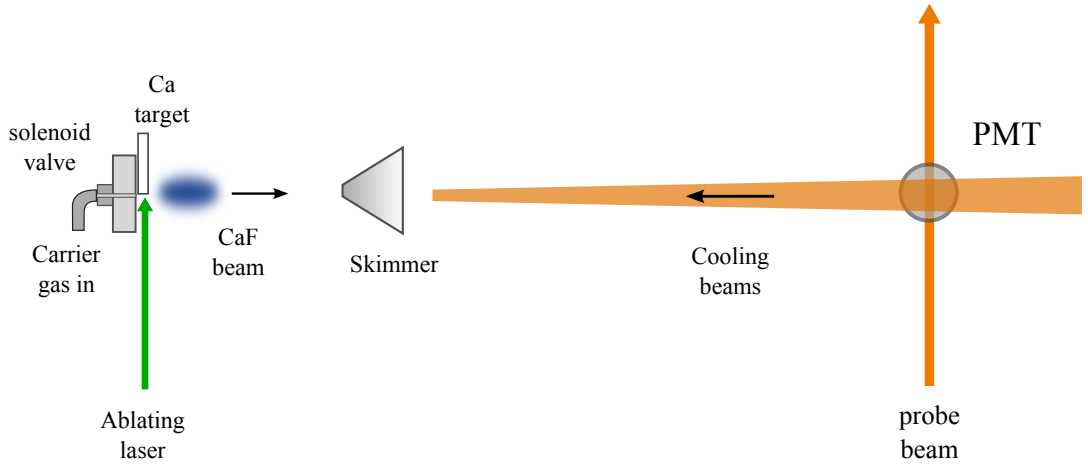

FIGURE 7.3: Schematic of the experiment. The laser cooling beams are counter-propagating to the molecular beam. A probe laser intersects the molecular beam orthogonally after they have interacted with the cooling beams.

line with a CCD camera (Thorlabs DCC1645C). All beams are shaped to have a Gaussian intensity profile. The beam intensity of each individual beam was measured at four positions

along the beam line and at each position the mean $1/e^2$ radius of the four beams determined. We then fit a linear function to the mean $1/e^2$ radii versus distance from the source. For the laser cooling experiments, we made sure that the size of the cooling beams is comparable to the spatial extent of the molecular pulse as shown in figure (7.4).

Typically, the available power in the cooling beams at the entrance of the vacuum chamber

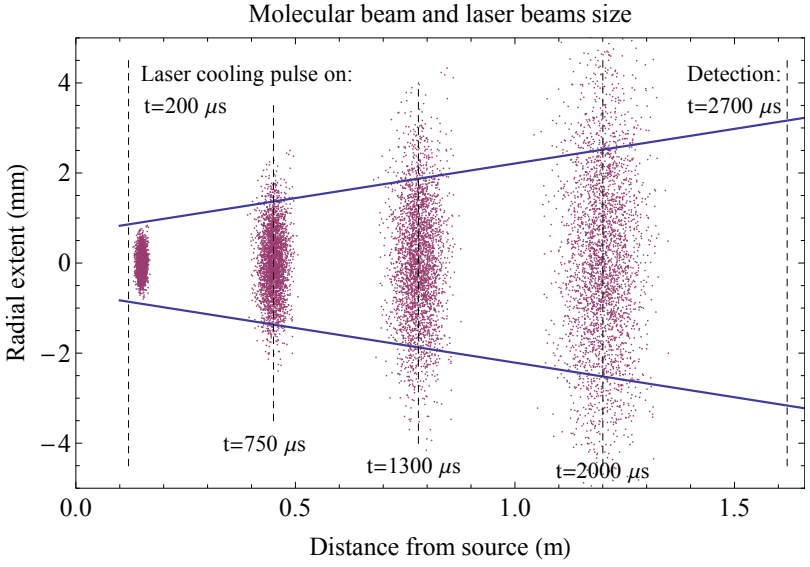

FIGURE 7.4: Overlap between the laser cooling beams and the molecules. Blue line - fit to the mean $1/e^2$ radii of the laser beams. Purple - the extent of the molecular pulse throughout the time of flight.

is approximately 22 mW and 20 mW for the v_{00} and v_{10} light respectively. These powers correspond to roughly 5 mW per hyperfine transition and an effective saturation intensity parameter s_{eff} as shown in figure (7.5). Although the intensity falls off with increasing distance from the source, the molecules are exposed to $s_{\text{eff}} \geq 0.5$ for the entire laser cooling pulse.

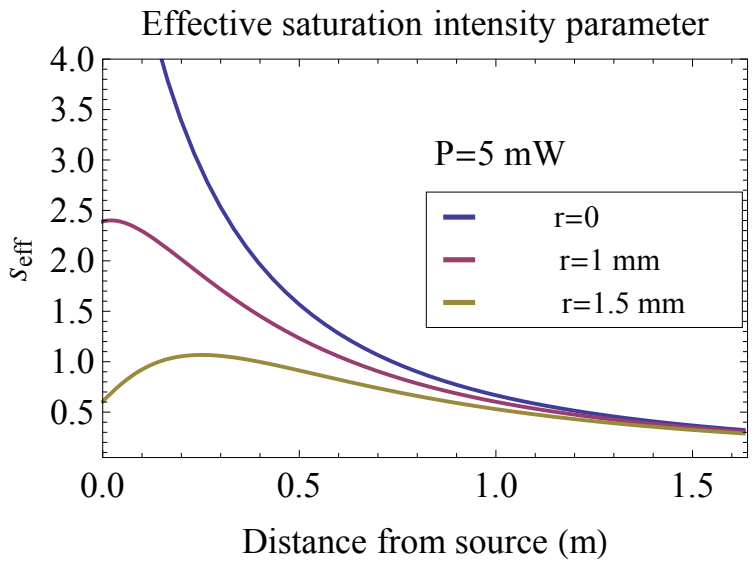

FIGURE 7.5: The effective saturation parameter versus distance from the source for three values of the radial distance from the beam line r. The power is 5 mW per hyperfine frequency.

7.4 Locking of the cooling lasers

The CaF source produces a molecular packet with a Gaussian distribution of forward velocities centered at approximately 600 $\mathrm{m\,s^{-1}}$ and with a FWHM of 45 $\mathrm{m\,s^{-1}}$. In order to interact with the greatest number of molecules, we lock the v_{00} and v_{10} lasers on resonance with the central velocity class. The locking is done with the Transfer Cavity Lock software as described in chapter 2.

The procedure for locking the v_{00} and v_{10} lasers is essentially the same. We first lock the v_{00} laser to maximize the molecular fluorescence. For each experimental shot, the v_{00} laser light with all hyperfine frequency sidebands is turned on when the molecules traveling at 600 $\mathrm{m\,s^{-1}}$ are arriving at the detection region. For example, when the detector is 1.63 m away from the source we turn the v_{00} light on at 2700 μs. The laser is then scanned within approximately 1 GHz over the $A-X(0-0)$ transition at 494430 GHz (taking into account the Doppler shift between the molecules and the counter-propagating laser). As the v_{00} laser is scanned, we see the usual multi-peak structure of the CaF spectrum as shown in figure (7.6 b). At the point of the laser scan when each hyperfine frequency is addressing its respective state there is a pronounced resonance peak. The ToF profile obtained with the v_{00} frequency at the resonance peak is shown in figure (7.6 a). We see half of the usual time of flight profile as the light is turned on at 2700 μs. The spectrum in figure (7.6 b) is the one obtained when the ToF profile is gated from 2700-2710 μs. The laser voltage corresponding to the resonance peak for that particular ToF profile gate is then chosen as the set point for locking the v_{00} laser with the Transfer Cavity lock.

After the v_{00} laser is locked, we add the v_{10} light and scan it over approximately 1 GHz

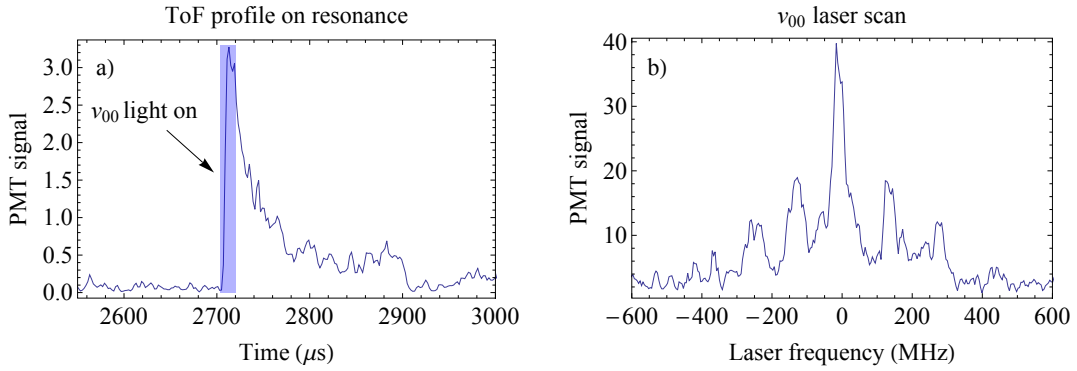

FIGURE 7.6: Locking of the v_{00} laser. a) The on-resonant longitudinal ToF profile with the v_{00} light pulsed on at the time when the molecules reach the PMT. b) The resonance features from the v_{00} scan corresponding to a ToF profile gate of 2700-2720 μs (blue rectangle in a)). The laser frequency is shown in MHz with respect to the resonance peak.

around the $A - X(0-1)$ transition at 476958 GHz. For each experimental shot, the v_{00} light pulse (recall that the v_{10} light is applied continuously) is turned on at 2450 μs to allow enough interaction time for the molecules to be pumped into the $X(N'' = 1, v'' = 1)$ state. An example scan of the v_{10} laser is shown in figure (7.7 b). As the v_{10} laser is scanned across the transition, the familiar multi-peak structure similar to the one in figure (7.6 b) can be resolved. This spectrum is obtained by gating the ToF profile between 2700 μs and 2750 μs. Figure (7.7 a) shows the ToF profiles obtained when the v_{10} laser is on resonance (blue) and off resonance (purple). The ToF profile sits on top of a large pedestal which is

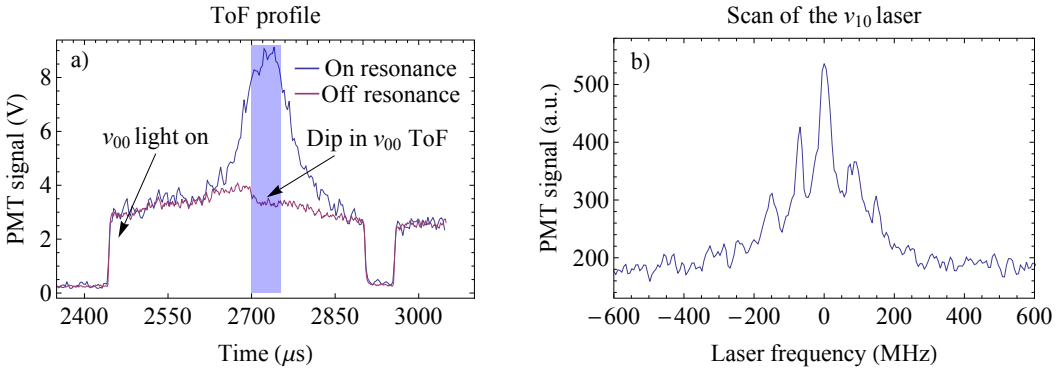

FIGURE 7.7: a) Longitudinal ToF profile as the v_{10} laser is scanned across resonance. When the v_{10} laser is off-resonance (purple) the ToF profile is pumped out by the resonant v_{00} light with the dip corresponding to the velocity class with respect to which the v_{00} laser is locked. When the repump light is on resonance (blue), the ToF profile is visible as the molecules are pumped out of the $X(N = 1, v'' = 1)$ state. b) Resonance features of the v_{10} scan. The ToF profile gate is 2700-2750 μs (blue rectangle in a)). The usual multi-peak structure is resolvable.

due to the scattered v_{00} laser light.

When the v_{10} laser is far from resonance, we can see that the detected ToF profile is depleted (purple line in figure (7.7 a)) as the molecules have been pumped out by the resonant v_{00} light. The dip in the middle of the ToF profile corresponds to the velocity class that is Doppler shifted into resonance with the v_{00} laser. When the v_{10} light is on resonance, however, a well-pronounced ToF profile can be seen as the molecules that have been pumped into the $X(N'' = 1, v'' = 1)$ state are brought back to the scattering cycle. The v_{10} laser voltage corresponding to the resonance peak in (7.7 b) for the given ToF profile gate is used as the set point to lock the v_{10} laser with the Transfer cavity lock.

We note that the most crucial step in the locking of the lasers is selecting the right ToF profile gate so that both the v_{00} and v_{10} lasers interact with the same (central) velocity class. The scan voltage corresponding to the resonance peak is very sensitive to the selected ToF gate, because different arrival times correspond to different velocities which have different Doppler shifts.

7.5 Before laser cooling - pumping-out experiments

The spread of molecular velocities corresponds to a distribution of Doppler shifts with a FWHM of 72 MHz. The laser cannot interact with all of these molecules. Recall that the excitation rate can be expressed as $R = \frac{\Gamma}{2}\frac{s_{\text{eff}}}{1+4\delta^2/\Gamma^2}$. When $\delta = \pm 2\pi \times 36$ MHz, the excitation rate is only 1.3% of its value on resonance.

To determine exactly which portion of the molecular pulse the lasers interact with, we did the following pump-out experiment. The v_{00} laser, locked with the molecules traveling at 600 m s^{-1}, is pulsed on for a short time. After interacting with the laser light the molecules are detected by the probe laser which is scanned around the $A - X(0-0)$ transition.

An example scan of the probe laser over the four hyperfine levels of the $A - X(0-0)$ transition after a v_{00} pump pulse of 20 μs is shown in figure (7.8). The relative peak heights

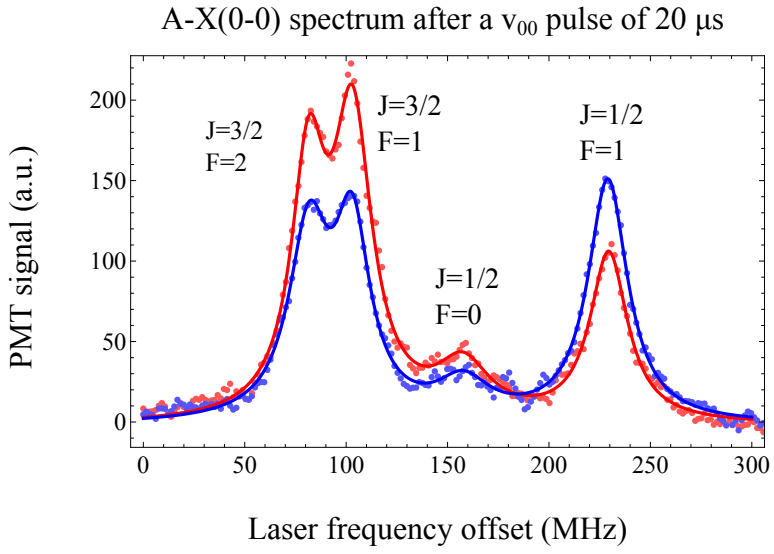

FIGURE 7.8: Probe laser scan over the $A - X(0-0)$ transition after a v_{00} pump pulse of 20 μs (blue) and without pump beam (red).

of the states have changed after the pump pulse as the interaction with the v_{00} light has re-distributed the molecular population among the hyperfine levels. The molecules have been pumped out of the $(J = 3/2, F = 2)$ and $(J = 3/2, F = 1)$ states and into the $(J = 1/2, F = 1)$ state. The tendency of the molecules to pile up in the latter state also holds for the longer v_{00} pulses and is indeed evident in the laser cooling experiments described later. This optical pumping is most likely due to the higher branching ratio from the excited state to that hyperfine level compared to the other three.

The exposure to the resonant v_{00} light causes the molecules to cycle around the four hyperfine states of the $X(N = 1, v = 0)$ manifold until they eventually get pumped into the $X(N'' = 1, v'' = 1)$ state. The ToF profiles averaged over the four hyperfine levels in

the $X(v = 0)$ state after a v_{00} pump pulse of duration 20, 50, 100 and 300 μs are shown in figure (7.9). The v_{00} pulse is turned on at 1200 μs and the molecules are detected at 2000 μs. As the pump pulse is applied, the molecules from the central part of the ToF profile are pumped out as they have interacted with the resonant light. The hole in the central part of the ToF profiles corresponding to the molecules that have been pumped in the $X(v'' = 1)$ state becomes wider and deeper with increasing pump pulse length. The measured ToF profiles agree very well with the simulated ones. This is a good indication that the scattering rate in the experiment is exactly as expected.

In this experiment the power in the v_{00} laser is 10 mW corresponding to a scattering

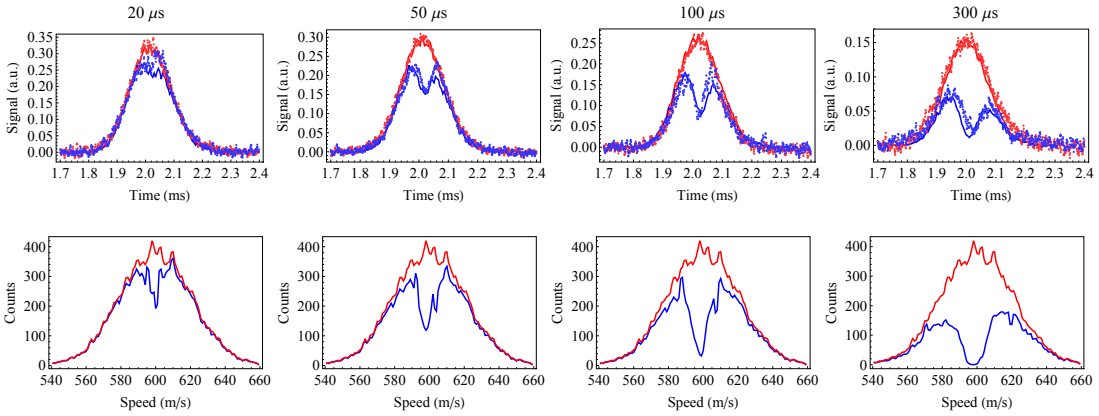

FIGURE 7.9: Top row - the ToF profiles gated over the four hyperfine states before (red) and after (blue) a pump pulse of v_{00} light of duration 20, 50, 100 and 300 μs. Solid lines - simulation results. Points - data. Bottom row - the velocity distribution predicted by the model.

rate of approximately 2 MHz. As it takes fewer than 100 scattered photons to pump the molecules into the $X(N'' = 1, v'' = 1)$ state, a v_{00} pulse $\geq$100 μs should be long enough to entirely pump out the target velocity class of the molecules. Nevertheless, the hole in the ToF profile in figure (7.9) does not go down to zero. The reason for this is that the source has a finite spatial extent. To illustrate this point, consider the following scenario - two molecules at the source are separated by 10 mm with the front one traveling 5 m s^{-1} slower than the one at the back. The velocity difference of 5 m s^{-1} corresponds to a change of the Doppler shifts of about one natural linewidth Γ. If one of the molecules is exactly on resonance with the counter-propagating beam, the other one will be detuned by one natural width and will scatter photons at a slower rate. The two molecules arrive at the detector at the same time. However, one of them is much more likely to have been optically pumped than the other. The effect is that the hole in the ToF profile does not reach zero even though a particular velocity class might be completely pumped out. This result is independent of where the pumping takes place with respect to the detector. The velocity profiles predicted by the simulation (figure (7.9)) indeed suggest that the target velocity class has been completely pumped out after a pulse of duration 100 μs or longer. In the

model the FWHM of the molecular beam in the z direction at the source has been taken to be 20 mm as this value best matches the depth of the hole in the experimentally measured ToF profiles.

Figure (7.10) shows the experimental and simulated ToF profiles for each hyperfine state and several different v_{00} pulse durations. Once again, the simulations agree well with the experiments, showing that the molecular dynamics are very well understood. Because of the many frequencies present in the pump beam it is difficult to anticipate what the ToF profiles gated on a given hyperfine state would look like in advance, but the model takes into account all laser frequency components present.

The $(J = 3/2, F = 2)$ state has most of the slower molecules pumped out due to the light

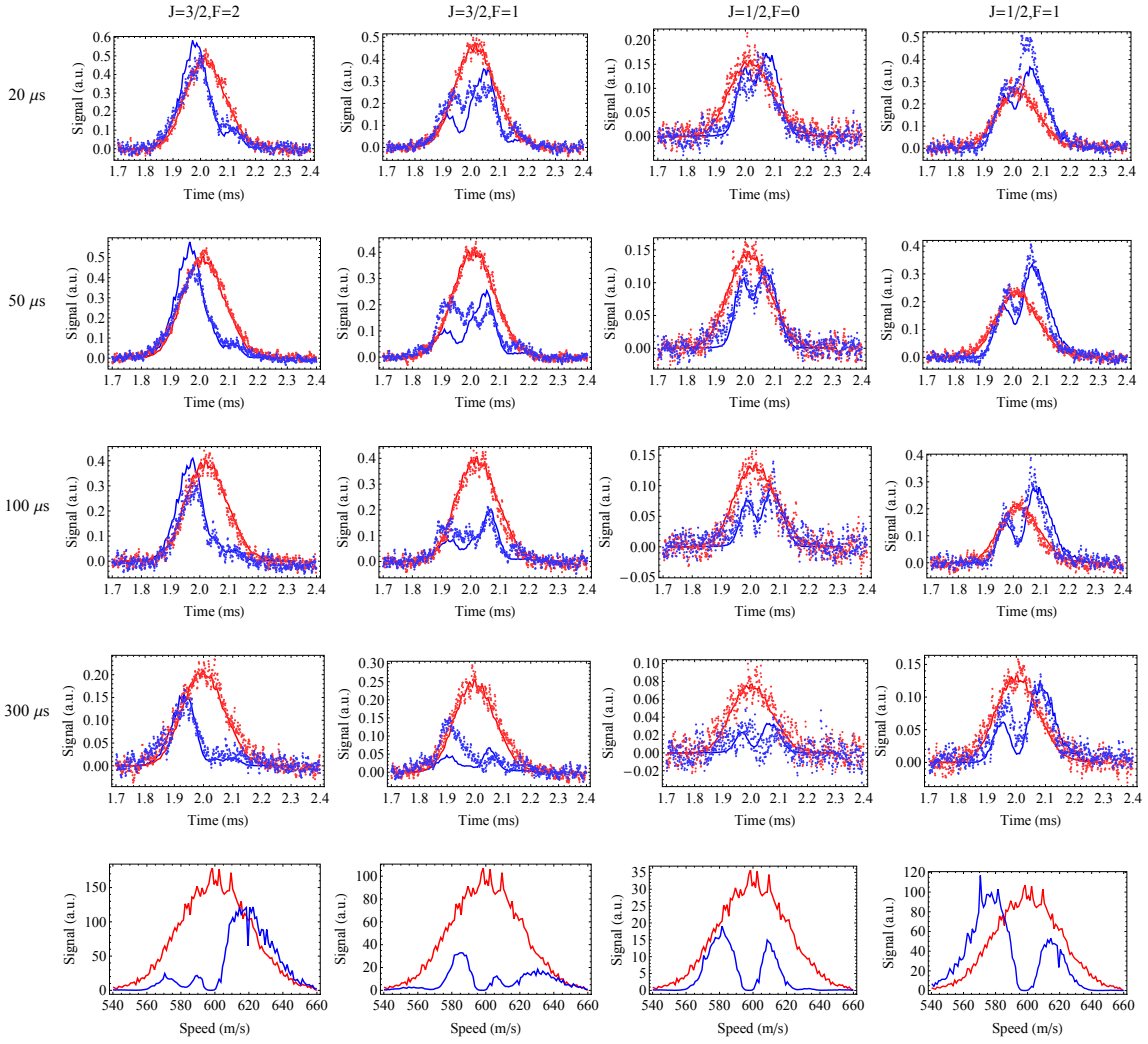

FIGURE 7.10: The ToF profiles gated over individual hyperfine states before (red) and after (blue) a v_{00} pump pulse. Solid lines - simulation results. Points - data. The bottom row shows the velocity profiles predicted by the simulation for the 300 μs pump pulse.

addressing the $(J = 3/2, F = 1)$ state which is blue-detuned by 25 MHz. In that state the simulation predicts a slightly higher optical pumping for the pump pulse of 20 μs - the

peak at about 1.96 ms is approximately 16% higher than we observe in the experiment but this discrepancy disappears with increasing pulse duration. The shape of the predicted and measured ToF profiles in that state agree very well.

The ToF profile gated on the $(J = 3/2, F = 1)$ state exhibits a double-dip feature particularly prominent after the 20 μs long pulse. The frequency separation between the two dips is approximately 70 MHz and is most likely due to the frequency sidebands in the v_{00} light separated by 72 MHz addressing the nearby $(J = 3/2, F = 2)$ and $(J = 1/2, F = 0)$ states. As the duration of the v_{00} pulse is increased, the molecules are very efficiently pumped out of the $(J = 3/2, F = 1)$ state.

The ToF profile gated on the $(J = 1/2, F = 0)$ state has a hole exactly in the middle. The ToF profile in that state does not have additional features as the frequency components addressing the two neighboring hyperfine states at -48 MHz and +72 MHz have a larger frequency span than the Doppler extent of the molecules within each pulse. The depth of the hole increases with increasing pulse duration.

Finally, the $(J = 1/2, F = 1)$ state shows a hole which is in the center of the ToF profile. The depth of the hole increases with increasing pulse duration. For the 20 μs pulse we observe a higher degree of optical pumping than predicted by the model - the peak at approximately 2.075 ms is 40% higher in the experiment, but the difference between the experiment and the model disappears with increasing pump pulse duration.

The bottom row of figure (7.10) shows the velocity profiles predicted by the simulation in the different hyperfine states after a pump pulse of 300 μs. We can see that slightly different velocity classes have been pumped out of each state as is evident from the ToF profiles. Nevertheless, when all states are averaged together we see a hole in the middle of both the ToF and velocity profiles that becomes deeper with increasing pulse duration as shown in figure (7.9).

The results in this section are important because we have demonstrated that we can pump-out a portion of the ToF profile exactly as predicted by the model. This means that the scattering rate in the model is reproduced in the experiment. In addition to this, the data shows that the v_{00} laser is stable enough to interact with a given velocity class of the molecules. When the repump beam is added, the central velocity class of the molecules is expected to be slowed and cooled down.

7.6 Longitudinal laser cooling

When exposed to resonant v_{00} light, the molecules get pumped into the $X(N''=1, v''=1)$ state and the number of molecules detected in the $X(N''=1, v''=0)$ state decreases with increasing v_{00} pulse duration. When the v_{10} repump light is added, the number of molecules detected on the $A - X(0-0)$ transition is conserved even for long pump pulses.
Figure (7.11) shows the fraction of molecules detected in the $X(v''=0)$ state after a pump pulse containing either the v_{00} or the v_{00} and v_{10} light. Each data point is the integral of the ToF profile with the v_{00} pump pulse applied, divided by the integral of the ToF profile without the pump. In the absence of a vibrational repump, the number of detected molecules decreases exponentially with pump pulse duration. When the v_{10} laser is added however, the decrease of detected molecules is more gradual, if present at all, as the molecules are slowly optically pumped into the $X(N''=1, v''=2)$ state.

When the cooling lasers are tuned to interact with the central velocity class of the

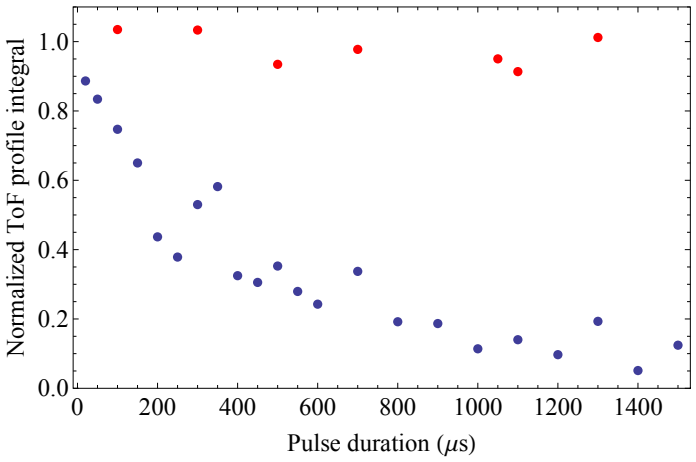

FIGURE 7.11: The normalized integral of the ToF profile gated over the four hyperfine states of the $X(v''=0)$ manifold detected after a pump pulse of v_{00} light only (blue) and a laser cooling pulse of both v_{00} and v_{10} (blue).

molecules, we expect the central part of the ToF profile to be shifted to a later arrival time. We have demonstrated the expected laser cooling effect in three experimental set-ups: a) with short vacuum chamber (PMT 1.2 m away from the source) and relatively small laser cooling beams (mean $1/e^2$ radii at the skimmer and detector of 0.27 mm and 1.71 mm respectively), b) with an extended vacuum chamber allowing for a longer interaction time (PMT 1.63 m away from the source) and small laser cooling beams and c) with a long vacuum chamber and expanded laser cooling beams (mean $1/e^2$ radii at the skimmer and detector of 0.78 mm and 3.81 mm respectively). The laser cooling effect was demonstrated in all three set-ups but was most significant in set-up c) and the results presented in this thesis are taken in that set-up.
In the laser cooling experiments presented here the v_{00} light is turned on at t =200 μs and

stays on for a duration τ varying from 0.1 ms to 1.8 ms. The v_{10} light remains on to ensure that molecules in $X(v = 1)$ are optically pumped to $X(v = 0)$ prior to detection. The duration τ is limited by the total flight time and the interaction time needed for this final optical pumping step. The cooling lasers are locked to interact with the central velocity class of the molecules. On the axis of the beamline, the laser powers available for cooling correspond to an effective saturation intensity per hyperfine transition of $s_{\text{eff}} \approx 4.5$ at the beginning and $s_{\text{eff}} \approx 0.5$ at the end of the 1.8 ms laser cooling pulse. For each laser cooling pulse duration τ the probe laser is scanned around the four hyperfine levels of either the $A - X(0 - 0)$, $A - X(1 - 1)$ or the $A - X(2 - 2)$ transitions at 494431 GHz, 494599 GHz and 494757 GHz to detect the molecular population in the $X(v'' = 0)$, $X(v'' = 1)$ and $X(v'' = 2)$ states following the laser cooling. The probe beam has a Gaussian intensity profile with $1/e^2$ radius of 1.5 mm and the probe power is approximately 0.3 mW.

7.6.1 Laser cooling - example data

An example probe scan over the $A - X(0 - 0)$ transition after a laser cooling pulse of 1.8 ms is shown in figure (7.12 a). The overall population over the spectrum has decreased by 24% after the laser cooling pulse as the molecules have been pumped into the $X(v'' = 2)$ state. The greatest fraction of molecules missing is from the first two states.
The ToF profiles gated on the individual hyperfine states are shown in figure (7.12 b). After the laser cooling pulse the ToF profiles in each hyperfine state exhibit a peak at approximately 2786 μs corresponding to the slowed molecules. The peak is particularly pronounced in the fourth state.
Since the molecules have been re-distributed among the hyperfine levels after the cooling, we need to account for the different photon yields when detecting molecules in each of these states. To do that, we measure the spectrum without laser cooling and find the weighting factors that the each peak needs to be multiplied by so that it reflects the degeneracy of the state. The weighting factors for the four hyperfine levels were found to be (1.26, 0.705, 0.891, 1.17). These calculated factors were then applied to both the on and off shots of the ToF profile gated on the respective state. This procedure ensures that the experimental ToF profiles are not further complicated by the effects of velocity-selective hyperfine pumping.
Figure (7.12 c) shows the ToF profile averaged over the four states with the appropriate weighting factors applied. The peak corresponding to the decelerated molecules is still visible and protrudes slightly above the uncooled ToF profile - this is an indication that new slower molecules have been created. If we use the simple $v = L/t$ relationship, where L is the distance traveled from the source, the position of the decelerated peak would suggest a velocity reduction of 10 $\mathrm{m\,s^{-1}}$ for the molecules traveling at 600 $\mathrm{m\,s^{-1}}$. This suggests that on average 1500 photons have been scattered. This is just a rough estimate but will

be later confirmed by the predicted and inferred velocity distribution of the molecules.

Scanning the probe laser over the $A-X(2-2)$ transition reveals that the missing molecules have appeared in the $X(v'' = 2)$ state (figure (7.13 a)). The initial population in that state has increased by a factor of 2.7 with all hyperfine levels equally populated after the laser cooling pulse. The ToF profiles gated on each hyperfine state have a peak at approximately 2750 μs (figure (7.13 b)) - the molecules pumped into the $X(v'' = 2)$ state are less decelerated than the ones that have remained in the cooling cycle. Figure (7.13 c) shows the ToF profile averaged over the four hyperfine states weighted by the same weighing factors as the ToF profiles detected in the $X(v'' = 0)$ state.

We also scanned the probe laser around the $A - X(1 - 1)$ transition but no molecules were detected in the $X(N'' = 1, v'' = 1)$ state as the v_{10} has acted efficiently as a clean-up beam.

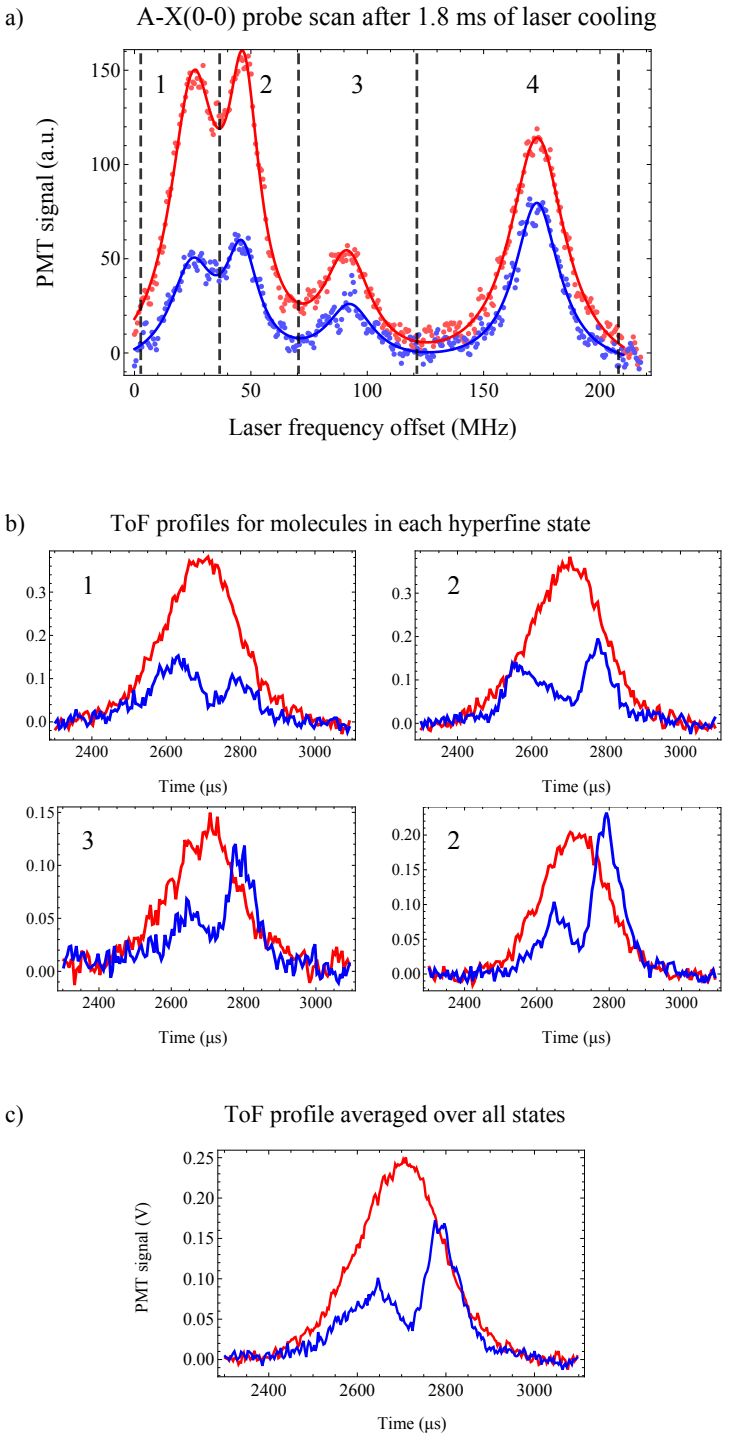

FIGURE 7.12: a) Probe scan over the four hyperfine levels of the $A-X(0-0)$ laser cooling transition before (red) and after (blue) a 1.8 ms laser cooling pulse. The data is fitted to a sum of four Lorentzian functions. Fewer molecules are detected after the laser cooling as some molecules have been pumped into the $X(v'' = 2)$ state. b) The ToF profiles for molecules in each hyperfine level - the peak at 2786 μs in all states indicates that the molecules from the central part of the packet have been slowed. The effect is most prominent in the 4^{th} state. c) The ToF profile averaged over the four hyperfine states.

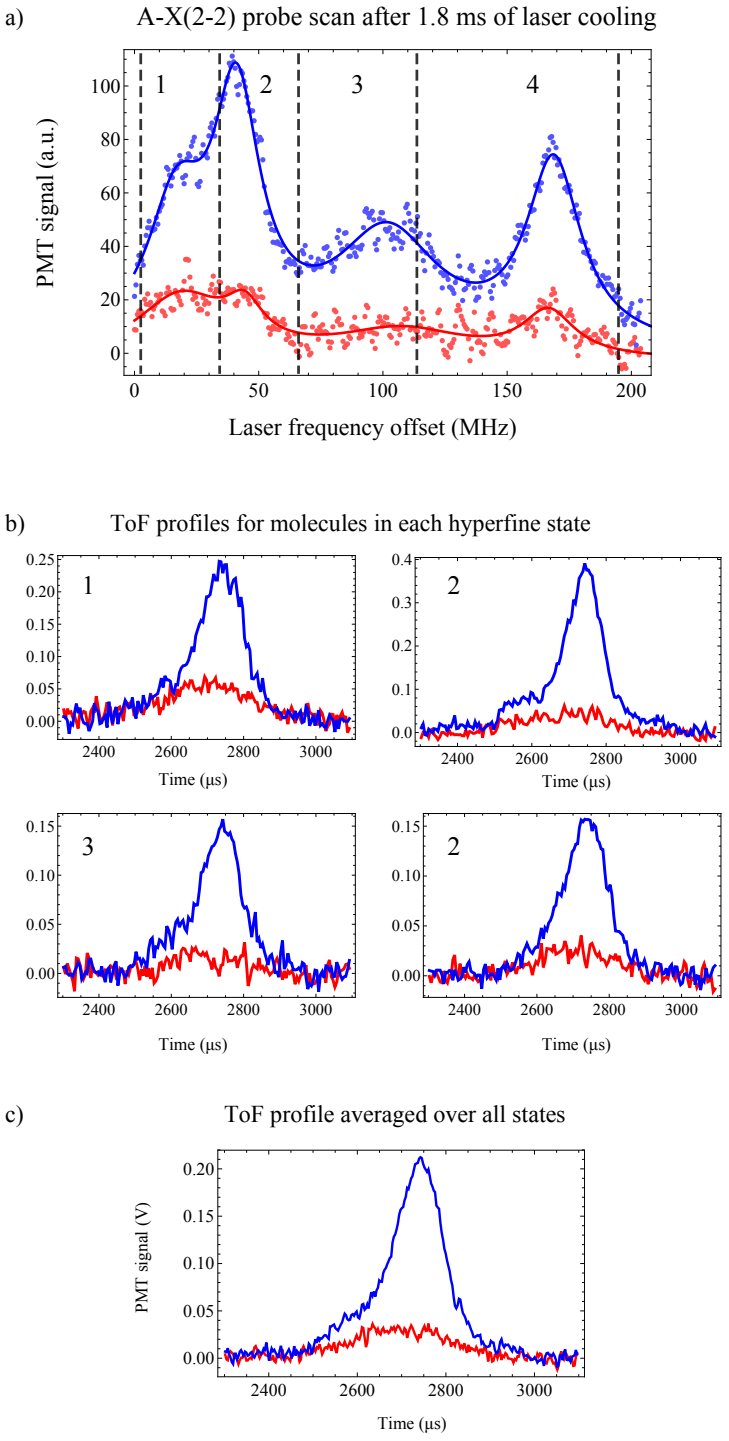

FIGURE 7.13: a) The $A-X(2-2)$ spectrum of the laser cooling transition before (red) and after (blue) a 1.8 ms laser cooling pulse. The data is fitted to a sum of four Lorentzian functions. After the laser cooling the population in this state has increased by a factor of 2.7. b) The ToF profiles for molecules in each hyperfine level - the molecules pumped into the $v'' = 2$ state have been slowed and have a mean arrival time approximately 50 μs later than the uncooled ToF . c) The ToF profile averaged over the four hyperfine states similarly shows the same peak at about 2750 μs which indicates that slower molecules have been created.

7.6.2 Effect of laser cooling on the ToF profiles - experiment and model

In this section, we will investigate how the molecular dynamics in the various states evolve as the laser cooling pulse duration τ is increased from 0.1 to 1.8 ms. We can compare the measured and modeled ToF profiles in any hyperfine state and the three vibrational manifolds involved.

7.6.2.1 The rate equation model

In the experiment we measure a time-of-flight profile instead of a velocity distribution. The rate equation model, on the other hand, gives the velocity distribution of the molecules in the different levels after the laser cooling. Because it is straightforward to generate a time-of-flight profile from the predicted by the rate equation model velocity distribution after the action of the laser cooling, we can predict what the ToF profile is expected to look like for the given experimental conditions. A comparison between the measured and simulated time-of-flight profiles thus can reveal if the cooling and slowing effect in the experiment is as expected.

Several parameters characterizing the molecular pulse are needed as input for the rate equation model. The shape of the modeled ToF profile depends most critically on two of them - the distribution of forward velocities of the molecules and the spatial extent of the molecular packet at the source in the forward direction. Consider first the velocity distribution. The measured ToF profile without laser cooling in the experiment is a direct estimate of the initial velocity distribution of the molecules in the forward direction as the detector is sufficiently far away from the source and there are no interactions between the molecules. In the model, we choose a center forward velocity and spread of velocities for the molecules so that the simulated ToF profile without laser cooling best matches the experimentally measured one. The source is thus taken to emit a Gaussian distribution of forward speeds centered at 600 $\mathrm{m\,s^{-1}}$ and with a temperature of 3.1 K (with FWHM of forward velocities of approximately 45 $\mathrm{m\,s^{-1}}$).

Consider now the spatial extent of the molecular pulse at the source along the z direction. In order to estimate this parameter, we use the results of the the pump-out experiment described in section (7.5). The best match between the measured and simulated hole in the ToF profile after the pump-out v_{00} pulse was found to be when in the model the source is taken to have an distribution of positions along z which is Gaussian with a FWHM of 20 mm. We use this estimate for the spatial extent of the molecular pulse in the z direction at the source. Finally, in the model we take the initial radial positions and speeds of the molecules to have FWHM of 1.2 mm and 25 $\mathrm{m\,s^{-1}}$ respectively but only molecules with small radial positions and speeds are detected so the simulation is insensitive to these values. The range of radial speeds which get detected in the model is chosen to be the same as in the experiment and is determined from geometry considerations (the distance between

the PMT and the source, the size of the detection region etc.).
The laser beams in the rate equation model are intended to reflect the experimental conditions as closely as possible. In the model we assume that the four laser beams are perfectly overlapped and focused to converge toward the source, similarly to the experimental design. Each laser beam in the model is taken to have a Gaussian intensity distribution with parameters as measured in the experiment. The frequency separation between the hyperfine components in the model is also taken to be as it is in the experiment and is determined by the driving rf frequencies of the AOM and EOM. In the experiment we measure the power in the v_{00} and v_{10} beams before they enter the vacuum chamber. In the model we assume that the laser power is equally distributed among the four frequency components in each vibrational manifold. Thus, in the rate equation model the driving intensities are taken to best match the experimentally measured values (recall that the scattering rate is completely determined by the intensity of the laser cooling light). Finally, in the model the cooling beams are assumed to be tuned to interact with the molecules traveling at 600 $\mathrm{m\,s^{-1}}$.
The choice of Franck-Condon factors in the rate equation model has a significant effect on the modeled ToF profile of the molecules in the different vibrational manifolds after the laser cooling. In the model the Franck-Condon factors $q_{v',v''}$ (where v' and v'' are the vibrational states in the ground and excited electronic manifolds respectively) are set to be $q_{0,0} = 0.972$ and $q_{1,0} = 1 - q_{0,0}$ as these values produce the ToF profiles after the laser cooling that best match the experimentally measured ones. For each molecule the simulation continues until the molecule decays to the $X(N'' = 1, v'' = 2)$ state which happens after scattering n photons. In the model, for each molecule, n is chosen at random from the probability distribution $q_{2,0}(1 - q_{2,0})^2$ where $q_{2,0} = 7.84 \times 10^{-4}$. The value of $q_{2,0}$ was chosen to best match the experimentally measured fraction of molecules pumped into the $X(v'' = 2)$ state.

7.6.2.2 The ToF profiles in the $v'' = 0$ state

Figure (7.14) shows the experimental and simulated ToF profiles of the molecules detected in the $v'' = 0$ state after a laser cooling pulse of duration τ. The modeled ToF profiles are simply summed over all the hyperfine levels while the experimental ones are averaged with the appropriate weighting factors applied as described in section (7.6.1). The shape of the experimentally measured ToF profiles is very well matched by the simulation. As the laser cooling pulse duration is increased, the molecules from the center of the ToF profile become more and more depleted as they have interacted with the cooling beams and been decelerated to later times. The central part of the ToF profile is almost completely pumped out after the 1.8 ms cooling time. At the same time, the ToF profiles exhibit a peak corresponding to the molecules that have been decelerated to a later time, marked

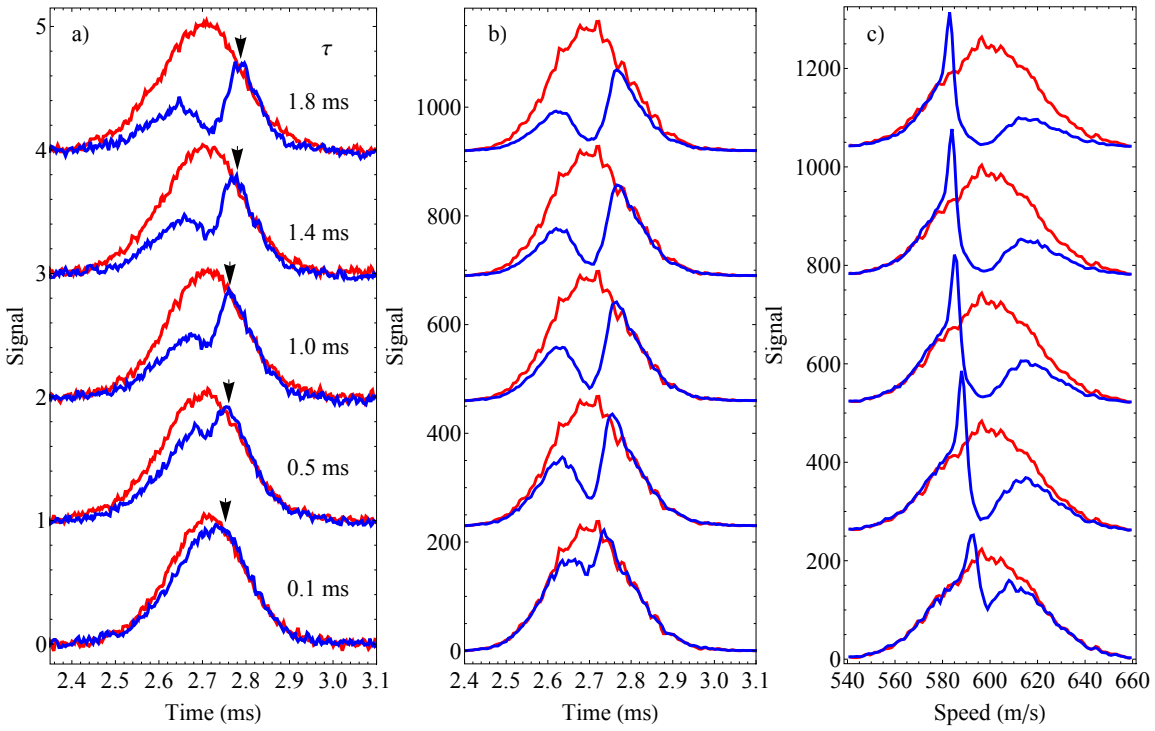

FIGURE 7.14: The experimental (a) and simulated (b) ToF profiles of the laser cooled molecules in the $v'' = 0$ states after a laser cooling pulse of duration τ. The arrow indicates the peak shifted to later times with increasing τ corresponding to the decelerated molecules. c) The velocity profiles from the simulation.

by an arrow in figure (7.14 a). In the experiment the position of the peak is shifted with increasing τ - from 2.741 ms for $\tau = 0.1$ ms to 2.780 ms for $\tau = 1.8$ ms (figure (7.15 a)). The velocity profiles predicted by the simulation (figure (7.14 c)) show that the central velocity class of the molecular packet has been decelerated and compressed. The molecules in that vibrational manifold have been decelerated from an initial velocity of v_i=600 m s^{-1} to a final velocity of $v_f = 592$ m s^{-1} for $\tau = 0.1$ and $v_f = 583$ m s^{-1} for $\tau = 1.8$ ms. This suggests that more than 1500 photons have been scattered.

The model predicts that the pumped-out hole in the middle of the ToF profile is more pronounced than we observe in the experiment, particularly for the short cooling times. This is most likely due to experimental imperfections which cause the scattering rate to be lower - for example, misalignment of the laser and molecular beams, imperfect overlap between the different frequency components, imperfect setting of the sideband frequencies, additional sidebands due to the EOM, non-optimal magnetic field, laser frequency jitter etc.

Figure (7.15 a) shows the position of the peak corresponding to the decelerated molecules as measured in the experiment and predicted by the simulation. The agreement between

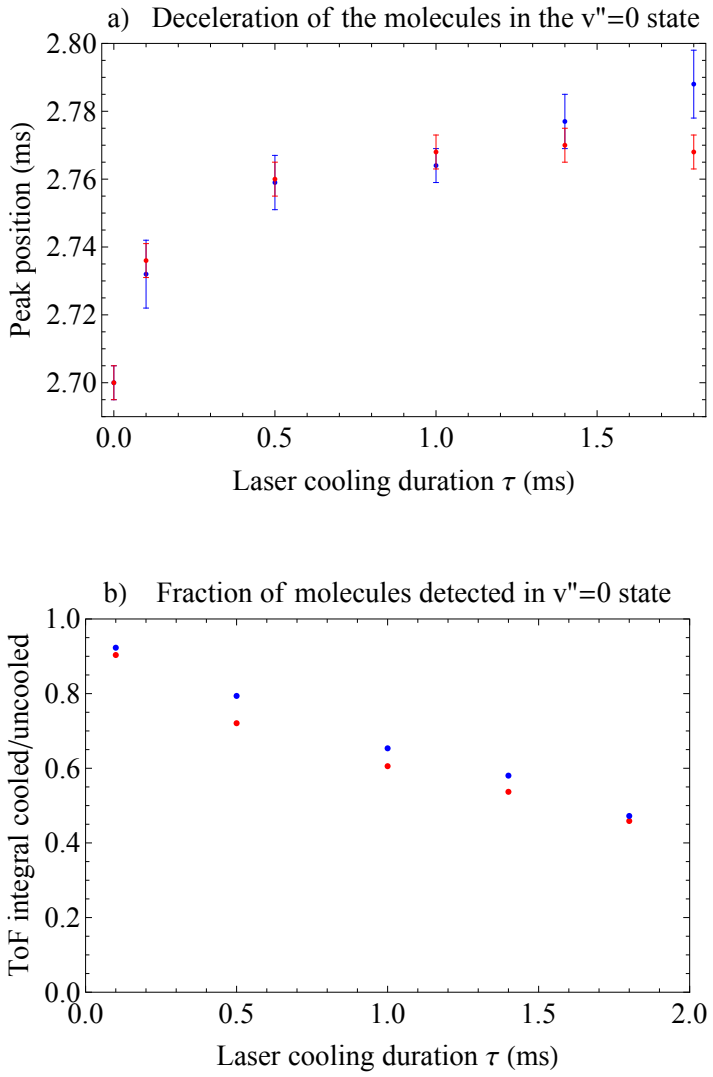

FIGURE 7.15: a) The position of the peak corresponding to the decelerated molecules and b) the fraction of molecules detected in the $v'' = 0$ state compared to the uncooled ToF profile for the five laser cooling durations τ. Blue - experiment, red - simulation.

experiment and model is good, particularly for the smaller values of τ. The deceleration measured in the experiment for $\tau = 1.4$ and $\tau = 1.8$ ms is a few μs higher than predicted in the model. This is most likely because the laser cooling beams in the experiment interact with a broader class of molecules because of frequency jitter and molecules which were slower to begin with are also decelerated.

Figure (7.15 b) shows the fractional decrease of the total number of molecules detected in the $v'' = 0$ state with increasing τ as the molecules are optically pumped into the $v'' = 2$ state as predicted by the model and measured in the experiment. In the experiment the fraction of remaining molecules detected in the $v'' = 0$ state falls from 0.94 for $\tau = 0.1$ ms

to 0.48 for $\tau = 1.8$ ms (figure (7.15 b)). The model predicts that a slightly higher fraction of molecules is pumped into the $v'' = 2$ state than experimentally measured. This is also due to the slower scattering rate in the experiment.

The overall shape of the ToF profiles, however, is very well reproduced by the model. The agreement is also evident when we compare the ToF profiles in the individual hyperfine states as shown in figure (7.16). The depth of the hole of in the middle of the ToF profiles

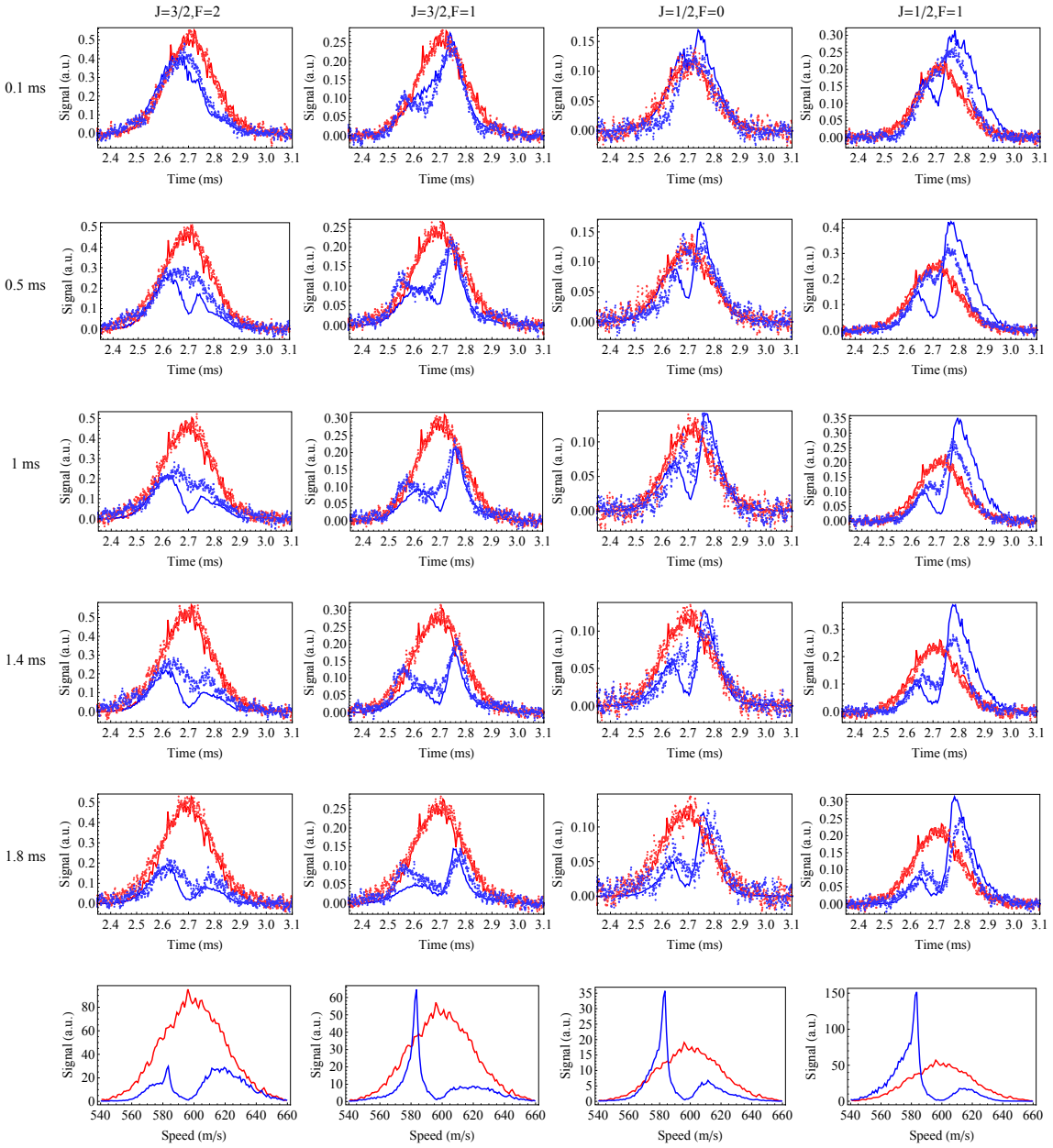

FIGURE 7.16: The measured (points) and simulated (solid lines) ToF profiles for each of the hyperfine states after a laser cooling pulse of duration 0.1, 0.5, 1, 1.4 and 1.8 ms. Bottom row - the velocity profiles predicted by the simulation after a laser cooling time of 1.8 ms.

in all states is slightly deeper in the simulation than it is in the experiment but this difference

is less significant for the longest laser cooling pulse. The majority of the molecules have been pumped out of the $(J = 3/2, F = 2)$ state and the molecules that have been cooled/slowed to the greatest extent end up in the $(J = 1/2, F = 1)$ state. The pumping out of the $(J = 3/2, F = 2)$ state and into the $(J = 1/2, F = 1)$ state is not as pronounced in the experiment, particularly for the cooling times shorter than 1.4 ms but the agreement between the data and model for the laser cooling of 1.8 ms is very good. The bottom row of figure (7.16) shows the velocity profiles of the molecules in the different hyperfine states after a laser cooling pulse of 1.8 ms.

7.6.2.3 The ToF profiles in the $v'' = 2$ state

Figure (7.17) shows the experimental and simulated ToF profiles of the molecules detected in the $v'' = 2$ state after the laser cooling pulse. In the experiment the original population in the $v'' = 2$ state, which is approximately 10% of the population in the $v'' = 0$ state as determined by the integral of the ToF profiles, has been subtracted. Both in the experiment and simulation the population in that state increases linearly with laser cooling time τ. All ToF profiles exhibit a peak which is slightly shifted with respect to the central arrival time of the uncooled molecules. The shape of the experimental ToF profiles is well reproduced by the simulation. The modeled velocity profiles show that the molecules pumped into the $v'' = 2$ state are slower on average and that there is no significant velocity bunching. The reason for this is that the molecules detected in the $v'' = 2$ state have fallen out of the cooling cycle at a random time.

Figure (7.18) shows the height and the center arrival time of the ToF profiles of the molecules detected in the $v'' = 2$ state after the laser cooling, relative to the height and center arrival time of the ToF profile of the uncooled molecules in the $v = 0$ state. The amplitude of the peak in the $v'' = 2$ ToF profiles increases with increasing laser cooling duration τ as the molecules have a higher probability of falling out of the cooling cycle the longer they have been exposed to the cooling light. The simulation predicts a higher value for that peak amplitude, especially for the shorter laser cooling times. The reason for the lower peak height in the experimental ToF profiles is the slower scattering rate in the experiment, as discussed in section (7.6.2.2). The molecules detected in the $v'' = 2$ state have on average later arrival time than the uncooled molecules. In addition to that, the position of the peak height of the ToF profiles is shifted to later times with increasing τ as the molecules scatter more photons before being optically pumped into the $v'' = 2$ state. The predicted by the model position of the peak of the ToF profiles of the molecules detected in $v'' = 2$ agrees with the experimental values, especially for the longer laser cooling times.

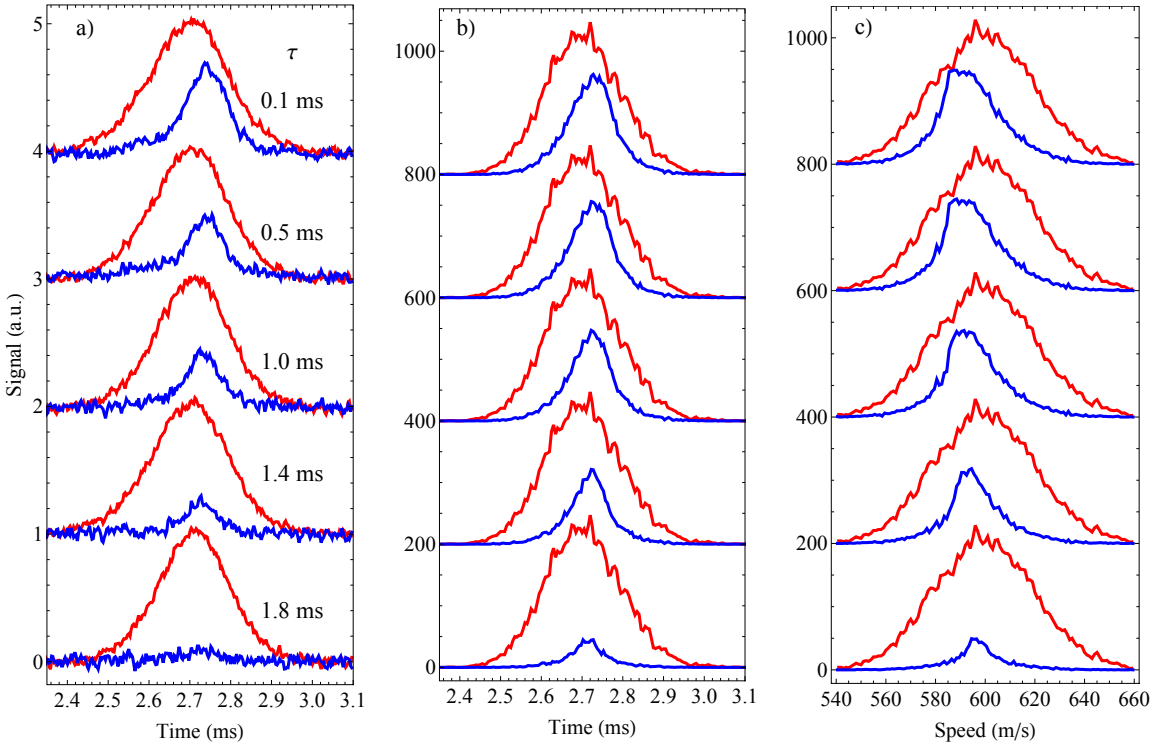

FIGURE 7.17: The experimental (a) and simulated (b) ToF profiles of molecules detected in the $v'' = 2$ state after a laser cooling pulse of duration τ (blue) compared to the uncooled ToF profile in the $v = 0$ state (red). c) The velocity profiles of the molecules in the $v'' = 2$ state (blue) and the uncooled molecules in the $v = 0$ state (red) predicted by the simulation.

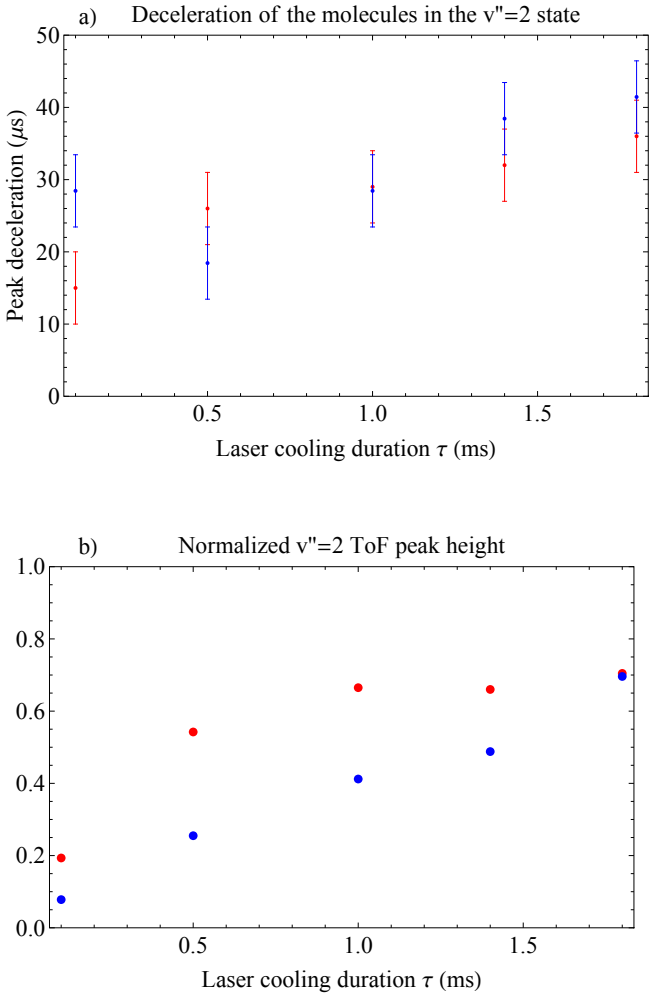

FIGURE 7.18: a) The position of the peak in the $v'' = 2$ ToF profiles with respect to the central arrival of the uncooled molecules in the $v = 0$ state for several laser cooling durations τ. b) The height of the ToF profile of the molecules detected in the $v'' = 2$ state after the laser cooling. Each point is normalized to the height of the uncooled ToF profile of the molecules in the $v = 0$ state. b) Blue - experiment, red - simulation.

In the experiment the fraction of molecules pumped into the $v'' = 2$ state increases linearly with increasing laser cooling pulse: from 4% for $\tau = 0.1$ ms to 36% when $\tau = 1.8$ ms. However, the model predicts that a slightly higher fraction of molecules has been pumped into that state, particularly for the shorter values of the laser cooling pulse. This is consistent with the results in section (7.6.2.2).

Table (7.1) shows the fraction of molecules detected in the $v'' = 0, 1, 2$ states after the laser cooling pulse. Each entry is the integral of the ToF profile of the molecules detected in the respective vibrational state divided by the integral of the uncooled ToF profile in the $v = 0$ state. The molecules in the experiment are pumped out of the $v = 0$ state at a slower rate than in the model due to the lower scattering rate. Also, there is no detectable population in the $v'' = 1$ state in the experiment. We note that the apparent loss of molecules in the experiment is most likely due to systematic long term drifts of the Ca target between the measurements in the three vibrational manifolds.

When the ToF profiles of the molecules detected in the two vibrational manifolds are

Cooling time (ms):	0.1	0.5	1.0	1.4	1.8
Model					
v"=0	0.904	0.721	0.605	0.537	0.459
v"=1	0.0021	0.01	0.0255	0.0489	0.0981
v"=2	0.088	0.263	0.363	0.408	0.437
Total:	1	1	1	1	1
Experiment					
v"=0	0.9425	0.8052	0.6599	0.6557	0.4895
v"=1	0	0	0	0	0
v"=2	0.039	0.114	0.192	0.28	0.364
Total:	0.962	0.908	0.845	0.86	0.836

TABLE 7.1: The fraction of molecules detected in the $v'' = 0, 1, 2$ vibrational manifolds after a laser cooling pulse of duration τ.

displayed on the same axis as shown in figure (7.19), we can see that the molecules detected both in the $v'' = 0$ and $v'' = 2$ states have been decelerated with respect to the central arrival time of the uncooled molecules. In addition to that, the peak in the $v'' = 2$ ToF profiles is at a slightly earlier time than the corresponding peak in the $v'' = 0$ state for all values of τ as the molecules detected in the latter state have been exposed to the laser cooling for longer. The position of the peak corresponding to the decelerated molecules in both vibrational states is observed at the place predicted by the model with the best agreement for τ =1.8 ms.

We also note that the ToF profile of the molecules in the $v'' = 2$ state is slightly asymmetric and weighted towards later times. The reason for this asymmetry is that the longer the laser cooling pulse is the more photons the molecules have scattered before being optically pumped into the $v'' = 2$ state. This asymmetry increases with τ and becomes even more

pronounced when the laser cooling light is chirped as will be discussed in section (7.7).

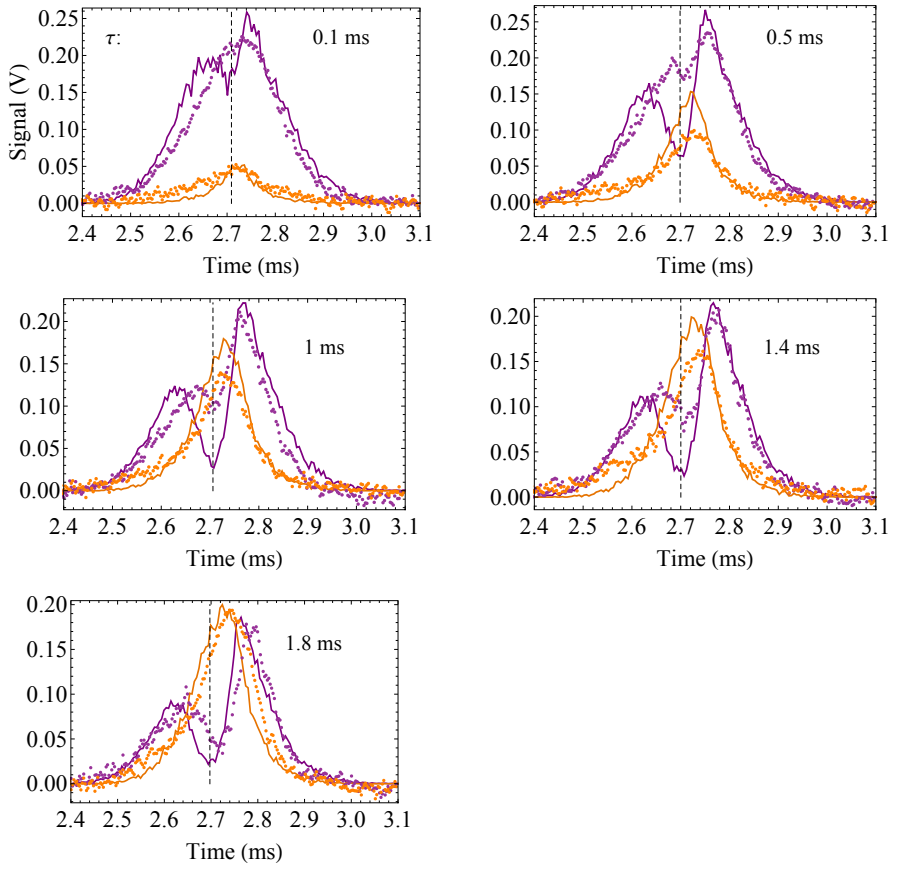

FIGURE 7.19: The ToF profiles of the molecules detected in the $v'' = 0$ state (purple) and $v'' = 2$ state (orange) after a laser cooling pulse of duration τ. Points - experiment, solid lines - model. The dashed lines indicate the central arrival time for the uncooled molecules.

7.6.2.4 The sum of the ToF profiles in the v"=0 and v"=2 states

When we add the ToF profiles of the molecules detected in the three vibrational states involved we see the expected laser cooling effect most clearly (figure (7.20)). The molecules removed from the original distribution are slowed and cooled and produce a peak that is both later and narrower. The peak's amplitude increases with increasing τ as more and more molecules pile up at the lower velocity. In addition, the peak corresponding to the laser cooled bunch is shifted to lower velocities with increasing laser cooling time. The modeled velocity distribution suggests that after a laser cooling pulse of 1.8 ms the molecules that have interacted with the cooling light have been decelerated from 600 $\mathrm{m\,s^{-1}}$ to 583 $\mathrm{m\,s^{-1}}$ while their temperature has been reduced from 2.97 K to 86 mK.

We note that for the laser cooling times of 0.1 and 0.5 ms, the simulation predicts a sharper and larger decelerated peak than we observe in the experiment. In particular, the

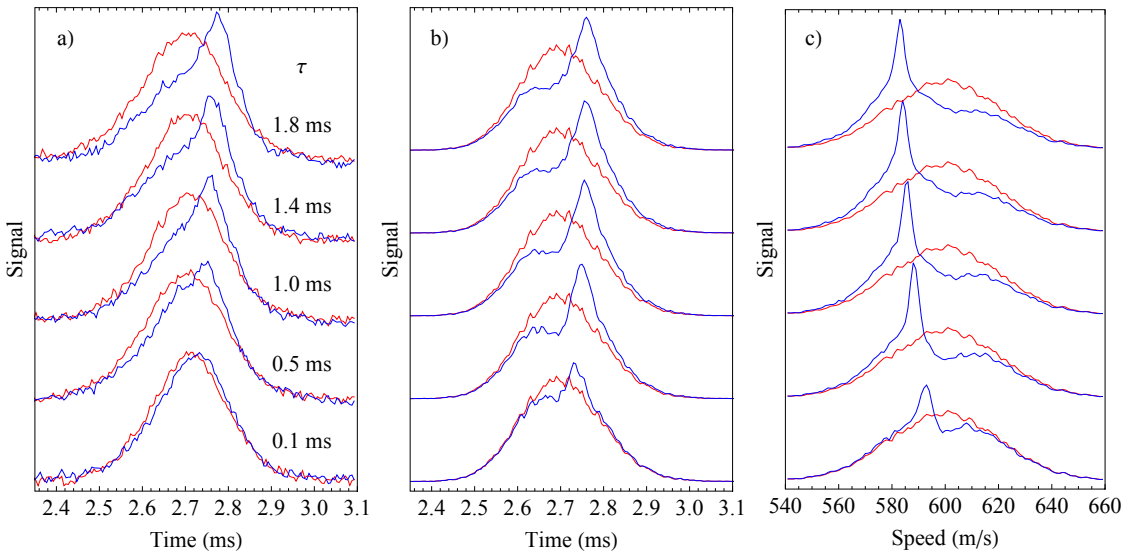

FIGURE 7.20: The sum of the ToF profiles of the molecules detected in all vibrational states before (red) and after (blue) a laser cooing pulse. a) Data. b) Simulation. c) The velocity profiles predicted by the simulation.

slowed/cooled bunch of molecules that is clearly present in the simulated ToF profile for the 0.1 ms cooling time has no corresponding feature in the experimental data, while the overall shift of the measured ToF profile for that laser cooling time is not reproduced in the calculated data. This discrepancy between experiment and simulation is also due to the slower scattering rate in the experiment than in the simulation, as we have seen before. The agreement between the experiment and model is better for the two longest laser cooling durations. It is interesting to note that for the 1.8 ms laser cooling the experimental ToF peak is approximately 30±5 μs later than the simulated one. The reason for this could be that in the experiment the cooling lasers have a wider range of capture velocities compared to the prediction of the simulation. We will come back to that point in section (7.6.3).

7.6.3 Extracting the velocity distribution from the measured ToF profiles

The experimental and simulated ToF profiles agree reasonably well but the agreement is not perfect. Since the measured ToF profiles suggest that the scattering rate in the experiment is slightly lower than expected, the modeled velocity profiles can only serve to give a lower limit to the temperature. A direct measurement of the velocity distribution would be ideal but is outside of the scope of the current work.

In this section, we present a method for inferring the velocity distribution from the measured ToF profiles without relying on the rate equations model.

The simplest way to estimate the velocity distribution from the measured ToF profiles is to use the relation $v = L/t$ where L is the distance traveled from the source to the detector. This approach is not entirely accurate, because it overlooks the fact that the molecules

undergo deceleration for part of the time. Nevertheless, it gives an upper limit to the temperature which is 450 mK for the 1.8 ms cooling time.

We can also extract the velocity distribution in a more accurate way. As the source is spatially compact, the measured ToF profile without laser cooling is a direct measure of the velocity distribution produced by the source. We can guess what kind of a force acted on the initial velocity distribution to convert it into one that produces the measured ToF profile after the laser cooling pulse. We assume a simple velocity-dependent form of the light force which has a characteristic symmetric shape with respect to a central velocity. We approximate the light force as a Gaussian function of the form: $F \exp\left(-(\frac{v-v_0}{\Delta})^2\right)$, where F characterizes the maximum value of the force, v_0 the central velocity and Δ the width. The cooling force is determined by the free parameters F, v_0 and Δ which are to be deduced from the measured ToF profile after each laser cooling pulse. Once the force function is specified, the arrival time at the detector corresponds to a unique value for both the initial and final velocity - so a measured ToF profile can be transformed into an initial velocity distribution and a final velocity distribution. We can vary the three parameters that define the force function to find the values that give the best fit between the generated and measured initial velocity distributions. A single choice of the fitting parameters reproduces well all the measured ToF profiles. We note that the exact form of the force function was found to be insignificant and a Lorentzian function produced similar results.

The ToF and velocity profiles obtained by this fitting procedure are shown in figures (7.21 a) and (7.21 b). The best fit parameters were found to have values $v_0 = 599 \pm 3$ m/s, $F = (0.012 \pm 0.003)h\Gamma/\lambda$, and $\Delta = 21^{+10}_{-4}$ m/s, all of which are reasonable. The value of v_0 is as expected as the lasers are locked to the central molecular velocity class. The value for Δ=21 m/s corresponds to a FWHM of the captured velocities of approximately 40 m/s. The intensity needed to power-broaden the linewidth of the transition in order to match this inferred capture velocity range is approximately $s_{\text{eff}} \approx 12$ which is higher than the intensity in the experiment. It is likely that the larger than expected velocity capture range is partly due to the frequency jitter on the cooling lasers but more importantly a consequence of the optical pumping of molecules into the $v'' = 2$ state which causes an effective broadening of the transition associated with the saturation of the number of scattered photons.

Consider now the F parameter. The maximum value of the force F is expected to be $P_{\text{ex}}\frac{h\Gamma}{\lambda}$ where P_{ex} is the probability of a molecule being in the excited state. Using the formula for excitation in a multi-level system from [55], taking an average value for the laser intensity and accounting for the small detunings of some frequencies from their ideal values, we find a value of $P_{\text{ex}} = 0.04$. However, for any duration of the laser cooling pulse, a fraction of the molecules are pumped into the $v'' = 2$ state, at which point the cooling/slowing stops. This is responsible for the lower average force that we infer.

The velocity profiles determined by the simple model can be fitted to a sum of two Gaussian functions to determine the final speed and temperature of the laser cooled molecules.

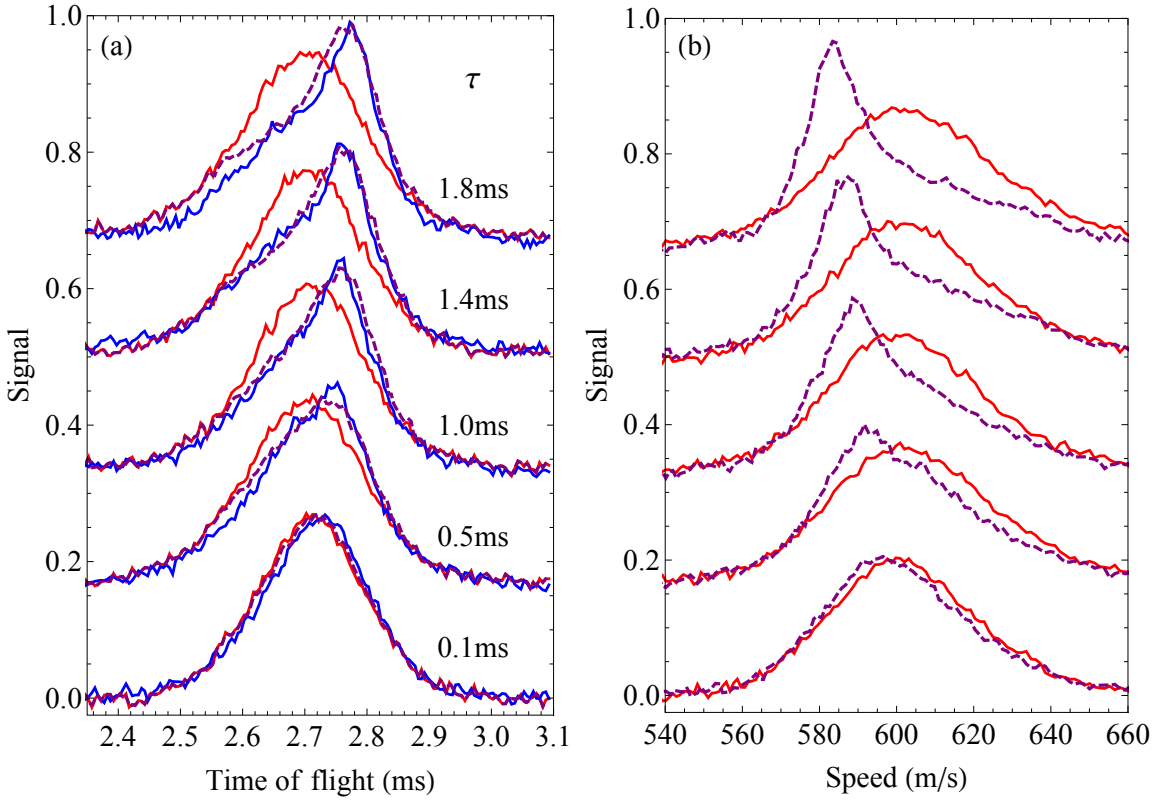

FIGURE 7.21: a) Solid lines - the experimentally measured ToF profiles before (red) and after (blue) a laser cooling pulse. Dashed lines - the best-fit ToF profiles predicted by a known initial velocity distribution and the simple model. b) Velocity profiles inferred from the measured ToF profiles in a) and the same simple model, with cooling off (solid red) and on (dashed purple).

Increasing the interaction time leads to slowing and narrowing of the velocity distribution of the molecules that have interacted with the laser light, as predicted by the numerical simulation. With increasing laser cooling time τ more molecules are piled at the lower velocity and the amplitude of the decelerated peak increases (figure 7.22) while its width gets narrower corresponding to lower temperatures (figure 7.23). After the longest laser cooling pulse, the forward velocity and temperature of the laser cooled molecules have been reduced to 583±2 m/s and 330±70 mK respectively.

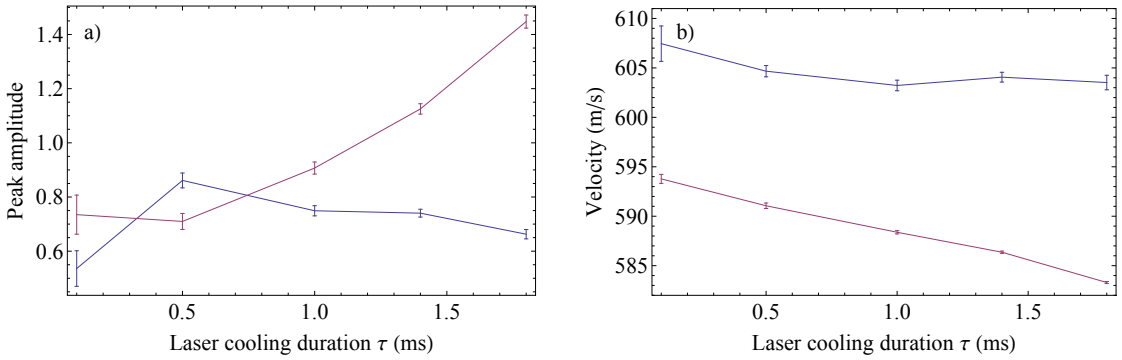

FIGURE 7.22: a) The amplitude of the uncooled Gaussian velocity distribution (blue) and the bunched peak (purple) after a laser cooling pulse of duration τ. b) The center velocity of the broad velocity distribution corresponding to the uncooled molecules (blue) and the laser-cooled bunch (purple) after the laser cooling pulse.

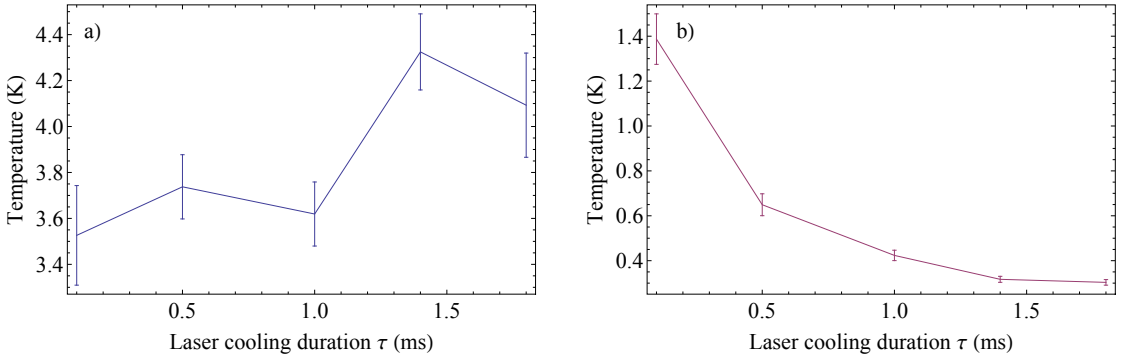

FIGURE 7.23: The temperature of the broader velocity distribution (a) and the laser cooled peak (b) after the laser cooling pulse.

7.6.4 Possible issues

We have demonstrated that the ToF profiles show a clear peak with molecules arriving in a narrower bunch and at a later time when the cooling is applied and that the peak is becoming more prominent when the cooling light is applied for a longer period. Our claim is that the observed effect on the measured ToF profiles is due to the laser cooling force. In principle, however, it is conceivable that a position rather than velocity dependent force focuses the molecules at the detector. Here we examine the possibility that either a non-laser-cooling force is at work or that some imperfection due to the design of the experiment leads to the observed effect on the measured ToF profiles. We reject both of these possibilities and conclude that the observed results are due to the expected laser cooling force.

7.6.4.1 Non-laser-cooling forces

The possibility of a position-dependent force was rejected on theoretical and experimental grounds. We have simulated the possible ToF profiles that would be generated by various

kinds of position-dependent forces but none of them was found to reproduce the bunching observed in the experiment. The only restriction we imposed on the conceivable forces that could be at action was that the maximum value of the force is determined by the maximum scattering rate. For example, a force which has the same form as the expected laser cooling force but is position dependent rather than velocity dependent was found to simply shift the whole ToF profile. In this case, the decelerated distribution is actually broader than the original one.

We also examined a variety of conspiratorial forces which turn on at different positions throughout the time of flight of the molecules. The only case in which a small bunching was observed was in the case where the force is zero throughout most of the time of flight and is turned on for a 2 cm region at z_{end} where it is very strongly peaked up to its maximum possible value (here z_{end} is the position of the molecules at the end of the laser cooling pulse). This worst case scenario does produce a small narrowing of the ToF profile, but it is far smaller than the narrowing we observe in the experiments.

The position-dependent force can also be rejected on experimental grounds. In the preliminary experiments described in section (7.5), the depth and the width of the hole due to the optical pumping of molecules into $v'' = 1$ agrees very well with the model and is a direct verification of the velocity-dependent scattering force. In addition to this, we have tried varying the position at which the v_{00} pulse is turned on to examine if there is some dependence of the scattering force on the position along the beam line. We found that there was none.

7.6.4.2 Possible focusing due to the experimental design and imperfections

We have also investigated the possibility that the convergence of the laser cooling beams focuses the molecular beam longitudinally by applying a force which is stronger at the back of the molecular pulse. This possibility was also rejected for the following reasons. The size of the molecular packet, for example in the middle of the vacuum chamber, is approximately 10 cm. The intensity at the back of the molecular pulse is approximately 20% highrer than the one at the front of the pusle. Thus, the molecules at the back of the pulse always experience a slightly higher scattering force. However, the change in arrival time corresponding to that force gradient for a laser cooling pulse of duration 1 ms and $s_{\text{eff}} = 1$ is only 6 μs so this effect is not enough to explain the bunching of the ToF profile.

We also explored the possibility that some misalignment of the laser cooling beams (e.g. not perfectly overlapped hyperfine frequency components or misalignment between the laser beams and the molecular beam) causes the molecules at the front of the molecular pulse to experience a higher force than the molecules at the back of the pulse. Because all molecules travel through the light pulse, the only difference in the force experienced by the molecules

is due to the spatial extent of the molecular packet at the beginning and at the end of the light pulse. Suppose that the force varies across the molecular packet linearly with position with a gradient of $\frac{\mathrm{d}F}{\mathrm{d}z}$, and that the molecular packet has a length of l_1 and l_2 respectively at the beginning and the end of the laser cooling pulse. Suppose next that the light is turned on when the center of the molecular pulse is at $z = 0$. The molecules at the head/back of the pulse experience a force $F_0 \pm \frac{\mathrm{d}F}{\mathrm{d}z}\frac{l_1}{2}$ at the beginning and $F_0 + \frac{\mathrm{d}F}{\mathrm{d}z}(L_{\mathrm{on}} \pm \frac{l_2}{2})$ at the end, where F_0 is the force at $z = 0$ and L_{on} is the distance traveled during the time the pulse is on. The average force that acts is $F_0 + \frac{\mathrm{d}F}{\mathrm{d}z}\frac{L_{\mathrm{on}}}{2} \pm \frac{\mathrm{d}F}{\mathrm{d}z}\frac{(l_1+l_2)}{2}$ while the difference in the average applied force is $\frac{\mathrm{d}F}{\mathrm{d}z}\frac{(l_1+l_2)}{2}$. We can place an upper limit to the value of the force gradient: $\frac{\mathrm{d}F}{\mathrm{d}z} \leq \frac{F_{\mathrm{max}}}{D}$ where $F_{\mathrm{max}} = \frac{h}{\lambda}\frac{\Gamma}{7}$ is the maximum possible scattering force in the multi-level system and D is the distance traveled during the longest duration of the laser cooling pulse. The length of the pulse is never more than 10% of the distance from the source, so $(l_1 + l_2)/2 < D/20$ which puts an upper limit to the mean difference in applied force of $\Delta F < F_{\mathrm{max}}/20$. If this difference is applied for the entire duration, the upper limit to the mean change in speed between the front and back of the pulse is 7 $\mathrm{m\,s^{-1}}$. If we take this to occur in the middle of the machine, so that the beam has a further 0.8 m to travel at a mean speed of 600 $\mathrm{m\,s^{-1}}$, then we get an upper limit to the reduction in the spread of arrival times which is 16 μs. This is a very small change and cannot be responsible for the observed peaks in the ToF profiles.

7.6.5 The phase-space distribution

For many application of cold molecules the phase-space density of the sample is important. In figure (7.24 a) we show the phase-space distribution of the molecules after laser cooling of 1.8 ms. We consider the scattering force expected from the rate equation model and the force inferred from the measured ToF profiles as described in section (7.6.3). In the latter case we have made the assumption that the force has acted throughout the entire duration of the laser cooling pulse.

The ideal scattering force predicted by the rate equation model produces a significant bunching in the phase-space density as expected. The force inferred by the simple model characterized by $F = 0.012\frac{h\Gamma}{\lambda}$ compresses the phase-space distribution only modestly. However, the molecules detected in the $v'' = 0$ state have most likely been exposed to a slightly stronger force characterized by the parameter $F = 0.04\frac{h\Gamma}{\lambda}$ which leads to a more significant compression of the phase-space density.

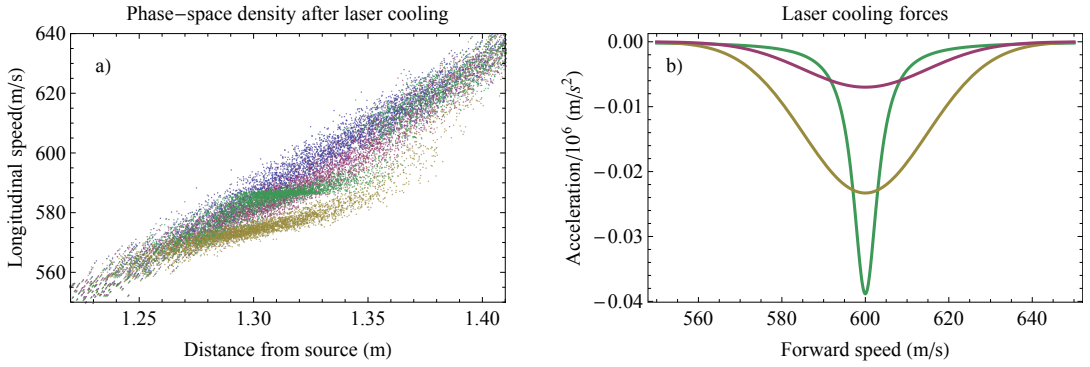

FIGURE 7.24: a) The longitudinal phase-space density of the molecular packet after laser cooling of 1.8 ms. Blue - the unperturbed molecular packet, purple - light force inferred from the the simple model with $F = 0.012\frac{h\Gamma}{\lambda}$, yellow - light force with $F = 0.04\frac{h\Gamma}{\lambda}$ and green - effective scattering force as determined by the rate equations model. b) The acceleration due to the three forces in a).

7.7 The frequency chirp

As a molecule scatters more and more photons, its velocity is reduced and it eventually gets shifted out of resonance with the cooling beams. This causes the scattering rate to decrease. For example, if $s_{\text{eff}} = 0.5$ a reduction of the velocity of 10 m/s leads to a 20% drop of the scattering rate. To ensure that the laser cooling/slowing is maximally efficient for the entire duration of the cooling pulse, we can chirp the frequency of the cooling lasers to higher values synchronously with the deceleration of the molecules to compensate for the change of Doppler shifts.
The Doppler shift between a molecule traveling at velocity v and the counter-propagating laser light is $f_{\text{D}} = -\frac{v}{\lambda}$. The change in Doppler shift per unit time can be expressed as:

$$\frac{\mathrm{d}f_{\text{D}}}{\mathrm{d}t} = \frac{hR_{\text{sc}}}{\lambda^2 m} \tag{7.1}$$

where R_{sc} is the scattering rate and we have used the fact that the change of velocity per unit time is $\frac{hR_{\text{sc}}}{\lambda m}$. The chirp that keeps the laser on resonance with the decelerating molecules is thus entirely determined by the scattering rate. The maximum scattering rate can be estimated as $R_{\text{sc}} = P_{\text{ex}}\Gamma$ where P_{ex} is the probability of being in the excited state and Γ is the excited state spontaneous decay rate. For $P_{\text{ex}} = 0.04$ the estimated chirp rate is $\frac{\mathrm{d}f_{\text{D}}}{\mathrm{d}t} = 38$ MHz/ms.

7.7.1 Frequency chirp - technical details

The frequency of the cooling lasers must be chirped by more than 50 MHz on a time scale of 1.8 ms. To implement this chirp, we use a broad-band AOM (AA Opto-Electronic MT 250-A0 1001, 5-VIS) with a center frequency of 250 MHz and a bandwidth of 100 MHz.
All laser cooling beams are combined and double-passed through the AOM in the so-called 'cat-eye' configuration. The schematic of the set-up is shown in figure (7.25). The AOM is positioned at the focal point of two 200 mm lenses. The incoming beam hits the first lens slightly above its center and is deflected downward as it passes through the AOM. The first diffracted order goes through the second lens and is retroreflected by a right-angle prism. The retroreflected beam is then modulated again through the AOM. The use of the two lenses and prism guarantees that the doubly-diffracted beam is anti-parallel to the incoming beam but vertically separated so that it can be picked off and sent to the experiment. When the AOM is driven at a frequency ω the total frequency shift in the double pass is $+2\omega$. The advantage of this set-up is that changing the AOM driving frequency ω does not cause spatial variation of the doubly-modulated beam.

The hardware control of the frequency chirp is shown in figure (7.26). A VCO, whose output is amplified and sent to the frequency chirp AOM, generates a frequency which is

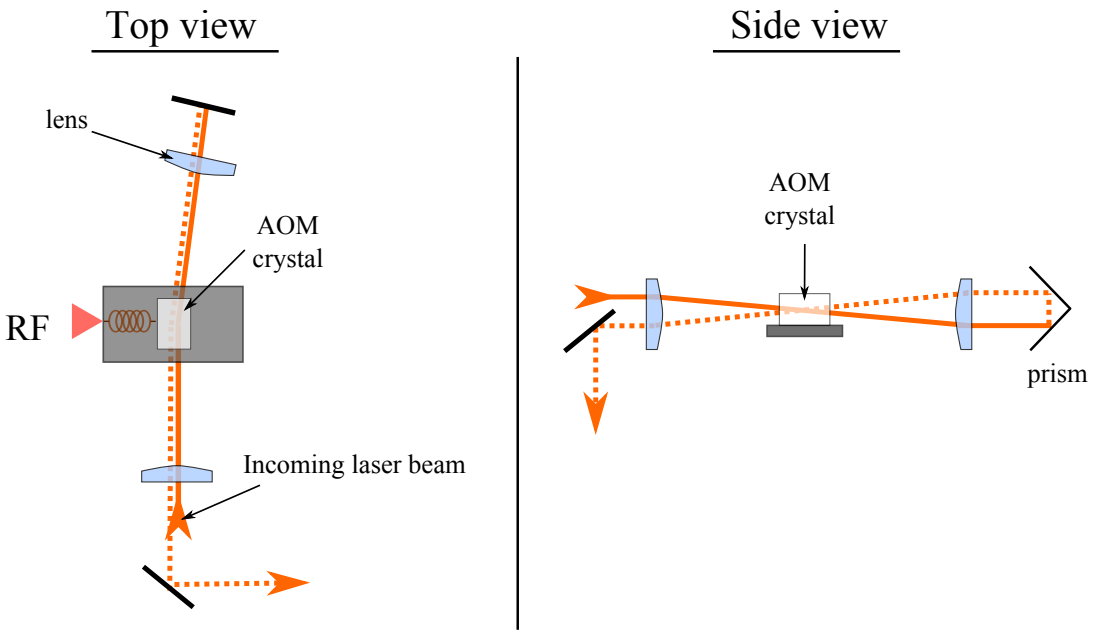

FIGURE 7.25: The top and side view of the optics for the frequency-chirp AOM in the cat-eye configuration.

linearly proportional to a given control voltage. The control voltage waveform is generated by TTi TG1010 Programmable 10 MHz function generator. The control voltage sent to the VCO is essentially a voltage ramp which is latched to its final value at the end of the cooling pulse. This latching ensures that the v_{10} repump is on resonance with the molecules that have been slowed down the most during the laser cooling pulse. The function generator

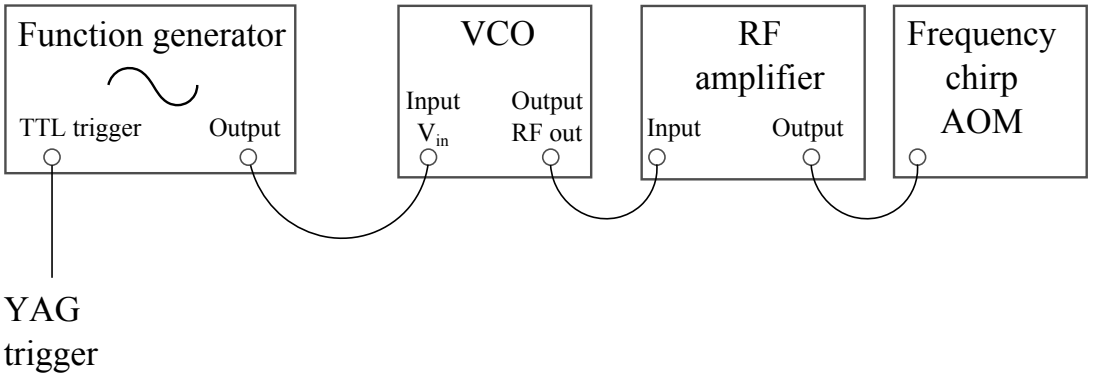

FIGURE 7.26: The hardware control of the frequency-chirping AOM.

pattern is triggered by the same TTL pulse which triggers the ablating YAG laser.
In the experiment we vary the chirp rate from 0 to 30 MHz/ms to see the effect on the detected ToF profiles. The chirp rate is selected by manually changing the slope of the

voltage ramp from the function generator box. Figure (7.27) shows the frequency-chirp pattern for the example case of chirp rate of 20 MHz/ms.

The chirping AOM efficiency is optimized for a driving frequency of 225 MHz. The AOM

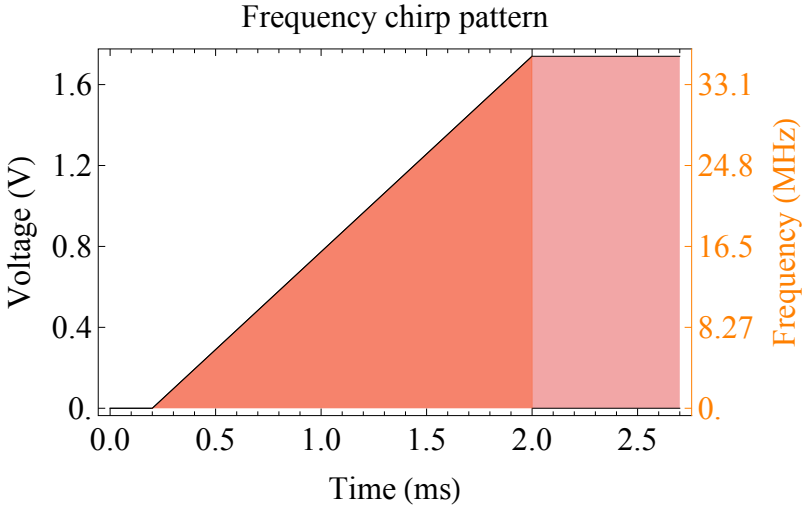

FIGURE 7.27: The frequency-chirp pattern for 20 MHz/ms chirp rate. The black line shows the control voltage sent to the VCO. The v_{00} light (yellow) is applied for 1.8 ms, while v_{10} repump (red) stays on for the whole duration of the experiment. The right-hand axis is the frequency shift corresponding to the given control voltage.

efficiency for this frequency in single and double pass is 80% and 64% respectively. When the AOM rf frequency is chirped this efficiency drops slightly as shown in figure (7.28). However, the corresponding change in intensity is small enough to not be a problem.

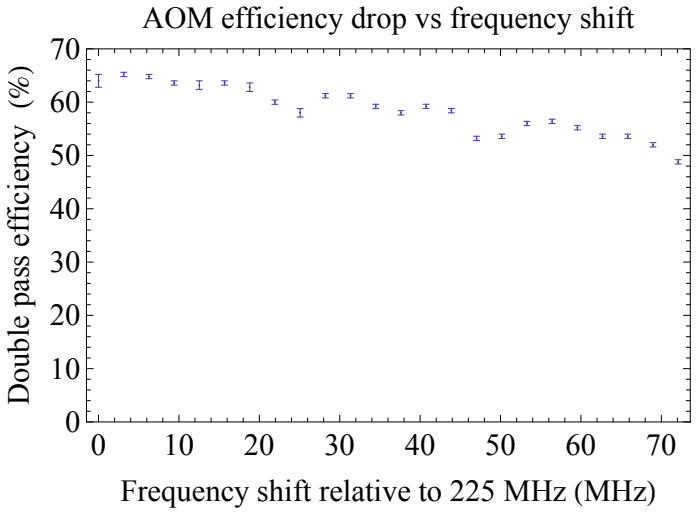

FIGURE 7.28: The drop of the frequency-chirp AOM efficiency with driving rf frequency.

7.7.2 Effect of the frequency chirp on the ToF profiles

In the frequency chirp experiments we fix the cooling pulse duration to $\tau = 1.8$ ms and apply the chirp rate β varying from 0 to 30 MHz/ms. For each value of β, we probe the molecules in the $v'' = 0, 1, 2$ states.

We note that chirping the lasers at a rate higher than $\frac{\mathrm{d}f_{\mathrm{D}}}{\mathrm{d}t}$ will cause a drop of the scattering rate. The problem is that first, we do not know exactly what the scattering rate is and second, the scattering rate drops with the intensity of the divergent cooling beams. It is thus useful to get both an upper and a lower limit for the scattering rate and make sure that the chirping rates we apply in the experiment do enhance the cooling. As an upper limit we can take the scattering rate given by the rate equations model for the variable intensity in the experiment. As a lower limit we can use the scattering rate as suggested by the simple model in section (7.6.3). We find that the experimental chirp rates increase the scattering in both cases. The reader is referred to appendix D for more details.

7.7.2.1 The ToF profiles in the $v'' = 0$ state

Figure (7.29 a) shows the experimentally measured and simulated ToF profiles of the molecules detected in the $v'' = 0$ state after laser cooling of duration $\tau = 1.8$ ms and applied chirp rates of $\beta = 0, 10, 20, 30$ MHz/ms. As the chirping rate is increased in the experiment, the peak corresponding to the decelerated molecules is shifted to later times: from 2788 μs for $\beta = 0$ to 2835 μs for $\beta = 30$ MHz/ms. This suggests that the number of scattered photons has increased from approximately 1500 for $\beta = 0$ to 2500 for $\beta = 30$ MHz/ms.

There are some features of the experimental ToF profiles that are worth examining in detail. First, the amplitude of the decelerated peak decreases with increasing β and for $\beta = 30$ MHz/ms it is reduced by 56% of its value for $\beta = 0$. This decrease is expected as only a small fraction of the molecules are scattering at the fastest rate. Second, the hole in the middle of the ToF profiles, which corresponds to the depleted molecules that have interacted with the laser light, gets broader with increasing β: the FWHM of the hole is approximately 67, 78, 93 and 99 μs for $\beta = 0, 10, 20, 30$ MHz/ms. In addition, the position of the centre of the hole shifts by approximately 10$\pm$3 μs per increase of β of 10 MHz/ms. The reason for this is that the chirped laser light interacts with a broader range of molecules compared to the fixed-frequency case. Third, consider the shoulder to the left of the hole in the ToF profiles. This shoulder corresponds to the molecules that are slightly faster than the central velocity class and scatter at a slower rate. The height of the shoulder increases with β and for $\beta = 30$ MHz/ms it has increased by 15% of its value for $\beta = 0$. The reason for this increase is that the chirped lasers shift even further out of resonance with these faster molecules which are less likely to be optically pumped.

The overall shape of the measured ToF profiles is very well reproduced in the model for all

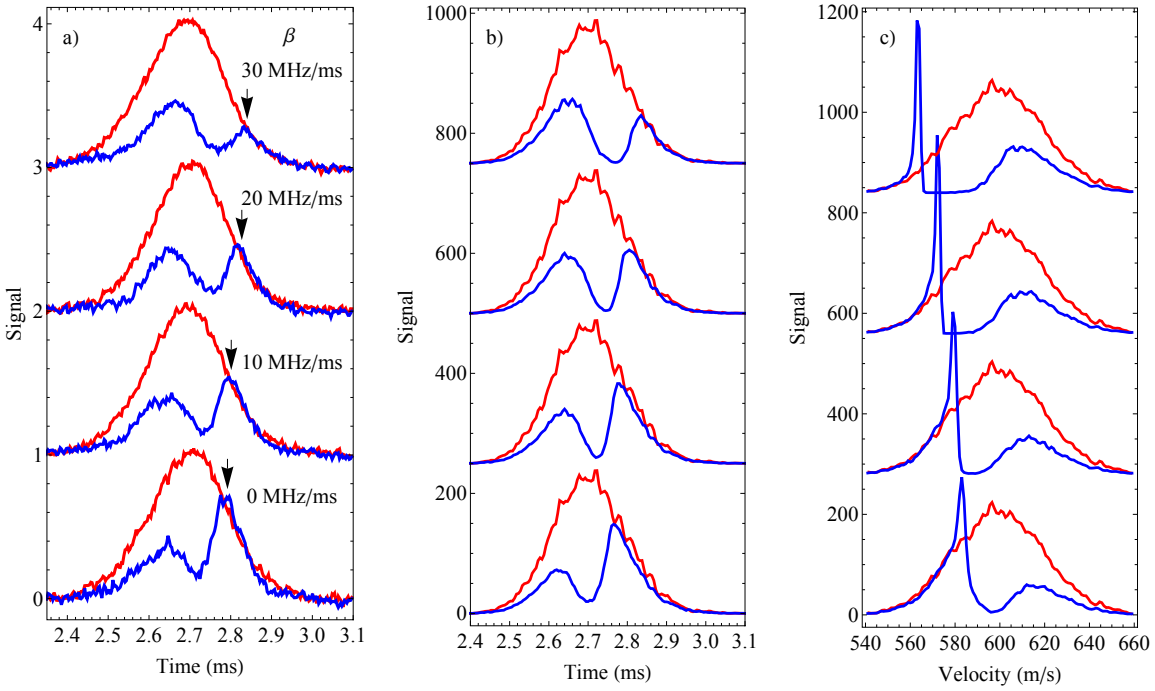

FIGURE 7.29: a) The measured ToF profiles of the molecules detected in the $v'' = 0$ state after 1.8 ms of laser cooling and a chirp rate of β =0, 10, 20 and 30 MHz/ms. The arrow indicates the peak corresponding to the slowed molecules decelerated to later times with increasing β. b) The simulated ToF profiles. c) The velocity profiles as predicted by the simulation.

values of β as shown in figure (7.29 b). The depth of the hole is deeper in the simulation but this is expected in light of the results in section (7.6.2) - this is most likely due to the lower scattering rate in the experiment. The position of the decelerated peak in the model agrees with the experimental results to within a few μs. Both the decrease of the decelerated peak height and the increase of the shoulder height is reproduced by the model, although to a greater extent than we observe in the experiment - the predicted decrease and increase are by -45% and 62% respectively. This again suggests that the scattering rate in the experiment is lower.

Figure (7.29 c) shows the simulated velocity profiles of the molecules detected in the $v'' = 0$ state. The frequency chirp has a dramatic effect - the molecules that have interacted with the lasers have been decelerated from 583 m/s for $\beta = 0$ to 562 m/s for $\beta = 30$ MHz/ms. In addition, the velocity spread of the slowed molecules has been considerably compressed. Figure (7.30) shows the experimental and simulated ToF profiles of the molecules in the individual hyperfine states of the $v'' = 0$ manifold. The agreement is very good with the only significant difference that the molecules in the experiment are less efficiently pumped

out of the $(J = 3/2, F = 1)$ state. The experimental ToF profile for that state shows a peak at approximately 2670 μs which is higher than predicted by the simulation by a factor of 2, 1.9 and 1.7 for $\beta = 10, 20$ and 30 MHz/ms respectively. This peak corresponds to the fast molecules that fall out of the cooling cycle as the cooling light is chirped. A possible explanation for the higher peak in the experiment is that since the $(J = 3/2, F = 1)$ frequency is addressed by a separate laser beam, some misalignment with the other frequency components when the light is chirped might cause the molecules in that state to scatter at a lower rate.

The simulation also suggests a more pronounced peak corresponding to the slowed/laser cooled molecules in the $(J = 1/2, 1)$ state than we observe in the experiment.

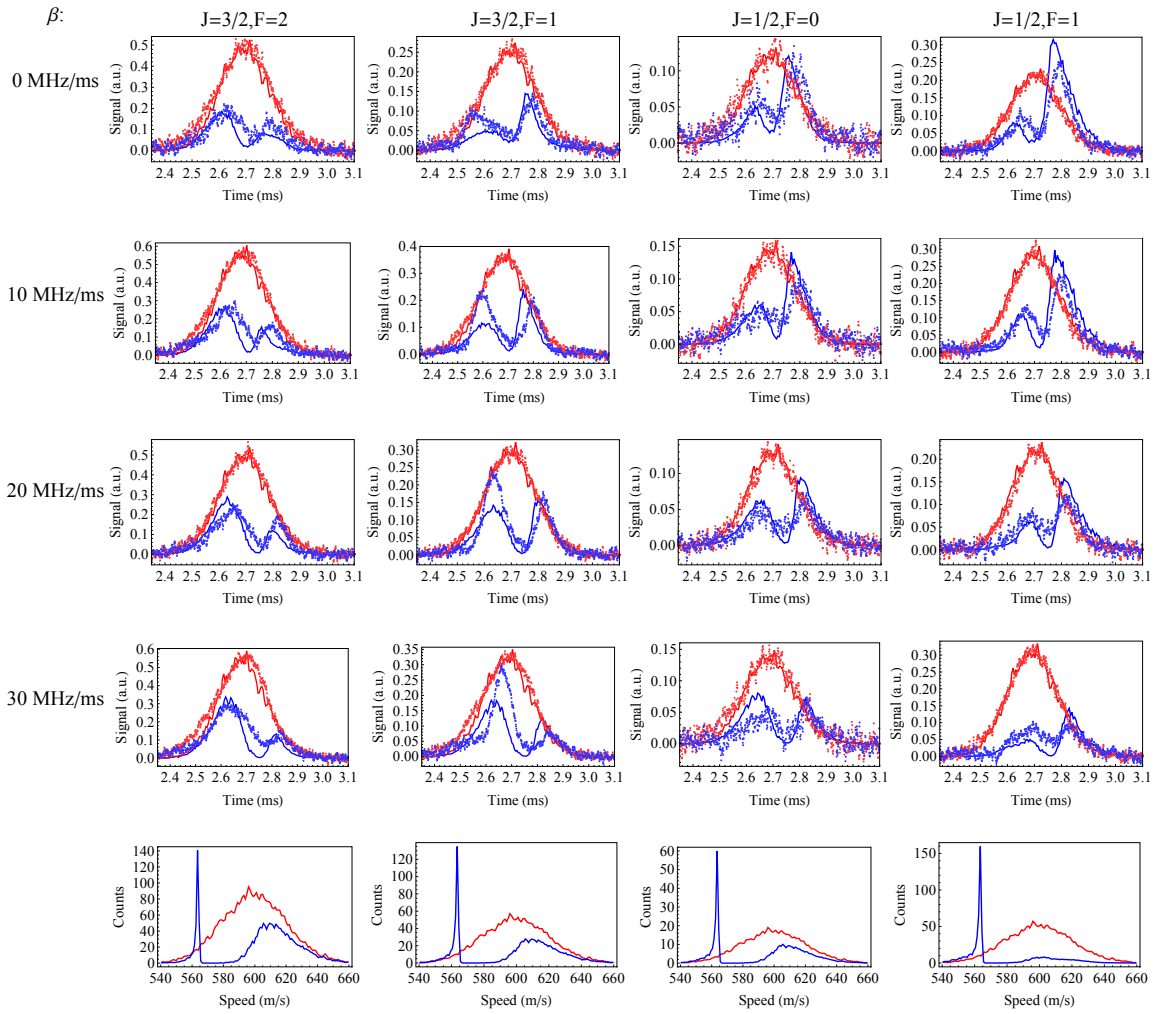

FIGURE 7.30: The ToF profiles of the molecules in the different hyperfine levels of the $v'' = 0$ state after laser cooling with applied chirp rate β=0, 10, 20 and 30 MHz/ms. Points - experiment, solid lines - simulation. The bottom row shows the predicted by the simulation velocity profiles for β =30 MHz/ms.

7.7.2.2 The ToF profiles in the $v'' = 2$ state

Figure (7.31 a) and (7.31 b) shows the experimentally measured and simulated ToF profiles of the molecules in the $v'' = 2$ state after a laser cooling with applied chirp β. As the chirping rate β is increased, the ToF profiles of the molecules detected in the $v'' = 2$ state become more asymmetric with the peak corresponding to the slowed molecules shifted from 2740±5 μs for $\beta = 0$ to 2788±5 μs for $\beta = 30$ MHz/ms, as shown in figure (7.31). The reason for this is that the chirping enhances the cooling and when molecules fall out of the $X(v = 0, 1) \leftrightarrow A(v' = 0)$ cooling cycle, their velocity is further reduced compared to the non-chirping case.

The simulated ToF profiles match the shape of the experimentally measured ones very well. The position of the peak in the modeled ToF profiles agrees with the experimental observation to within 10 μs. There is, however, one significant difference. In the model the number of molecules pumped into the $v'' = 2$ state increases gradually with chirp rate and for β =30 MHz/ms the increase reaches 17%. This effect is expected as with higher chirp rates applied the molecules scatter more and more photons and have a higher probability of decaying to the $v'' = 2$ state. In the experiment, on the other hand, we observe a gradual loss of molecules with increasing chirp rate and for $\beta = 30$ MHz/ms the observed loss is 32%. Currently, we do not know what is the cause of the loss of the molecules from that state in the experiment.

Figure (7.31 c) shows the modeled velocity profiles in the molecules in the $v'' = 2$ state. Chirping the laser light does not lead to cooling in that state but it does create slower molecules.

It is useful to show the $v'' = 0$ and $v'' = 2$ ToF profiles on the same scale to highlight the agreement between the data and the model (figure (7.32)). Despite the apparent loss of slowed molecules from the $v'' = 2$ state in the experiment, the overall features of the measured ToF profiles in the two vibrational manifolds agree very well with the modeled ones. It is clear that the deceleration of the molecules detected in both the $v'' = 0$ and $v'' = 2$ states with respect to the central arrival of the uncooled ToF profile (dashed line in figure (7.32)) increases with chirp rate.

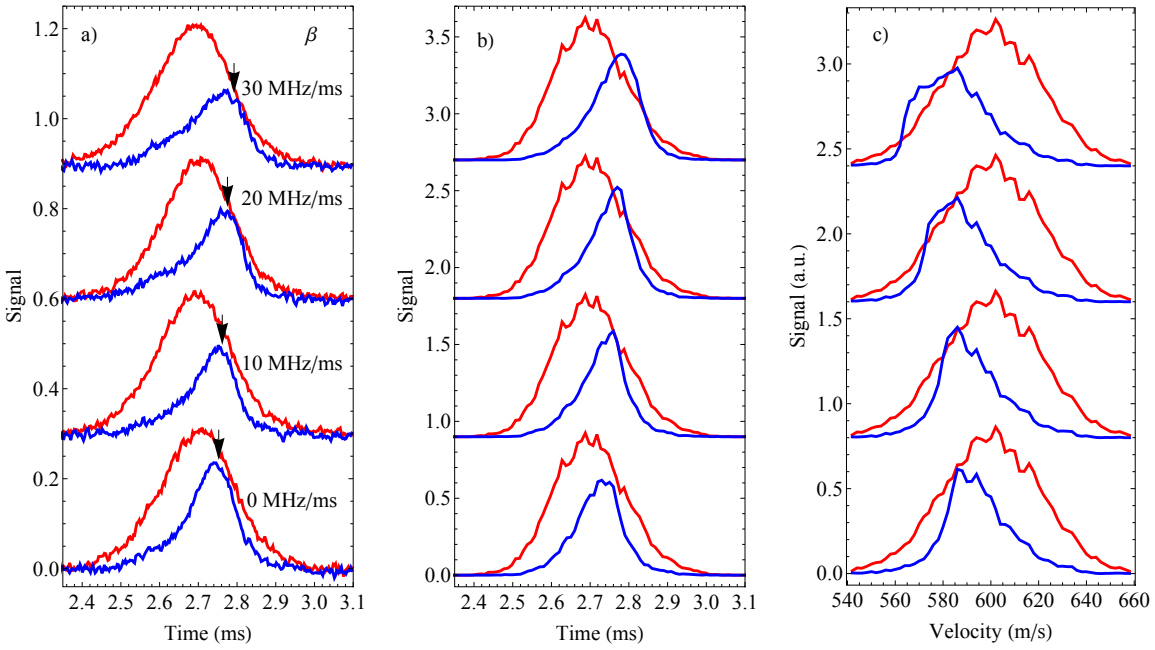

FIGURE 7.31: The measured (a) and simulated (b) ToF profiles of the molecules detected in the $v'' = 2$ state after a laser cooling pulse of 1.8 ms and chirp rate β (blue) compared to the uncooled ToF profile in the $v = 0$ state (red). The arrow indicates the peak corresponding to the slowed molecules which is shifted to later times with increasing β. c) The velocity profiles predicted by the simulation.

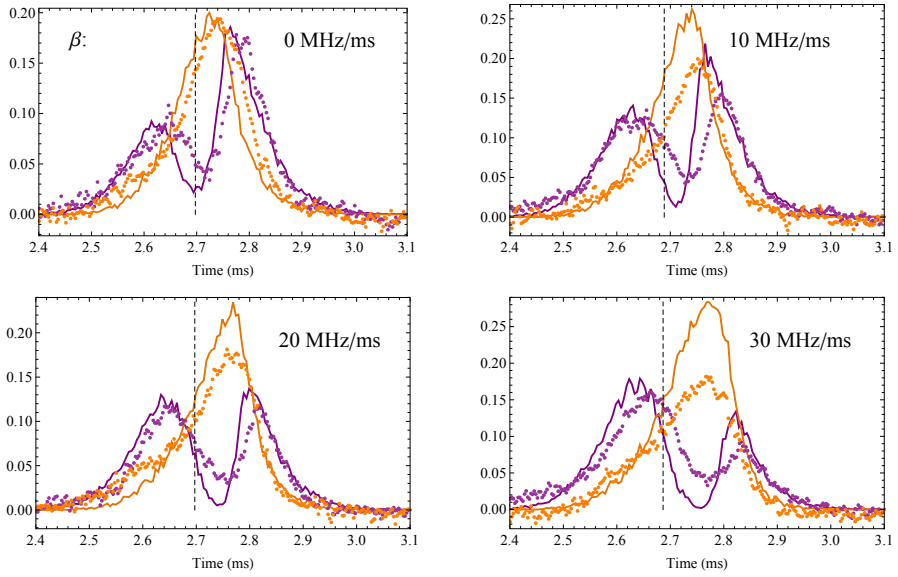

FIGURE 7.32: The ToF profiles of the molecules detected in the $v'' = 0$ state (purple) and $v'' = 2$ state (orange) after a laser cooling pulse chirped at a rate β. Points - experiment, solid lines - model. The dashed line indicates the central arrival time for the uncooled molecules.

7.7.2.3 Molecular population in the $v'' = 1$ state

When the chirp is applied, both the v_{00} and v_{10} lasers follow a particular class of decelerating molecules. Without the frequency chirp there is no population in the $X(N = 1, v = 1)$ state both on the 'on' and 'off' shots of the experiment. However, when the chirp is applied, some residual population is left behind in that state. This is because the un-decelerated molecules are further from resonance with the v_{10} light when it is chirped, and so the final stage of optical pumping is less effective.

Figure (7.33 a) shows an example spectrum over the $A - X(1 - 1)$ transition for the four chirp rates β. When the chirp is applied the first two hyperfine states in that vibrational manifold are populated. The population in that state does not seem to increase significantly with chirp rate. However, we note that there is no population in the $X(v = 1)$ state on the 'off' shots and the signal cannot be normalized to eliminate the fluctuations of the source. The molecules detected in the $v'' = 1$ state in the experiment have central arrival time of approximately 2660±20 μs (figure (7.33 b)) - slightly earlier than the central arrival time of the uncooled molecules. This is expected as the chirped laser frequencies interact with the slower molecules.

Figure (7.34) shows the experimental and simulated ToF profiles of the molecules de-

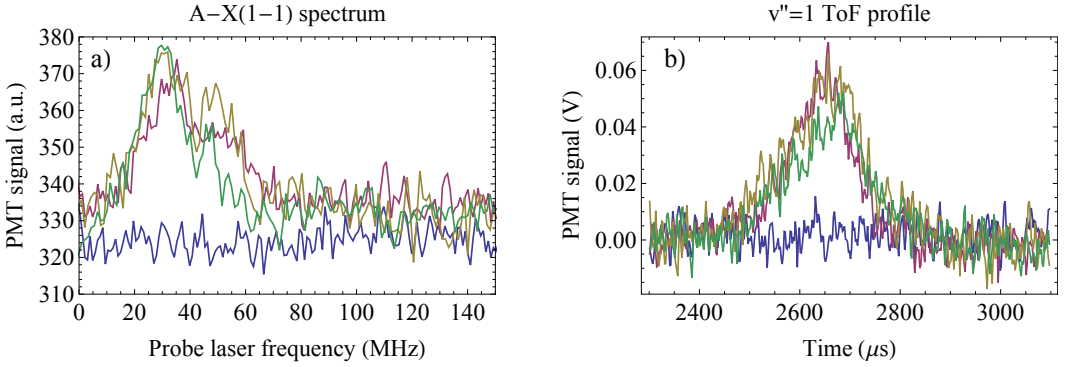

FIGURE 7.33: Scan over the $A-X(1-1)$ transition (a) and the corresponding ToF profiles (b) of the molecules detected in the $v'' = 1$ state after a laser cooling pulse with chirp rate β of 0 (blue), 10 (purple), 20 (green) and 30 (yellow) MHz/ms.

tected in the $v'' = 0, 1, 2$ vibrational manifolds for chirp rates of 10 and 30 MHz/ms. The simulation suggests that the molecules in the $v'' = 1$ state have a mean arrival time of approximately 2.6 ms - slightly earlier than in the experiment. In addition to that, in the experiment a higher fraction of molecules is pumped into the $v'' = 1$ state than predicted by the model.

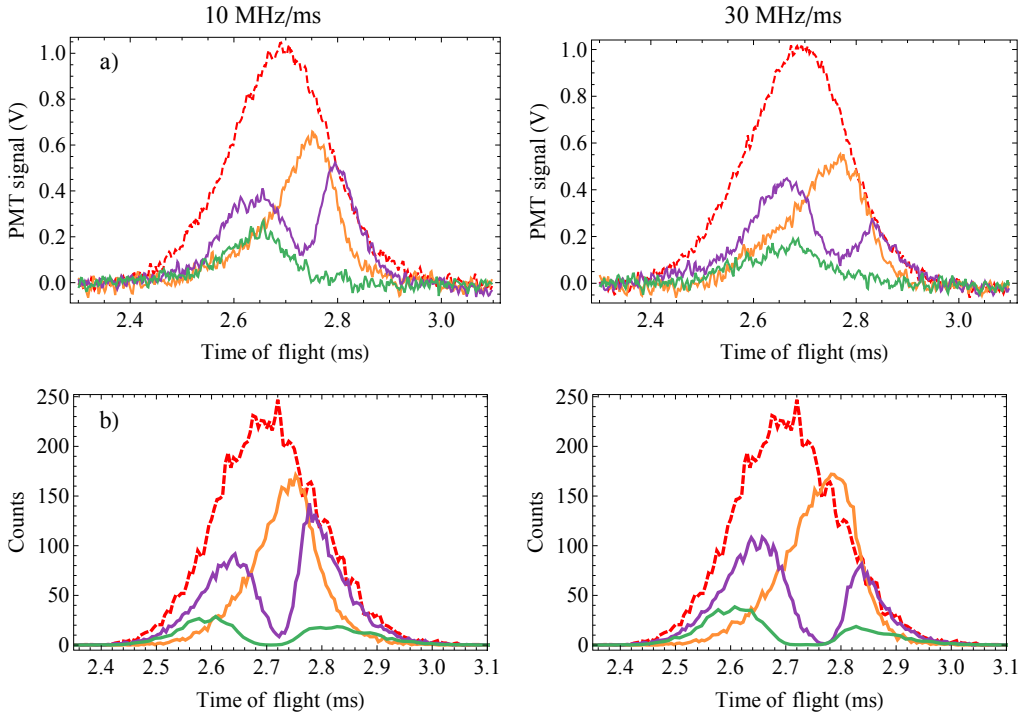

FIGURE 7.34: The ToF profiles of the uncooled molecules in the $v = 0$ state (dashed red line) and the laser-cooled molecules detected in the $v'' = 0$ state (purple), $v'' = 2$ state (orange) and $v'' = 1$ state (green) after the laser cooling pulse and frequency chirp of 10 and 30 MHz/ms. a) Experiment. b) Simulation.

Table (7.2) shows the fraction of molecules detected in the $v'' = 0, 1, 2$ states after the laser cooling pulse. The fraction of molecules detected in the $v'' = 0$ state with increasing β is slightly higher in the model, but this is consistent with the results so far. In the experiment a larger fraction of molecules are left in the $v'' = 1$ state, which can be only partially explained by the drop of v_{10} light intensity with increasing β. In addition, in the experiment we observe a loss of molecules from the $v'' = 2$ state which cannot be explained only by variations in the source flux.

Chirp rate β (MHz/ms):	0	10	20	30
Model				
v"=0	0.459	0.452	0.428	0.398
v"=1	0.0981	0.0974	0.0941	0.0829
v"=2	0.437	0.444	0.471	0.512
Total:	1	1	1	1
Experiment				
v"=0	0.4895	0.4773	0.4341	0.4156
v"=1	0	0.149	0.151	0.124
v"=2	0.364	0.311	0.33	0.31
Total:	0.836	0.877	0.864	0.818

TABLE 7.2: The fraction of molecules detected in the $v'' = 0, 1, 2$ vibrational manifolds after a 1.8 ms laser cooling pulse and chirp β.

7.7.2.4 The ToF profiles summed over all vibrational states

Finally, in figure (7.35) we present the sum of the ToF profiles in all vibrational manifolds after the laser cooling with applied chirp β. The deceleration predicted by the model (indicated by the dashed line) is matched in the experiment. The model predicts that the

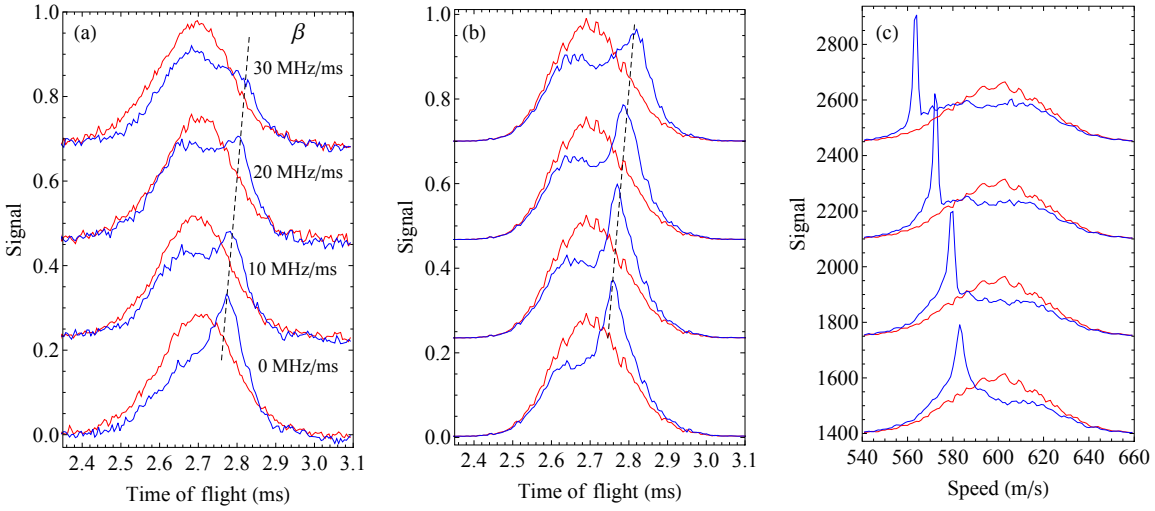

FIGURE 7.35: The sum of the ToF profiles of the molecules detected in the $v'' = 0, 1, 2$ vibrational manifolds before (red) and after (blue) a laser cooling with chirp β. The dashed line indicates the decelerated peak a) Experiment. b) Simulation. c) Velocity profiles taken from the simulation.

laser cooled molecules have been decelerated from 582 m/s for $\beta = 0$ to 562 m/s for β =30 MHz/ms. In addition, the final temperature for the highest chirp rate has been reduced to 7 mK.

Chirping the cooling frequency has a significant effect on the detected ToF profiles, with the deceleration exactly as predicted by the simulation. The only problem is the loss of molecules in the experiment with increasing chirp rate, particularly from the $v'' = 2$ state. Because of this loss, fitting the sum of the measured ToF profiles in the three vibrational states to infer the velocity distribution as described in section (7.6.3) does not give meaningful results.

Currently, we do not know what causes the observed loss of molecules with increasing chirp. Applying chirp rates higher than 30 MHz/ms in the experiments (the highest chirp rate that we tried was 40 MHz/ms) led to further loss of molecules but not appreciable further deceleration.

7.7.2.5 The phase-space density

The molecules that have been detected in the $v'' = 0$ states have experienced the maximum laser cooling force as they have stayed in the cooling cycle throughout the whole laser cooling pulse. We can include an extra time-dependent term in the expression for the scattering force to account for the frequency chirp. The phase-space distribution of the molecules for the three chirp rates β following the action of the force predicted by the rate equations is shown in figure (7.36 a). Increasing the chirp rate significantly compresses the longitudinal velocity spread of the molecules. This velocity bunching can be beneficial for loading a Stark decelerator as suggested in [93].

The phase-space compression in (7.36 a) is the maximum compression that can be achieved. The actual laser cooling force acting in the experiment is most likely weaker as the scattering rate is lower. Figure (7.36 b) shows the phase-space distribution for the force inferred from the measured ToF profiles with $F = 0.04h\Gamma/\lambda$. Although this force leads to a further deceleration reaching a final mean forward speed of approximately 560 m/s for $\beta = 30$ MHz/ms, there is no significant increase in the phase-space density with increasing β.

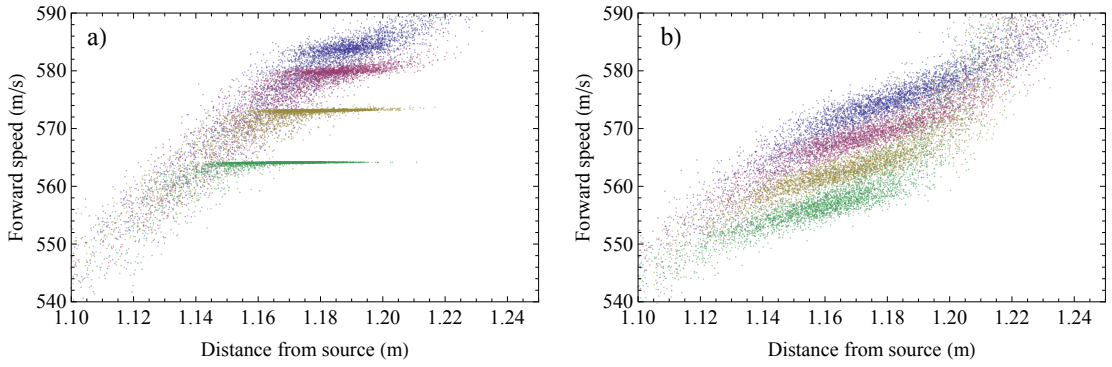

FIGURE 7.36: The phase-space density at the end of the laser cooling pulse for β =0 (blue), 10 (purple), 20 (yellow) and 30 (green) MHz/ms. a) Force as predicted by the rate equations model. b) Force inferred from the measured ToF profiles characterized by $F = 0.04h\Gamma/\lambda$.

7.7.3 Effect of the spontaneous emission

After each emission of a photon, the molecule makes a random walk in momentum space of size $\hbar k$. This random walk introduces heating to the sample proportional to the square of the number of photons scattered. According to the random-walk theory, after the emission of N photons, the mean square momentum along a given dimension is $\langle p_x^2 \rangle = \hbar^2 k^2 N$ [199] with a corresponding spread of velocity of $\langle v_x \rangle = \sqrt{N}\frac{\hbar k}{m}$.
In the longitudinal laser cooling experiment heating of the molecular beam in the transverse direction can cause the beam to diverge and because of that fewer molecules will be detected. This heating was found to be the dominant mechanism for loss of molecules in the longitudinal radiation pressure slowing of SrF [200] because of the high number of photons scattered ($\gtrsim 10^4$) and low starting velocities ($\sim$140 m/s). However, in the laser cooling of CaF experiment described in this thesis this heating is not significant and cannot explain the observed loss of molecules in the frequency-chirp experiments. If we assume that the number of photons scattered in the experiment is $N = 2000$, then $\langle v_x \rangle \approx$0.5 m/s. Since the mean time of flight of the molecules is $\sim$2.7 ms, the increase of the spread of transverse positions at the detector is only $\approx$1 mm.

7.8 Conclusion

We have demonstrated longitudinal slowing and cooling of a supersonic beam of CaF radicals using the quasi-closed vibrational and closed rotational $X(N = 1, v = 0, 1) \leftrightarrow A(J = 1/2, v' = 0)$ cycling transition. The molecules that have interacted with the lasers are decelerated by approximately 20 m/s and cooled to 330 mK from an initial temperature of $\approx$ 3.5 K when the cooling light of fixed frequency is applied for 1.8 ms. With chirping the deceleration was roughly doubled. Comparison with the detailed numerical model shows that the deceleration is well understood, as is the optical pumping into the $v'' = 2$ state state, while the cooling is not quite as strong in the experiment as predicted.
We compared the measured ToF profiles of molecules to the ones predicted by the numerical simulation and in all cases the agreement is very good. However in the chirping experiments there is a loss of the slowed molecules with increasing chirp rate, particularly in the molecules detected in the $v'' = 2$ state. This loss needs to be investigated in future experiments.

Chapter 8

Conclusions and future directions

In this thesis I presented work on longitudinal laser cooling and slowing of a supersonic beam of CaF molecules. The observed enhancement of the molecular fluorescence when the transition is closed only rotationally was found to be in good agreement with the prediction of a rate equations model describing the evolution of the molecular population in the multi-level system. When the vibrational repump is added so that the molecules are scattering photons on the $X(N = 1, v = 0, 1) \leftrightarrow A(J' = 1/2, v' = 0)$ transition, each molecule can scatter more than a thousand photons which is enough to demonstrate a measurable laser cooling and slowing effect. We demonstrated longitudinal laser cooling in which the resonant class of molecules is slowed from an initial speed of 600 $\mathrm{m\,s^{-1}}$ to a final speed of 580 $\mathrm{m\,s^{-1}}$, and the spread of forward velocities was reduced from a temperature of 3 K down to 300 mK. By applying a frequency chirp to keep the lasers on resonance with the decelerating molecules, we were able to double the deceleration. The effectiveness of the laser cooling was limited by the optical pumping of the molecules into the $X(v'' = 2)$ state. The results are very encouraging in light of the fact that we have only used one vibrational repump laser and given the high starting velocity of the molecular beam.
Calcium fluoride may prove to be an attractive candidate to investigate the properties of polar diatomic molecules such as the long-range dipole-dipole interactions. Laser cooling of CaF has proven to be a fruitful project which has demonstrated good results and also opened up many possibilities for future work.

8.1 The future of laser cooling CaF

8.1.1 Solid state laser system

The first improvement that needs to be done to the experiment is to replace the existing dye laser system with a solid state one. Due to recent advances in solid state frequency-doubled fiber lasers it is now possible to buy a laser that gives out more than 1 W of laser light at

606 nm (the wavelength of the main cooling transition). The vibrational repump dye laser at 628 nm, on the other hand, can be replaced by a home made diode system as described in [201].

8.1.2 Measurement of the velocity distribution

It would be beneficial to have a direct measurement of the velocity distribution of the molecules after the laser cooling. This would provide unequivocal information about the effect of the laser cooling and slowing that is demonstrated experimentally, without relying on any model to interpret the measured ToF profiles.

There are several ways to do such a velocity measurement. Perhaps the most straightforward way to analyze the velocity distribution of the molecules after the laser cooling is to scan the probe laser around the four hyperfine levels of the laser cooling transition while it is intersecting the molecular beam at an angle. In this way, the velocity distribution of the beam can be determined from the measured Doppler shift. This technique was used in the first experiments on laser cooling of atoms [16, 21]. In the laser cooling of CaF experiment, one can arrange the probe beam so that it is almost counter-propagating to the molecular beam so that the maximum Doppler shift is achieved. In such a geometry the difference in Doppler shifts of the molecules traveling at a velocity of 580 $\mathrm{m\,s^{-1}}$ and 600 $\mathrm{m\,s^{-1}}$ is of the order of 30 MHz which is enough to measure unambiguously. If the probe laser is scanned over the four hyperfine states of the laser cooling transition in the respective vibrational manifold, the newly produced slowed molecules will be removed from the original distribution and will exhibit a peak in the spectrum shifted to higher frequencies by about 30 MHz, similarly to the experiment described in [16]. Such a measurement would be relatively straightforward to do in the current experimental set-up, with only minor modifications to the existing apparatus.

Alternatively, it is possible to measure the velocity distribution of the molecules by detecting them with an ICCD camera [169] or by using two probe beams from the same probe laser which intersect the molecular beam perpendicularly at two PMT detection regions at different positions after the laser cooling is applied, as described in [202]. However, the latter method will most likely involve some complications due to the re-distribution of molecules among the four hyperfine levels following the interaction with the first probe beam.

8.1.3 Towards a CaF MOT

In order to ensure enough scattered photons for a significant reduction of the speed and temperature, the leak to the $X(v'' = 2)$ state must be eliminated. This can be done with a vibrational repump laser acting on the $X(v = 2) \rightarrow A(v' = 1)$ transition at 626.6 nm accessible by the same type of diode laser as the v_{10} repump laser. The second repump

laser will dramatically increase the number of photons scattered per molecule. If we use the Franck-Condon factors from section (3.2.3), plugging the leak to the $X(v'' = 2)$ state should increase the number of photons scattered to more than 3×10^5. However, the starting velocities of the supersonic source are too high to realize the scattering of this number of photons within a reasonable distance. Replacing the supersonic source with a buffer gas one would mean a much lower starting velocity of $\sim$140 $\mathrm{m\,s^{-1}}$ [71] allowing for a longer interaction time of 5 ms in only 1 m. With this interaction time even modest driving intensities of $s_{\mathrm{eff}} \approx 1$ per hyperfine transition would ensure enough scattering events to bring the molecules to rest. The molecular beam can be also simultaneously cooled in the transverse direction. The next step would be to capture the slowed molecules in a magneto-optical trap (MOT) in a scheme similar to the one described in Ref. [168].

8.1.4 Magnetic Sisyphus slowing

A particularly intriguing prospect is to apply Sisyphus type of slowing to CaF in a scheme similar to the one suggested by Comparat in [203]. The idea described in [203] is the following - the kinetic energy of a molecule can be modified by using external electric or magnetic fields. A so-called 'one-way' or irreversible step has to be included to avoid the reverse process which would otherwise heat the sample. For the scheme to work, two states which experience a different gain in potential energy in an external field must be coupled to each other, for example through an excited state.

In this Sisyphus cooling scheme the scattering of a single photon can remove a substantial amount of the molecular kinetic energy. Unlike the traditional laser cooling, based on photon momentum transfer in which a single scattering event reduces the temperature by a few μK, in the Sisyphus cooling an absorption-spontaneous emission step can reduce the temperature by a few mK. The technique promises to allow for a 1000-fold reduction in the temperature and, in some cases, a compression of the phase-space density by a factor of 10^7.

Comparat discusses Sisyphus cooling in the context of molecules in a magnetic or electric trap. However, the idea can be extended to more complex trapping potentials and can be applied during deceleration stages, similarly to the suggestion by Hudson in [204] but including a spontaneous emission step.

In the case of CaF, it is conceivable to use the counter-propagating laser cooling light together with a field pattern with alternating regions of high and low magnetic field to pump the molecules into a state which is always climbing a potential hill and thus considerably slow them down. If both the high and low magnetic field regions are high enough, the hyperfine structure in the ground $X^2\Sigma^+(N = 1, J = 1/2, 3/2)$ state becomes irrelevant as all magnetic sublevels evolve into one of two states whose projection onto the axis defined by the magnetic field is $M_S = \pm 1/2$. Each of these two states can be selectively coupled to

the excited $A^2\Pi_{1/2}(J' = 1/2)$ (which is insensitive to magnetic fields) by laser light which is resonant with each state for a different value of the magnetic field. For example, consider a sinusoidally varying magnetic field with a lowest value of 0.1 T and a highest value of 1 T. If the $M_S = -1/2$ state is shifted into resonance with the excited state for $B = 0.1$ T, the molecules will be pumped into the $M_S = 1/2$ state which experiences a gain of potential energy in the increasing magnetic field leading to a loss of kinetic energy. Near the top of the potential hill, the molecules in the $M_S = 1/2$ state are shifted into resonance with the excited state and pumped into the $M_S = -1/2$ state which experiences a potential hill as the value of the magnetic field decreases. The process can be repeated many times. The change of kinetic energy experienced per one cycle is $\Delta E = \mu_B \Delta B$ where μ_B is the Bohr magneton and ΔB is the difference in magnetic field at which the two states are resonant with the exited state. For $\Delta B = 0.9$ T, the change in energy experienced per Sisyphus slowing cycle is $\Delta E = 13$ GHz. If a buffer gas source is used the starting forward velocity of the CaF radicals is $\sim 140\ \mathrm{m\,s^{-1}}$ and the molecules can be brought to rest after scattering only ~ 100 photons.

This Sisyphus slowing scheme is particularly well suited to CaF due to its short excited state lifetime and highly diagonal Franck-Condon matrix. Although some details need to be further investigated - such as the exact magnetic field profile needed and a way to transversely confine the molecules as they slow down, this magnetic Sisyphus slower is quite promising. It should be relatively easy to realize the needed field pattern with permanent magnets. Due to the high amount of kinetic energy removed per photon scattered, not too many deceleration stages are needed. Once sufficiently slowed, the molecules can be captured in a MOT or a microwave trap as described below.

8.1.5 Different repump scheme

Recall that the scattering rate in a multi-level system is reduced compared to the two-level case due to the presence of many ground state levels connected to the same excited state. It might be beneficial to employ an alternative repump scheme so that the main cooling and repump lasers are not connected to the same excited state and thus improve the scattering rate. Instead of repumping the molecules on the $X(v = 1) \rightarrow A(v' = 0)$ transition, one can use a repump laser on the the $X(v = 1) \rightarrow B(v' = 0)$ transition at 531 nm [171]. This would increase the scattering rate from $\Gamma/7$ to $\Gamma/4$. When excited to the $B(v' = 0)$ state, a molecule can decay to either of the X or A states but decays to the A state are suppressed by approximately a factor of $\left(\frac{\omega_{BX}}{\omega_{BA}}\right)^3 \left(\frac{d_{BX}}{d_{BA}}\right)^2 \sim 10^4$ where ω_{ij} is the angular frequency of the transition and d_{ij} is the transition dipole moment (here we have used the calculated dipole moments from [205]). The FCFs for the $B - X$ transitions are particularly favorable with the $B - X(0 - 0)$ Franck-Condon factor of 0.9980. The FCFs for the three bands $A - X$, $B - X$ and $A - B$ calculated using the symplectic integrator [189] are presented in

tables (8.1), (8.2) and (8.3).

$A - X$ band				
	$A(v'=0)$	$A(v'=1)$	$A(v'=2)$	$A(v'=3)$
$X(v=0)$	0.9776	0.02234	1.719×10^{-5}	4.2667×10^{-7}
$X(v=1)$	0.02161	0.9348	0.04353	4.515×10^{-5}
$X(v=2)$	7.134×10^{-4}	0.04073	0.8948	0.06365
$X(v=3)$	2.689×10^{-5}	0.002019	0.05755	0.8575

TABLE 8.1: The $A - X(v' - v)$ Franck-Condon matrix for $v = 0, 1, 2, 3$.

$B - X$ band				
	$B(v'=0)$	$B(v'=1)$	$B(v'=2)$	$B(v'=3)$
$X(v=0)$	0.9980	0.001954	1.654×10^{-5}	1.158×10^{-6}
$X(v=1)$	0.001921	0.9935	0.004567	4.103×10^{-5}
$X(v=2)$	5.024×10^{-5}	0.004424	0.9875	0.007925
$X(v=3)$	2.969×10^{-8}	1.566×10^{-4}	0.007568	0.9801

TABLE 8.2: The $B - X(v' - v)$ Franck-Condon matrix for $v = 0, 1, 2, 3$.

$B - A$ band				
	$B(v'=0)$	$B(v'=1)$	$B(v'=2)$	$B(v'=3)$
$A(v=0)$	0.9634	0.03554	0.001025	2.91229×10^{-5}
$A(v=1)$	0.03619	0.8916	0.06905	0.003069
$A(v=2)$	4.014×10^{-4}	0.07165	0.8211	0.1004
$A(v=3)$	1.573×10^{-6}	0.001237	0.1062	0.7524

TABLE 8.3: The $B - A(v' - v)$ Franck-Condon matrix for $v = 0, 1, 2, 3$.

8.1.6 Trapping laser-cooled CaF in a microwave trap

The Doppler temperature of CaF $T_{\mathrm{D}} = \frac{\hbar\Gamma}{2k_{\mathrm{B}}}$ =200 μK is still too high to explore some of the most exciting properties of polar molecules such as the long range anisotropic dipole-dipole interactions. Even if the molecules are captured in a MOT and sub-Doppler cooling mechanisms such as polarization gradient cooling are at work, the temperature can only be further decreased by a factor of 10 in the best case scenario. In fact, it is likely that it will prove challenging to reach even the Doppler temperature in a type-II MOT [168].

In order to reach temperatures in the sub-mK regime, techniques other than laser cooling must be employed. One possibility to achieve such ultralow temperatures is through evaporative or sympathetic cooling with ultracold atoms in a trap.

It is possible to trap the laser cooled and slowed CaF molecules in a microwave trap as described in [112]. The $X(N = 1)$ state is normally a low-field seeking state in a red-detuned microwave trap and cannot be trapped. Thus, the molecules must be transferred to the absolute ground state via optical pumping or resonant microwaves. Ordinarily, parity selection rules forbid transferring molecules through the excited state to the $X(N = 0)$ ground state. However, this selection rule is broken in the presence of microwaves which presents a convenient way to accumulate the cooled molecules in the trap over time. As an added bonus, the fact that the molecules are already cold relaxes the requirements on the trapping fields meaning that the input power to the cavity can be lowered to a few watts [112]. Once trapped in the microwave cavity, it is possible to achieve high enough densities and low enough temperatures to apply evaporative cooling and eventually reach quantum degeneracy.

Alternatively, once in the trap, it is possible to sympathetically cool the molecules further with an ultracold atomic sample. The microwave trap confines the molecules in their absolute ground state which means that detrimental inelastic atom-molecule or molecule-molecule collisions are suppressed.

Appendix A

Excitation in a multi-level system

This appendix is based on [55] and explains the population dynamics of a multi-level system.

Consider a molecule in which N ground states (labeled as g_j) are connected to one excited state e by laser beams. The probability of occupying a ground or excited state are n_j or n_e respectively and satisfy the normalization condition:

$$n_e + \sum_{j=1}^{N} n_j = 1 \tag{A.1}$$

One can write a set of rate equations:

$$\frac{\partial n_j}{\partial t} = A_j n_e + R_j(n_e - n_j) \tag{A.2}$$

where A_j is the partial spontaneous decay rate from e to g_j and R_j is the excitation rate for that transition. In the steady state limit $\frac{\partial n_j}{\partial t} = 0$. Solving equations (6.2) and using (A.1) we obtain:

$$n_e = \frac{1}{(N+1) + \sum_{j=1}^{N} A_j/R_j} \tag{A.3}$$

The ratio A_j/R_j can be expressed as $2I_{\text{sat},j}/I_j$ where $I_{\text{sat},j} = \pi hc\Gamma/(3\lambda_j^3)$ is the saturation intensity for the j^{th} transition and I_j is the intensity of the light driving that transition. Equation 6.2 can then be written as:

$$n_e \simeq \frac{1}{(N+1) + 2\sum_{j=1}^{N} I_{\text{sat},j}/I_j} \tag{A.4}$$

We note that the wavelengths of the laser cooling transitions in the two vibrational manifolds are sufficiently similar to each other so that the saturation intensities $I_{\text{sat},j}$ can be

approximated by one constant I_{sat} and equation (A.4) reduces to:

$$n_e \simeq \frac{1}{(N+1) + 2I_{\text{sat}} \sum_{j=1}^{N} 1/I_j} \tag{A.5}$$

In order to maximize the scattering rate, one has to make n_e as high as possible. If the total given intensity is I_{tot}, then n_e and thus the cooling rate is maximized by equally spreading I_{tot} among all transitions so that $I_j = I_{\text{tot}}/N$. The excited state probability of occupation is then:

$$n_e \simeq \frac{1}{(N+1) + 2N^2 I_{\text{sat}}/I_{\text{tot}}} \tag{A.6}$$

and each of the ground state occupancy probabilities is equal to $n_j = (1 - n_e)/N$.

There are two limits to consider to obtain an expression for n_e. In the low intensity limit $I_{\text{tot}} \ll \frac{2N^2 I_{\text{sat}}}{(N+1)}$ and:

$$n_e \simeq \frac{I_{\text{tot}}/(N+1)}{I_{\text{tot}} + 2N^2 I_{\text{sat}}/(N+1)} \simeq \frac{I_{\text{tot}}}{2N^2 I_{\text{sat}}} \tag{A.7}$$

On the other hand, in the high-intensity limit when $I_{\text{tot}} \gg \frac{2N^2 I_{\text{sat}}}{(N+1)}$, the molecular population is shared equally among all levels: $n_e = n_j \approx \frac{1}{N+1}$.

In the more complicated case where there are N_e excited state and N_g ground state levels, the laser cooling is similarly most efficient if all transitions are driven with the same intensity. The total excited state probability is given by:

$$n_e \simeq \frac{N_e}{(N_g + N_e) + 2N_g^2 I_{\text{sat}}/I_{\text{tot}}} \tag{A.8}$$

Appendix B

Branching ratios

The matrix below gives the branching ratio between the $X^2\Sigma^+(N=1)$ and $A^2\Pi_{1/2}(J'=1/2)$ states of CaF (calculated by M. Tarbutt). Each row corresponds to a ground electronic state level labeled by (N, J, F, m_F) and each column corresponds to an excited state level labeled by (F, m_F).

(N_X,J_X,F_X,m_X)/(F_A,m_A)	(1,1)	(1,0)	(1,-1)	(0,0)
(1,3/2,2,2)	0.166667	0	0	0
(1,3/2,2,1)	0.083333	0.083333	0	0
(1,3/2,2,0)	0.027778	0.11111	0.027778	0
(1,3/2,2,-1)	0	0.083333	0.083333	0
(1,3/2,2,-2)	0	0	0.166667	0
(1,3/2,1,1)	0.189917	0.189917	0	0.003532
(1,3/2,1,0)	0.189917	0	0.189917	0.00353183
(1,3/2,1,-1)	0	0.189917	0.189917	0.00353183
(1,1/2,1,1)	0.0600833	0.0600833	0	0.329802
(1,1/2,1,0)	0.0600833	0	0.0600833	0.329802
(1,1/2,1,-1)	0	0.0600833	0.0600833	0.329802
(1,1/2,0,0)	0.222222	0.222222	0.222222	0

TABLE B.1: Branching ratios for the $X(N=1) \rightarrow A(J'=1/2)$ transition.

Appendix C

Building an EOM in-house

It is easy to construct a home-built EOM. Crystals are available for purchase from Leysop Ltd. The voltage is applied to the two sides which are gold-plated for electrical contact. The capacitance of the crystal of area A and thickness d is given by $C = \frac{A\epsilon_r\epsilon_0}{d}$, where ϵ_r is the RF dielectric constant. The only difficult aspect of making a home-made EOM circuit is finding the right inductor - a teflon rod with copper wire windings is a good place to start. It is important to realize that at such a high frequency, the inductor and capacitor have equivalent reactances of $X_L = \omega L$ and $X_c = 1/(\omega C)$ respectively [206]. Thus, it is essential that the behavior of the circuit is characterized with an RF network analyzer for rf frequencies around the designed resonant frequency. It is also important to find the Q-value of the circuit ($Q = f_{\text{res}}/\Delta f$) as on resonance the voltage across the crystal is increased by a factor of Q with respect to the voltage applied to the circuit. To step the voltage down, a transformer is usually used (e.g. 16:1 transformer XFA-0101-16UH). Finally, the circuit has to be impedance-matched to eliminate reflections from the rf-source. The reader is referred to [113] and [196] for more details regarding making a home-built EOM.

Appendix D

Scattering rate for different chirp rates

Figure (D.1) shows the scattering rate of the molecules traveling at 600 $\mathrm{m\,s^{-1}}$ for several values of the chirp rate β as predicted by the rate equation model. The scattering rate drops for all values of β because of the divergence of the laser cooling beams. For chirp rates up to 40 MHz/ms the scattering rate increases. Chirping the laser frequencies at 60 MHz/ms reduces the scattering.

Figure (D.2) shows the scattering rate as estimated by the simple model in chapter (7),

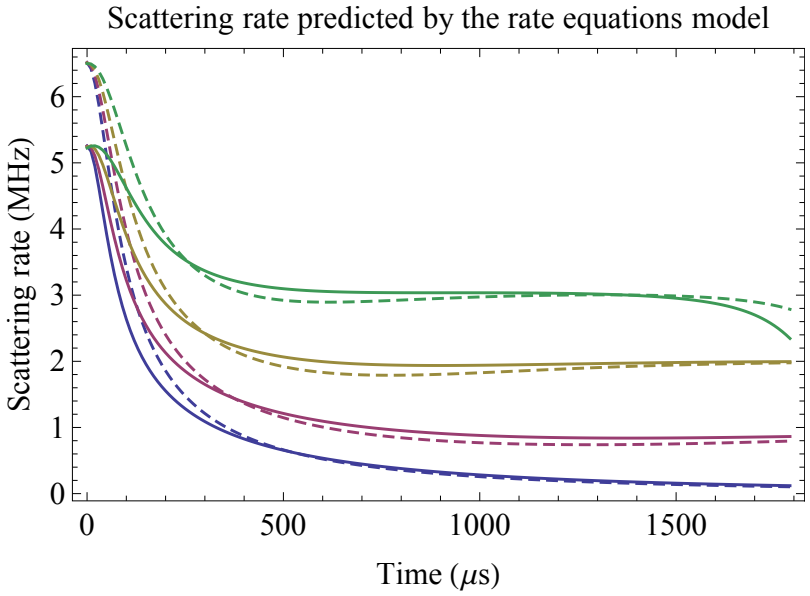

FIGURE D.1: The scattering rate for molecules traveling at 600 $\mathrm{m\,s^{-1}}$ for chirp rates of β =0 (blue), 20 (purple), 40 (green) and 60 (yellow) MHz/ms on the beam line (dashed lines) and at a distance $r = 1$ mm (solid lines).

section (7.6.3). Chirping the cooling lasers at rates higher than β =40 MHz/ms reduces the scattering rate.

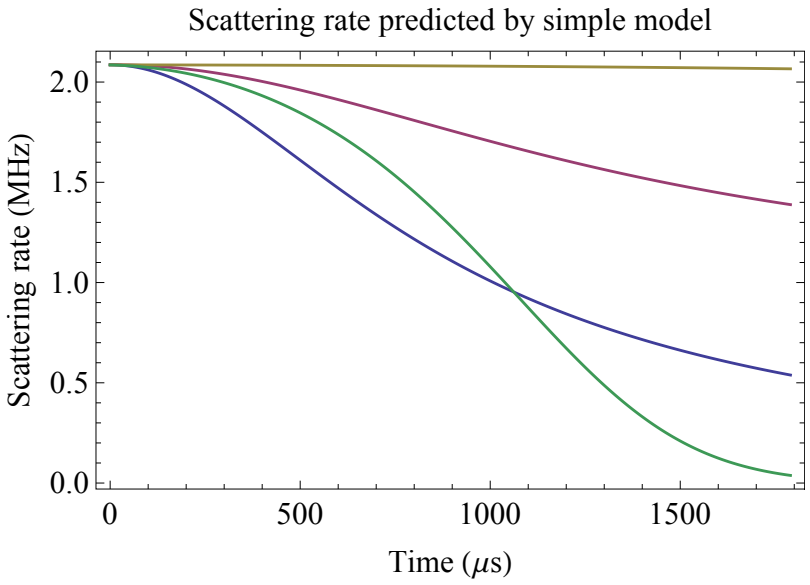

FIGURE D.2: The scattering rate for chirp rates of β =0 (blue), 20 (purple), 40 (yellow) and 60 (green) MHz/ms.

Appendix E

Photographs of the experiment

Here are some pictures of the laser cooling of CaF experiment.

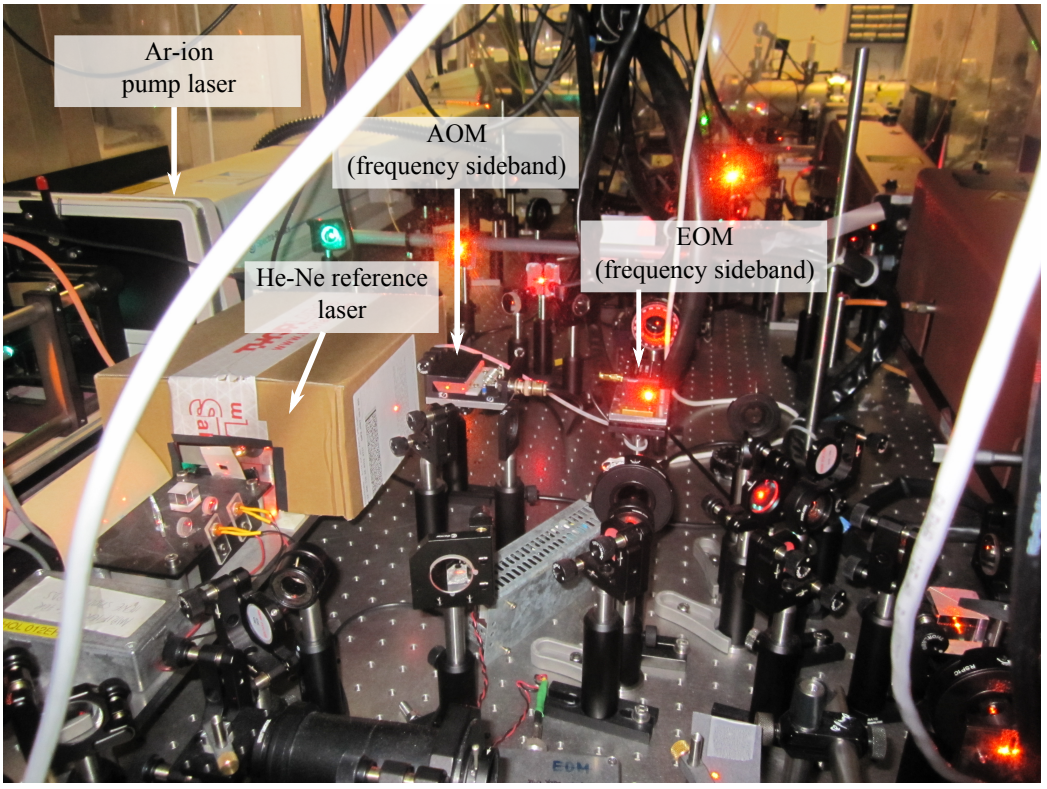

FIGURE E.1: Frequency reference He-Ne laser and some of the optics for generating the frequency sidebands. The orange light is from the v_{00} main cooling laser, while the red light is from the vibrational repump v_{10}.

FIGURE E.2: The frequency-chirp AOM. All laser cooling frequencies from the v_{00} and v_{10} lasers are combined and double-passed through a broad-band AOM with starting frequency of 225 MHz.

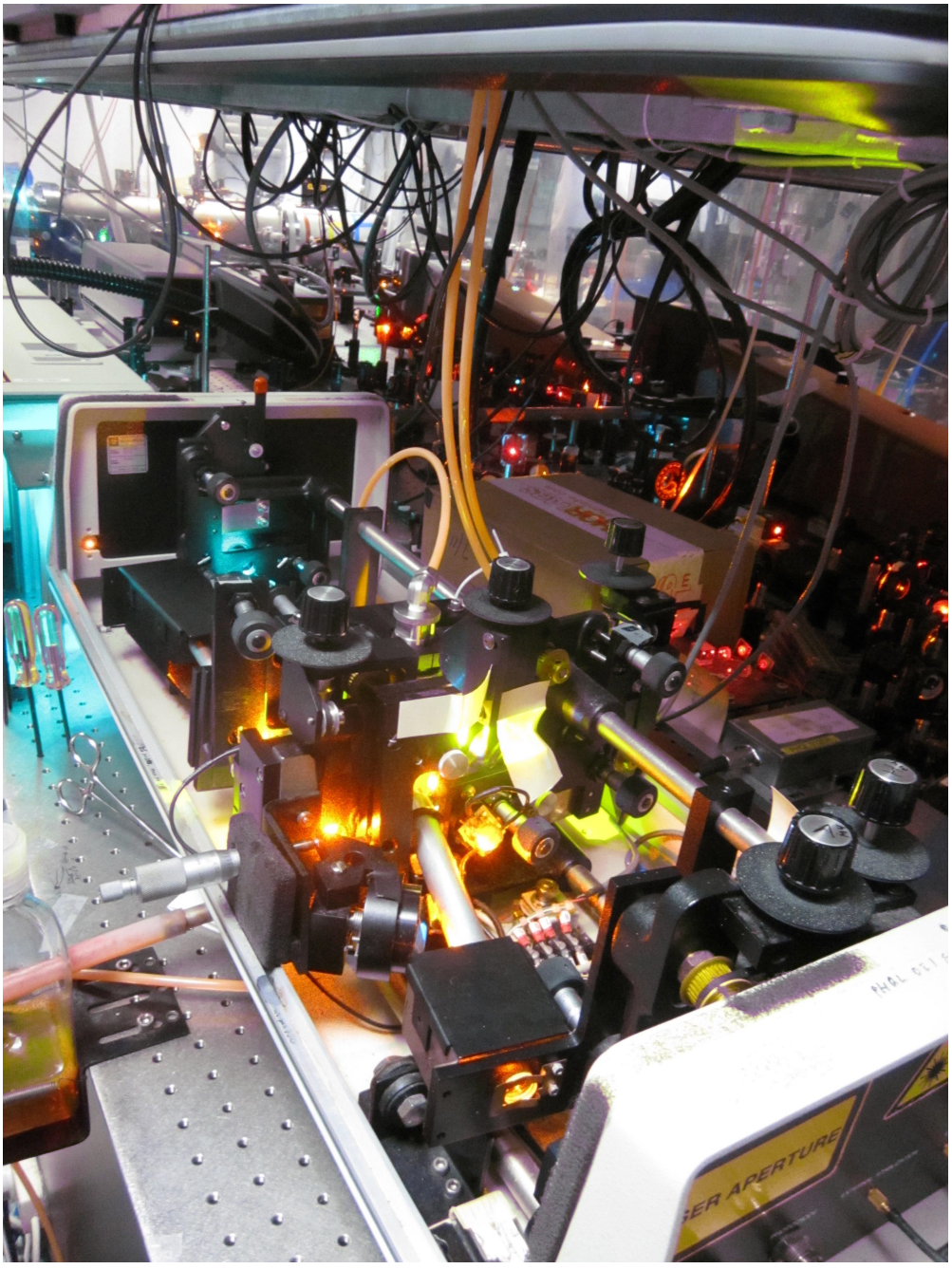

FIGURE E.3: The Spectra Physics laser used as a probe.

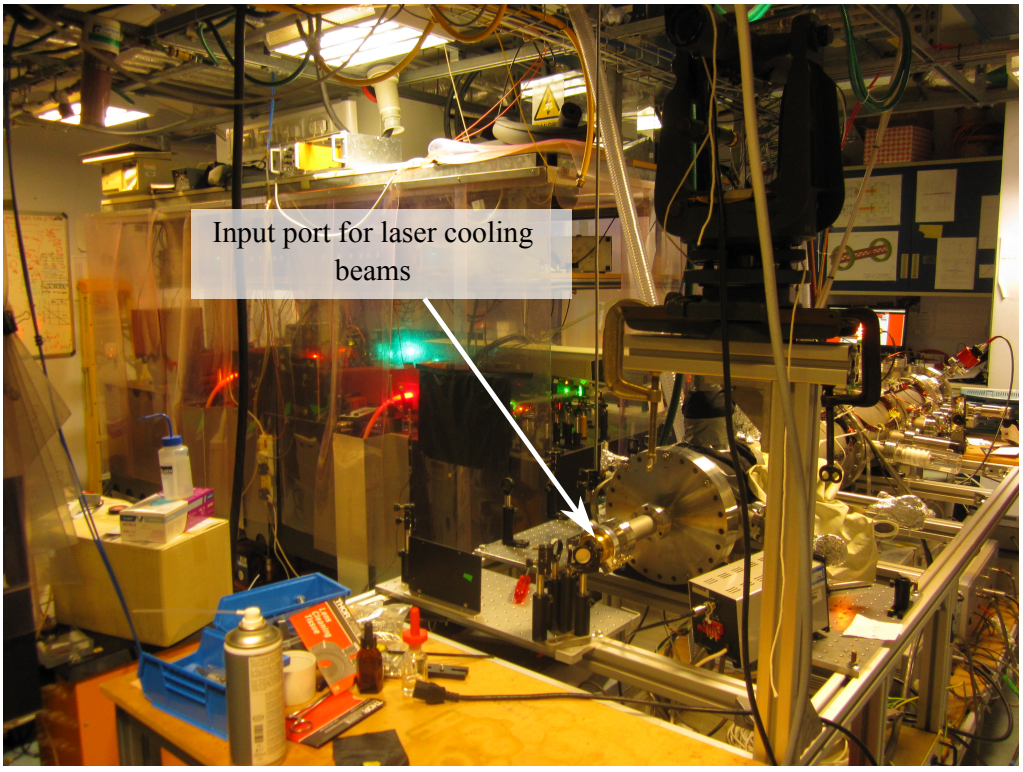

FIGURE E.4: The vacuum chamber and the input port for the laser cooling beams.

FIGURE E.5: Inside the Coherent 699 v_{00} laser - the bow type of cavity. *Image courtesy of the BBC.*

Bibliography

[1] R.V. Krems, W.C. Stwalley, and B. Friedrich. *Cold Molecules: Theory, Experiment, Applications*. CRC Press, 2009.

[2] M.D. DiRosa. Laser cooling molecules. *Eur. Phys. J. D*, 31:395, 2004.

[3] B.K. Stuhl, B.C. Sawyer, D. Wang, and J. Ye. Magneto-optical trap for polar molecules. *Phys. Rev. Lett.*, 101:243002–1:243002:4, 2008.

[4] W.D. Phillips, J.V. Prodan, and H.J. Metcalf. Laser cooling and electromagnetic trapping of neutral atoms. *J. Opt. Soc. Am. B*, 2:1751–1767, 1985.

[5] H.J. Metcalf and P. van der Straten. *Laser Cooling and Trapping*. Springer, 1999.

[6] D.P. DiVincenzo. Quantum computation. *Science*, 270:255–261, 1995.

[7] E.A. Cornell and C.E. Wieman. Bose-Einstein Condensation in a Dilute Gas: The First 70 Years and some Recent Experiments (Nobel Lecture). *Chem. Phys. Chem.*, 3:476–493, 2002.

[8] O.R. Frisch. *Z. Phys.*, 86:42, 1933.

[9] G.A. Askar'yan. Effects of the field gradient of an intense electromagnetic beam on electrons and atoms. *Zh. Eksp. Theor. Fiz.*, 42:1567–1570, 1962.

[10] V.S. Letokhov and P.N. Lebedev. Narrowing of the Doppler width in a standing light wave. *Zh. Eksp. Theor. Fiz.*, 7:348–351, 1968.

[11] A. Ashkin. Atomic-beam deflection by resonance-radiation pressure. *Phys. Rev. Lett.*, 25:1321–1324, 1970.

[12] R. Schieder, H. Walther, and L. Woste. Atomic beam deflection by the light of a tunable dye laser. *Opt. Commun.*, 5:337, 1972.

[13] T.W. Hänsch and A.L. Schawlow. Cooling of gases by radiation pressure. *Opt. Commun.*, 13:68–69, 1975.

[14] D.J. Wineland and H. Dehmelt. Proposed 10^{14} $\delta\nu/\nu$ laser fluorescence spectroscopy on Tl^+ mono-ion oscillator III. *Bull. Am. Phys. Soc.*, 20:637, 1975.

[15] D.J. Wineland, R.E. Drullinger, and F.L. Walls. Radiation-pressure cooling of bound resonant absorbers. *Phys. Rev. Lett.*, 40:1639, 1978.

[16] W.D. Phillips and H. Metcalf. Laser Deceleration of an Atomic Beam. *Phys. Rev. Lett.*, 48:596–599, 1982.

[17] W.D. Phillips. Nobel lecture: Laser cooling and trapping of neutral atoms. *Rev. Mod. Phys.*, 70:721–741, 1998.

[18] V.G. Minogin. Deceleration and monochromatization of atomic beams by laser radiation pressure. *Opt. Commun.*, 34:265–268, 1980.

[19] S. Andreev, V. Balykin, V. Letokhov, and V. Minogin. Radiative slowing and reduction of the energy spread of a beam of sodium atoms to 1.5 K in an oppositely directed laser beam. *Zh. Eksp. Theor. Fiz.*, 34:463, 1981.

[20] V.I. Balykin, V.S. Letokhov, and V.I. Mishin. Cooling of sodium atoms by resonant laser emission. *Zh. Eksp. Theor. Fiz.*, 78:1376–1385, 1980.

[21] J.V. Prodan, W.D. Phillips, and H. Metcalf. Laser production of a very slow monoenergetic atomic beam. *Phys. Rev. Lett.*, 49:1149, 1982.

[22] V.S. Letokhov, V.G. Minogin, and B.D. Pavlik. Cooling and trapping of atoms and molecules by a resonant laser field. *Opt. Commun.*, 19:72–75, 1976.

[23] W.D. Phillips. Rapid frequency scanning of ring dye lasers. *Appl. Optics*, 20:3826, 1981.

[24] J.V. Prodan and W.D. Phillips. Chirping the light-fantastic? Recent NBS atom cooling experiments. *Prog. Quantum Electron.*, 8:231, 1984.

[25] J. Prodan, A. Migdall, and W.D. Phillips. Stopping atoms with laser light. *Phys. Rev. Lett.*, 54:992, 1985.

[26] W. Ertmer, R. Blatt, J. L. Hall, and M. Zhu. Laser manipulation of atomic beam velocities: demonstration of stopped atoms and velocity reversal. *Phys. Rev. Lett.*, 54:996, 1985.

[27] Steven Chu, L. Hollberg, J. E. Bjorkholm, Alex Cable, and A. Ashkin. Three-dimensional viscous confinement and cooling of atoms by resonance radiation pressure. *Phys. Rev. Lett.*, 55:48–51, Jul 1985.

[28] C. Salomon, J. Dalibard, W. D. Phillips, A. Clairon, and S. Guellati. Laser Cooling of Cesium Atoms Below 3μK. *Europhys. Lett.*, 12(8):683, 1990.

[29] E.L. Raab, M. Prentiss, A. Cable, S. Chu, and D.E. Pritchard. Trapping of neutral sodium atoms with radiation pressure. *Phys. Rev. Lett.*, 59:2631, 1987.

[30] M. H. Anderson, J. R. Ensher, M. R. Matthews, C. E. Wieman, and E. A. Cornell. Observation of Bose-Einstein Condensation in a Dilute Atomic Vapor. *Science*, 269(5221):198–201, 1995.

[31] L.D. Carr, D. DeMille, R.V. Krems, and Jun Ye. Cold and ultracold molecules: science, technology and applications. *N. J. Phys.*, 11:055049, 2009.

[32] M. Greiner, C.A. Regal, and D.S. Jin. Emergence of a molecular Bose-Einstein condensate from a Fermi gas. *Nature*, 426:537–540, 2003.

[33] S. Jochim, M. Bartenstein, A. Altmeyer, G. Hendl, S. Riedl, C. Chin, J.H. Denschlag, and R. Grimm. Bose-Eisntein condensation of molecules. *Science*, 302:2101–2103, 2003.

[34] C. Regal, M. Greiner, and D.S. Jin. Observation of resonance condensation of fermionic atom pairs. *Phys. Rev. Lett.*, 92:040403, 2004.

[35] N.T. Zinner, B. Wunsch, D. Pekker, and D.-W. Wang. BCS-BEC crossover in bilayers of cold fermionic polar molecules. *Phys. Rev. A*, 85:013603, 2012.

[36] A. Altmeyer, S. Riedl, C. Kohstall, M. J. Wright, R. Geursen, M. Bartenstein, C. Chin, J. Hecker Denschlag, and R. Grimm. Precision Measurements of Collective Oscillations in the BEC-BCS Crossover. *Phys. Rev. Lett.*, 98:040401, Jan 2007.

[37] D.M. Eagles. Possible paring without superconductivity at low carrier concentrations in bulk and thin-film superconducting semiconductors. *Phys. Rev.*, 186:456–463, 1969.

[38] A.J. Leggett. *Modern Trends in the Theory of Condensed Matter*. Springer-Verlag, 1980.

[39] R. Barrett, D. Petrov, M. Lukin, and E. Delmer. Quantum magnetism with multicomponent dipolar molecules in an optical lattice. *Phys. Rev. Lett.*, 96:190410, 2006.

[40] K. Góral, L. Santos, and M. Lewenstein. Quantum phases of dipolar bosons in optical lattices. *Phys. Rev. Lett.*, 88:170406, 2002.

[41] J.P. Uzan. The fundamental constants and their variation: observational and theoretical status. *Rev. Mod. Phys.*, 75:403–455, 2003.

[42] J.P. Uzan. Varying constants, gravitation and cosmology. *Living Rev. Relativ.*, 14:2, 2011.

[43] J. Khoury and A. Weltman. Chameleon fields: awaiting surprises for tests of Gravity in Space. *Phys. Rev. Lett.*, 93:171104, 2004.

[44] J.K. Webb, M.T. Murphy, V.V. Flambaum, V.A. Dzuba, J.D. Barrow, C.W. Churchill, J.X. Prochaska, and A.M. Wolfe. Further evidence for cosmological evolution of the fine structure constant. *Phys. Rev. Lett.*, 87:091301, 2001.

[45] E. Reinhold, R. Buning, U. Hollenstein, A. Ivanchik, P. Petitjean, and W. Ubachs. Indication of a cosmological variation of the proton-electron mass ratio based on laboratory measurements and reanalysis of H_2 spectra. *Phys. Rev. Lett.*, 96:151101, 2006.

[46] R. Srianand, H. Chand, P. Petitjean, and B. Aracil. Limits to the time variation of the electromagnetic fine-structure constant in the low energy limit from absorption lines in the spectra of distant quasars. *Phys. Rev. Lett.*, 92:121302, 2004.

[47] N. Kanekar, C.L. Carilli, G.I. Langston, G. Rocha, F. Combes, R. Subrahmanyan, J.T. Stocke, K.M. Menten, F.H. Briggs, and T. Wiklind. Constraints on changes in fundamental constants from a cosmologically distant OH absorber or emitter. *Phys. Rev. Lett.*, 95:261301, 2005.

[48] S. Truppe, R.J. Hendricks, S.K. Tokunaga, H.J. Lewandowski, M.G. Kozlov, C. Henkel, E.A Hinds, and M.R. Tarbutt. A search for varying fundamental constants using hertz-level frequency measurements of cold CH molecules. *Nat. Com.*, 4:2600, 2013.

[49] H.L. Bethlem, M. Kajta, B. Sartakov, G. Meijer, and W. Ubachs. Prospects for precision measurements on ammonia molecules in a fountain. *Eur. Phys. J.*, 163:55–69, 2008.

[50] C. S. Wu, E. Ambler, R. W. Hayward, D. D. Hoppes, and R. P. Hudson. Experimental Test of Parity Conservation in Beta Decay. *Phys. Rev.*, 105:1413–1415, Feb 1957.

[51] M. Pospelov and A. Ritz. Electric dipole moments as probes of new physics. *Ann. Phys.*, 318:119–169, 2005.

[52] L.I. Schiff. Measureability of nuclear electric dipole moments. *Phys. Rev.*, 132:2194, 1963.

[53] J.J. Hudson, D.M. Kara, I.J. Smallman, B.E. Sauer, M.R. Tarbutt, and E.A. Hinds. Improved measurement of the shape of the electron. *Nature*, 473:493–496, 2011.

[54] The ACME Collaboration, J. Baron, W. C. Campbell, D. DeMille, J. M. Doyle, G. Gabrielse, Y. V. Gurevich, P. W. Hess, N. R. Hutzler, E. Kirilov, I. Kozyryev, B. R. OLeary, C. D. Panda, M. F. Parsons, E. S. Petrik, B. Spaun, A. C. Vutha, and A. D. West. Order of Magnitude Smaller Limit on the Electric Dipole Moment of the Electron. *Science*, 343(6168):269–272, 2014.

[55] M R Tarbutt, B E Sauer, J J Hudson, and E A Hinds. Design for a fountain of YbF molecules to measure the electron's electric dipole moment. *New Journal of Physics*, 15(5):053034, 2013.

[56] S. C. Bennett and C. E. Wieman. Measurement of the 6S $\rightarrow$7S Transition Polarizability in Atomic Cesium and an Improved Test of the Standard Model. *Phys. Rev. Lett.*, 82:2484–2487, Mar 1999.

[57] M. Quack. How important is parity violation for molecular and biomolecular chilarity? *Angew. Chem. Int. Ed.*, 41:4618–4630, 2002.

[58] Peter Schwerdtfeger, Jon K. Laerdahl, and Christian Chardonnet. Calculation of parity-violation effects for the C-F stretching mode of chiral methyl fluorides. *Phys. Rev. A*, 65:042508, Apr 2002.

[59] M. Ziskind, C. Daussy, T. Marrel, and Ch. Chardonnet. Improved sensitivity in the search for a parity-violating energy difference in the vibrational spectrum of the enantiomers of CHFClBr. *Eur. Phys. J. D*, 20:219, 2002.

[60] P. Schwerdtfeger and R. Bast. Large parity violation effects in the vibrational spectrum of organometallic compounds. *J. Am. Chem. Soc.*, 126:1652, 2004.

[61] W.C. Haxton and C.-P. Liu. Nuclear anapole moments. *Phys. Rev. C.*, 65:045502, 2002.

[62] T. A. Isaev, S. Hoekstra, and R. Berger. Laser-cooled RaF as a promising candidate to measure molecular parity violation. *Phys. Rev. A*, 82:052521, Nov 2010.

[63] J.E. van den Berg, S.C. Mathavan, C. Meinema, J. Nauta, T.H. Nijbroek, K. Jungmann, H.L. Bethlem, and S. Hoekstra. Traveling-wave deceleration of SrF molecules. *J. Mol. Spec.*, 300(0):22–25, 2014.

[64] D. DeMille. Quantum information processing with trapped polar molecules. *Phys. Rev. Lett.*, 88:067901, 2002.

[65] A. Andre. A coherent all-electrical interface between polar molecules and mesoscopic superconducting resonators. *Nature Physics*, 2:636–642, 2006.

[66] R.V. Krems. Cold controlled chemistry. *Phys. Chem. Chem. Phys.*, 10:4079–4092, 2008.

[67] P.F. Weck and N. Balakrishnan. Importance of long-range interactions in chemical reactions at cold and ultracold temperatures. *Int. Rev. Chem. Phys.*, 25:283–311, 2006.

[68] N. Balakrishnan and A. Dalgarno. Chemistry at ultracold temeratures. *Chem. Phys. Lett.*, 341:652–656, 2001.

[69] B. Friedrich and J.M. Doyle. Why are cold molecules so hot? *European Journal of Chemical Physics and Physical Chemistry*, 10:604–623, 2009.

[70] S.E. Maxwell, N. Brahms, R. deCarvalho, D.R. Glenn, J.S. Helton, S.V. Nguyen, D. Patterson, J. Petricka, D. DeMille, and J.M. Doyle. High-flux beam source of cold, slow atoms or molecules. *Phys. Rev. Lett.*, 95:173201, 2005.

[71] N. E. Bulleid, S. M. Skoff, R. J. Hendricks, B. E. Sauer, E. A. Hinds, and M. R. Tarbutt. Characterization of a cryogenic beam source for atoms and molecules. *Phys. Chem. Chem. Phys.*, 15:12299–12307, 2013.

[72] John M. Doyle, Bretislav Friedrich, Jinha Kim, and David Patterson. Buffer-gas loading of atoms and molecules into a magnetic trap. *Phys. Rev. A*, 52:R2515–R2518, Oct 1995.

[73] D. DeMille, D.R. Glenn, and J. Petricka. Microwave traps for cold polar molecules. *Eur. Phys. J. D*, 31:375–384, 2004.

[74] R. deCarvalho, J.M. Doyle, B. Friedrich, T. Guillet, J. Kim, D. Patterson, and J.D. Weinstein. Buffer-gas loaded magnetic traps for atoms and molecules: A primer. *Eur. Phys. J. D*, 7(3):289–309, 1999.

[75] S.M. Skoff. *Buffer gas cooling of YbF molecules*. PhD thesis, Imperial College, 2011.

[76] David Patterson and John M. Doyle. Bright, guided molecular beam with hydrodynamic enhancement. *The Journal of Chemical Physics*, 126(15):154307, 2007.

[77] Hsin-I Lu, Julia Rasmussen, Matthew J. Wright, Dave Patterson, and John M. Doyle. A cold and slow molecular beam. *Phys. Chem. Chem. Phys.*, 13:18986–18990, 2011.

[78] J.D. Weinstein, R. deCarvalho, T. Guillet, B. Friedrich, and J.M. Doyle. Magnetic trapping of calcium monohydride molecules at millikelvin temperatures. *Nature*, 395:148, 1998.

[79] A.C. Vutha, W.C. Campbell, Y.V. Gurevich, N.R. Hutzler, M. Parsons, D. Patterson, E. Petrik, B. Spaun, J.M. Doyle, G. Gabrielse, and D. DeMille. Search for the electric dipole moment of the electron with thorium monoxide. *J. Phys. B: At. Mol. Opt. Phys.*, 43:074007, 2010.

[80] S. M. Skoff, R. J. Hendricks, C. D. J. Sinclair, J. J. Hudson, D. M. Segal, B. E. Sauer, E. A. Hinds, and M. R. Tarbutt. Diffusion, thermalization, and optical pumping of YbF molecules in a cold buffer-gas cell. *Phys. Rev. A*, 83:023418, Feb 2011.

[81] Hsin-I Lu, Ivan Kozyryev, Boerge Hemmerling, Julia Piskorski, and John M. Doyle. Magnetic Trapping of Molecules via Optical Loading and Magnetic Slowing. *Phys. Rev. Lett.*, 112:113006, Mar 2014.

[82] Nicholas R. Hutzler, Hsin-I Lu, and John M. Doyle. The Buffer Gas Beam: An Intense, Cold, and Slow Source for Atoms and Molecules. *Chem. Rev.*, 112(9):4803–4827, 2012.

[83] Jinha Kim, Bretislav Friedrich, Daniel P. Katz, David Patterson, Jonathan D. Weinstein, Robert DeCarvalho, and John M. Doyle. Buffer-Gas Loading and Magnetic Trapping of Atomic Europium. *Phys. Rev. Lett.*, 78:3665–3668, May 1997.

[84] S.K. Tokunaga, W. Skomorowski, P.S. Żuchowski, R. Moszynski, J.M. Hutson, E.A. Hinds, and M.R. Tarbutt. Prospects for sympathetic cooling of molecules in electrostatic, ac and microwave traps. *Eur. Phys. J. D*, 65(1-2):141–149, 2011.

[85] Pavel Soldan, Piotr S. Zuchowski, and Jeremy M. Hutson. Prospects for sympathetic cooling of polar molecules: NH with alkali-metal and alkaline-earth atoms - a new hope. *Faraday Discuss.*, 142:191–201, 2009.

[86] Wade G. Rellergert, Scott T. Sullivan, Steven J. Schowalter, Svetlana Kotochigova, Kuang Chen, and Eric R. Hudson. Evidence for sympathetic vibrational cooling of translationally cold molecules. *Nature*, 495(7442):490–494, 2013.

[87] S.Y.T. van de Meerakker, H.L. Bethlem, N. Vanhaecke, and G. Meijer. Manipulation and control of molecular beams. *Chem. Rev.*, 112 (9):4828–4878, 2012.

[88] Hendrick L. Bethlem, Giel Berden, and Gerard Meijer. Decelerating Neutral Dipolar Molecules. *Phys. Rev. Lett.*, 83:1558–1561, Aug 1999.

[89] Hendrick L. Bethlem, Floris M. H. Crompvoets, Rienk T. Jongma, Sebastiaan Y. T. van de Meerakker, and Gerard Meijer. Deceleration and trapping of ammonia using time-varying electric fields. *Phys. Rev. A*, 65:053416, May 2002.

[90] J. R. Bochinski, Eric R. Hudson, H. J. Lewandowski, Gerard Meijer, and Jun Ye. Phase Space Manipulation of Cold Free Radical OH Molecules. *Phys. Rev. Lett.*, 91:243001, Dec 2003.

[91] M. R. Tarbutt, H. L. Bethlem, J. J. Hudson, V. L. Ryabov, V. A. Ryzhov, B. E. Sauer, G. Meijer, and E. A. Hinds. Slowing Heavy, Ground-State Molecules using an Alternating Gradient Decelerator. *Phys. Rev. Lett.*, 92:173002, Apr 2004.

[92] N. E. Bulleid, R. J. Hendricks, E. A. Hinds, Samuel A. Meek, Gerard Meijer, Andreas Osterwalder, and M. R. Tarbutt. Traveling-wave deceleration of heavy polar molecules in low-field-seeking states. *Phys. Rev. A*, 86:021404, Aug 2012.

[93] T.E. Wall, J.F. Kanem, J.M. Dyne, J.J. Hudson, B.E. Sauer, E.A. Hinds, and M.R. Tarbutt. Stark decelaration of CaF molecules in strong- and weak-field seeking states. *Phys. Chem. Chem. Phys.*, 13:18991, 2011.

[94] Andreas Osterwalder, Samuel A. Meek, Georg Hammer, Henrik Haak, and Gerard Meijer. Deceleration of neutral molecules in macroscopic traveling traps. *Phys. Rev. A*, 81:051401, May 2010.

[95] S. D. Hogan, D. Sprecher, M. Andrist, N. Vanhaecke, and F. Merkt. Zeeman deceleration of H and D. *Phys. Rev. A*, 76:023412, Aug 2007.

[96] Edvardas Narevicius, Adam Libson, Christian G. Parthey, Isaac Chavez, Julia Narevicius, Uzi Even, and Mark G. Raizen. Stopping Supersonic Beams with a Series of Pulsed Electromagnetic Coils: An Atomic Coilgun. *Phys. Rev. Lett.*, 100:093003, Mar 2008.

[97] R. Fulton, A.I. Bishop, M.N. Shneider, and P.F. Barker. Controlling the motion of cold molecules with deep periodic optical potentials. *Nature Physics*, 2:465, 2006.

[98] Roger W. Anderson. Tracks of Symmetric Top Molecules in Hexapole Electric Fields. *J. Phys. Chem. A*, 101(41):7664–7673, 1997.

[99] F.M.H. Crompvoets, H.L. Bethlem, R.T. Jongma, and G. Meijer. A prototype storage ring for neutral molecules. *Nature*, 411:174, 2001.

[100] Rienk T. Jongma, Theo Rasing, and Gerard Meijer. Two-dimensional imaging of metastable CO molecules. *J. Chem. Phys.*, 102(5):1925–1933, 1995.

[101] S. A. Rangwala, T. Junglen, T. Rieger, P. W. H. Pinkse, and G. Rempe. Continuous source of translationally cold dipolar molecules. *Phys. Rev. A*, 67:043406, Apr 2003.

[102] Hidenobu Tsuji, Takao Sekiguchi, Tetsuya Mori, Takamasa Momose, and Hideto Kanamori. Stark velocity filter for nonlinear polar molecules. *J. Phys. B: At. Mol. Opt. Phys.*, 43(9):095202, 2010.

[103] Peter C. Zieger, Sebastiaan Y. T. van de Meerakker, Cynthia E. Heiner, Hendrick L. Bethlem, André J. A. van Roij, and Gerard Meijer. Multiple Packets of Neutral Molecules Revolving for over a Mile. *Phys. Rev. Lett.*, 105:173001, Oct 2010.

[104] H.L. Bethlem, M.R. Tarbutt, J. Kupper, D. Carty, K. Wohlfart, E.A. Hinds, and G. Meijer. Alternating gradient focusing and deceleration of polar molecules. *J. Phys. B: At. Mol. Opt. Phys.*, 39:R263, 2006.

[105] T. Junglen, T. Rieger, S. A. Rangwala, P. W. H. Pinkse, and G. Rempe. Two-Dimensional Trapping of Dipolar Molecules in Time-Varying Electric Fields. *Phys. Rev. Lett.*, 92:223001, Jun 2004.

[106] T. E. Wall, S. Armitage, J. J. Hudson, B. E. Sauer, J. M. Dyne, E. A. Hinds, and M. R. Tarbutt. Transport of polar molecules by an alternating-gradient guide. *Phys. Rev. A*, 80:043407, Oct 2009.

[107] Sebastiaan Y. T. van de Meerakker, Paul H. M. Smeets, Nicolas Vanhaecke, Rienk T. Jongma, and Gerard Meijer. Deceleration and Electrostatic Trapping of OH Radicals. *Phys. Rev. Lett.*, 94:023004, Jan 2005.

[108] B.K. Stuhl, M.T. Hummon, M. Yeo, G. Quemener, J. L. Bohn, and J. Ye. Evaporative cooling of the dipolar hydroxyl radical. *Nature*, 492(7429):396–400, 2012.

[109] Jacqueline van Veldhoven, Hendrick L. Bethlem, and Gerard Meijer. ac Electric Trap for Ground-State Molecules. *Phys. Rev. Lett.*, 94:083001, Mar 2005.

[110] Rudolf Grimm, Matthias Weidemller, and Yurii B. Ovchinnikov. Optical dipole traps for neutral atoms. 1999.

[111] T. Takekoshi, B. M. Patterson, and R. J. Knize. Observation of Optically Trapped Cold Cesium Molecules. *Phys. Rev. Lett.*, 81:5105–5108, Dec 1998.

[112] S. Truppe. *New Physics with Cold Molecules: Precise Microwave Spectroscopy of CH and the Development of a Microwave Trap.* PhD thesis, Imperial College London, 2013.

[113] David R. Glenn. *Development of Techniques for Cooling and Trapping Polar Diatomic Molecules.* PhD thesis, Yale University, 2010.

[114] Manish Gupta and Dudley Herschbach. A Mechanical Means to Produce Intense Beams of Slow Molecules. *J. Phys. Chem. A*, 103(50):10670–10673, 1999.

[115] M. Gupta and D. Herschbach. Slowing and Speeding Molecular Beams by Means of a Rapidly Rotating Source. *J. Phys. Chem. A*, 105:1626–1637, 2001.

[116] Michael S. Elioff, James J. Valentini, and David W. Chandler. Subkelvin Cooling NO Molecules via "Billiard-like" Collisions with Argon. *Science*, 302(5652):1940–1943, 2003.

[117] Benjamin L. Lev, András Vukics, Eric R. Hudson, Brian C. Sawyer, Peter Domokos, Helmut Ritsch, and Jun Ye. Prospects for the cavity-assisted laser cooling of molecules. *Phys. Rev. A*, 77:023402, Feb 2008.

[118] M. Zeppenfeld, M. Motsch, P. W. H. Pinkse, and G. Rempe. Optoelectrical cooling of polar molecules. *Phys. Rev. A*, 80:041401, Oct 2009.

[119] Kevin M. Jones, Eite Tiesinga, Paul D. Lett, and Paul S. Julienne. Ultracold photoassociation spectroscopy: Long-range molecules and atomic scattering. *Rev. Mod. Phys.*, 78:483–535, May 2006.

[120] M.E. Wagshul, K. Helmerson, P.D. Lett, S.L. Rolston, W.D. Phillips, R. Heather, and P.S. Julienne. Hyperfine effects on associative ionization of ultracold sodium. *Phys. Rev. Lett.*, 70:2074–2077, Apr 1993.

[121] J. D. Miller, R. A. Cline, and D. J. Heinzen. Photoassociation spectrum of ultracold Rb atoms. *Phys. Rev. Lett.*, 71:2204–2207, Oct 1993.

[122] A. Fioretti, D. Comparat, A. Crubellier, O. Dulieu, F. Masnou-Seeuws, and P. Pillet. Formation of Cold Cs_2 Molecules through Photoassociation. *Phys. Rev. Lett.*, 80:4402–4405, May 1998.

[123] William C. Stwalley and He Wang. Photoassociation of Ultracold Atoms: A New Spectroscopic Technique. *J. Mol. Spec.*, 195(2):194 – 228, 1999.

[124] He Wang and William C. Stwalley. Ultracold photoassociative spectroscopy of heteronuclear alkali-metal diatomic molecules. *J. Chem. Phys.*, 108(14):5767–5771, 1998.

[125] J. P. Shaffer, W. Chalupczak, and N. P. Bigelow. Photoassociative Ionization of Heteronuclear Molecules in a Novel Two-Species Magneto-optical Trap. *Phys. Rev. Lett.*, 82:1124–1127, Feb 1999.

[126] Andrew J. Kerman, Jeremy M. Sage, Sunil Sainis, Thomas Bergeman, and David DeMille. Production of Ultracold, Polar RbCs* Molecules via Photoassociation. *Phys. Rev. Lett.*, 92:033004, Jan 2004.

[127] J. Deiglmayr, A. Grochola, M. Repp, K. Mortlbauer, C. Gluck, J. Lange, O. Duliue, R. Wester, and M. Weidemuller. Formation of ultracold polar molecules in the rovibrational ground state. *Phys. Rev. Lett.*, 101:133004, 2008.

[128] C. Haimberger, J. Kleinert, P. Zabawa, A. Wakim, and N.P. Bigelow. Formation of ultracold, highly polar $X^1\Sigma^+$ NaCs molecules. *N. J. Phys.*, 11(5):055042, 2009.

[129] Elizabeth A. Donley, Niel R. Clausen, Sarah T. Thompson, and Carl E. Wieman. Atom-molecule coherence in a Bose-Einstein condensate. *Nature*, 417:529, 2002.

[130] Jens Herbig, Tobias Kraemer, Michael Mark, Tino Weber, Cheng Chin, Hanns-Christoph Nägerl, and Rudolf Grimm. Preparation of a Pure Molecular Quantum Gas. *Science*, 301(5639):1510–1513, 2003.

[131] S. Dürr, T. Volz, A. Marte, and G. Rempe. Observation of molecules produced from a BoseEinstein condensate. *Phys. Rev. Lett.*, 92:020406, 2004.

[132] K. Xu, T. Mukaiyama, J. R. Abo-Shaeer, J. K. Chin, D. E. Miller, and W. Ketterle. Formation of Quantum-Degenerate Sodium Molecules. *Phys. Rev. Lett.*, 91:210402, Nov 2003.

[133] Ticknor C. Bohn J.L. Regal, C.A. and D.S. Jin. Creation of ultracold molecules from a Fermi gas of atoms. *Nature*, 424:47, 2003.

[134] J. Cubizolles, T. Bourdel, S. J. J. M. F. Kokkelmans, G. V. Shlyapnikov, and C. Salomon. Production of Long-Lived Ultracold Li_2 Molecules from a Fermi Gas. *Phys. Rev. Lett.*, 91:240401, Dec 2003.

[135] M.W. Zwierlein, C.A. Stan, C.H. Schunck, S.M.F. Raupach, S. Gupta, Z. Hadzibabic, and W. Ketterle. Observation of Bose-Einstein Condensation of molecules. *Phys. Rev. Lett.*, 91:250401, 2003.

[136] S. B. Papp and C. E. Wieman. Observation of Heteronuclear Feshbach Molecules from a ^{85}Rb-^{87}Rb Gas. *Phys. Rev. Lett.*, 97:180404, Oct 2006.

[137] C. Weber, G. Barontini, J. Catani, G. Thalhammer, M. Inguscio, and F. Minardi. Association of ultracold double-species bosonic molecules. *Phys. Rev. A*, 78:061601, Dec 2008.

[138] K.-K. Ni, S. Ospelkaus, M. H. G. de Miranda, A. Pe'er, B. Neyenhuis, J. J. Zirbel, S. Kotochigova, P. S. Julienne, D. S. Jin, and J. Ye. A High Phase-Space-Density Gas of Polar Molecules. *Science*, 322(5899):231–235, 2008.

[139] Bo Yan, S.A. Moses, B. Gadway, J.P. Covey, K.R A. Hazzard, A.M. Rey, D.S. Jin, and Jun Ye. Observation of dipolar spin-exchange interactions with lattice-confined polar molecules. *Nature*, 501:521–525, 2013.

[140] Götz Zinner, Tomas Binnewies, Fritz Riehle, and Eberhard Tiemann. Photoassociation of Cold Ca Atoms. *Phys. Rev. Lett.*, 85:2292–2295, Sep 2000.

[141] G. Igel-Mann, U. Wedig, P. Fuentealba, and H. Stoll. Ground-state properties of alkali dimers XY (X, Y=Li to Cs). *J. Chem. Phys.*, 84(9):5007–5012, 1986.

[142] J. F. Barry, E. S. Shuman, and D. DeMille. A bright, slow cryogenic molecular beam source for free radicals. *Phys. Chem. Chem. Phys.*, 13:18936–18947, 2011.

[143] Matthew T. Hummon, Wesley C. Campbell, Hsin-I Lu, Edem Tsikata, Yihua Wang, and John M. Doyle. Magnetic trapping of atomic nitrogen (^{14}N) and cotrapping of NH ($X^2\Sigma^-$). *Phys. Rev. A*, 78:050702, Nov 2008.

[144] Jeremy M. Sage, Sunil Sainis, Thomas Bergeman, and David DeMille. Optical Production of Ultracold Polar Molecules. *Phys. Rev. Lett.*, 94:203001, May 2005.

[145] J. T. Bahns, W. C. Stwalley, and P. L. Gould. Laser cooling of molecules: A sequential scheme for rotation, translation, and vibration. *J. Chem. Phys.*, 104(24):9689–9697, 1996.

[146] H. J. Metcalf and P. van der Straten. Laser cooling and trapping of atoms. *J. Opt. Soc. Am. B*, 20(5):887–908, May 2003.

[147] L. R. Hunter, S. K. Peck, A. S. Greenspon, S. Saad Alam, and D. DeMille. Prospects for laser cooling TlF. *Phys. Rev. A*, 85:012511, Jan 2012.

[148] X. Zhouang, A. Le, T.C. Steimley, N.E. Bullied, I.J. Smallman, R.J. Hendricks, S.M. Skoff, J.J. Hudson, B.E. Sauer, E.A Hinds, and M.R. Tarbutt. Franck-Condon factors and radiative lifetimes of the $A^2\Pi_{1/2} - X^2\Sigma^+$ transition of Ytterbium Monofluoride, YbF. *Phys. Chem. Chem. Phys.*, 13:19013, 2011.

[149] T.A. Isaev and R. Berger. Lasercooled radium monofluoride: A molecular all-in-one probe for new physics. 2013. http://arxiv.org/abs/1302.5682.

[150] Ian C. Lane. Ultracold fluorine production via Doppler cooled BeF. *Phys. Chem. Chem. Phys.*, 14:15078–15087, 2012.

[151] Nathan Wells and Ian C. Lane. Prospects for ultracold carbon via charge exchange reactions and laser cooled carbides. *Phys. Chem. Chem. Phys.*, 13:19036–19051, 2011.

[152] Nathan Wells and Ian C. Lane. Electronic states and spin-forbidden cooling transitions of AlH and AlF. *Phys. Chem. Chem. Phys.*, 13:19018–19025, 2011.

[153] R.J. Hendricks, D.A. Holland, S. Truppe, B.E. Sauer, and M.R. Tarbutt. Vibrational branching ratios and hyperfine structure of ^{11}BH and its suitability for laser cooling. 2014. http://arxiv.org/abs/1404.6174v1.

[154] E.S. Shuman, J.F. Barry, and D. DeMille. Laser cooling of a diatomic molecule. *Nature*, 467:820–823, 2010.

[155] M.T. Hummon, M. Yeo, B.K. Stuhl, A.L. Collopy, Y. Xia, and J. Ye. 2D Magneto-optical traping of diatomic molecules. *Phys. Rev. Lett.*, 110:143001, 2013.

[156] V. Zhelyazkova, A. Cournol, T. E. Wall, A. Matsushima, J. J. Hudson, E. A. Hinds, M. R. Tarbutt, and B. E. Sauer. Laser cooling and slowing of CaF molecules. *Phys. Rev. A*, 89:053416, May 2014.

[157] A. Bernard and R. Gravina. The emission spectrum of Yttrium Monoxide: New rotational and vibrational results on the $A^2\Pi - X^2\Sigma^+$ system. *Astrophys. J. Suppl. Ser.*, 52:443, 1983.

[158] M. R. Tarbutt, J. J. Hudson, B. E. Sauer, and E. A. Hinds. Prospects for measuring the electric dipole moment of the electron using electrically trapped polar molecules. *Faraday Discuss.*, 142:37–56, 2009.

[159] D. DeMille, S.B. Cahn, D. Murphee, D.A. Rahmlow, and M.G. Kozlov. Using molecules to measure nuclear spin-dependent parity violation. *Phys. Rev. Lett.*, 100:023003, Jan 2008.

[160] A. Micheli, G.K. Brennen, and P. Zoller. A toolbox for lattice-spin models with polar molecules. *Nat. Phys.*, 2:341–347, 2006.

[161] E.S. Shuman, J.F. Barry, D.R. Glenn, and D. DeMille. Radiative Force from Optical Cycling on a Diatomic Molecule. *Phys. Rev. Lett.*, 103:223001–1:223001–4, 2009.

[162] J.F. Barry, E.S. Shuman, E.B. Norrgard, and D. D. DeMille. Laser Radiation Pressure Slowing of a Molecular Beam. *Phys. Rev. Lett.*, 108:103002, 2012.

[163] M. Prentiss, E. L. Raab, D. E. Pritchard, A. Cable, J. E. Bjorkholm, and Steven Chu. Atomic-density-dependent losses in an optical trap. *Opt. Lett.*, 13(6):452–454, Jun 1988.

[164] J. Flemming, A.M. Tuboy, D.M.B.P. Milori, L.G. Marcassa, S.C. Zilio, and V.S. Bagnato. Magneto-optical trap for sodium atoms operating on the D_1 line. *Optics Communications*, 135(46):269 – 272, 1997.

[165] D. Milori, M.T. de Araujo, I. Guedes, S.C. Zilio, and V.S. Bagnato. Analysis of a Vapor-Cell Magneto-Optical Trap for Sodium Atoms Based on a Two-Level Doppler Theory. *Braz. J. Phys.*, 27:025301, 1997.

[166] V. B. Tiwari, S. Singh, H. S. Rawat, and S. C. Mehendale. Cooling and trapping of ^{85}Rb atoms in the ground hyperfine F=2 state. *Phys. Rev. A*, 78:063421, Dec 2008.

[167] D.J. Berkeland and M.G. Boshier. Destabilization of dark states and optical spectroscopy in Zeeman-degenerate atomic systems. *Phys. Rev. A*, 65:033413, 2002.

[168] J.F. Barry, D.J. McCarron, E.B. Norrgard, M.H. Steinecker, and D. DeMille. Magneto-optical trapping of a diatomic molecule. 2014. http://arxiv.org/abs/1404.5680v1.

[169] John F. Barry. *Laser cooling and slowing of a diatomic molecule*. PhD thesis, Yale University, 2013.

[170] M.R. Tarbutt, J.J. Hudson, B.E. Sauer, E.A. Hinds, V.A. Ryzhov, V.L. Ryabov, and V.F. Ezhov. A jet beam source of cold YbF radicals. *J. Phys. B*, 35:5013–5022, 2002.

[171] L.A. Kaledin, J.C. Bloch, M.C. McCarthy, and R.W. Field. Analysis and deperturbation of the $A^2\Pi$ and $B^2\Sigma^+$ states of CaF. *J. Mol. Spec.*, 197:289–296, 1999.

[172] B.H. Bransden and C.J. Joachain. *Physics of Atoms and Molecules*. Prentice Hall, 2003.

[173] G. Herzberg. *Molecular spectra and molecular structure*. van Nostrand Reinhold, 1950.

[174] P. Atkins and R. Friedman. *Molecular quantum mechanics*. Oxford University Press, 2005.

[175] R.C. Johnson. The band spectra of the alkaline earth halides.I. CaF, SrF. *Proc. R. Soc. London A*, 122:161, 1929.

[176] A. Harvey. Interpretation of the spectra of CaF and SrF. *Proc. R. Soc. London A*, 133:336, 1931.

[177] K.V. Subbaram and D.R. Rao. New bands in the A-X systems of CaF. *Indian J. Phys.*, 43:312, 1969.

[178] R.W. Field, D.O. Harris, and T. Tanaka. Continous wave dye laser excitation spectroscopy CaF $A^2\Pi_r - X^2\Sigma^+$. *J. Mol. Spec.*, 57:107, 1975.

[179] J. Nakagawa, P.J. Domaille, T.C. Steimle, and D.O. Harris. Microwave optical double resonance and reanalysis of the the CaF $A^2\Pi_r - X^2\Sigma$ band system. *J. Mol. Spec.*, 70:374–385, 1987.

[180] W.J. Childs and L.S. Goodman. High-precision laser-rf double-resonance spectroscopy of the $^2\Sigma$ state in CaF. *Phys. Rev. A*, 21:1216–1221, 1980.

[181] T. E. Wall, J. F. Kanem, J. J. Hudson, B. E. Sauer, D. Cho, M. G. Boshier, E. A. Hinds, and M. R. Tarbutt. Lifetime of the A(v'=0) state and Franck-Condon factor of the A-X(0-0) transition of CaF measured by the saturation of laser-induced fluorescence. *Phys. Rev. A*, 78:062509, Dec 2008.

[182] W.J. Childs, L.S. Goodman, U. Nielsen, and V. Pfeufer. Electric-dipole moment of CaF ($X^2\Sigma^+$) by molecular beam, laser-rf, double resonance study of Stark splittings. *J. Chem. Phys.*, 80:2283–2287, 1984.

[183] T.E. Wall. *Guidung and Decelerating Cold, Heavy, Polar Molecules*. PhD thesis, Imperial College, October 2010.

[184] T.E. Wall, S.K. Tokunaga, E.A. Hinds, and M.R. Tarbutt. Nonadiabatic transitions in a Stark decelarator. *Phys. Rev. A*, 81:033414, 2010.

[185] K.P. Huber and G. Herzberg. *Constants of diatomic molecules*. Van Nostrand Reinhold Company, 1934.

[186] W.J. Childs, G.L. Goodman, and L.S. Goodman. Precise Determination of the v and N Dependence of the of the Spin-Rotation and Hyperfine Interactions in the CaF $X^2\Sigma_{1/2}$ Ground State. *J. Mol. Spec.*, 86:365–392, 1981.

[187] B.E. Sauer, Jun Wang, and E.A Hinds. Laser rf double resonance spectroscopy of ^{147}YbF in the $X^2\Sigma^+$ state. *J. Chem. Phys.*, 105:7412, 1996.

[188] M. Pelegrini, C.S. Vivacqua, O. Roberto-Neto, F.R. Ornellas, and F.B.C Machado. Radiative transition probabilities and lifetimes for the band systems $A^2\Pi - X^2\Sigma^+$ of the isovalent molecules BeF, MgF and CaF. *Braz. J. Phys.*, 35:950–956, 2005.

[189] Dan Farkas and Daniel Comparat. http://www.yale.edu/demillegroup/sharedfiles.html.

[190] G. Scoles. *Atomic and molecular beam methods*. Oxford University Press, 1988.

[191] R.V.B. Darnley. *Electrodynamic Guidung and Decelaration of Polar Diatomic Molecules*. PhD thesis, University of London, 2007.

[192] http://encyclopedia.airliquide.com/Encyclopedia.asp?GasID=34.

[193] J.H.T. Burke, O. Garcia, K.J. Hughes, B. Livedalen, and C.A. Sackett. Compact implementation of a scanning transfer cavity lock. *Rev. Sci. Instrum.*, 76:116105 1–3, 2005.

[194] E.A. Donley, T.P. Heavner, F. Levi, M.O. Tataw, and S.R. Jefferts. Double-pass acousto-optic modulator system. *Rev. Sci. Instrum.*, 76:063112–1:063112–6, 2005.

[195] Amnon Yariv. *Introduction to optical electronics*. Holt, Rinehart and Winston, 1976.

[196] D.J. McCarron, S.A. King, and S.L. Cornish. Modulation transfer spectroscopy in atomic rubidium. *Meas. Sci. Technol.*, 19:105601, 2008.

[197] C. Mok, M. Weel, E. Rotberg, and A. Kumarakrishnan. Design and construction of an efficient electro-optic modulator for laser spectroscopy. *Can. J. Phys.*, 84:775–786, 2006.

[198] Theresa A. Maldonado. *Handbook of Optics - devices, measurement and properties, volume II*. McGraw-Hill Books, 1995.

[199] W.D. Phillips. Laser cooling and Trapping of Neutral atoms. Enrico Fermi Summer School on Laser manipulation of Atoms and Ions, Varenna 1981, Lecture notes.

[200] J.F. Barry, E.S. Shuman, E.B. Norrgard, and D. DeMille. Laser Radiation Pressure Slowing of a Molecular Beam. *Phys. Rev. Lett.*, 108:103002, 2012.

[201] H. Ball, M.W. Lee, and S.D. Gensemer M.J. Biercuk. A high-power 626 nm diode laser system for Beryllium ion trapping. *Rev. Sci. Instrum.*, 84:063107, 2013.

[202] Aki Matsushima. *Transverse laser cooling of SrF*. PhD thesis, Imperial College, 2013.

[203] D. Comparat. A study of molecular cooling via Sisyphus processes. 2014. http://arxiv.org/abs/1404.2689.

[204] Eric R. Hudson. Deceleration of continuous molecular beams. *Phys. Rev. A*, 79:061407, Jun 2009.

[205] S. Raouafi, G.-H. Jeung, and Ch. Jungen. Permanent and transition dipole moments in CaF and CaCl. *J. Chem. Phys.*, 115(16):7450–7459, 2001.

[206] Chris Bowick. *RF circuit design*. Newnes, 2008.